Title
Design of Complex Systems to Achieve Passive Safety: Natural Circulation Cooling of Liquid Salt Pebble Bed Reactors

Author
Scarlat, Raluca Olga

Publication Date
2012

Peer reviewed|Thesis/dissertation

Design of Complex Systems to Achieve Passive Safety: Natural Circulation Cooling of Liquid Salt Pebble Bed Reactors

by

Raluca Olga Scarlat

A dissertation submitted in partial satisfaction

of the requirements for the degree of

Doctor of Philosophy

in

Engineering - Nuclear Engineering

and the Designated Emphasis in Energy Science and Technology

in

the Graduate Division of the

University of California, Berkeley

Committee in charge:
Professor Per F. Peterson, Chair
Professor Ehud Greenspan
Professor Brian D. Wirth
Professor Berend Smit

Fall 2012

Design of Complex Systems to Achieve Passive Safety: Natural Circulation Cooling of Liquid Salt Pebble Bed Reactors

by

Raluca Olga Scarlat

Abstract

Design of Complex Systems to Achieve Passive Safety: Natural Circulation Cooling of Liquid Salt Pebble Bed Reactors

by
Raluca Olga Scarlat

Doctor of Philosophy in Engineering-Nuclear Engineering
with Designated Emphasis in Energy Science and Technology

University of California, Berkeley
Professor Per F. Peterson, Chair

This dissertation treats system design, modeling of transient system response, and characterization of individual phenomena and demonstrates a framework for integration of these three activities early in the design process of a complex engineered system. A system analysis framework for prioritization of experiments, modeling, and development of detailed design is proposed. Two fundamental topics in thermal-hydraulics are discussed, which illustrate the integration of modeling and experimentation with nuclear reactor design and safety analysis: thermal-hydraulic modeling of heat generating pebble bed cores, and scaled experiments for natural circulation heat removal with Boussinesq liquids. The case studies used in this dissertation are derived from the design and safety analysis of a pebble bed fluoride salt cooled high temperature nuclear reactor (PB-FHR), currently under development in the United States at the university and national laboratories level.

In the context of the phenomena identification and ranking table (PIRT) methodology, new tools and approaches are proposed and demonstrated here, which are specifically relevant to technology in the early stages of development, and to analysis of passive safety features. A system decomposition approach is proposed. Definition of system functional requirements complements identification and compilation of the current knowledge base for the behavior of the system. Two new graphical tools are developed for ranking of phenomena importance: a phenomena ranking map, and a phenomena identification and ranking matrix (PIRM). The functional requirements established through this methodology were used for the design and optimization of the reactor core, and for the transient analysis and design of the passive natural circulation driven decay heat removal system for the PB-FHR.

A numerical modeling approach for heat-generating porous media, with multi-dimensional fluid flow is presented. The application of this modeling approach to the PB-FHR annular pebble bed core cooled by fluoride salt mixtures generated a model that is called *Pod*. *Pod* was used to show the resilience of the PB-FHR core to generation of hot spots or cold spots, due to the effect of buoyancy on the flow and temperature distribution in the packed bed. *Pod* was used to investigate the PB-FHR response to ATWS transients. Based on the functional requirements for the core, *Pod* was used to generate an optimized design of the flow distribution in the core.

An analysis of natural circulation loops cooled by single-phase Boussinesq fluids is presented here, in the context of reactor design that relies on natural circulation decay heat removal, and design of scaled experiments. The scaling arguments are established for a transient natural

circulation loop, for loops that have long fluid residence time, and negligible contribution of fluid inertia to the momentum equation. The design of integral effects tests for the loss of forced circulation (LOFC) for PB-FHR is discussed. The special case of natural circulation decay heat removal from a pebble bed reactor was analyzed. A way to define the Reynolds number in a multi-dimensional pebble bed was identified. The scaling methodology for replicating pebble bed friction losses using an electrically resistance heated annular pipe and a needle valve was developed. The thermophysical properties of liquid fluoride salts lead to design of systems with low flow velocities, and hence long fluid residence times. A comparison among liquid coolants for the performance of steady state natural circulation heat removal from a pebble bed was performed.

Transient natural circulation experimental data with simulant fluids for fluoride salts is given here. The low flow velocity and the relatively high viscosity of the fluoride salts lead to low Reynolds number flows, and a low Reynolds number in conjunction with a sufficiently high coefficient of thermal expansion makes the system susceptible to local buoyancy effects Experiments indicate that slow exchange of stagnant fluid in static legs can play a significant role in the transient response of natural circulation loops. The effect of non-linear temperature profiles on the hot or cold legs or other segments of the flow loop, which may develop during transient scenarios, should be considered when modeling the performance of natural circulation loops. The data provided here can be used for validation of the application of thermal-hydraulic systems codes to the modeling of heat removal by natural circulation with liquid fluoride salts and its simulant fluids.

To those who hope for a better world and
believe in the power of teaching.

To my mentors and my mentees, who have inspired me
to find art in the work that we do.

Table of Contents

List of Figures

List of Tables

Acronyms

ATWS	anticipated transient without scram
BDBE	beyond design basis event
BEPU	best estimate plus uncertainty
BU	burn-up
CHM	carbon to heavy metal ratio
CSAU	code scaling applicability and uncertainty
DBA	design basis accident
DBE	design basis events
DF	degree of freedom
DHX	DRACS salt-to-salt heat exchanger
DNB	departure from nucleate boiling
DRACS	direct reactor auxiliary cooling system
FEM	finite element model
FHR	fluoride salt cooled high temperature class of reactors
IET	integral effects test
INL	Idaho National Laboratory
KL	knowledge level
LBE	licensing basis events
LEU	low enriched uranium
LMR	liquid metal reactor
LOFC	loss of forced circulation
LOHS	loss of heat sink
LWR	light water reactor
MCNP	continuous energy Monte-Carlo neutronic modeling
NC	natural circulation
NDHX	natural air draft DRACS salt-to-air heat exchanger
NRC	Nuclear Regulatory Commission
PB-AHTR	pebble bed advanced high temperature reactor, an FHR
PB-FHR	pebble bed fluoride salt cooled high temperature class of reactors
PBMR	the Pebble Bed Modular Reactor
PIRM	phenomena identification and ranking matrix
PIRT	phenomena identification and ranking table
PWR	pressurized water reactor
QA	quality assurance
SDC	safety design criteria
SET	separate effects test
SG	steam generators
SMR	small modular reactor
SONGS	San Onofre Nuclear Generating Station
V&V	verification and validation

Introduction

"Everybody gets so much information all day long that they lose their common sense. They listen so much that they forget to be natural. This is a nice story."

Gertrude Stein, "Reflection on the Atomic Bomb" (1946)

How do we design innovative nuclear reactors in a cost and time-efficient manner, and how do we prove that they are safer than reactor technology for which the industry has decades of operational experience for hundreds of reactors? More broadly posed, the question that motivates this dissertation is how do we demonstrate the safety of complex engineered systems for which the experience base is very small or none at all?

Passive safety systems are systems that do not rely on external sources of energy for operation, and they have been adopted as a way to simplify design and lead to cheaper more reliable systems. They have capability to provide more robust safety, and this capability must be demonstrated. This dissertation demonstrates how passive safety features are designed for integration within complex engineered systems, and how the capability to predict system behavior and evaluate its safety is developed early in the conceptual design process of the complex system. Natural circulation cooling of a pebble bed reactor is analyzed here from the point of view of reactor design, transient system response, and individual underlying phenomenology. A systematic methodology is proposed for the interaction among these three types of activities that are needed for the technological development of this passive safety feature, and for its integration in the design of a large complex system, a nuclear power plant.

In the United States, the safety goal of nuclear facilities is defined by a 1986 policy statement, which sets forth qualitative and quantitative health objectives. The quantitative objective is defined in terms of prompt fatality and cancer mortality. The risk of cancer or prompt fatality posed to an individual in the vicinity of a nuclear plant must be below 0.1% of all the risks from all other causes to which the U.S. population is exposed. The value of 0.1% was chosen because it represents the year-to-year variation in the sum of the risks all other causes. Conceptually, the goal is for the incremental risks caused by nuclear plants to be within the noise of the sum of risks from all other sources[1]. For a nuclear plant, the main hazard is emission of radionuclides, so the quantitative health objective is generally translated into radioactive dose to which a person would be exposed at the site boundary, from external exposure to radiation, inhalation of contaminated air, and ingestion of contaminated water. Thus, demonstrating the safety of a nuclear plant requires demonstrating that operation of the plant will not lead to radionuclide release outside the site boundary that can pose significant risk to the population.

The paradigm for ensuring the safety of nuclear power plants centers around the defense in depth concept for preventing release of radionuclides to the environment, which can be briefly summarized as follows. Several barriers between the source term and the environment independently prevent release. Reactor safety systems maintain the conditions to which the barriers are exposed below their respective degradation limits, in order to ensure the integrity of

the barriers to release of radioisotopes. The safety systems and the barriers to release are designed to be redundant and diverse[2–4]. The source term for release of radioactive material that is primary considered in this dissertation is the fuel inside of the reactor core.

In the design for safety of complex engineered systems, the first level of defense is inherent safety, which entails elimination or reduction of the source of risk. One such example is elimination of the sources of stored mechanical energy from a reactor, such as a pressurized vessel, which could drive dispersion of radioactive material in the environment. The second level of defense is passive safety systems, which rely on the inherent physics to protect the system. Natural circulation is an example of a passive safety system. Heat transfer from the core to ambient air is driven by solely by the temperature difference between the core and the ambient air, with no need for moving mechanical parts, or external sources of energy. The third level of defense is active systems. A pump that provides forced circulation cooling of the core is one such example. The last level of defense is procedural, or operator action in the event of transients to which the plant was not designed to respond automatically.

Safety risks are quantified in a two-dimensional space: probability of event versus consequence of event. Figure 1 shows a schematic illustration. The metric used on the consequence axis depends on the scope of the analysis. At the highest level analysis of the entire plant across all scenarios, the metric is dose at the site boundary. For more detailed analysis of a subset of scenarios and a group of subsystems, the consequence metric may be the peak temperature or pressure to which one of the barriers to release is exposed, and it is subordinate to the higher level consequence metrics. For nuclear reactors, a two-dimensional representation of risk is more appropriate than a one-dimensional representation of risk (frequency multiplied by consequence), because a high probability low consequence event is managed differently from a low probability high consequence event[5,6]. Plant events are grouped in three broad categories, based on their estimated frequency. Anticipated Operational Occurrences (AOOs) have frequencies of 0.01 per year per plant or higher; they are expected to happen at least once in the lifetime of a plant. Design basis events (DBEs) have frequencies of 10^{-4} or higher; they are expected to happen once in the lifetime of a fleet of 100 reactors. Beyond design basis events (BDBEs) have frequencies of 10^{-6} or higher; they are very low probability events, which are not expected to happen in the lifetime of a plant, for an entire fleet. The three sets of scenarios, AOOs, DBEs, and BDBEs, are generally termed licensing basis events (LBEs)[7,8]. LBEs can be initiated by internal events, such as a component failure or operator error, or external events, such as earthquakes or airplane crashes. They are systematically identified and plotted on the frequency versus consequence plot, also termed the Farmer's chart. The safety limits are also plotted on the Farmer's chart. An isorisk line on the Farmer's chart has a slope of negative one, and the product of frequency times consequence is equal at any point on the line. A risk-adverse line has a steeper slope than the isorisk line; the product of frequency times consequence is lower at higher values of consequence and lower values of frequency. Nuclear plant licensing adopts a risk-adverse set of limits.

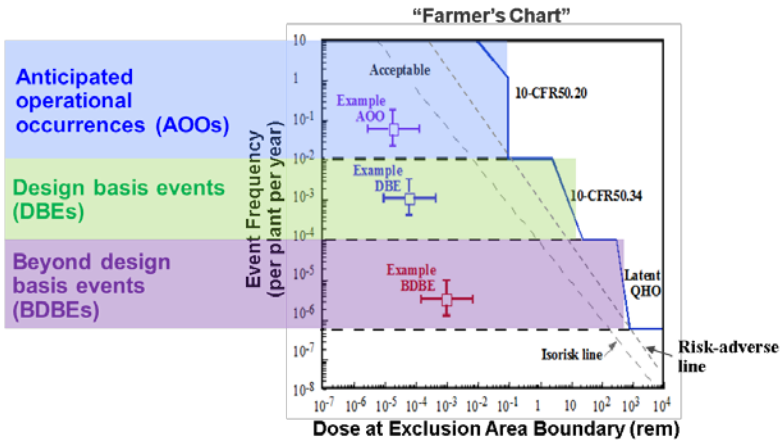

Figure 1. Probabilistic quantification of safety risk

It must be demonstrated that all the LBEs for the reactor design remain to the left and below of the safety limit lines. The magnitude of the consequence is evaluated by system models that model the transient response of the reactor. For active systems, the frequency is evaluated through probabilistic risk assessment (PRA), which computes the probability of scenarios based on event trees and component reliability data at prototypical conditions. Modeling of phenomena with very large time-scales, which can lead to component failure, such as material degradation, also contributes to generating event frequency data.

Reactor licensing is performed by the nuclear regulatory body of the country in which the reactor is to be built and operated. In the United States, nuclear reactors are licensed by the Nuclear Regulatory Commission (NRC). The reactor vendor must demonstrate, through analysis supported by sufficient experimental data, that the reactor meets a range of regulatory requirements, which include limits on the risk of radiation exposure for members of the public.

There are two licensing approaches: deterministic and probabilistic. Deterministic safety analysis relies on prescribed design recommendations, which are based on previous operating experience with similar technology, and on conservative safety margins. The probabilistic approach is more flexible and permits analysis of technology for which the experience base is limited; it also permits a realistic quantification of the safety margins, enabling prioritization of resources for the scenarios that lead to the smallest safety margins. Probabilistic safety analysis relies on computation of scenario probabilities and consequences and uncertainty quantification for both of these dimensions. The 95/95 rule for error bands is generally accepted as providing sufficient confidence: 95% confidence for the 95th percentile of the distribution of the variable. Recognizing that incomplete information and understanding also introduce uncertainty, both deterministic and probabilistic methods also require that principals of defense in depth be used in design.

Reactor design and safety analysis activities can be classified into three categories: system design, modeling of system response to specific scenarios, and characterization of individual phenomena. Figure 2 illustrates the role of modeling and experimentation in demonstrating reactor safety and in developing a reactor design. System design is iterative with identification of system states and transient scenarios. Modeling of system response relies on simplified models for behavior of the subsystems and the components and focuses on accurately representing the response of the overall system to the specific scenarios of interest. The system transient models

must be validated by experiments termed integral effects tests (IETs), which demonstrate that the system model accurately predicts the behavior of the system. Characterization of phenomena focuses on establishing the knowledge base for the underlying individual phenomenology, and it can be based on empirical measurements, analytical or numerical models that require experimental validation, or semi-empirical models. The experiments in support of phenomena characterization are termed separate effects experiments (SETs). Interactions among these activities follow a combination of top-down and bottom-up approaches.

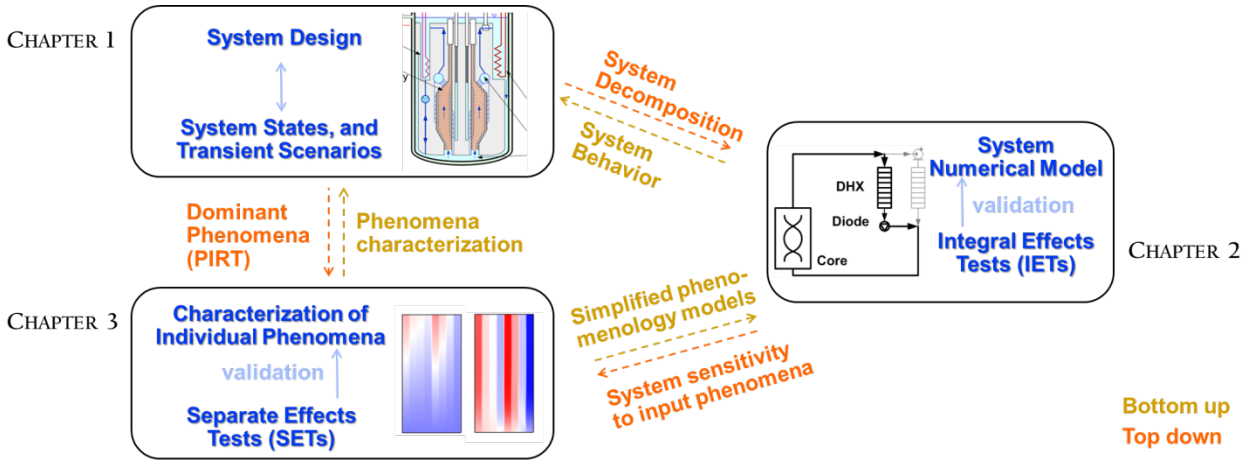

Figure 2. The role of modeling and experimentation in demonstrating reactor safety

In a top-down approach, the system design and scenario description (i.e., LBEs) drive the system decomposition, which dictates the structure of the transient system model and the simplification assumptions. The transient system model prioritizes efforts for characterization of phenomenology, based on sensitivity analysis to input phenomena. The system design and scenario definition also prioritize the need for phenomenology characterization, based on expert opinion. In a bottom-up approach, phenomena characterization provides phenomenological models that are used as inputs for the system transient model. The system transient model informs the design such that complex system behavior and the possibility for system instability are avoided as much as possible. Phenomena characterization informs system design such that desirable features are exploited and phenomena that are difficult to characterize are preferably eliminated from the design. The top-down and bottom-up approaches are complementary, and they are used iteratively.

The use of passive safety systems to meet the safety-related functions of nuclear reactors eliminates the need for external power sources to perform safety functions. The equipment used in passive safety systems is generally simpler than for active systems and does not require routine operator surveillance. Thus passive safety equipment can commonly be placed in locations where access can be infrequent, which also simplifies physical security requirements. The regulatory definition of a passive system used by U.S. Nuclear Regulatory Commission also requires that no operator action or off-site support be needed for 72 hours after the initiation of an accident[9]. Advanced light water reactors incorporate various types of passive safety features, such as gravity-draining cooling water tanks, and natural-circulation decay heat removal[53,59]. In order to ensure diversity, redundant passive and active systems will be designed to meet the safety functions, whenever possible. Passive systems are typically designed with few or no

moving mechanical parts (commonly moving parts are limited to automatic valves) and do not rely on external sources of energy, and their performance is dominated by the inherent physics of the overall system. By definition, the reliability of their constituent components is not the dominant factor that determines the likelihood of the passive system to perform its function when it is needed. The ability of passive systems to perform their function is sensitive to system conditions, and the prediction capability for the performance of passive systems is sensitive to uncertainties in model inputs such as material properties, characterization of individual phenomena, system geometry, and other model inputs. Thus, for LBEs that rely on the function of passive systems, both the consequence and the probability are evaluated by system models and integration among the activities presented in Figure 2 is further emphasized for reactors that use passive safety features.

This dissertation investigates two fundamental topics in thermal-hydraulics that illustrate the integration of modeling and experimentation with reactor design and safety analysis. Chapter 2 studies thermal-hydraulic modeling of heat generating pebble bed cores, and Chapter 3 studies scaled experiments for natural circulation heat removal with Boussinesq liquids. Examples of natural circulation systems in nature are abundant, among which magma flow, ocean circulation, atmospheric circulation[54]. In the energy field, natural circulation systems have applications such as water circulation in solar water heaters[60], and passive extraction of heat from a geothermal reservoir. Porous media thermal-hydraulics has applications to other heat generating media, such as biological tissue[21], packed bed chemical reactors[22], and heat removal or heat addition to a solid porous media for the purpose of thermal storage[26].

Chapter 1 presents a system analysis framework for prioritization of experiments and modeling, which is applicable to technology early in the development path. System reliability and safety analysis performed in the first stages of design of complex systems has high influence on the design at small cost expenditures, whereas in the subsequent phases of design the influence decreases rapidly and the expenditures rise sharply[10]. This dissertation presents examples for reactor design, integral effect experiments design for validation of system transient models, and characterization of individual phenomena, and demonstrates the framework for interactions among these activities.

Case studies used in this dissertation are derived from the design and safety analysis of a pebble bed fluoride salt cooled high temperature class of nuclear reactor (PB-FHRs). The FHR concept is currently under development in the United States at the university and national laboratories level. PB-FHRs are cooled by liquid fluoride salt eutectic mixtures, with a randomly packed bed of heat generating fuel pebbles, which rely on natural circulation for emergency decay heat removal to ambient air. Water and heat transfer oils can be used as liquid salt simulant fluids and they provide the tremendous advantage of low distortion thermal-hydraulic experiments at significantly lower temperatures, reduced geometric scale, and reduced thermal power input. The phenomena analysis presented in Chapter 2 and Chapter 3 contribute significantly to understanding the thermal-hydraulic behavior of PB-FHR systems, which has important implications for the design optimization and safety analysis of this class of reactors. The goal of FHRs is to provide an energy technology with a short commercialization timeline, with significant safety advantages compared to advanced light water nuclear reactors currently under construction, and at costs that are competitive with natural gas. The framework developed in this dissertation provides a structured methodology for prioritization of time and resources and integration of safety analysis in reactor design from very early in the technology development path of a reactor.

Acknowledgements

I want to thank the undergraduate students who were motivated to join me on this journey, who asked insightful questions that shed light on what I knew and on what I needed to understand better, and who contributed with time, creativity, and effort to the construction of the experimental facility and of the modeling tools. And above all, I want to thank them for the motivation that they gave me to keep going, because if I learned more, then they would too, and how much more rewarding I found it to see them share the aha moments, than to have my aha moments in the first place.

I am grateful to Jeffrey E. Bickel and AJ Gubser for the endless hours of conscientious work that they have put into designing, constructing, operating, and documenting the experimental loop. It is not an easy task to construct a facility for a design that is continuously evolving, for which I was to blame. I was lucky to have the help of Gordon and Mick, who have made me always look forward to projects in the machine shop - there's always a way, and it's ok if the first couple of drill bits break.

I would like to thank Professor Kastenberg for inspiring me to come to UC Berkeley to study risk analysis. I have very fond memories of Professor Olander's examinations - one should never forget the most fundamental of whys. I would like to thank professor Greenspan for the very much needed feedback that he has provided to me across the years. He has always reminded me to be thorough, to ask the blunt questions, and to follow the paths that I find most interesting.

I am thankful to Professor Wirth for always having an open door. My withdrawal syndrome from material science and chemical engineering was much soothed by attending his group meetings, sometimes hanging out with the students in in group and, serendipitously, marrying one of them. I am also thankful to professor Smit for his advice and support - he seemed to anticipate my next hurdle and provide me in advance with just the right piece of advice.

I couldn't have hoped for a better peer to work with than Nicolas Zweibaum. Our conversations often ended because we ran out of time, not out of ideas. A good part of this dissertation would not have been possible without Anselmo T. Cisneros, who provided the input for the neutronics calculations, and together with whom I had many conversations about reactor design. I have enjoyed the conversations with Professor Blandford; it often sounded like we disagreed, but it was just a more thorough way of agreeing with each other.

I want to thank Gabriel Meric de Bellefon, my partner, with whom I've had lengthy discussions about natural circulation, and who has many times lend structure to my thoughts. I want to thank Cristian Scarlat, my father, for our conversations about turbines and power plants, which made the implications of this thesis feel more tangible. I want to thank Sanda Scarlat, my mother, for always reaching for the bigger question, the bigger dream. Olga Selma, my daughter, I can't say that you've taught me about thermal-hydraulics, but thank you for keeping me company during the long nights of working on this dissertation.

This dissertation would not have been possible without the guidance and mentoring of Professor Peterson, whom I would like to thank for his patience, and for the constant reminder to seek simple answers. Such answers are the hardest to find, because they address the problem at the most fundamental level.

This research was performed using funding received from the U.S. Department of Energy Office of Nuclear Energy's Nuclear Energy University Programs.

Curriculum Vitae

Raluca O. Scarlat **ros2@cornell.edu**

Career objective: an academic career in the area of thermal-hydraulics and thermodynamics, risk analysis, and energy systems.

EDUCATION

Ph. D. Nuclear Engineering with Designated Emphasis in Energy Science and Technology, UC Berkeley, 2012
M.S. Nuclear Engineering, UC Berkeley, 2009
Certificate in Management of Technology, Haas School of Business, UC Berkeley, 2009
B.S. Chemical and Biomolecular Engineering, Cum Laude, Cornell University, 2006

RESEARCH EXPERIENCE

THERMAL-HYDRAULICS LABORATORY, Ph.D. Student June 2008 – Dec. 2012
Peterson Research Group, Nuclear Engineering University of California, Berkeley

- Ph.D. thesis title: "Design of Complex Systems to Achieve Passive Safety: Natural Circulation Cooling of Liquid Salt Pebble Bed Reactors "
- Research objective: Establish a top-down framework for design, risk and safety analysis of complex engineering systems, and apply it to the Pebble Bed Fluoride Salt Cooled Reactor (PB-FHR) concept.
- Studied natural circulation heat removal systems, high Prandtl number fluids, convection in pebble beds, and performed experiments for phenomena characterization and validation of system models.
- Developed a multi-scale numerical model of the pebble bed core, to identify relative importance of phenomena in salt-cooled pebble beds, and provide a tool for prioritizing experimental work and design optimization.
- Software and codes: COMSOL, Thermoflex, OriginPro, Mathematica, Matlab, LabView, SolidWorks. Thermal-hydraulic experimental tools: brazing, metal machining, thermocouple welding, data acquisition systems.

MESOPOROUS NONOXIDE CERAMICS, Undergraduate Researcher June 2004 – May 2006
Wiesner Research Group, Material Science and Engineering Cornell University

- Mesoporous nonoxide ceramics are high temperature-resistant and have application in power generation and power conversion.
- Developed synthesis methods of porous non-oxide ceramics with control of nano, meso and micro hierarchical structure.
- Contributed to development of block copolymer-directed synthesis of mesoporous SiCN and SiC ceramics, and initiated development of two-photon lithography process for generating high resolution three-dimensional micro-structures.
- Analytical tools: SAXS, IR, SEM.

GREEN TIRE TECHNOLOGY, Summer Research Intern May 2005 – August 2005
GE Global Research Center, Polymer and Chemical Technology Group Niskayuna, NY

- Novel material development for the truck tire rubber, targeting an increase in truck efficiency and safety, and reduction of tire wear.
- Tested a candidate functionalized polymer as filler for a reinforced elastomer, and characterized filler-elastomer interactions.
- Scaled-up organic synthesis of functionalized polymers, and developed processes for manufacturing of nano-particle precipitates.
- Analytical tools: NMR, BET, DSC, TGA, TGA-IR, GC-MS, XRF, GPC.

TEACHING EXPERIENCE

Lecturer

- Abnormal Event Detection Off-line Process Modeling. 20 plant engineers and application developers. ExxonMobil Corporation, 2006
- Advanced Excellence Workshop for Linear Algebra. 10-15 undergraduate students. Cornell University, 2006.
- Thermal aspects of nuclear reactors. 2-3 lectures. 10-15 graduate students. UC Berkeley, 2011, 2012.

Graduate Student Instructor

- Energy and Society. 1 lecture, and 16 recitations. 150-200 multi-disciplinary students. UC Berkeley, 2008
- Engineering Thermodynamics. 16 recitations. 50 undergraduate students. UC Berkeley, 2007
- Introduction to Nuclear Reactor Theory. 4 recitations. 20 students. UC Berkeley, 2008

Education Training

- Designing Courses and Course Syllabi to Enhance Motivation, Psychology Course, UC Berkeley, 2010
- Teaching Conference for Graduate Student Instructors, UC Berkeley, 2007
- Training Seminar for Advanced Excellence Workshop Facilitator, Cornell University, 2005

PROFESSIONAL EXPERIENCE

REACTOR ENGINEERING, Engineering Intern September 2011 - October 2011
Hitachi-GE Power Systems, Plant Engineering Department Hitachi, Japan

- Studied Fukushima Daiichi Unit 1 accident progression, investigated optimal timing for PVC venting, and used MAAP models to understand the most likely current status of the core.
- Modeled ABWR response to extended station black-out, and identified severe accident management strategies for the Japanese fleet.

ABNORMAL EVENT DETECTION, Operator Guidance Tools Engineer July 2006 – August 2007
ExxonMobil Research & Engineering, Automation and Optimization Division Fairfax, VA

- Developed and deployed Abnormal Event Detection (AED) advanced controls applications for petroleum refinery and chemical process units; AED applications are designed to prevent process upsets and the consequent pollutant air emissions.
- Streamlined application deployment by building automated tools for data processing and model building.

SILICONES CHEMICAL PLANT, Engineering Co-op August 2004 – January 2005
GE Silicones, Continuous Improvement Team, Technology Department Waterford, NY

- Designed and built semi-automated laboratory-scale scaled model of an operating chemical processing unit.
- Developed process options and a preliminary cost estimate for a new product line, and led production of an experimental grade.
- Completed online Six Sigma training, and gained preliminary experience in using project management and statistical tools.

SELECTED AWARDS

Excellence Award, Nuclear Energy Fuel Cycle R&D, US Department of Energy, 2009
Graduate Fellowship, Nuclear Engineering University Programs (NEUP), US Department of Energy, 2009-2012
Outstanding Graduate Student Instructor, University of California Berkeley, 2007-2008
Leadership Award, ExxonMobil Automation & Optimization Division, 2006
Undergraduate Research Grant, Engineering Learning Initiatives, Cornell University. 2005, 2006
Exemplary Mathematics Achievement, The California Mathematics Council and the California Department of Education, 2000-2001
Literature and Written Composition Honors, 2001 Golden State Examination

PERSONAL INFORMATION

Professional Affiliations

- Berkeley Energy and Resources Collaborative (BERC), VP of Nuclear Engineering Membership (2011)
- American Nuclear Society (ANS), Outreach Co-Chair for UC Berkeley Chapter (2009-2010)
- American Institute of Chemical Engineers, Corporate Relations Chair for Cornell University Chapter ('05-'06)

Professional Training

- Presenting Data and Information: a one-day course taught by Edward Tufte, San Francisco, CA 2011
- Modeling Experimentation and Validation Summer School (MEV), Idaho Falls, ID, 2009
- Public Policy and Nuclear Threats Course, Institute for Global Conflict & Cooperation (IGCC), San Diego, '10
- ICTP-IAEA Course on Natural Circulation Phenomena and Passive Safety Systems, Trieste, Italy, 2010
- Public Policy and Biological Threats Summer Training Workshop, IGCC, San Diego, CA, 2009
- The LeaderShape® Institute Leadership Retreat, 2004

Other Activities

- Technical Team Leader, Platform Retrofit Ocean Geothermal Energy (PRO-Geo) Project
- Community involvement: ATOM Science Kids' Day, and Thurston High School Lectures in Oakland California

Languages

- Romanian and French (fluent), Italian and Japanese (basic)

PUBLICATIONS

R. O. Scarlat, P. F. Peterson. The current status of fluoride salt cooled high temperature reactor (FHR) technology and its overlap with HIF target chamber concepts. *Proceedings of the 19th International Symposium on Heavy Ion Inertial Fusion (HIF2012)*. Berkeley, California. August 2012.

Scarlat, R. O., Cisneros, A. T., Koutchesfahani, T., Hong, R. & Peterson, P. F. Preliminary safety analysis of a PBMR supplying process heat to a co-located ethylene production plant. *Nuclear Engineering and Design (2012)*.

R.O. Scarlat, M. Laufer, A.T. Cisneros, N. Zweibaum, J. Seifried. "Preliminary Fluoride Salt-Cooled High Temperature Reactor (FHR) Subsystems Definition, Functional Requirement Definition and Licensing Basis (LBE) Identification White Paper." Department of Nuclear Engineering, University of California Berkeley. March 2012.

R. Scarlat and E. Greenspan "Maximizing Power of Hydride Fuelled Pressurized Water Reactor Cores." *Proceedings of the Joint International Workshop on Nuclear Technology and Society – Needs for the Next Generation.* Berkeley, CA 2008.

M. Kamperman, P. Du, R. Scarlat, E. Herz, U. Werner-Zwanziger, R. Graf, J. Zwanziger, H. Spiess, U. Wiesner. "Composition and Morphology Control in Ordered Mesostructured High-Temperature Ceramics from Block Copolymer Mesophases." *Macromolecular Chemistry and Physics.* 2007, 208(19-20), 2096-2108.

CHAPTER 1

A structured methodology for conceptual design of complex engineered systems

In the design of large complex engineered systems, as the design progresses, changes become increasingly costly and challenging to implement. Post et. al. shows that 65% of the lifetime cost for a chemical process plant is committed in the planning phase, and 80% is committed in the preliminary design phase; he argues that system reliability and safety analysis performed in the first stages of design has high influence on the design at small cost expenditures, whereas in the subsequent phases of design the influence decreases rapidly and the expenditures rise sharply[10]. Most complex engineered systems, including nuclear reactors, are regulated to assure that their safety, public health, environmental, and security impacts are acceptable. If the analysis tools used to assess safety and other regulatory performance requirements can only be applied to a well-developed design, then the cost of meeting regulatory performance criteria requirements can be high, and the ability to improve beyond minimal compliance doubtful. As problems are identified, the lack of robustness in the system design can lead to costly back fits or premature decommissioning.

For example, methodologies that are common practice for the safety analysis of nuclear reactors, such as CSAU, PIRT, and H2TS[11], while flexible in the sense that they are technology-neutral, require well defined designs. This pushes system designers towards incremental changes to evolutionary systems, which rely on the experience with previous technology in order to design for safety and other regulatory performance requirements. Thus, tools that enable integration of safety analysis and other types of risk analysis very early on in the design process of a complex engineered system are needed for the development of revolutionary technologies.

The system analysis framework demonstrated in this chapter is derived from safety analysis methodology, specifically Phenomena Identification and Ranking Tables (PIRT), but with significant modifications to account for the fact that the system being studied does not have a well-defined detailed design. For complex engineered systems that are still early in the development path, several options are pursued in parallel for many of the design choices, in order to manage the failure risks of implementing new technologies. Directly applying safety analysis methodology at this stage in the design would be unreasonably time-consuming, requiring specific analysis of each combination of design options.

The case study treated in this chapter is the characterization of the thermal-hydraulic behavior of the primary coolant system in PB-FHR. This case study generates a *prioritized map* of the modeling tools and experiments that are needed. As opposed to a *prioritized list*, a prioritized map more rapidly adapts to changes in design, and more easily integrates new understanding of the underlying phenomenology.

1.1 PIRT Exercise for PB-FHR Thermal-Hydraulics - Background

Best Estimate Plus Uncertainty (BEPU) methodologies were developed by the NRC in the 1990s, as an effort to complement the existing rule-based, deterministic licensing approach. The BEPU approach includes the Code, Scaling, Applicability and Uncertainty (CSAU) methodology[12]. CSAU is a structured methodology to identify the phenomena that need to be modeled for a specific transient of a specific nuclear plant, to select an applicable code, and to quantify the aggregate uncertainty to the prediction of a representative metric for the specific transient being studied. While CSAU is a thorough methodology for quantifying uncertainty, because it is time and computationally-expensive it has not been broadly adopted in its entirety.

Embedded in the CSAU methodology is the Phenomena Identification and Ranking Table (PIRT) methodology, which has been much more broadly adopted. PIRT is a methodology that relies on analysis, scaling, and expert judgment to identify and rank key phenomenology for a specific system undergoing a specific time phase of a specific transient. The PIRT process generates a prioritized list of key phenomena that need to be characterized and modeled for each component of the system. It also ranks the knowledge level for each key phenomena for each component, thus identifying critical gaps in the understanding of specific phenomena. In the CSAU methodology, the step that follows PIRT is identification of a code that is appropriate for modeling the system with the key phenomenology that was identified in the PIRT results.

Previously, the PIRT process has been applied to reactors in operation, or reactors for which detailed engineering design exists, and for reactor designs where a wider base of expert knowledge exists. We are interested here in applying the PIRT process much earlier in the design of the reactor, which allows for integration of safety analysis early on in reactor design.

The methodology presented in this chapter very closely parallels the PIRT methodology, however the system to which it is applied and the goals of this PIRT exercise differ from a conventional PIRT. Firstly, the methodology is applied to a system where detailed design does not yet exist and where a large number of design options remain and are developed in parallel. Secondly, *the set of scenarios is spanned*, but for a *narrow set of phenomenology*. As described in the Next Generation Nuclear Plant (NGNP) Phenomena Identification and Ranking Table (PIRT) Report, "the PIRT is a structured expert elicitation process designed to support decision making[13]." The approach taken here follows the same distinct steps as the NGNP PIRT, with modifications to some of the steps, which are summarized in Table 1-1.

Table 1-1. Deviation from PIRT methodology for application of safety analysis early in the design path

	PIRT Methodology	Modifications
Step 1	define the issue that is driving the need for a PIRT	
Step 2	define the specific objectives for the PIRT	
Step 3	define the hardware and the scenario for the PIRT	PASSC + H2TS decomposition
Step 4	define the evaluation criteria	
Step 5	identify, compile, and review the current knowledge base	define functional requirements
Step 6	identify the plausible phenomena	span a range of transients
Step 7	develop importance ranking for phenomena	ranking maps, and interaction matrices (PIRM)
Step 8	assess knowledge level for phenomena	
Step 9	document PIRT results	

1.2 Step 1: Define the issue

There are three top level issues that motivate this exercise:

1. Design development.

- A systematic methodology to guide reactor design, with early integration of safety analysis is needed.
- The subsystems and components that need further detailed design, in order to better characterize the transient behavior of the system, need to be prioritized.
- If dominant not well-characterized phenomena can be excluded from the design, PIRT will help to identify these early in the development process.
- The phenomena interactions that lead to complexity need to be identified, and design revisions shall be proposed to reduce these.

2. Construction of system-level transient modeling tools and integral effects experimental facilities.

- The modeling tools and experiments that are needed for design and safety analysis need to be identified and prioritized.
- A system decomposition framework for system modeling, and design of scaled integral effects tests needs to be provided.

3. Construction of separate effects experiments and modeling tools for the characterization of individual phenomena and phenomena coupling.

- Dominant phenomena that are not well characterized need to be identified and prioritized. Future SETs and simulation efforts that are needed to reduce system model uncertainty and experimental distortion need to be defined and prioritized.
- Dominant phenomena coupling that is not well characterized needs to be identified.
- The potential areas or components for which multi-physics and multi-dimensional modeling are needed, need to be identified and prioritized.

1.3 Step 2: Define specific objectives

The case study treated in this chapter is the characterization of the thermal-hydraulic behavior of the primary coolant system in PB-FHR. The specific objectives of this exercise are as follows:

1. Establish evaluation criteria for the thermal-hydraulic performance of PB-FHR.
2. Establish a decomposition scheme for the system.
3. List the functional requirements that form the basis of design assumptions that are used for the development of this PIRT.
4. Identify the dominant thermal-hydraulic phenomena that are not well characterized.
5. Identify and rank the thermal-hydraulic coupling among subsystems and components.

1.4 Step 3: Hardware and scenario

1.4.1 System Decomposition

The system decomposition approach proposed here integrates the higher-level plant, areas, systems, subsystems, and components (PASSC) break-down convention[14] used by NGNP with the decomposition paradigm for hierarchical two-tier scaling analysis (H2TS) methodology[11]. Figure 1-1 shows schematically the integration of the two system decomposition approaches.

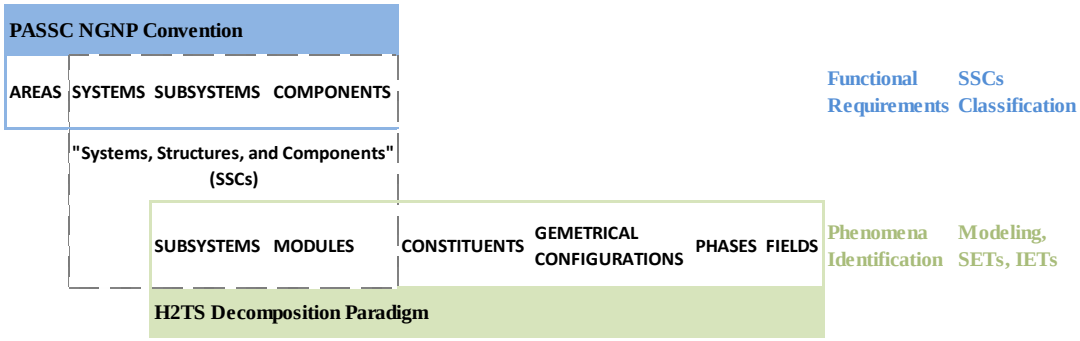

Figure 1-1. System decomposition paradigm used with the PIRT methodology

The PASSC convention includes areas, systems, subsystems, and components. It is convenient to use this convention because the "systems, structures, and components (SSCs)" terminology is important in safety classification established by 10 CFR 50.69[15] and it easily maps onto the systems, subsystems, and components levels of the PASSC convention.

Hierarchical two-tier scaling is a methodology for decomposing a system based on temporal and spatial scales and phenomenology coupling. This enables the breakdown of a large system in smaller systems that can be more easily studied, and which contribute to the understanding of the overall system with little distortion due to their separation from the larger complex system. It also enables the study of simplified larger systems, with little distortion due to the simplified treatment of the subsystem. The methodology has been very powerful in enabling an understanding of the system evolution in response to disturbances, or initiating events, and it has enabled better management of the safety of nuclear plants, and better understanding of the system vulnerabilities[11].

The H2TS system decomposition paradigm includes the system, subsystems, modules, constituents, geometrical configurations, physical phases (gas, liquid, solid), fields and phenomena. Fields are chosen to be consistent with scaling methods. For PB-FHR, fields include energy, fluid momentum, pebble momentum, neutron flux, chemical potential, cover gas pressure, and mechanical stresses in solid components. The example in this chapter focuses specifically on the energy field. Using this paradigm allows for direct application of the Phenomena Identification and Ranking Table (PIRT) results to the design of scaled experiments. It also facilitates application of analytical calculations to support qualitative phenomena ranking rationale.

In the FHR system decomposition, the module level of the H2TS paradigm coincides with the component level of the PASSC convention. Figure 1-1 compares the decomposition levels for the two conventions, and the way that they are used for a consistent FHR decomposition scheme. Functional requirement definition (discussed in Step 5) and safety classification are done at the system, subsystem and component levels; phenomena identification and ranking (discussed in Step 6 and Step 7) and subsequent prioritization of modeling and experimental efforts additionally use the lower levels of the system decomposition. Integration of the two decomposition approaches enables an iterative process between the identification of system behavior and identification of individual phenomena, which makes the PIRT methodology applicable to complex technology for which a complete system description is not yet available.

1.4.2 Hardware description

Table 1-1, Figure 1-2 and Figure 1-3 summarize and depict the key areas, systems and subsystems for PB-FHR. Only two of the system areas, Nuclear Heat Supply and Heat Transport, are used for the analysis in this chapter. Further detail about the PB-FHR reactor design is given in Appendix A. The FHR decomposition approach presented here was selected to be generic enough to encompass a broad range of FHR design options.

Table 1-2. Summary of Key FHR Systems and Subsystems

AREAS	SYSTEMS	SUBSYSTEMS
Nuclear Heat Supply	Reactor	Fuel
		Primary coolant
		Primary pump
		Graphite reflectors
		Core barrel & downcomer
		Upper core support structures
	Reactivity Control	Reactivity control system
		Reserve reactivity control system
	DRACS	DRACS heat exchanger & diode (DHX)
		DRACS piping & insulation/ electrical heating
		Natural Decay Heat Exchanger (NDHX) and Air Stack
	Reactor Vessel and Reactor Cavity	Reactor Vessel/Guard Vessel
		Reactor cavity cooling & insulation
		Electrical heating subsystem
		Buffer salt subsystem (if used)
		Concrete walls
Heat Transport	Intermediate Loop	Intermediate heat exchanger (IHX)
		Power conversion heat exchanger (PCHX)
		Process heat exchanger (PHX)
		Shutdown cooling and maintenance heat removal subsystem
		Piping and drain tank subsystem
Main Support Systems	Coolant chemistry, particulates & inventory control	
	Cover gas chemistry, particulates & inventory control	
	Fuel handling and storage	
	Plant instrumentation and control (I&C)	
Power Units	Power conversion system Process heat system	
Balance of Plant	Fire protection system Reactor citadel Seismic base isolation External event shield Heating, ventilation, and air conditioning Component cooling & service water system Radioactive waste handling AC/DC power supply and distribution Control rooms	

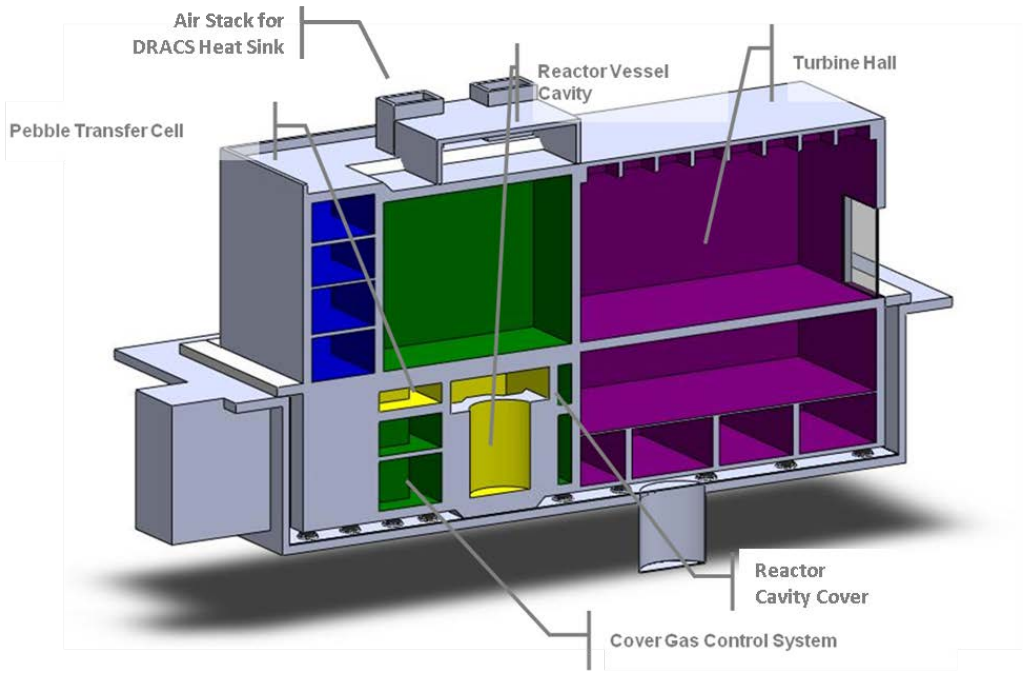

Figure 1-2. FHR Reactor Building Schematic16: reactor cavity (yellow), filtered confinement (green), and external event shell (blue/purple)

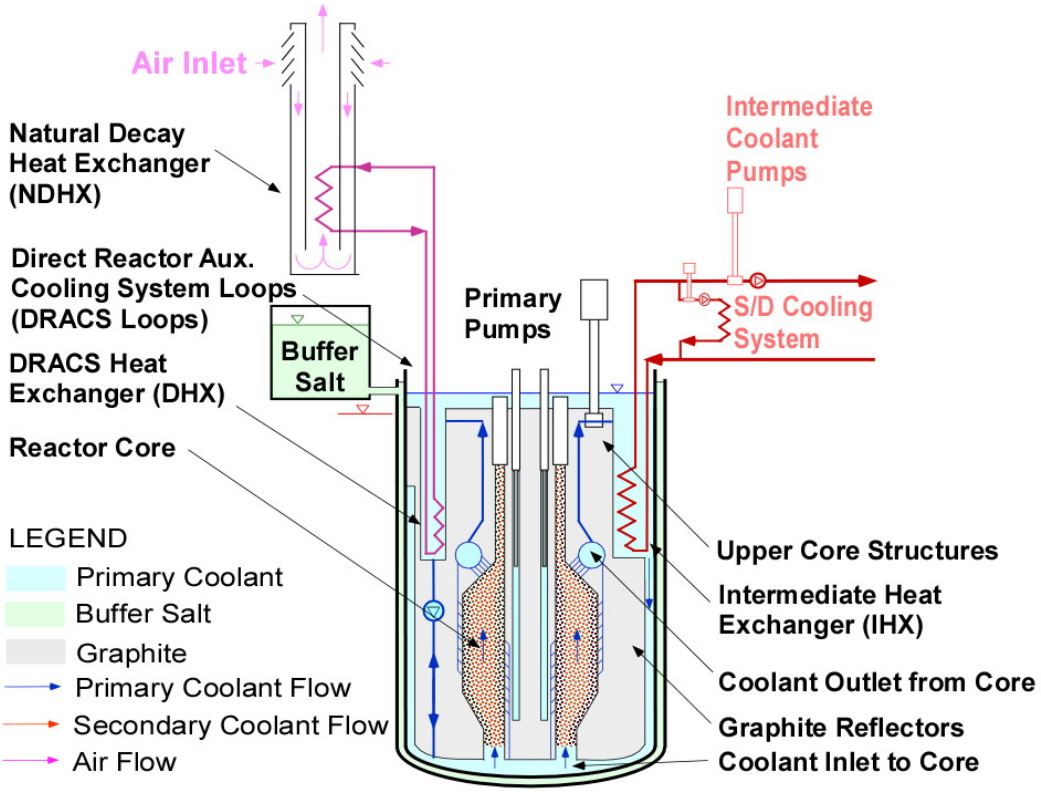

Figure 1-3. PB-FHR Schematic Diagram

1.4.3 Scenarios

Modeling and experimentation programs need to be established that are capable of spanning a wide range of potential transients, which for nuclear applications are termed licensing basis events (LBEs), including (1) steady-state behavior, (2) short term anticipated transients (such as start-up and shutdown), (3) short term design basis events (DBEs) and beyond design basis events (BDBEs), and (4) long term material degradation under steady-state operation.

LBE identification is an extensive process, and it is iterative with functional requirement identification[17]. To keep the scope of the present exercise manageable, only a subset of LBEs are identified here, which are representative of the span of phenomenology that the system may exhibit[17,18]:

- Loss of forced circulation (LOFC) with or without SCRAM, with passive decay heat removal.
- Loss of heat sink (LOHS) with or without SCRAM, with passive decay heat removal.
- Normal start-up and shutdown transients, using the normal heat removal systems.

1.5 Step 4: Define the evaluation criteria

The evaluation criteria for FHRs are:

1. Peak coolant outlet temperature, which is directly related to peak temperature of metal structural materials.
2. Minimum primary coolant temperature and margin to freezing.
3. Average fuel temperature, which affects ATWS response.
4. Peak fuel temperature, which correlates with the fraction of failed TRISO particles.
5. Sharp local temperature transients, and large local temperature gradients leading to thermal shock, thermal striping, thermal gradient, and differential thermal expansion of components, which can lead to stresses on the structural components.

1.6 Step 5: Identify and compile the current knowledge base

The knowledge base depends on the one hand on the availability of design information for each of the subsystems and components (or potentially similar systems), and on the other hand on the fundamental understanding of the phenomena governing their behavior. For complex systems that are early in the technology development, the knowledge base for the systems for which detailed design is not available is replaced with functional requirements for the system behavior. These functional requirements document the basis of assumptions used for the development of this PIRT analysis. An iterative series of refinement of the system design and PIRT analysis provides a systematic methodology for technology development.

1.6.1 Functional requirements definition

As the design options are explored, assumptions must be made about how the systems and subsystems might perform. Functional requirement definition provides a systematic method to document assumptions about system behavior that are made before the detailed design is available. Functional requirements then guide detailed design. A *hierarchical approach to functional*

requirements, following the system decomposition scheme established in Step 3, should be adopted.

Table 1-3 provides the top level design requirements for FHRs, and one of these requirements is to ensure and demonstrate safety. The safety design criteria (SDCs) are used to define a high-level strategy for ensuring safety of FHRs, and they are listed in Table 1-4. The SDCs proposed here to assess the safety of FHRs are adapted from similar top level safety-related design criteria that have been established for other reactor technologies. The six FHR "SDCs" are equivalent to the eight LMR "Top Level Safety Functions" and the six PBMR "Required Safety Functions."[15,19] The PBMR "Safety Functions" are organized in a hierarchical structure that includes the first four of their "Required Safety Functions" along with the additional "supporting safety functions," which are not required, but provide defense in depth. Before addressing specific licensing requirements for FHRs, the initial step is to define the overall safety philosophy for FHRs. The SDCs and the strategy for meeting them will guide the review of nuclear reactor licensing requirements for applicability to FHRs, and will provide a framework for ensuring completeness of the FHR safety strategy.

Table 1-3. Top level FHR design requirements

Top Level Requirements	Motivation
Safety Design Criteria (SDCs)	Ensure safety
Economics (E)	End-user
Investment Protection (IP)	
Safeguards (SG)	Nonproliferation and security
Physical Security (PS)	

Each SDC defines a class of lower-level safety functions, which guide design. As an example, Table 1-5 lists the safety functions subordinate to SDC 3, control of heat removal and addition. The control of heat removal is important to prevent overheating of reactor structures and to limit thermal stresses and thermal creep deformation during transients and accidents. The control of heat addition and excessive heat removal is important to prevent and to recover from overcooling transients that might cause localized freezing of the primary or secondary coolants, and subsequently inhibit control of heat removal.

Table 1-4. Proposed FHR Safety Design Criteria (SDCs)

FHR SDCs
1. Maintain control of radionuclides
2. Control heat generation (reactivity)
3. Control heat removal and addition
4. Control primary coolant inventory
5. Maintain core and reactor vessel geometry
6. Maintain reactor building structural integrity

The safety functions lead to a subset of the system and subsystem functional requirements. Appendix A has a more extensive list of functional requirements for the reactor system and its subsystems. A subset of these are further discussed in Chapter 2 and Chapter 3, in the context of system design and optimization.

Table 1-5. Engineered safety functions primarily related to SDC 3

SDC 3: Control Heat Removal and Addition
1. Normal heat load (power units)
2. Shutdown, start-up, and maintenance cooling
3. Passive decay heat removal (DRACS)
4. Reserve shutdown cooling for decay heat removal (if used)
5. Reactor cavity cooling
6. Heat sink throttling for parasitic heat load control
6. Reactor cavity thermal insulation and electrical heating
7. Electrical heating systems for salt inventories external to reactor cavity

1.7 Step 6: Identify the plausible phenomena

This PIRT exercise focuses strictly on energy transport phenomena. To a very limited extent, it may also include momentum transport phenomena, in the cases in which these are tightly coupled with the energy transport phenomena.

Thus the set of plausible phenomena is: nuclear heat generation (fission and decay heat), irradiation heat deposition, convection, mixing, conduction, thermal radiation, temperature boundary condition, and heat flux boundary condition.

1.8 Step 7: Rank the phenomena

1.8.1 Phenomena ranking map

Phenomena importance is specific to each component, and of course to each scenario. Mapping the importance of specific phenomenology across the system is a useful graphical tool, which is instrumental in refining the system decomposition, and defining system boundaries of integral effects experiments and numerical systems models that will lead to minimal distortion of the system behavior.

Figure 1-4 is a simple example of such a map, which ranks the mass flow rate in various flow paths, and the thermal mass of the solid components for the primary coolant circuit of PB-FHR. The blue boxes indicate the solid constituents in contact with the primary coolant. Purple indicates the primary coolant free surfaces, where the coolant is in contact with the cover gas. The temperatures are representative temperatures of the primary coolant during normal operation. The darkness of the black lines ranks the importance of the respective flow paths. Thick black lines indicate regions of high flow rate or high fluid inventory, thin gray lines indicate regions of low flow rate and low fluid inventory. The width of the blue boxes indicates the relative thermal mass of the solid component. Wide boxes indicate high thermal mass, narrow boxes indicate low thermal mass components.

Figure 1-4. Phenomena ranking map: PB-FHR Primary coolant flow paths and the major solid components in contact with the primary coolant.

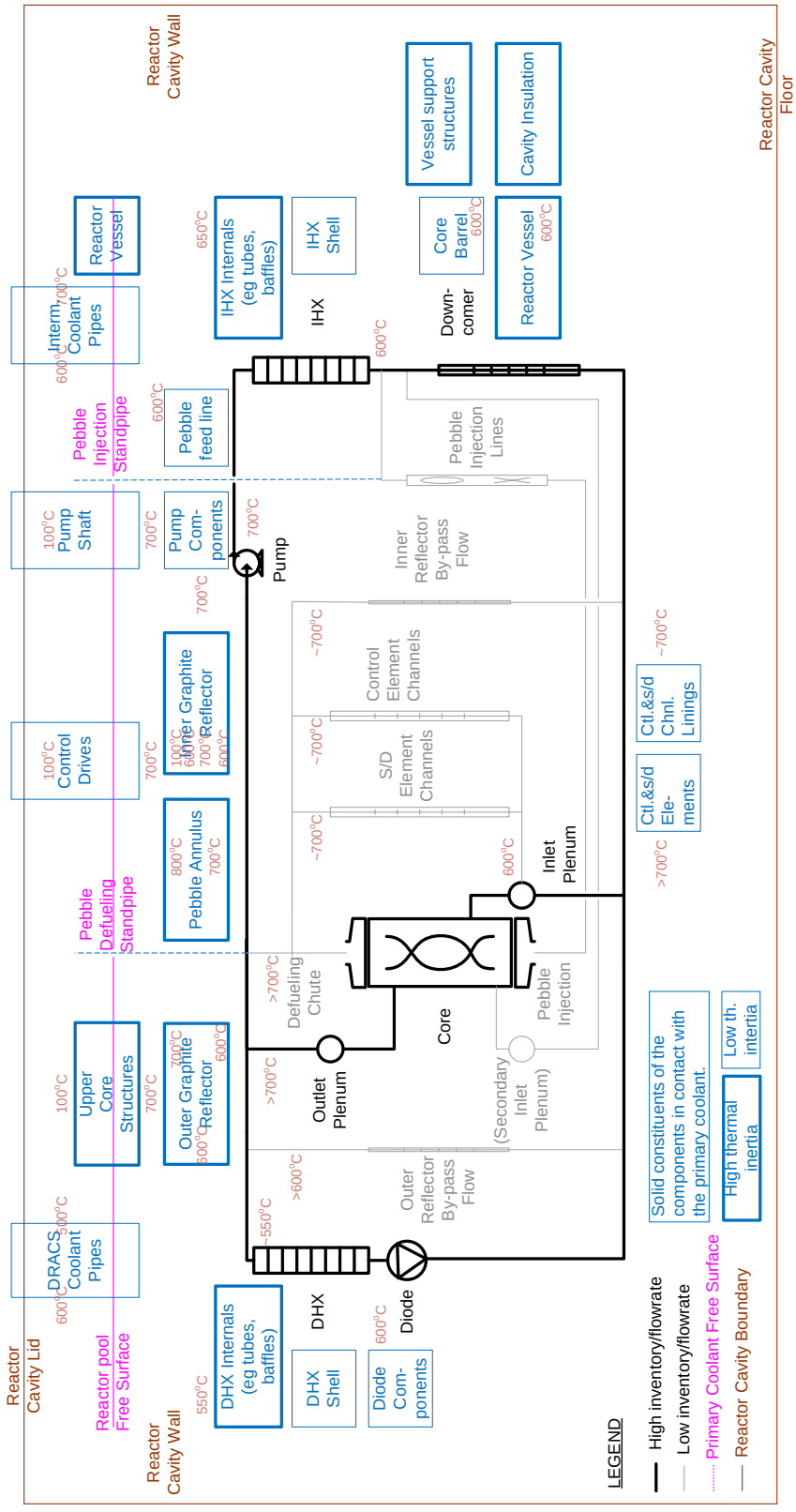

A scaled integral effects experiment for the dominant coolant flow path identified by Figure 1-4 is discussed in Chapter 3. Future iterations of this experiment will be built to also take into account the thermal inertia of the dominant solid components identified in Figure 1-4.

1.8.2 Phenomena Identification and Ranking Matrix (PIRM)

In addition to prioritizing the key phenomena for each of the components, it is also crucial to understand the importance ranking of the coupling among components. Thus, the phenomena identification and ranking table (PIRT), more appropriately becomes a phenomena identification and ranking matrix (PIRM).

PIRM is a square matrix, with each row representing a component, and the columns representing the components that may affect the behavior of this component. Each cell lists and ranks the dominant phenomena by which each two components are coupled. The phenomena and component coupling are ranked based on three levels of importance: (1) dominant effect, (2) secondary effect, or (3) negligible effect. The level of importance is scenario-specific. Since this PIRT is focused on identifying the modeling and experimentation capabilities that are needed, the highest importance level across all scenarios will be listed in the PIRM.

Table 1-6 shows the PIRM results for heat transfer phenomena in the primary coolant circuit of a PB-FHR, across the range of transients defined in Step 3. For example, the outer graphite reflector (row 3) will exchange heat with the core (column 1) by convection and thermal radiation, with convection being a dominant phenomenon. The reflector is also heated by neutrons and gammas coming from the core; this is also a dominant coupling. Reading across the first row, the key components which affect the behavior of the core can be identified. The diagonal of the PIRM identifies and ranks the phenomena relevant within each component, and it is in effect equivalent to a PIRT table. The PIRM matrix is not necessarily symmetrical, since component coupling is not always two-way, or it may not have the same ranking in both directions.

PIRM is a useful tool in guiding modeling work and design of integral and separate effect experiments. As an example, Table 1-7 shows a simplified version of the larger Table 1-6. For modeling the thermal behavior of the core, the PIRM results show that heat generation and convective heat transfer are key phenomena inside the core. The effect of external components on the behavior of the core will have to be accounted for through boundary conditions. The primary external component that affects the core is the inlet plenum, which will specify the core inlet coolant temperature. Secondary external components are the secondary inlet plenum, inner reflector, outer reflector, and other primary coolant flows. In an initial modeling of the core, the coupling to these components can be neglected. Such an initial numerical model for the PB-FHR core was built, and is discussed in Chapter 2. For a more accurate model of the core, the boundary conditions will be adjusted to take into account the effects of these secondary components; this achieves only a one-way coupling. For an even more accurate model of the core, the boundary of the model will expand to include components with which the core couples; this achieves a two-way coupling.

Table 1-6. Energy Field PIRM for PB-FHR Primary Coolant Circuit, with grouping for modeling of primary coolant natural circulation loop.

	Active Core: Pebble Annulus	Inner Reflector	Outer Reflector	Upper core structures	Inlet Plenum + piping	Pebble Feed & Secondary Inlet Plenum	Outlet Plenum + piping	Other outer reflector primary coolant flows	Defueling chute	Shut-down element channels	Control element channels	Other inner reflector primary coolant flows	IHX & Pump	DHX & Diode	Downcomer & core barrel	Reactor vessel	Reactor Vessel Insulation & Top thermal shield	Reactor Cavity Walls	DRACS Piping	NDHX	Intermediate Coolant Pipes	PHX
	1	2	3	4	5	6	7	8	9	10	11	12	13	14	15	16	17	18	19	20	21	22
1	G, CV, R, CD	CV, R, CD	CV, R, CD	--	T	T	--	--	--	--	--	T	--	--	--	--	--	--	--	--	--	--
2	CV, D, R, CD	CD, D	--	--	CV	--	--	--	CV	CV	CV	CV	--	--	--	R	CD	--	--	--	--	--
3	CV, D, R, CD	--	CD, D	CD	--	CV	CV	CV	--	--	--	--	--	--	CD	R	--	--	--	--	--	--
4	--	--	CD	CD	--	CV	CV	CV	CV, CD, R	--	--	--	CD	CD	CD	CD	CD	--	CD	--	CD	--
5	--	--	--	--	--	T	--	T	--	--	--	--	--	T	T	--	--	--	--	--	--	--
6	--	--	--	--	--	G, CV	--	--	--	--	--	--	T	--	--	--	--	CD	--	--	--	--
7	T	--	CV	CV	--	--	M	T	--	--	--	T	--	--	--	--	--	--	--	--	--	--
8	T	--	CV	CV	--	T	T	--	T	--	--	CV	T	T	T	--	--	--	--	--	--	--
9	T	CV, R, CD	CV, R, CD	--	--	--	--	T	G, CV	T	T	T	--	--	--	--	--	CD	--	--	--	--
10	--	CV, R	--	--	T	--	--	--	--	D	--	--	--	--	--	--	--	--	--	--	--	--
11	--	CV, R	--	--	T	--	--	--	--	--	D	--	--	--	--	--	--	--	--	--	--	--
12	T	CV	--	--	T	T	--	--	--	T	T	M, D	--	--	--	--	--	--	--	--	--	--
13	--	--	--	CD, R	--	--	T	T	T	--	--	--	CV	CD, T	--	CD	--	--	--	--	T	--
14	--	--	--	CD, R	T	--	T	T	T	--	--	--	CD, T	CV	T	CD	--	--	T	--	--	--
15	--	--	CD, R	CD, R	--	--	--	T	--	--	--	--	T	T	CV	CV, R	--	--	--	--	--	--
16	--	R	R	CD	--	--	--	--	--	--	--	--	--	--	CV, R	CD	CD	--	--	--	--	--
17	--	CD	--	CD, R	--	CD	--	--	CD	CD	CD	--	--	--	--	CD	CD	CD	CD	--	CD	--
18	--	--	--	--	--	CD	--	--	CD	--	--	--	--	--	--	--	CD	CD, G	CD	--	CD	--
19	--	--	--	CD, R	--	--	--	--	--	--	--	--	--	T	--	--	CD, R	CD, R	G	T	??	--
20	--	--	--	--	--	--	--	--	--	--	--	--	--	--	--	--	--	--	T	CV, R	--	--
21	--	--	--	CD, R	--	--	--	--	--	--	--	--	T	--	--	--	--	--	--	--	G	T
22	--	--	--	--	--	--	--	--	--	--	--	--	--	--	--	--	--	--	--	--	T	CV, R

X = dominant effect
X = secondary effect
-- = negligible

CD = conduction, R = thermal radition, CV=convection, T = temperature boundary condition
G = heat gen/extenal heat sink, D = irradiation heat deposition, F = heat flux boundary condition
M = mixing

Table 1-7.Simplified energy field PIRM for PB-FHR primary coolant circuit, Expansion of the active core cell to a two-by-two matrix

	Active core	Outer reflector	Inner reflector	Inlet plenum
	1	2	3	4
1	**CV, G,** CD, R	**CV,** CD, R	**CV,** CD, R	**T**
2	**CV, D,** CD, R	**CD**	--	--
3	**CV, D,** CD, R	--	**CD**	--
4	--	--	--	--

	Coolant	Pebble bed	Outer reflector	Inner reflector	Inlet plenum
	1	2	3	4	5
1	D, R	**CV,** R	**CV**	**CV**	**T**
2	**CV,** R	**G,** CD	CD, R	CD, R	--
3	**CV**	**D,** CD, R	**CD**	--	--
4	**CV**	**D,** CD, R	--	**CD**	--
5	--	--	--	--	--

X = dominant effect CD = conduction, R = thermal radition, CV=convection, T = temperature boundary condition
X = secondary effect G = heat gen/extenal heat sink, D = irradiation heat deposition, F = heat flux boundary condition
-- = negligible M = mixing

Once the boundaries of the system have been expanded, the analysis is repeated. The convenience of PIRM is that a single matrix is needed for analyzing models at multiple scales, that is, models consisting of a single component or a group of a large number of components. As a second example at a larger scale, Table 1-6 considers the system that includes the first nine components in the matrix, such that all of the components that couple with the core behavior are included. The interior of the nine-by-nine matrix provides a map of key phenomenology that the model must include. The exterior of the nine-by-nine matrix provides a guide to the external component coupling that needs to be accounted for when specifying the boundary conditions. Reading to the right of the nine-by-nine matrix, the primary components with which this system couples are the upper core structures, IHX, DHX, diode, and downcomer. Reading below the nine-by-nine matrix, one can identify that the coupling with the upper core structures, the IHX, and the DHX is bi-directional, so a decision may be made to additionally include these components within the boundary of the model, to increase its fidelity.

It is possible to also reduce the detail of the matrix by essentially compressing a group of components to a single cell. The nine-by-nine matrix discussed above can be converted to a single cell, with regards to its interactions with some of the components, while maintaining the higher level of detail for the interaction with the rest of the components. The outcome of such a selective compaction is illustrated in Table 1-8. This is a useful feature for bridging scales and characterizing interactions at the scales at which they are most relevant and best understood.

Irrespective of the scale of the model, containing a single component or a large number of components, the PIRM is read in a similar manner. Each group of components can be joined together in a single subsystem. Each component can be expanded into its constituent sub-components. This is illustrated in Table 1-7. The rows of PIRM can represent components or subsystems of very different scales, without generating inconsistencies. This is possible because the coupling effects are ranked, and the matrix is not symmetrical. For example “pump” (Table 1-6, row 12) is at a different scale than “reactor cavity walls” (Table 1-6, row 18).

Table 1-8. Energy Field PIRM for PB-FHR Primary Coolant Circuit, with compacted subsystem interactions.

	Active Core: Pebble Annulus	Inner Reflector	Inlet Plenum + piping	Pebble Feed & Secondary Inlet Plenum	Outlet Plenum + piping	Shut-down element channels	Control element channels	Other primary coolant flows	Outer Reflector	Upper core structures	Defueling chute	Pump	IHX	DHX	Diode	Downcomer & core barrel	Reactor vessel (+ guard vessel is used)	Reactor Cavity	DRACS Piping	NDHX	PHX
	1	8	2	3	4	5	6	7	9	10	11	12	13	14	15	16	17	18	19	20	21
1	G, CV	CV, R	T	T	--	--	--	T	CV, R			--	--	--	--	--	--	--	--	--	--
8	CV, D, R	CD, D	CV	--	--	CV	CV	CV	--			--	--	--	--	--	CD	--	--	--	--
2	--	CV	--	--	--	--	--	T	--			--	--	--	T	T	--	--	--	--	--
3	--	--	--	G, D	--	--	--	T	CV, R			--	T	--	T	--	--	--	--	--	--
4	T	--	--	--	M	--	--	T	CV	CD, CV	CV, T	--	R	R	--	--	--	--	--	--	--
5	R	CV, R	T	--	--	D	R	T	--			--	--	--	--	--	--	--	--	--	--
6	R	CV, R	T	--	--	R	D	T	--			--	--	--	--	--	--	--	--	--	--
7	T	CV	T	T	T	T	T	M, D	CV			--	T	T	T	T	CV	--	--	--	--
9	CV, D, R	--	--	CV	CV	--	--	CV	CD, D			--	CD	CD	--	CV, CD	R	--	--	--	--
10	CD, CV									CD	CV, CD, R	--	CV	CV	--	--	CD	CV, R	CV	--	--
11	T, CV									CV, R	G	--	R	R	--	--	--	--	--	--	--
12	--	--	--	--	T	T	T	T	R, CV	CD	T	M, G	R	T, R	--	--	--	--	--	--	--
13	--	--	--	--	R	--	--	T	R, CD	CV	R	T	CV	R, CD	--	--	R, CD	R	--	--	CF, T
14	--	--	--	--	T	T	T	T	R, CD	CV	T, R	--	R, CD	CV	T	--	R, CD	R	CF, T	--	--
15	R	--	--	--	--	T	T	T	--	CD, R	T	--	--	T	CV	T	CD	--	--	--	--
16	--	--	--	--	--	--	--	T	R, CD	--	--	--	T, R	R	--	CV	R, CV	R	--	--	--
17	R	CD	--	--	--	--	--	CV	R	CD	--	--	R	R	--	CV	CV, CD	R	--	--	--
18	--	--	--	--	--	--	--	--	R	CV, R	--	--	R	R	R	R	CV, R	CV, CD	--	--	--
19	--	--	--	--	--	--	--	--	--	CV	--	--	--	T	--	--	--	R, CD	CV, G	T	--
20	--	--	--	--	--	--	--	--	--	--	--	--	--	--	--	--	--	--	CF, T	CV	--
21	--	--	--	--	--	--	--	--	--	--	--	--	CV, T	--	--	--	--	--	--	--	CV

X = dominant effect
X = secondary effect
-- = negligible

CD = conduction, R = thermal radition, CV=convection, T = temperature boundary condition
G = heat gen/extenal heat sink, D = irradiation heat deposition, F = heat flux boundary condition
M = mixing

A discussion of the reasoning behind the rankings in the matrix should be documented as part of the PIRM exercise. As an example, the ranking rationale for Table 1-7 is given here (cell referencing: [row, column]). The salt is somewhat transparent to thermal radiation, so thermal radiation between the fuel pebbles and the salt will lead to an effective increase in the convection coefficient (cells [1,2] and [2,1]). During steady state operation, heat transfer between the core and the inner and outer reflector are designed to be minimal. However, during transients, the reflectors have a large thermal inertia and heat exchange between them and the core must be characterized. Thermal radiation can occur between the graphite reflectors and the salt, but because the temperature difference between the two is much lower than the temperature difference between the fuel and the salt, radiation is negligible (cells [1,3] and [3,1]). Conduction and thermal radiation between pebbles and the adjacent graphite reflector wall will

lead to some heat transfer between the two, but generally heat transfer between these two components via convection with the salt will be prevalent (cells [1,3] and [2,3]; [3,1] and [3,2]). The inner and outer reflectors are physically separated by the active core and they are not coupled (cells [3,4], [4,3]). The surface area of the inlet plenum is small, and the residence time of the fluid in the inlet plenum is also small, thus from an energy field point of view, the inlet plenum is essentially decoupled from the rest of the components in this matrix (cells [5,i] and [i>1,5]), with the exception of the coolant in the core, for which it provides the inlet boundary condition (cell [1,5]).

1.9 Step 8: Rank the knowledge level

Knowledge level ranking helps identify significant gaps in understanding of the fundamental phenomenology, or of the behavior of specific coupling between components. Overlaying knowledge level ranking on the PIRM tables helps prioritize separate effects experiments, and numerical models for the characterization of individual phenomena and of specific coupling between components.

Three knowledge level (KL) categories are used here, for the KL ranking: sufficient understanding, significant gaps, and little understanding. The KL ranking categories for PIRM were titled to emphasize that the KL is ranked with respect to the KL that is necessary for the specific application being investigated. The NGNP PIRTs defined the ranking levels as high being 70-100% complete knowledge and understanding, medium being 30-70%, and low being 0-30%[20]. These KL ranking levels were not adopted for PIRM because their quantitative nature does not have utility in the context of a PIRM that needs to be done relatively quickly in order to be useful early in the design process. The PIRM KL categories do however closely parallel the those of the NGNP PIRT.

Table 1-9 gives an example of KL ranking for the simplified energy field PIRM table for PB-FHR. There is one dominant phenomena that has significant gaps in the knowledge level: convection in the core. A modeling tool for heat transfer in a pebble bed core is presented in Chapter 2 of this dissertation; the modeling results identify the dominant effects, and they guide the design of experiments for investigating convective heat transfer in the pebble bed core. The KL ranking also identifies that detailed design is needed for the inner and outer reflectors.

1.10 Step 9: Documentation of the PIRT Results

This PIRT exercise studied the thermal-hydraulic behavior of the primary coolant system in the PB-FHR. The following documentation material was generated as part of this exercise:

- Functional requirements for the PB-FHR Reactor System and its subsystems.
- Representative set of scenarios that spans the PB-FHR phenomenology.
- Evaluation criteria for the thermal-hydraulic performance of the PB-FHR system.
- Phenomena ranking map for the momentum field of the coolant (primary coolant flow paths), and for the energy field of the solid components.
- Phenomena identification and ranking matrix (PIRM) for the energy field.
- Knowledge level ranking of a simplified PIRM for the reactor system.

Table 1-9. Energy Field PIRM for PB-FHR primary coolant circuit, with Knowledge Level Ranking

	Active core	Outer reflector	Inner reflector	Inlet plenum
	1	2	3	4
1	CV, G, CD, R	CV, CD, R	CV, CD, R	T
2	CV, D, CD, R	CD	--	--
3	CV, D, CD, R	--	CD	--
4	--	--	--	--

Knowledge Level Ranking
- Sufficient understanding
- Significant gaps
- Little understanding

Phenomena Importance Ranking
- X = dominant effect
- X = secondary effect
- -- = negligible

CD = conduction, R = thermal radition, CV=convection, T = temperature boundary condition
G = heat gen/extenal heat sink, D = irradiation heat deposition, F = heat flux boundary condition
M = mixing

1.11 Conclusions

The phenomena identification and ranking table is a structured methodology that relies on expert elicitation to identify and prioritize modeling capabilities and experimental facilities that are needed for design and analysis of complex systems. PIRT was developed as one of the tools in the probabilistic safety analysis of nuclear reactors, and it has applicability to any well defined complex system. Previously, the PIRT process has been applied to reactors in operation, or reactors for which detailed engineering design exists, and for reactor designs where a wider base of expert knowledge exists. This chapter studied the application of the PIRT process much earlier in the design of the reactor, at the preconceptual design stage. In the context of the PIRT methodology, new tools and approaches were proposed and demonstrated here, which are specifically relevant to technology in the early stages of development. The case study discussed here was thermal-hydraulic analysis of the PB-FHR.

The PASSC and H2TS system decomposition schemes were applied in a complementary manner. Definition of system functional requirements complemented identification and compilation of the current knowledge base for the behavior of the system. Two graphical tools were developed for ranking of phenomena: phenomena ranking map, and phenomena identification and ranking matrix (PIRM). Phenomena ranking is performed for each of the fields defined by the H2TS scheme, and an important element that these new tools add is the ranking of system and subsystem coupling.

The functional requirements established here are further discusses in the Chapters 2 and 3, in the context of design and optimization of the core, and of the passive decay heat removal system for PB-FHR. The PIRM results guide the modeling approach for the annular pebble bed reactor core, which is presented in Chapter 2. The phenomena ranking map guides the design of integral effects experiments for the natural circulation decay heat removal system, which is discussed in Chapter 3. The knowledge level ranking applied to the PIRM, identifies convective heat transfer in pebble beds as an important phenomena with significant knowledge gaps.

Future PIRM studies should map system coupling across multiple fields: neutronics, fluid momentum equation, etc. As further understanding is gained about the PB-FHR system, the matrices should be updated.

CHAPTER 2

Heat Generating Packed Pebble Beds Thermal-Hydraulic Modeling

This chapter presents a numerical modeling approach for fluid flow and heat transfer in porous media with internal heat generation. Two-dimensional incompressible flow in cylindrical and spherical coordinates leads to a continuously changing flow velocity, and hence to a non-uniform Reynolds number in the porous media. This in turn leads to non-uniform friction losses and non-uniform convective heat transfer between the solid media and the coolant. Temperature dependent fluid viscosity and buoyancy are implemented in the model. An approach for coupling this porous media thermal model with neutronic calculations for nuclear reactor pebble beds is also presented.

Steady state flow through porous media with heat transfer between the liquid and the solid has applications to heat generating media, such as biological tissue[21], endothermic or exothermic reactions that occur at the surface of the packing material for a packed bed[22], pebble bed nuclear reactors[23], and molten nuclear reactor core debris following accidents such as the ones at the Fukushima Dai-Ichi Plant in 2011[24], and at Three Mile Island Plant in 1979[25]. It may also be applicable to quasi-steady state problems for heat removal or heat addition to a solid porous media, such as a pebble bed or a rock pile, for the purpose of thermal storage[26]. The treatment of coupling of the thermal-hydraulic modeling with the kinetics of the nuclear reactor core is more difficult to extend outside the nuclear reactor field; one could envision a chemical system with reduced reaction kinetics at higher temperatures, but no specific examples can be cited.

For illustration, this modeling approach is applied here to calculating the steady state temperature and flow distribution in the annular pebble bed core of the pebble bed fluoride salt-cooled high temperature reactor. These calculations provide a reference point for the steady state temperature and flow distribution and for the pressure drop in the reactor core, during normal operation and during decay heat removal. This information is needed for design development of the reactor systems and subsystems, for safety analysis of PB-FHRs, and for design and prioritization of separate effects and integral effects experiments.

The porous media investigated here is a randomly packed pebble bed with pebbles of uniform size. The coolant investigated is liquid flibe, a high Prandtl number coolant with high volumetric heat capacity, and relatively high viscosity. The thermophysical properties of the coolant lead to moderate Reynolds numbers in the packed bed, so that both viscous effects and form losses contribute significantly to the momentum equation of the fluid.

Section 2.1 describes the model inputs and the details of the PB-FHR core, based upon a 2009 point design for a Pebble Bed Advanced High Temperature Reactor, referred to here as the 2009 PB-AHTR[27]. Section 2.2 describes the constitutive equations and some details pertaining to the numerical solver, and highlights the model capabilities and limitations. Section 0 presents an optimization study for the flow distribution in the core during full power operation with forced circulation through the core. The optimization objectives are derived from the core functional requirements identified in Chapter 2. It also calculates the pressure drop through the optimized core, as a function of mass flow rate; these results are needed for the characterization of natural circulation heat removal from the core, which is discussed in Chapter 3. Section 2.4 studies the sensitivity of flow and temperature distribution to buoyancy effects, and

temperature-dependent viscosity. Section 2.5 summarizes the results and conclusions presented in this chapter, and gives recommendations for future work.

2.1 Model Case Study: Pod

A thermal-hydraulic model was developed for the PB-FHR annular pebble bed core, and the model name is *Pod*, the "Pb-fhr cOmsol moDel." *Pod* is primarily a tool for reactor design optimization, and for design of experiments. It can generate high resolution temperature and flow distributions, it is flexible in terms of changing the geometry and adding features or additional phenomenology, and the solving time is relatively short (tens of seconds or minutes on a Intel i7 processor, with 6.00 GB of memory, and 64-bit operating system). Parametric studies can be automatically set-up, for optimization studies, or sensitivity studies.

The objectives of thermal-hydraulic modeling of the core are: (1) to predict the coolant and fuel temperature distribution in the core, (2) to predict pressure drop in the core, and (3) to predict the temperature distribution along the fluid inlet and outlet faces. The following parameters are determined by subsystems external to the core, and are not considered in this analysis: (1) minimum coolant temperature, and (2) bulk coolant temperature rise across the core.

Pod also generates important data that can be used for code-to-code comparisons for thermal-hydraulic system codes used to model the transient response of PB-FHRs. For PB-FHR thermal-hydraulic system transient response analysis, two systems codes are being investigated: RELAP5-3D and Flownex. These system codes have quality assurance (QA) pedigree, and either or both may be appropriate for FHR safety analysis calculations. However, neither of these codes has gone through verification and validation (V&V) for modeling salt-cooled pebble bed cores. An important component of V&V is comparison with independent calculations using different modeling tools, and *Pod* provides this capability. It is also a tool to investigate the sensitivity of the core behavior to various simplifications and input parameters, and thus informs the decision to develop additional features in the system codes for better fidelity models of the pebble bed core.

RELAP5-3D was developed by Idaho National Laboratory (INL) and the U.S. Nuclear Regulatory Commission (NRC); it has been used for the licensing of light water reactors (LWRs), along with an extensive code verification pedigree and a validation base for modeling of LWRs[28]. Flownex SE is an engineering simulation environment, which was developed by M-Tech under QA standards[29]. The Flownex Nuclear module was developed for the safety analysis and licensing of the pebble bed modular reactor (PBMR) in South Africa, which is a gas-cooled reactor that uses fuel similar to the PB-FHR fuel. Capabilities and modeling approaches of *Pod* are compared with those of these system codes, whenever relevant to the steady state modeling of the PB-FHR core, or the ATWS transient response modeling.

2.1.1 Description of the PB-FHR Pebble Bed Core

This section describes the model inputs that are specific to the PB-FHR core studied here. The 2009 PB-AHTR is the specific core design that is studied here, and it is part of the PB-FHR class of reactors. The core is a packed bed of pebbles that are buoyant in the coolant. The core consists of an annular region filled with randomly packed pebbles, through which coolant flows upwards and radially outwards.

Pebble fuel allows for continuous and fast throughput online refueling. The pebbles are circulated several times through the reactor, before they reach full burn-up (BU). Before being returned to the core, the pebbles have a brief cooling time outside of the core to allow Pa-233 to decay, preventing generation of neutron poisons in the fuel and increasing the final BU of the fuel. Once the fuel composition in the core reaches equilibrium, the core operates with very little excess reactivity, and the radioactive material source term is smaller, compared to that of batch-refueled cores.

Figure 2-1 provides the geometry and dimensions for the 2009 PB-AHTR reactor core that is studied here. The core has five distinct regions. The shape and the naming of these regions comes from the pebble fuel movement requirements through the core. Region 5 at the bottom of the core is the Fueling Chute, through which fuel pebbles are inserted into the core. It is designed to be sufficiently wide to allow for radial zoning of the fuel, sufficiently narrow to ensure subcriticality of this region, and sufficiently tall to lead to reduced neutron flux at the bottom of the fueling chute, where separating rings for radial fuel zoning are located. Region 5 is assumed to be fully packed, with the pebble bed free surface located below the bottom of the region. Region 4 is the Diverging Region, which expands the width of the bed to the dimensions determined by reactor physics optimization studies. The fuel then moves vertically in plug flow through region 1, the Central Core Region, and then through region 2, the Converging region, which reduces the thickness of the bed to that of the defueling chute. Region 3, the Defueling Chute, is a long and narrow region, which is subcritical, and just sufficiently wide to prevent pebble bridging and pebble flow blockages[30].

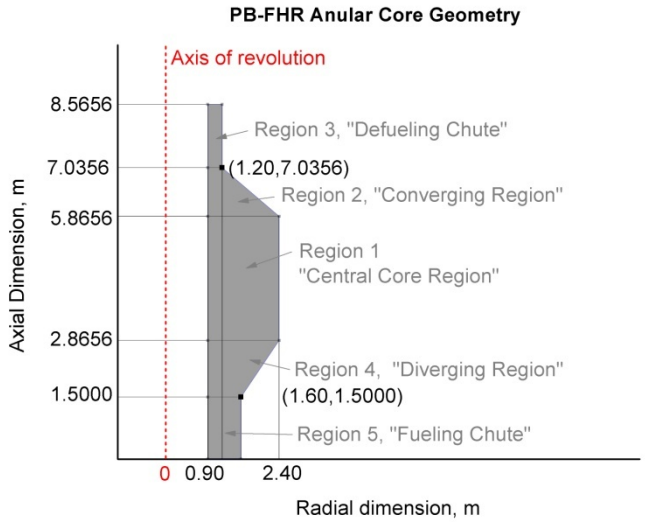

Figure 2-1. 2009 AHTR Geometry and dimensions of the 2009 PB-AHTR Annular Pebble Bed Core27

Figure 2-2 shows typical locations of the inlets and outlets for the coolant. The detailed distribution of these flow sources and sinks is optimized to provide uniform heat removal from the core and low pressure drop, and thus depends upon the detailed design of the core. Each of the faces marked in the figure will have ports for coolant inlet or outlet, and the density and location of these ports on each of these faces determines the coolant flow distribution in the core

and are core optimization parameters. The results of the optimization study for the coolant inlet and outlet port distributions are given in section 0.

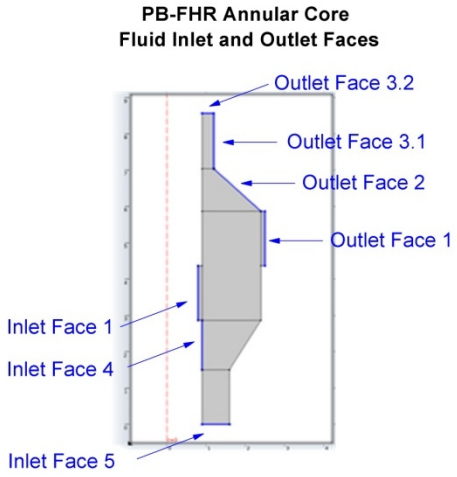

Figure 2-2. Schematic location of the coolant inlet and outlet ports for the 2009 PB-AHTR Annular Pebble Bed Core

When considering whether core thermal-hydraulics can be decoupled from pebble motion there are two issues: (1) the bed recirculates slowly, and (2) pebbles can move individually or in clusters in discrete sudden movements, when the static friction forces break. After taking into account these two considerations, for all thermal-hydraulics studies the pebbles are assumed to be stationary. The timescales of pebble movement in the core are significantly longer than the timescales of fluid dynamics and heat transfer. Pebbles are recirculated through the core at very slow speeds, with residence time of around one month compared to coolant residence time of minutes. The recirculation of pebbles results in a non-uniform distribution of porosity, with experiments and simulation showing porosities of 43% in converging region of the core, compared to the expected 40% value for an infinite randomly packed pebble bed. The porosity in the diverging region is expected to be similar to that in the converging region[31,32]. In the analysis presented here the porosity is assumed to be uniform.

The movement of pebbles in discrete intervals, as the static friction forces break, creates time-dependent, localized changes in porosity. The timescales of localized porosity variation are below a second. The time scale of discrete and rapid pebble motion when pebbles slip is defined as the time for a pebble to move the length of its radius under gravity, starting from zero velocity. For PB-AHTR it is 0.15 seconds, with one pebble radius being a conservative overestimation of the average slip distance for a pebble. In summary, the duration is under a second and the spatial scale is small, for the regions of local porosity variations and high pebble velocity that are created when the bed recirculates due to the non-continuous motion of the pebbles[32].

When averaged over larger volumes, the porosity and permeability take on quasi-steady values even with the localized, time-dependent variability that occurs due to individual pebble slip-stick movement. The quasi-steady porosity varies compared to the expected 40% average value in regions where the pebble flow area expands or contracts, in the range of 37% to 43% porosity[32]. In the analysis presented here the pebble bed is assumed to be stationary, and this

variability of the quasi-steady porosity is neglected. Localized porosity variations are not expected to significantly affect the volume-averaged heat transfer or hydrodynamic behavior of the core. Heat transfer to individual pebbles may be affected, but variability of individual pebble temperatures compared to average values is not considered to be particularly important due to the large thermal margins for FHR fuel. Sensitivity studies should be performed to demonstrate the validity of these assumptions.

The power peaking map was generated by MCNP neutronic modeling of the core at isothermal coolant temperatures of 650°C and isothermal kernel temperatures of 800°C. Figure 2-3 shows the power density distribution in the core. The central core region is radially zoned, with a high BU LEU region closest to the center reflector, a low BU LEU region, and then a thorium region at the interface with the outer reflector wall. A coarse, 8-element radial mesh was used in MCNP for region 1, to generate the power peaking map shown in Figure 2-3. For the rest of the regions no radial discretization was applied, and the fuel was modeled as a radially homogeneous mixture. Thus, the axial power profile was available from MCNP modeling for each of the regions, and the radial power profile was available only for region 1.

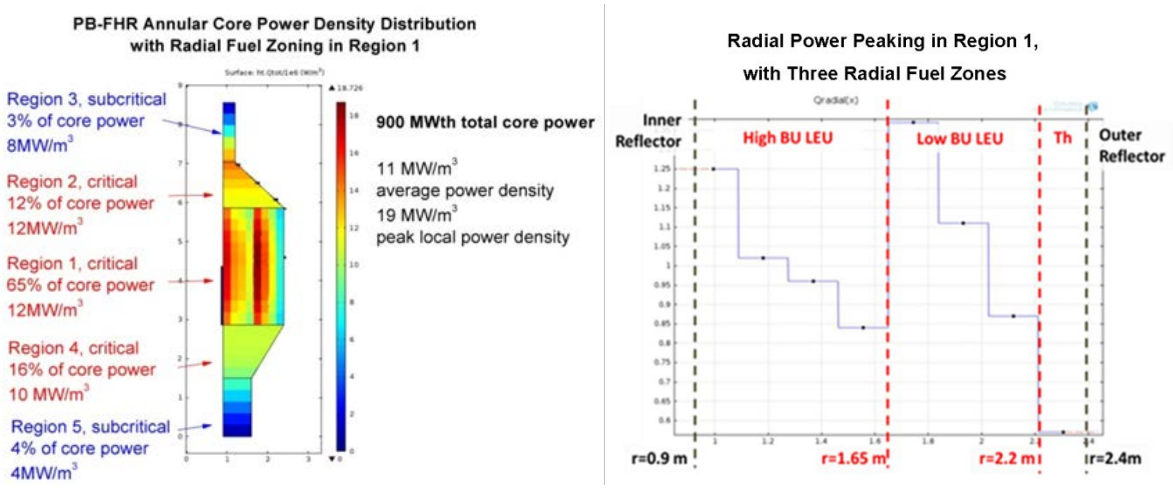

Figure 2-3. Power distribution for the PB-FHR Annular Pebble Bed (left), and radial power peaking in the Central Core Region (right)

The volumetric heat generation term, $Q(r,z)$, for each region was input in the following form:

$$Q(r,z)[W/m^3] = Q_{core}/V_{core} \cdot Q_{axial}(z) \cdot Q_{radial}(r) \quad (2\text{-}1)$$

where Q_{core} is the total core power, V_{core} the total core volume, $Q_{axial}(z)$ the axial power peaking function, and $Q_{radial}(r)$ the radial power peaking function.

Fuel radial zoning affects the power peaking profile in the core. Radial zoning of the pebble fuel in the core creates physical separation among different types of fuel, without the need for solid walls exposed to a high radiation environment. The zoning pattern is established in the fueling chute, and it remains as such as the fuel moves upwards through the core. Radial zoning of the pebble fuel permits the creation of fuel zones of varying burn-up, leading to a more radially uniform power density in the core. It also permits the creation of thorium fuel blanket, with approximately 25% of the total energy generation from the thorium fuel. Thorium fuel is potentially cheaper than uranium fuel, because thorium is a waste stream from some rare-earth

mines (rare-earths are used in the semiconductor industry) and also otherwise abundant, and because thorium fuel does not require enrichment, which is an energy intensive and expensive step of uranium nuclear fuel production[33,34]. Lastly, if a blanket of thorium fuel or inert graphite pebbles is used at the interface with the graphite reflectors, the walls of the reflectors are exposed to a lower neutron flux, extending their lifetime.

The fuel pebbles are 3 cm in diameter, and they have an internal structure that consists of an inner graphite core, an annular fuel region, and a final thin graphite layer. The annular fuel region consists of coated particle fuel embedded in a graphite matrix. The coated fuel particles have a diameter of 1 mm or less, and they consist of fuel kernels coated with subsequent layers of graphite and silicon carbide, as depicted in Figure 2-4[35]. Nominal values for the detailed dimensions and thermophysical properties for the fuel element are given in Appendix B.

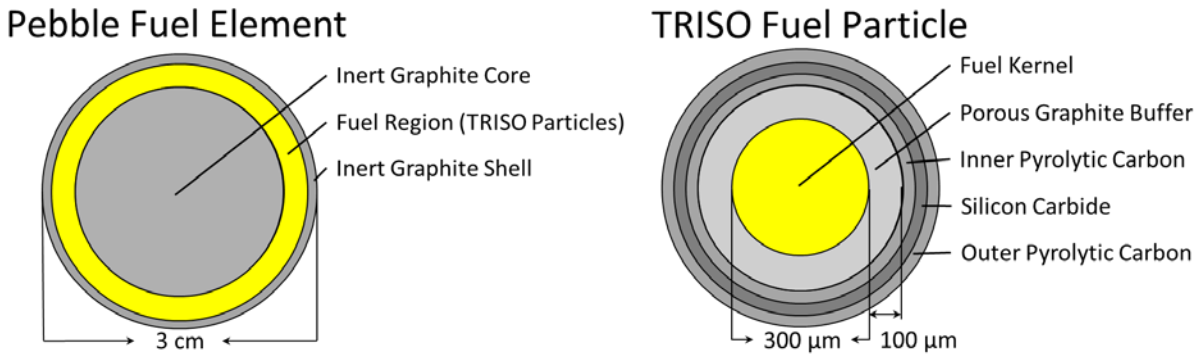

Figure 2-4. PB-FHR Fuel (drawings by A. T. Cisneros)

The coolant investigated is liquid flibe, a high Prandtl number coolant with high volumetric heat capacity and relatively high viscosity. The thermophysical properties of the coolant lead to moderate Reynolds numbers in the packed bed, for which both viscous effects and form losses contribute significantly to the momentum equation of the fluid. Fluid properties are evaluated at the average temperature of 650°C; the temperature-dependent thermophysical properties for flibe fluoride salt mixture are given in Appendix C.

Table 2-1. Summary of Nominal PB-FHR Parameters

Primary coolant	flibe
Core Power	900 MWth
Core geometry	annular core with radial fuel zoning
Nominal coolant temperature rise in the core	100 °C
Coolant inlet temperature	600 °C
Nominal temperature for coolant thermophysical properties evaluation	650°C
Pebble fuel diameter	3 cm
Pebble fuel design	annular fuel zone
Fuel form	coated particle (TRISO fuel)

The modified PIRT exercise in Chapter 1 established as a set of thermal-hydraulic performance metrics, and a set of functional requirements for the subsystems of the PB-FHR

core. The subset of requirements applicable to thermal-hydraulic modeling of the reactor pebble bed core is listed in Table 2-2. Each requirement is associated with metrics that are calculated from *Pod* results.

Table 2-2. Reactor functional requirements related to thermal-hydraulic modeling of the pebble bed core

	Functional Requirements	Top level req.‡	Metrics computed by *Pod*
	PRIMARY COOLANT		
1-1	Provide negative temperature feedback	SDC 2	Predict temperature distribution in the core
1-2	Coolant remains in liquid phase	SDCs 3, 5	Control minimum coolant temperature
1-3	Maintain low temperature for coolant in vicinity of reactor vessel and other core metallic components	SDCs 5	Maximum outlet coolant temperature
1-4	Provide sufficient flow to maintain design basis core temperature rise	E	Core temperature rise
1-5	Control reflector by-pass leakage	E	Minimize core pressure drop
	GRAPHITE REFLECTORS		
2-1	Provide thermal inertia	SDCs 5	Quantify heat transfer flux between the graphite reflectors and the coolant
	FUELING STAND-PIPES		
3-1	Prevent primary coolant inventory loss	SDC 4	Minimize core inlet pressure (i.e. core pressure drop)
	FUEL SUBSYSTEM		
4-1	Transfer heat to the coolant	SDC 3	Predict temperature drop across the fuel element; Predict core pressure drop during natural circulation, which determines natural circulation flowrate
4-2	Fuel element manufacturability (and fuel qualification requirements)	E	Fuel element geometry should respect manufacturability limits
4-3	Provide the first barrier to radionuclide emission	SDC 1	Predict peak fuel temperature
4-4	Provide negative temperature reactivity feedback	SDC 2	Predict temperature distribution in the core
4-5	Minimize difference between average fuel and coolant temperatures at full power operation (for ATWS response)	IP	Minimize coolant to fuel temperature difference

‡ System functional requirements are subordinate to top level performance requirements, listed in Appendix A. E is economic optimization, and IP investment protection. SDCs are safety design criteria. For FHRs, there are six SDCs and they are listed in Chapter 2.

2.1.2 Application for *Pod*: ATWS Point Reactor Model

One of the functional requirements for FHR core design is to minimize the temperature difference between the coolant and the fuel (Table 2-2, requirement 4-5), which motivated the inclusion of the fuel temperature equations in the steady state *Pod* model. This functional requirement is driven by the reactor response to ATWS scenarios. Some back-ground on the

ATWS transients for FHRs is given here, in order to provide a context for the way the fuel temperature was modeled, and the way that *Pod* results for the fuel temperature should be interpreted.

Anticipated Transients Without SCRAM (ATWS) is a class of nuclear reactor transient scenarios in which the normal and reserve shut down systems do not function, and reactor shut down relies solely on the negative temperature reactivity feedback of the core. There are two typical anticipated operational occurrences where a reactor scram should normally occur, Loss of Forced Circulation (LOFC) and Loss of Heat Sink (LOHS). In an ATWS accident the normal and reserve shutdown systems would not function, and the temperature of the core would rise until the reactor core becomes sub-critical and the reactor shuts down at a new, elevated quasi-steady state core temperature. The key design question for the ATWS accident is whether this elevated temperature exceeds the safety limits for metallic primary structures including the reactor vessel.

The FHR class of reactors has the unique potential of ATWS response that leads to temperatures sufficiently low that the reactor systems remains within designed operating temperatures, and thus does not lead to damage of the fuel or the structural materials of the reactor. In addition to the reactor control system, the reactor shutdown system and the reserve shutdown system are designed for high reliability, and the probability of all these systems failing and leading to an ATWS event is low enough that ATWS events are beyond-design-basis events (BDBE) and it is an open debate as to whether these types of events need to be studied, for the licensing or design of an FHR. Mild ATWS response can provide an attractive feature for investors, since such a feature provides investment protection, ensuring that the reactor system will continue to be operable even after a low probability ATWS event. Furthermore, a fully passive ATWS response coupled with fully passive natural-circulation decay heat removal with ultimate heat sink to ambient air greatly increases the intrinsic capability of the reactor to cope with events such as station blackout without the need for operator intervention or external sources of energy. Lastly, the ATWS response of FHR systems has unique differences from LWRs and HTGRs, due to the very low volatility and significant contribution to moderation provided by the FHR coolant. So ATWS merits investigation, at least as a bounding event for evaluation of FHR safety, and because it has phenomenology that is unique to FHRs.

The desired endpoint of ATWS is safe shutdown; in safe shutdown the core is subcritical and the fuel generates power at decay heat levels. At full power operation the temperature difference between the fuel kernels and the coolant is on the order of 100°C. At decay heat levels of power generation, the fuel kernel and bulk coolant temperatures are almost equal, because the temperature difference between the coolant and the fuel kernels is driven by the power density. Figure 2-5 depicts the fuel and coolant temperatures at normal operation, and at decay heat power levels. If the coolant temperature increases to a value below that of the fuel kernel temperature, then the negative reactivity insertion due to the rise in coolant temperature will be counterbalanced by positive reactivity insertion due to the drop in fuel kernel temperature at the decay heat power level. Similarly, if the coolant temperature increases to a value below that of the average temperature of the carbon in the fuel pebble, then the carbon in the fuel pebble will contribute with positive reactivity. Conversely, if the coolant temperature increases above the average temperature of the carbon in the fuel pebble, then the carbon in the fuel pebble contributes with negative reactivity insertion.

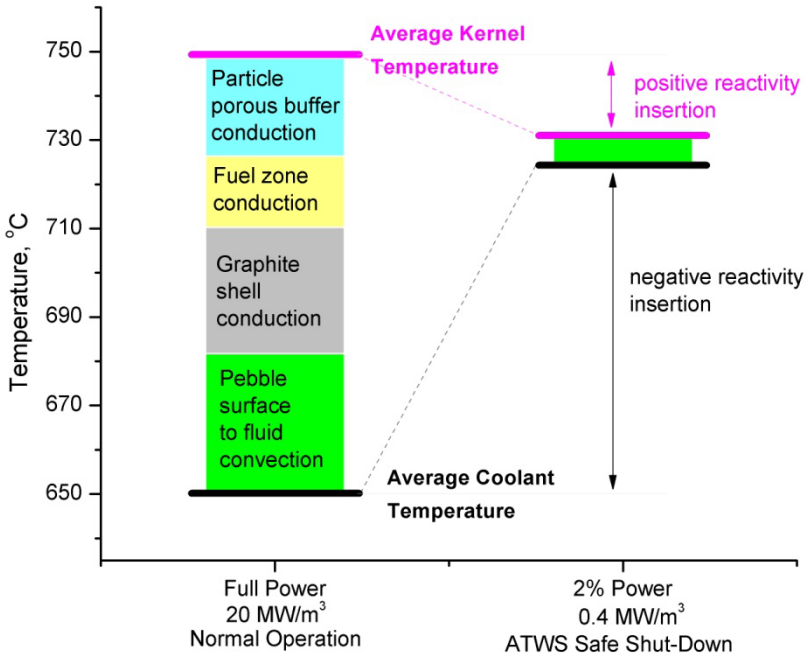

Figure 2-5. Schematic diagram of fuel and coolant temperatures at the beginning and end of ATWS transient

The temperature of the graphite reflectors also affects neutronics. Predicting its transient evolution requires larger system models, as those described in Chapter 3 , which take into account the evolution of the heat sinks and heat sources in the entire circuit of the primary coolant flow, which was mapped out in Chapter 1. The present analysis is concerned with steady state conditions, when the graphite can be assumed to be in thermal equilibrium with the coolant. Hence, in this steady state model of the core the effective reactivity associated with the coolant, is actually the sum of the coolant reactivity plus the graphite reflector reactivity. The assumption of thermal equilibrium between the coolant and the graphite reflectors disregards gamma heat generation in the graphite reflectors, which leads to a temperature difference between the graphite and the coolant. This temperature difference is likely very small compared to the temperature rise across the fuel pebble, since the power density of gamma heating is significantly lower than the power density in the core.

Thus, the minimum coolant temperature rise that will allow for ATWS safe shutdown is the temperature at which the sum of positive and negative reactivity insertion from the coolant, the fuel, the carbon in the fuel pebbles, and the graphite reflectors sum to zero. For a given core design, this temperature is determined by the coolant to fuel temperature difference at full power. Coolant flow in the FHR core should be designed such that it minimizes this temperature difference (Table 2-2, requirement 4-5). Pod was used to perform this optimization of the coolant flow in the core.

ATWS response is driven by the feedback between the neutron physics of the core and the temperature distribution of the core, so coupling of neutronic and thermal-hydraulic modeling is necessary in order to understand ATWS response. It remains to be investigated how tight the coupling between the two models needs to be, and the spatial and temporal fidelity needed from each of the models to accurately model this transient.

An initial estimate of the ATWS response can be calculated by assuming that the temperature reactivity coefficients are constant within a temperature range and that core reactivity can be described using a point reactor model that depends on the respective temperatures of fuel kernels, carbon, and coolant in the core.

Design studies that optimize across a large number of flow and temperature distributions in the core do not permit iteration of *Pod* and MCNP for each of the cases, and an approximate treatment of the reactivity of the constituents is needed. Driscoll et al. recommends power density as the most appropriate weighing factor for reactivity averaging[1]. Core optimization with regards to ATWS response uses the volume averaged temperatures for each constituent weighted by the power density distribution in the core. The RELAP5-3D systems code, which has been used in the licensing of LWRs, implements the same approach to point kinetics: every volume element of the mesh has a weighing factor, which must be specified as an input by the user. The Flownex systems code, whose nuclear module was developed for the licensing of the PBMR, calculates only a volume-averaged temperature of the constituents in the core, with no weighing factor; this is a more simplistic approach, but for a core with no significant power peaking, it remains a reasonable approximation.

Figure 2-6 illustrates the loose coupling between thermal-hydraulic and neutronic models, for the purpose of predicting the minimum temperature rise of the coolant at which the core can be in ATWS safe shutdown. A core power distribution generated by a code like the Continuous Energy Monte-Carlo neutronic (MCNP) based on an average core temperature is used by Pod to calculate the core temperature distribution at full power. Fuel, coolant, moderator and reflector reactivity coefficients also generated by steady state MCNP calculations at a set of average constituents temperatures are used to predict the equilibrium constituents temperature at the ATWS shutdown state as a function of the power level. The temperature distributions estimated for the shutdown conditions are then used in neutron transport modeling to calculate the k-effective to verify that safe shut down is indeed reached at the predicted average temperatures in the ATWS scenario. *Pod* can generate core temperature distributions of the coolant, fuel kernels, and fuel graphite for input into MCNP. *Pod* uses the power distribution in the core, and the fuel, graphite and coolant temperature reactivity coefficients as inputs from MCNP.

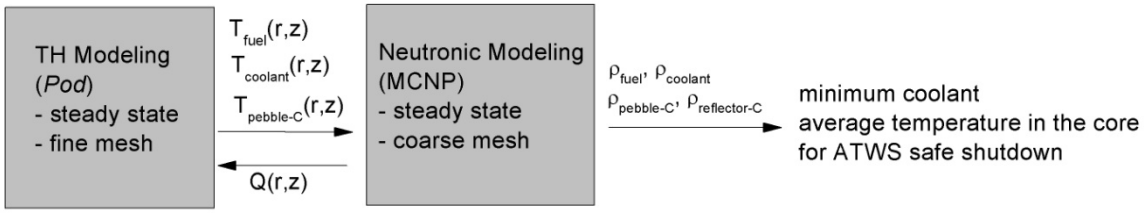

T_{fuel} is the average temperature of the fuel kernel, $T_{coolant}$ the bulk coolant temperature, Tpebble-C the average temperature of the carbon in the fuel pebble, (r,z) are the spatial coordinates in cylindrical pebble bed geometry, ρ_{fuel}, $\rho_{coolant}$, $\rho_{pebble\text{-}C}$, $\rho_{reflector\text{-}C}$ the neutronic temperature reactivity coefficients for the fuel kernels, the coolant, the carbon in the fuel pebble, and the graphite reflectors, respectively.

Figure 2-6. Loose coupling between thermal-hydraulic and neutronic models, for ATWS modeling

2.2 Governing Equations and Model Development

A steady state numerical model of temperature and flow distribution through an annular heat generating pebble bed was built in COMSOL, which is a commercially available finite element method (FEM) differential equation solver. The momentum and energy equations for the fluid were modeled using the modules *Porous Media Flow* and *Porous Media Heat Transfer*, respectively[37]. These two modules are predefined differential equations built in COMSOL and they are described in this section. The temperature of the fuel kernels is derived from the coolant temperature; this calculation was manually implemented in COMSOL, and it relies on a data table that provides the temperature rise between the pebble surface temperature and the average temperature of the fuel kernels as a function of local power density. This data table was generated by solving the conduction equations for the pebble fuel, using *Mathematica* code, which is described in this section.

Pod demonstrates the ability to model flow and heat transport in porous media, in cylindrical coordinates, with three-dimensional fluid flow, non-uniform heat generation in the porous media, temperature-dependent thermo-physical properties, and buoyancy effects. It has a high spatial resolution, and quick solving time. Basic verification calculations were built-in, and their results are calculated and exported with every data set generated by *Pod*.

Pod has the capability to model spatially dependent porosity, but verification and mesh refinement studies have not yet been done for this feature. Thermal radiation heat transport between fuel surfaces and the fluid, which may absorb and emit in the infrared, is recommended as a future development, but it is not treated in this study. Other future developments for *Pod*, which require relatively little effort include addition of dispersion effects for flow in porous media, migration for the *Mathematica* code for the fuel element conduction equation to the COMSOL model, and design of a temperature data output file that matches the mesh uses in the neutronics model.

More elaborate developments for *Pod* include demonstrating capability to run transient problems, and implementing semi-permeable walls as boundary conditions for the fluid outlet faces. As features are added to *Pod*, the built-in verification calculations should be updated and additional checks should be added, as appropriate. Implementing transient problems is challenging primarily because of the heat capacity of the fluid and the fuel, which are modeled as homogenized coupled media. For transients that rely on the temperature reactivity feedback of the core's fuel, graphite, and coolant, point kinetics or coupling with a neutronics code will also have to be implemented.

The fluid outlet boundary conditions are currently set as uniform outlet pressure boundaries. In reality, the outlet faces contain a certain number of circular outlet ports, all of which duct fluid to a common outlet plenum. The distribution of outlet flow on the outlet face depends on the distribution and dimension of outlet ports, or otherwise described, it depends on the distribution of outlet flow area over the outlet faces. *Pod* currently models this as a set of fictitious very thin outlet disks of varying location and outlet flow area. This approach allows for the optimization of the flow distribution in the core. The downsides of this approach are that it poses some meshing challenges in the vicinity of the outlet ports, makes the model slower, and it renders some problems more difficult to converge to a solution. One alternative to this approach is to define the outlet condition as a non-uniform pressure boundary. This approach functions in the 4.3 version of COMSOL, but it did not function in previous software versions.

So, while this approach has been implemented here, it hasn't yet been fully tested, because a large part of the *Pod* development work was done before transitioning to the 4.3 version of COMSOL. The ideal approach would be the possibility to implement an outlet boundary of constant pressure, but varying outflow cross-sectional area. This would be the closest to the physical approach, and numerically the most straight-forward solution. At present, there is no default COMSOL option for such a boundary condition, so this will have to be implemented either by manually editing the boundary condition equations in the COMSOL differential equations solver, or by constructing an ingenious set of fictitious outlet geometries, or geometry transformations.

The results of any simulation are only as good as its inputs. The friction losses are implemented as Ergun correlation coefficients, which are semi-empirical and based on data for straight channel flow. These coefficients are applied here for multi-dimensional flow in cylindrical coordinates, and they may no longer be valid. Experiments that demonstrate that these friction coefficients are appropriate in more complex geometries are needed. Sensitivity studies for the fluid and solid thermophysical properties should also be performed, particularly because there is large uncertainty for some of these values. Finally, to demonstrate the validity of the modeling approach described here, experimental data should be obtained, and code-to-code benchmarking should be performed. In the future, if *Pod* will be used and developed by several users, some form of version control will have to be implemented.

2.2.1 Momentum Equation

The momentum equation for fluid flow in the pebble bed is written in terms of the superficial velocity, $\bar{u}$ or u_D, as defined in the COMSOL module for *Porous Media Flow with Forcheimer Drag*[38]:

inertia = pressure gradient + viscous dissipation + porous media friction losses + body force

$$\frac{\rho}{\epsilon_p}\left[(\bar{u}\cdot\bar{\nabla})\frac{\bar{u}}{\epsilon_p}\right] + \rho\bar{\nabla}\cdot\bar{u} = \bar{\nabla}\left[-p\bar{I} + \left(\frac{\mu}{\epsilon_p}(\bar{\nabla}\bar{u} + (\bar{\nabla}\bar{u})^T) - \frac{2\mu}{3\epsilon_p}(\bar{\nabla}\cdot\bar{u})\bar{I}\right)\right] - \left(\frac{\mu}{k_{br}} + \beta_F|\bar{u}| + \rho\bar{\nabla}\cdot\bar{u}\right)\bar{u} + \bar{F} \quad (2\text{-}2)$$

$$\epsilon_p = \varepsilon = \frac{V_f}{V_f + V_s} \quad (2\text{-}3)$$

where V is volume, and the subscripts s and f refer to properties intrinsic to the solid and the fluid in the porous medium, respectively.

For *Pod* the only body force is buoyancy, and it is defined as

$$\bar{F} = \rho g\beta[T(r,z) - T_{av}]\hat{\boldsymbol{e}}_{\boldsymbol{z}} \quad (2\text{-}4)$$

The body force is defined such that it models buoyancy, not gravity. The hydrostatic pressure is not modeled, because for a closed flow loop it makes no difference if the hydrostatic pressure field is modeled or not.

The momentum boundary conditions are specified as a slip condition in the locations where the walls are impermeable[37]. For the surfaces where injection occurs into the bed, either the inlet velocity perpendicular to boundary surface is specified, or the total mass flow rate through the bounding surface. The actual injection flow distribution will be more complicated, but it is assumed that the injection manifold will include orificing that provides a controlled distribution of injection flow similar to the rates imposed artificially in these calculations. The outlet

boundaries are set to zero pressure. For each specific reactor power, the total inlet mass flow rate is calculated based on the target average coolant temperature rise through the core:

$$m_L = \frac{Q_{core}}{cp_L \cdot \Delta T} \tag{2-5}$$

where m_L is the coolant mass flow rate, Q_{core} the core thermal power, c_{pL} the specific heat of the coolant, and ΔT the coolant bulk temperature change across the core.

The pressure losses in the pebble bed are modeled using the Ergun correlation[39–42], which was developed for axial flow through packed beds. The Ergun correlation assumes that pressure drop in a packed bed occurs dominantly due to viscous effects at very low Reynolds numbers, and due to kinetic effects, or form losses, at high Reynolds numbers. At intermediate Reynolds numbers, the transition from one type of flow to another is smooth. He postulates that the viscous effects are proportional to those in a set of thin parallel tubes that have the same liquid volume and surface area as the porous media. He also postulates that the kinetic term is analogous to the kinetic term for capillary flow, except that the entrance effects observed for capillary flow should repeat a number of times that is proportional to the length of the bed. Thus, the Ergun correlation for pressure loss in packed beds is a summation of two friction coefficients, the viscous term or drag that is inversely proportional to Reynolds number, and the kinetic term or form losses that is independent of Reynolds number. The two terms are multiplied by coefficients, E_1 and E_2, which are empirically determined. In the literature, the friction loss correlation is expressed as several algebraically equivalent forms, each of them with different pairs of semi-empirical coefficients. Table 2-3 summarizes the equation forms and Table 2-4 provides the relationships between the various coefficients and the Ergun coefficients, which are a priori independent of porosity, flow velocity, or pebble diameter. Table 2-5 provides several cases of corresponding values for these pairs of coefficients, which are available in the literature[39]. The "Case 1" are the Ergun coefficients, and they are used in this thesis as the reference values for pressure drop calculations. They are based on experimental data for $0.1 < Re_D < 10{,}000$, with water and gases.

The user-input parameters that characterize the porous media flow in COMSOL are porosity, ε, permeability, K, and the Forcheimer drag coefficient, β_F. The latter two are computed from the Ergun coefficients, based on the equations in Table 2-4. Sensitivity analysis for the Ergun correlation coefficients should be performed. Furthermore, these coefficients were derived for isothermal beds. For heat generating beds, with a fluid viscosity that varies exponentially with temperature, the coefficients may be significantly different. Experimental measurements of the friction losses in a heat-generating packed bed, at steady state and during thermal transients should be performed. Also, the Ergun coefficients were measured for one-dimensional axial flow through a packed bed, but we apply them here for three-dimensional flow in cylindrical coordinates. Experiments should be performed to verify that the Ergun coefficients still hold for multi-dimensional flow through a packed bed.

Table 2-3. Equivalent semi-empirical expressions for the pressure drop in a packed bed.

Forcheimer flow (used in COMSOL)[38]		$\frac{dp}{dx} = \frac{\mu}{K} \cdot u_D + \beta_F \cdot u_D^2$	
Forcheimer flow[43]		$\frac{dp}{dx} = \frac{\mu}{K} \cdot u_D + c_F \cdot \frac{\rho \cdot u_D^2}{\sqrt{K}}$	
Ergun correlation[44]		$\frac{dp}{dx} = E_1 \cdot \frac{(1-\varepsilon)^2}{\varepsilon^3} \frac{\mu \cdot u_D}{d^2} + E_2 \cdot \frac{1-\varepsilon}{\varepsilon^3} \frac{\rho \cdot u_D^2}{d}$	
Friction factor	$Re_d = \frac{\rho u_D d}{\mu}$	$\frac{dp}{dx} = \frac{f}{d}\left(\frac{\rho {u_D}^2}{2}\right)$	$f = \frac{f_1}{Re_d} + f_2 = \left[\frac{f_1/f_2}{Re_d} + 1\right] f_2$
	$Re = \frac{\rho u_p d}{\mu} = \frac{Re_d}{\varepsilon}$	$\frac{dp}{dx} = \frac{f_p}{d}\left(\frac{\rho {u_p}^2}{2}\right)$	$f_p = \frac{f_{1p}}{Re} + f_{2p} = \left[\frac{f_{1p}/f_{2p}}{Re} + 1\right] f_{2p}$
p is the pressure, x the spatial dimension, μ and ρ the fluid viscosity and density, respectively, evaluated at the local bulk fluid temperature, d the pebble diameter, ε the bed porosity, u_D the superficial velocity, u_p the pore velocity. K [m²] is Brinkman permeability, β_F [kg/m⁴] the Forcheimer drag coefficient, c_F the nondimensional form of the Forcheimer drag coefficient, E_1 and E_2 Ergun correlation coefficients, f, f_1, f_2 friction coefficients based on superficial velocity, and f_p, f_{1p}, f_{2p} friction coefficients based on pore velocity; these are semi-empirical coefficients.			

Table 2-4. Algebraic equivalence among different expressions of the semi-empirical coefficients for the pressure drop in a packed bed.

Permeability (K)	$K = \frac{1}{E_1} \frac{\varepsilon^3 \cdot d^2}{(1-\varepsilon)^2}$	
Forcheimer drag coefficient[43] **(c_F)**	$c_F = \frac{E_2}{\varepsilon^{1.5}\sqrt{E_1}}$ with wall effects: $c_{F,w} = c_F \cdot \left(1 - 5.5\frac{d}{D}\right)$	$\beta_F = c_F \cdot \frac{\rho}{\sqrt{K}}$
Friction coefficients	$f_1 = 2E_1 \frac{(1-\varepsilon)^2}{\varepsilon^3} = \frac{2d^2}{K}$ $f_2 = 2E_2 \frac{(1-\varepsilon)}{\varepsilon^3} = \frac{2c_F d}{\sqrt{K}}$	$\frac{f_1}{f_2} = \frac{E_1}{E_2}(1-\varepsilon)$ $f_p = f\varepsilon^2$
	$f_{1,p} = 2E_1\left(\frac{1-\varepsilon}{\varepsilon}\right)^2 = f_1\varepsilon$ $f_{2,p} = 2E_2 \frac{1-\varepsilon}{\varepsilon} = f_2\varepsilon^2$	$\frac{f_{1,p}}{f_{2,p}} = \frac{E_1}{E_2}\frac{1-\varepsilon}{\varepsilon}$
d is the pebble diameter, D the packed bed diameter, ε the bed porosity, ρ the fluid density evaluated at the local bulk fluid temperature. K [m²] is the Brinkman permeability, β_F [kg/m⁴] the Forcheimer drag coefficient, c_F the nondimensional form of the Forcheimer drag coefficient, E_1 and E_2 Ergun correlation coefficients, f, f_1, f_2 friction coefficients based on superficial velocity, and f_p, f_{1p}, f_{2p} friction coefficients based on pore velocity; these are semi-empirical coefficients.		

Table 2-5. Semi-empirical coefficients for the friction losses through a porous media with 40% porosity, and 3-cm pebble diameter, derived from two sets of Ergun coefficients.

	Case 1 Blake-Carman-Kozeny[40,44] (base case)	**Case 2 Macdonald[39]**
E_1	150	180
E_2	1.75	1.75
f_1	1,688	2,025
f_2	33	33
f_{1p}	675	810
f_{2p}	5.25	5.25
c_F	0.56	0.52
β_F	1.1E+06	1.1E+06
K	1.1E-06	8.9E-07
f_1/f_2	51	62
f_{1p}/f_{2p}	129	154

Porosity is modeled as a constant in *Pod*, and wall effects are not taken into account. For smaller bed dimension to pebble diameter aspect ratio, modeling the bed with a spatially dependent porosity that is lower at the walls may be sufficient to account for the wall effects, but this would need to be verified experimentally, for multi-dimensional flows, and non-isothermal beds.

For the pebble bed, the definition of flow cross sectional area can be based on the empty bed or the filled bed. In this chapter, which is concerned with the analysis of flow within the pebble bed, the cross-sectional area of the empty bed is used to calculate the superficial velocity of the fluid. This convention is followed in order to be consistent with the built in equation for COMSOL porous media flow. In Chapter 3 , which models the overall behavior of a pebble bed within a larger fluid system, the converse convention is used, and the 1D momentum conservation equation is written in terms of the pore velocity, in order to be consistent with how all the other components of the fluid system are treated. The conversion between the friction coefficients based on superficial velocity, and those based on pore velocity is given in Table 2-4.

The first term of the pressure drop correlations is the Reynolds-dependent term of the friction coefficient, and the second term is Reynolds-independent. The Reynolds-dependent term becomes negligible for values of $Re_d \gtrsim (10\ f_1/f_2)$. This means that at higher Reynolds numbers, friction losses are viscosity-independent and the momentum equation couples to the energy equation only through the buoyancy term. At low Reynolds values, the pressure drop and velocity distribution in the bed are also coupled to the temperature of the fluid in the bed through the viscosity dependence on the bulk fluid temperature. The f_1/f_2 ratio is proportional to the packing fraction. A lower packing fraction leads to a lower threshold Reynolds at which the Reynolds-dependent term becomes negligible. The Reynolds-independent term becomes negligible at values of $Re_d < (0.01 f_1/f_2)$.

2.2.2 Fluid energy equation

The energy equation for the fluid in the pebble bed, as defined in the COMSOL module for Heat Transfer in Liquids[37], is

$$\rho c_p \bar{u} \cdot \bar{\nabla} T = \bar{\nabla} \cdot (k \bar{\nabla} T) + Q \overset{Pe \gg 1}{\Longrightarrow} \rho c_p \bar{u} \cdot \bar{\nabla} T = Q \tag{2-6}$$

To expand this model to a transient thermal model, heat transfer between the solid and the liquid must be added, heat generation must be modeled as present only in the solid (neglecting gamma and neutron heating in the fluid), and the thermal inertia of the fuel must be taken into account (ρc_p).

The energy boundary conditions are adiabatic at the walls and user-specified temperature at the inlet faces. For normal operation the coolant inlet temperature is 600°C.

This equation neglects dispersion and thermal conductivity of the bed and of the fuel, which is a valid assumption for values of Peclet number that are much greater than unity. In addition to the fluid thermal diffusivity, fluid dispersion in the porous bed also contributes to the effective thermal diffusion term.

$$\frac{1}{Pe} = \frac{\alpha_{eff}}{d \cdot \bar{u}} \tag{2-7}$$

$$\alpha_{eff} = \alpha_{disp} + \alpha_f \tag{2-8}$$

$$\alpha_f = \frac{k}{\rho c_p} \tag{2-9}$$

where α_{disp} is the thermal diffusivity due to dispersion in the porous media, α_f is the thermal diffusivity of the fluid.

2.2.3 Fuel Energy Equation

The fuel energy equation was added to the model to determine the average fuel kernel temperature at steady state. This information is necessary for loose coupling to neutronics calculations, for ATWS response scoping analysis. It is to be noted that the neutronic timescales are most likely much shorter than the thermal response timescales, and in most cases loose coupling between neutronics and thermal-hydraulic analysis of the core may be sufficient; however, this assumption merits further investigation.

The average kernel temperature is calculated at every point in the core by adding the difference between average fuel temperature and the bulk coolant temperature, $\Delta T_{av,FC}$. The $\Delta T_{av,FC}$ is calculated based on the core local power density and local fluid flow conditions, and it is a sum of temperature rises across the following domains:

$$\Delta T_{av,FC} = \Delta T_{conv} + \Delta T_3 + \Delta T_{av,2} + \Delta T_{buf} \tag{2-10}$$

A schematic diagram of the temperature distribution in the pebble fuel element if given in Figure 2-7. The thermal conductivity of the fuel layer was assumed to be the same with that of the graphite in the outer graphite shell; this is likely a conservative assumption.

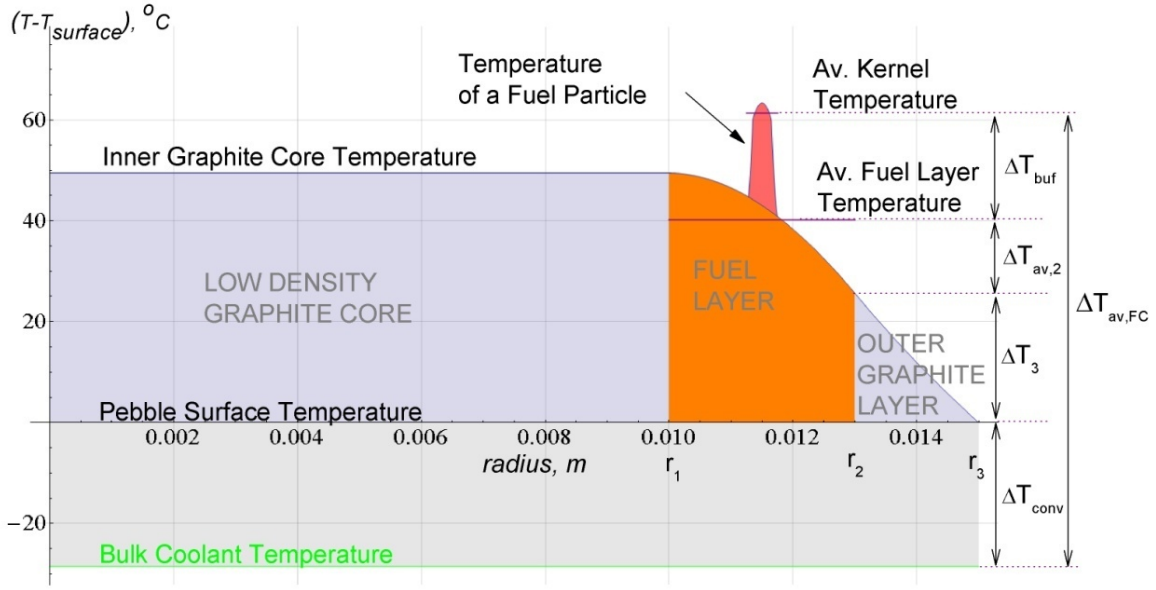

Figure 2-7. Example of the temperature distribution inside a fuel pebble, referenced to the temperature at the surface of the pebble. (Fuel design parameters: 20 MW/m3, 47 mW/kernel, 38% particle packing fraction, 300 μm kernel diameter, 1 cm graphite core diameter, 1340 kg/m3 graphite core density.)

The temperature rise from the bulk coolant temperature to the fuel pebble surface, ΔT_{conv}, is calculated directly in COMSOL, by evaluating the following equations in the post-processing segment of the COMSOL model.

$$\Delta T_{conv} = T_{surf} - T_{fluid} = \frac{q_{pebble}}{A_{pebble}} \cdot \frac{1}{h} \tag{2-11}$$

$$h = Nu \cdot \frac{k_f}{d} = 2 + 1.1 \cdot Pr^{\frac{1}{3}} \cdot Re_d{}^{0.6} \tag{2-12}$$

$$T_{surf} = T_{fluid} + \Delta T_{conv} \tag{2-13}$$

where T_{surf} is the pebble surface temperature, T_{fluid} the bulk fluid temperature at the point where the pebble is located, q_{pebble} the power generation per pebble, A_{pebble} the exterior surface area of the pebble, h the convective heat transfer coefficient, k_f the fluid thermal conductivity, d the pebble diameter, Pr the Prandtl number of the fluid evaluated at T_{fluid}, Re_d the Reynolds number of the fluid at the point where the pebble is located calculated based on the superficial velocity of the fluid at the point in the pebble bed where the pebble is located.

The temperature difference between the pebble surface and the kernel temperature is calculated by solving the conduction equations for the graphite outer shell of the pebble, the fuel shell of the pebble, and the buffer layer of the TRISO particle. The complete set of equations is given in Appendix D. The boundary conditions for the graphite outer shell are heat flux on both surfaces, and temperature continuity at the pebble surface. The boundary conditions for the fuel zone are given heat flux and temperature at the outer surface, and adiabatic inner surface. The volumetric average temperature of the fuel zone in the fuel pebble, $T_{av,2}$, is used as the outer temperature boundary condition for the buffer region in the TRISO particle, as defined by equation (2-14).

$$T_{av,2} = \frac{\int_{r_1}^{r_2} T(r) r^2 dr}{\int_{r_1}^{r_2} r^2 dr}; \Delta T_{av,2} = T_{av,2} - T(r_2) \quad (2\text{-}14)$$

where r_2 is the interface between the graphite shell and the fuel shell in the fuel pebble.

This approach is similar to that adopted for the modeling of gas-cooled reactor fuel in that the temperature profile in the TRISO particle is superimposed to the temperature profile in the pebble fuel element (see Figure 2-8) [45,46]. For both models, the primary temperature drop in the TRISO particle is across the porous buffer layer, which has much lower thermal conductivity than the pyrocarbon and silicon carbide layers. In the fuel element both the temperature rise across the fuel region, and across the outer graphite shell contribute significantly to the temperature rise across the pebble. The temperature rise across the TRISO kernel is slightly higher due to the higher power density of the FHR fuel, and the temperature gradient in the outer graphite shell is also higher due to the higher heat flux at the surface of the FHR pebble.

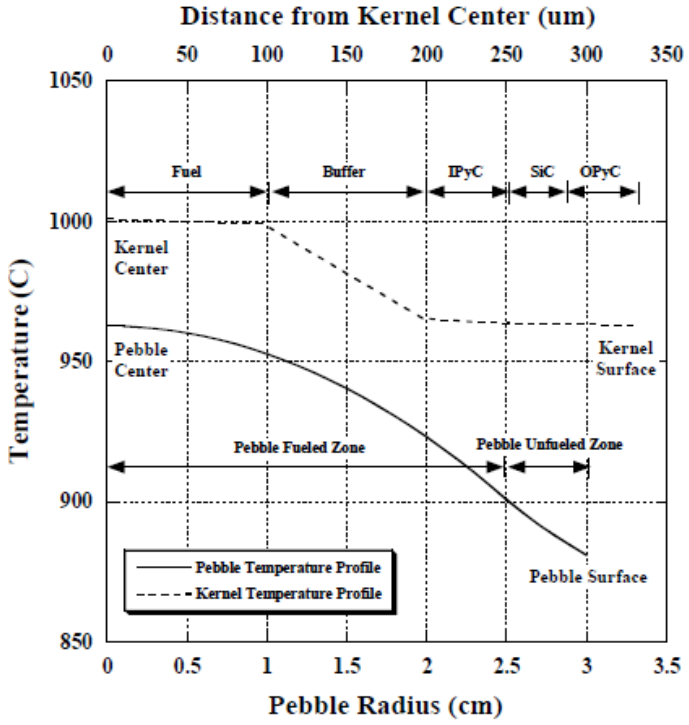

Figure 2-8. Temperature profile for gas reactor pebble fuel, as modeled by TIMCOAT[46].

There are two important differences between the thermal models for gas reactor fuel and FHR fuel. (1) To assess fuel temperature reactivity feedback, the metric of interest is the average temperature of the fuel kernel, not the peak fuel temperature that is of interest for loosing fission product retention in the fuel particles. The boundary condition for the TRISO surface temperature is the volume-averaged temperature of the fuel zone in the pebble. For gas-cooled reactors the TRISO surface temperature is calculated as the peak temperature in the fuel element. (2) The pebble fuel has a graphite core, with the fuel in an annular region at the periphery of the pebble; FHRs cores have higher power densities than gas cooled reactors do, and the inner graphite core helps keep the fuel temperatures low and enables high power

density operation. FHR power densities are in the range of 10 to 30 MW/m^3, with nominal values given in Figure 2-9, for the 900 MWth PB-AHTR; gas cooled reactor power densities are 4.8 MW/m^3 for the 400 MWth pebble bed modular helium reactor (PBMR), and 6.6 MW/m^3 for the 600 MWth gas turbine modular helium reactor (GT-MHR) [47,48].

A relationship between the local core power density is established, and implemented as a function in COMSOL (see Figure 2-9). The relationship is linear. Temperature rise across the layers in the fuel pebble is proportional to the total power generation in the pebble, and temperature rise across the TRISO particle is proportional to the total power generation in the kernel. For a given pebble and particle fuel design, they are both linearly related to the local power density in the core. For future studies, if peak fuel temperature is of interest, instead of average fuel temperature, a similar correlation can be developed and additionally implemented in the COMSOL model, with very little effort.

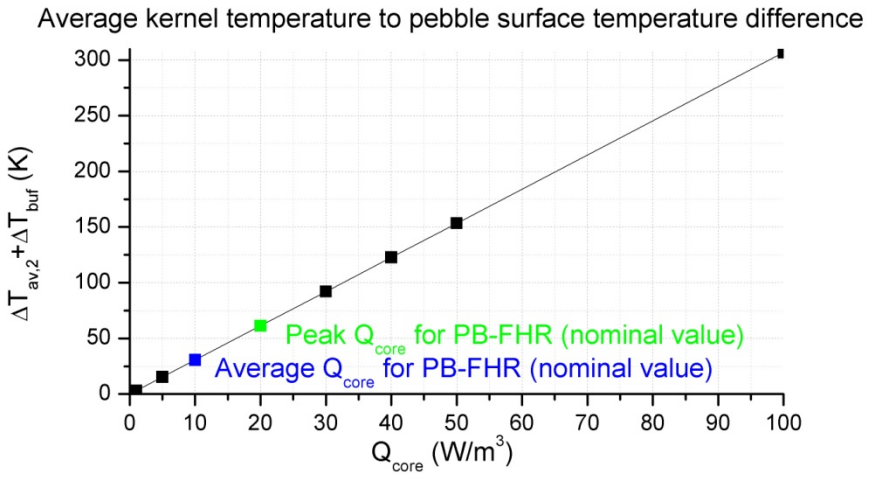

Figure 2-9. Fuel temperature rise as a function of power density

2.2.4 Meshing

The mesh is generated in COMSOL. The mesh elements are triangular. Mesh refinement studies were performed to verify model convergence, and they are discussed in section 2.2.4. Boundary layer meshing is important for convergence of the energy equation, because of the adiabatic boundary conditions at the walls.

For coarse meshes the mesh is elongated 5:1 in the axial direction, to create more mesh points along the radial direction. For flow in cylindrical or spherical coordinates, it is important to have narrow discretization in the radial direction, to ensure a low error on radial velocity component in each mesh element. This is especially important at lower radial locations in the core. For finite element models in COMSOL, there is also the alternative option to increase the polynomial order of the test function, instead of decreasing the size of the mesh. For the central core, the coarser meshes had a maximum element size of 0.25 m in the axial dimension and 0.05 m in the radial direction, and extra fine meshes had maximum element size of 0.03 m.

As a comparison to *Pod*, RELAP5-3D models of reactor cores are currently limited to a nine by nine rectangular mesh, and the fluid velocity in each element is evaluated based on the flow cross sectional area for each element. The flow cross sectional area for each element is a user

input parameter, and it should be defined such that it leads to appropriate calculation of friction losses, heat transfer coefficient, and fluid momentum inertia. Code-to-code comparison of RELAP5-3D results against *Pod* results will be very important to demonstrate appropriate implementation of the coarse mesh.

2.2.5 Model Verification

Model verification is an important step of any numerical modeling. COMSOL is an FEM code, and simple verifications, such as overall energy and mass conservation, are not inherent to the code. It is important also to demonstrate that these conservation conditions are not sensitive to the mesh, in order to demonstrate that a sufficiently fine mesh was used.

COMSOL is a finite element solver for differential equations, that is not specifically designed for thermal-hydraulic modeling. The differential conservation equations are solved for the discretized system, and the integral conservation equations are not applied to the overall system, as a convergence criteria. Hence, the mesh makes a difference for the overall conservation equations. For example, if a uniform triangular mesh, that is coarse and without boundary layer meshing along the adiabatic walls will lead to a mass flow rate 7% higher than the inlet flow rate, a core temperature rise is 5 degrees lower than expected, and 17% heat loss through the adiabatic walls. Table 2-6 presents these results for three different meshes.

Table 2-6. Verification calculations for Pod, showing integral conservation equations sensitivity to meshing

	Mesh maximum element size (m)	Core temperature rise (K)		Heat Flux			Mass flow rate/inlet mass flow rate			Pressure (Pa)	
		Expected	Calculated	Total heat gen (MW)	Total normal heat flux (MW)	Heat Flux at Adiabatic Walls (MW)	Inlet	Outlet	Walls	Expected	Calculated
Mesh 1	0.03088	100	100.0	900.00002	869.9001	-7.6	1.0000	0.99653	-0.000029	8,187	8,160
Mesh 2	0.39161	100	100.07	900.00002	867.01622	0.02	1.0000	0.99616	-0.000001	8,187	8,153
Mesh 3	0.11382	100	94.9	900.00002	1478.0003	-151.2	1.0000	1.07163	0.000033	8,187	9,014

Mesh 1 is a fine uniform mesh, with boundary layer meshing in the vicinity of the adiabatic walls; Mesh 2 is a fine mesh in the radial direction, it is five times coarser in the axial direction, and it has boundary layer meshing; Mesh 3 is a coarse uniform mesh. All meshes have triangular mesh elements.

The importance of model verification is well illustrated by the very large economic consequences of a computational error that Mitsubishi made in modeling steam flow in the San Onofre Nuclear Generating Station (SONGS) steam generators (SG). In January of 2012, a steam generator tube leak was detected, and the cause was later identified to be tube-to-tube wear due to fluid-elastic instability in the U-region of the steam generator tubes. The Mitsubishi FIT-III thermal-hydraulic models under-predicted the flow velocity by a factor of 3 to 4 and resulted in errors in the design of the tube supports, which lead to significant tube vibration and consequent tube-to-tube wear. In light of the 0.5 design value for the ratio between the design velocity and the critical velocity, this error in the calculation results is very large. Code-to-code comparisons were recently performed, and showed a high discrepancy between Mistsubishi FIT-II models and four other numerical models of the SONGS replacement steam generators at Units 3 and 2[49]. This error could most likely have been found with simple verification calculations of the consistency of overall flow continuity, applied to the core velocities

calculated by the model. This thermal-hydraulic calculation error caused an outage of almost a year, to date, at units 2 and 3 of the SONGS plant. SONGS has proposed to restart Unit 2at 70% power in order to limit the flow velocities in the SG, and hundreds of the SG tubes have been plugged. The plan for Unit 3 restart are not yet known[50].

Pod performs a set of verification calculations for every run. The verification calculations are set-up in COMSOL to be automatically calculated and exported with the data files, and they are as follows: total mass conservation, energy conservation, temperature rise, no energy flux at adiabatic boundary conditions, no mass flux at the walls. Table 2-7 gives verification calculations implemented in COMSOL, using the COMSOL variable names.

For simplified cases, the pressure drop results can be compared against the analytical calculation of pressure loss. Verification calculations for various power levels, for the central core region with radial and axial flow are given in Table 2-8. For axial flow, the model calculations perfectly match the analytical calculations with a very coarse mesh, and are insensitive to mesh refinement. For radial flow through the core, the model calculations can have below 1% error on the core pressure drop, for the coarse mesh.

For higher complexity problems, such as radial flow with buoyancy effects, the convergence of the solver may be dependent on the initial guess. The default option for the initial guess is the zero solution. When the solver is not successful with this guess, a simpler version of the problem is solved, and then the solution is used as the initial guess for the more complex problem. For example, the problem is solved with no buoyancy effects, and then the solution is used as an initial guess for the same problem with buoyancy effects. Alternatively, the buoyancy force can be gradually increased from zero to the desired value, solving the problem in several discrete steps, each of which provides the initial guess for the subsequent step.

Table 2-7. Pod verification calculations implemented in COMSOL

Verification Calculations		Definitions
1. mass conservation: inlet mass flux	$\frac{\rho_L \iint_{inlet\ faces} udS}{m_L} = 1$	m_L is the inlet mass flow rate (user input) L subscript indicates liquid properties
2. total net mass flux	$\iint_{\substack{inlet\ and\\ outlet\\ surfaces}} udS = 0$	
3. core temperature rise	$\frac{\iint_{\substack{outlet\\ faces}} TudA}{\iint_{\substack{outlet\\ faces}} udA} - \frac{\iint_{\substack{inlet\\ faces}} TudA}{\iint_{\substack{inlet\\ faces}} udA} = \frac{\iiint_{domain} ht.Qtot\ dV}{cpL \cdot \rho \iint_{\substack{inlet\\ faces}} udS}$	ht.Qtot = heat generation, in W/m3
4. adiabatic walls	$\iint_{\substack{adibatic\\ face}} ht.ntflux = 0$	ht.ntflux = heat flux normal to the surface
5. total net heat flux	$\iint_{\substack{all\\ faces}} ht.ntflux = \iiint_{domain} ht.Qtot\ dV$	
6. total heat generation	$\frac{\iiint_{core} ht.Qtot\ dV}{Qth \cdot decay} = 1$	Qth = core total power, in W decay = decay heat power fraction of the total core power
Analytical estimations for central core radial and axial flow		**Definitions**
7. Reynolds number	$Re_{estimated} = \frac{m_L}{\mu_L}\frac{d}{A}$ $Re_{Pod} = \frac{\rho_L d}{\mu_L} br.U(r,z)\varepsilon$	$A_{axial} = 6.22\ m^2$ $A_{radial} = 10.6\ m^2$ br.U = magnitude of superficial velocity
8. Pressure drop	$\Delta P = \frac{{m_L}^2}{2\rho_L}\left(\frac{L}{A^2 d}\right)\left(\frac{f_{1,p}}{Re} + f_{2,p}\right)$	$L_{axial} = 3.0\ m$ $L_{radial} = 1.4\ m$

Table 2-8. Verification calculations for pressure drop, coarse mesh

	decay heat fraction	Pressure (Pa)		Error
		Pod results	Analytical Calculations	
Radial flow	1	8,156	8,187	-0.37%
	0.06	64.8	64.9	-0.14%
	0.02	15.6	15.6	-0.07%
	0.01	7.03	7.03	-0.04%
Axial flow	1	50,303	50,303	0.00%
	0.06	312	312	0.00%
	0.02	65.7	65.7	0.00%
	0.01	28.1	28.1	0.00%

New COMSOL software versions are frequently issued by COMSOL Inc., and the development of the PB-FHR core has been done in versions 3.5, 3.5a, 4.0, 4.1, 4.2, 4.2a, and 4.3. The results for the 2009 PB-AHTR core were generated in COMSOL 4.2a, version number 4.2.1.166. The results for the central core region were generated in COMSOL 4.3, version number 4.3.0.151.

2.3 Flow distribution optimization

An optimization study of the flow distribution in the core was performed, based on the subset of the system functional requirements that applies to the thermal-hydraulic behavior of the reactor core, which are listed in Table 2-2. The primary objectives for this optimization study are: (1) minimize the temperature range for the core outlet temperature across all the outlet ports, (2) minimize the difference between the average fuel temperature and the bulk fluid temperature, (3) minimize core pressure drop during forced circulation (4) maximize heat transfer with the graphite reflectors during transients, and manage bypass flow and neutron and gamma heating in the graphite reflectors. The optimization is done for the forced circulation mode, at full power heat generation. The optimizing parameters are the location of the inlet and outlet faces, and the pressure distribution across these faces.

Conceptually, the objective of coolant flow distribution through the core is to route higher flow rates of cold coolant in the regions of high power density, for two reasons. (1) This will lead to a uniform temperature distribution across the outlet faces. Outlet temperatures that are significantly above the average coolant outlet temperature indicate inefficiencies in the cooling of the core. Furthermore, a uniform distribution of the temperatures in the outlet manifold will minimize thermal stresses on the graphite reflectors and other structural components associated with the outlet plenum, and thermo-chemical gradients that may accelerate corrosion. (2) Efficient cooling of the high power density regions will keep the fuel temperatures closer to the coolant temperature in these regions. These regions also have a higher weighting factor for their contribution to the temperature nuclear reactivity feedback, and a smaller difference between the fluid temperature and the fuel kernel temperature leads to lower temperatures at which subcriticality is achieved under the influence of the temperature reactivity feedback.

Lastly, maintaining a high radial component for the flow will ensure lower pressure drops across the pebble bed core, which is important for two reasons. (1) The elevation rise of the fluid level in the fueling standpipe above the fluid level in the reactor pool is proportional to the head at the inlet of the core. This is a limiting design parameter for the normal operation mode. (2) The elevation requirement of the primary coolant natural circulation loop for decay heat removal increases with higher pressure drop across the core. This is a limiting design parameter for the decay heat removal mode.

2.3.1 Boundary conditions

The total mass flow rate was always set such that the core temperature rise is 100°C, for any given total heat generation in the core. Inlet boundary conditions were set on three faces (see Figure 2-2 for the numbering scheme for the faces). For the inlets on the Inner Reflector wall, faces 1 and 4, a uniform inlet velocity was set. The fraction of mass flow rate through Face 1 with respect to Face 4 was an optimization parameter. For the inlet at the bottom of the defueling chute, Face 5, a constant pressure boundary condition was set, because this face connects directly with the inlet plenum, and no orificing would be feasible. The COMSOL input for this boundary condition is actually a desired total mass flow rate; COMSOL will then solve for the value of uniform pressure at this boundary condition which yields the specified mass flow rate. The fraction of the total mass flow rate that enters the core through Face 5 was an optimization parameter.

The fluid outlet boundary conditions were set as zero pressure boundaries. In reality, the outlet faces, Faces 1, 2, and 3.1, contain a certain number of circular outlet ports, all of which duct fluid to a common outlet plenum. The distribution of outlet flow on the outlet face depends on the distribution and dimension of outlet ports, or otherwise described, it depends on the distribution of outlet flow area over the outlet faces. *Pod* currently models this as a set of fictitious very thin outlet disks. The location and outlet flow area of each of the outlet disks were optimization parameters. The top of the defueling chute, Face 3.2, connects directly to a large plenum, and there is no orificing across this face, so the entire face is set as a zero pressure outlet boundary condition.

2.3.2 Results

The temperature and flow distributions for the full power operation of the optimized core are shown in Figure 2-10. The pressure drop is 58.7 kPa. The Reynolds number based on pore velocity ranges from 3500 at the inlet Face 1 and at the bottom of the defueling chute, 1800 in the center of Regions 1 and 2, and 500 in Regions 4 and 5 at the inlet of the core. The peak temperatures for the bulk coolant and the fuel kernels are 723°C, and 780°C, respectively. The power density-weighed volume averaged temperatures for the coolant and fuel kernels are 650.7°C, and 711.2°C, respectively. Thus, $\Delta T_{av,FC}$ is 61°C, which indicates that it may be possible to design a PB-FHR core that maintains the coolant core outlet temperature below 800°C and does not lead to reactor damage under ATWS scenarios, which rely on temperature reactivity feedback for shutdown.

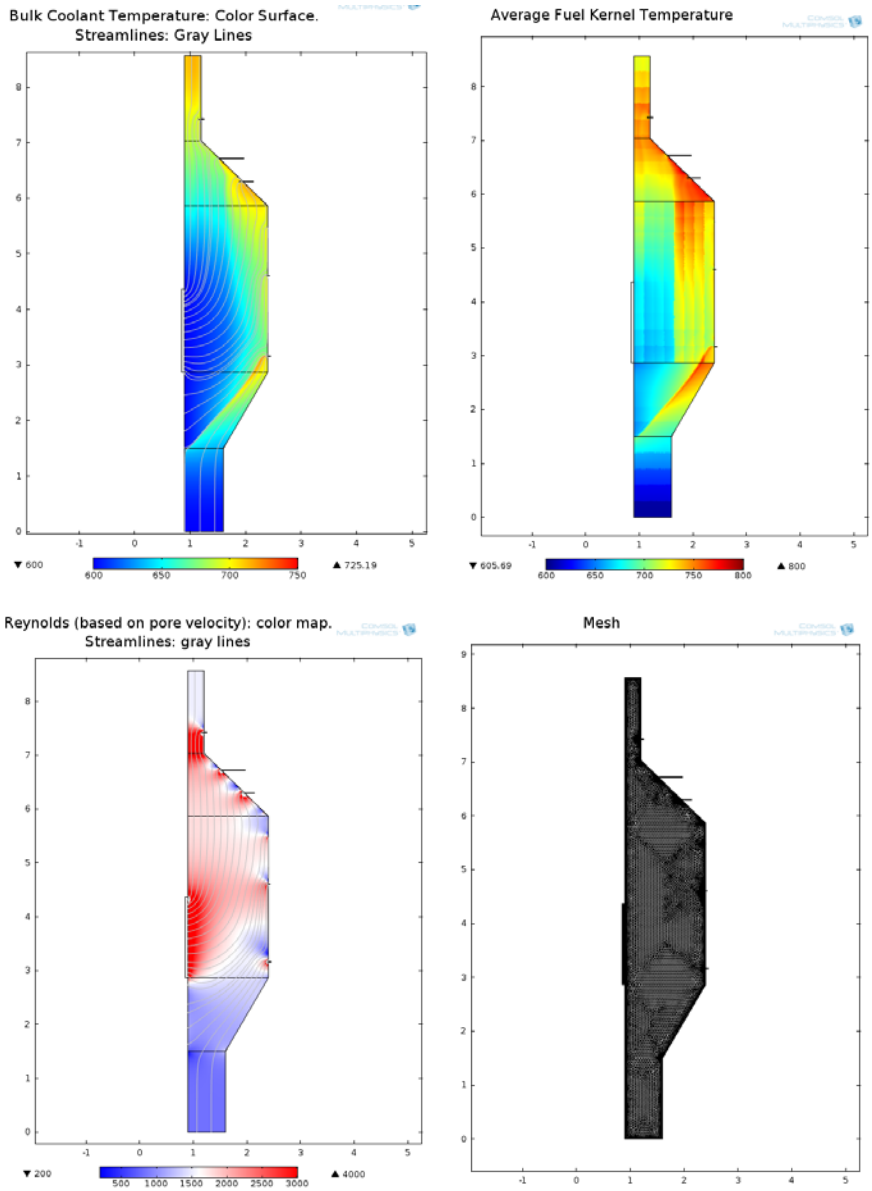

Figure 2-10. 2009 PB-AHTR Core with Optimized Flow Distribution, at Full Power Operation

The contributions to pressure drop from the various regions of the core are plotted in Figure 2-11. Regions 2 and 3 account for half the pressure drop in the core, while generating only 15% of the total core power. This is partly due to the fact that there is a region of local power peaking at the interface between the converging region (region 2) and the defueling chute (region 3), and in order to provide sufficient cooling, flow must be forced upwards through the defueling chute. It is also due to the fact that the defueling chute is long, narrow, and located at the smallest radial location, so its cross-sectional area is small, and the flow is strictly axial. If the design permits, it is best either to bring cold fluid to the bottom of the defueling chute, from one of the core bypass flows, or to route the core outlet coolant radially instead of axially through the defueling chute.

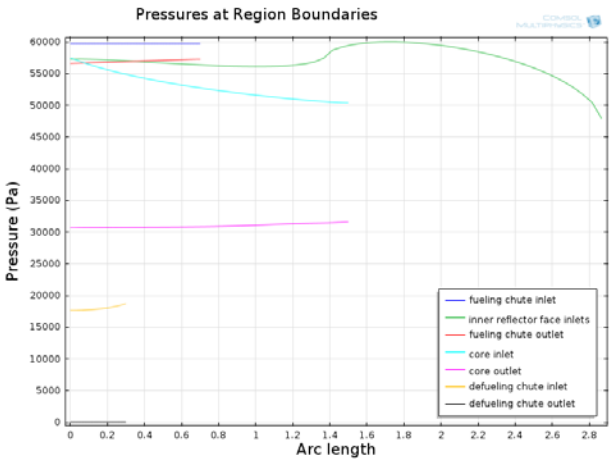

Figure 2-11. Pressure at domain boundaries for the 2009 PB-AHTR Core with Optimized Flow Distribution, at Full Power Operational Mode.

The distribution of the coolant outlet temperatures is between 680 to 720°C. When the flow rate drops to the 2% decay heat removal level, the distribution of coolant outlet temperature broadens, and it ranges from 670 to 730°C. This occurs because the lower Reynolds numbers, the friction coefficient becomes much more dependent on Reynolds number, and the high Reynolds number regions become starved of flow. For example, the fractional mass flow rate exiting at the top of the defueling chute drops from 7% to 3%, while the fractional power generation in the region remains the same. This effect may be counterbalanced by local buoyancy effects, which become significant at low flow rates, and merits further investigation. Temperature-dependent fluid viscosity, and thermal dispersion in the pebble bed may lead to further uniformization of the core outlet temperature, but these are expected to be second order effects because temperature gradients in the core are small. Figure 2-12 provides a side-by-side comparison of the temperature and flow distributions in the core at full power, and at 2% decay heat removal. Figure 2-13 plots the coolant temperatures along the walls of the core, and shows the distributions of coolant outlet temperatures.

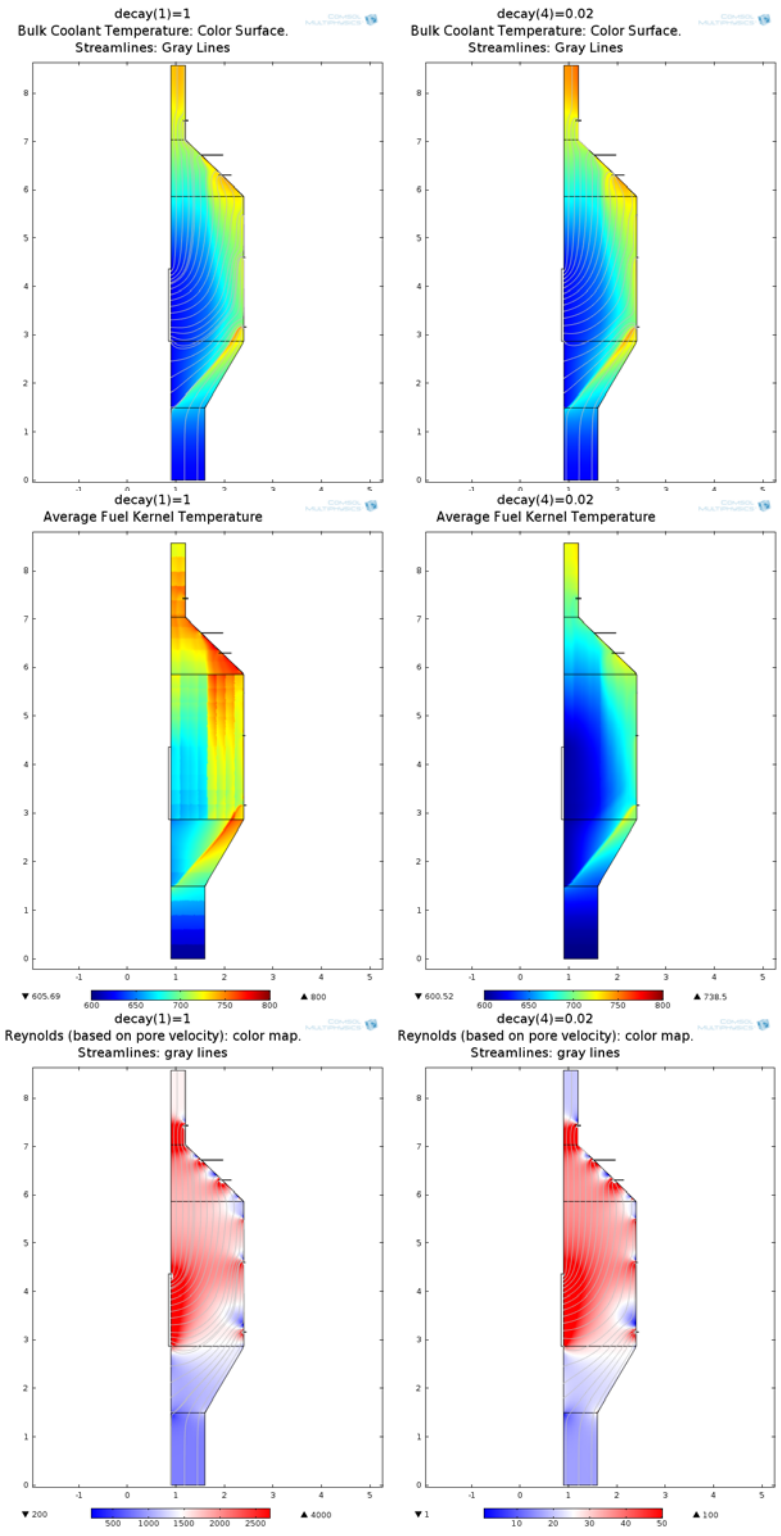

Figure 2-12. Comparison of core parameters between full power operation (left column) and 2% decay heat (right column), with the same average coolant temperature rise across the core, for the 2009 PB-AHTR core with optimized flow distribution.

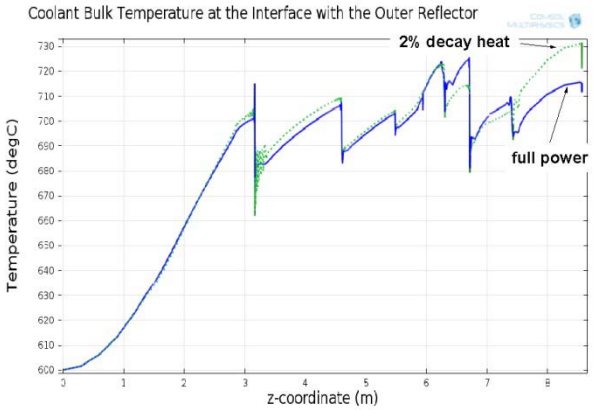

Figure 2-13. Bulk coolant temperature at the interface with the graphite reflector walls, for the 2009 PB-AHTR core with optimized flow distribution.

For the characterization of natural circulation heat removal from the core, the evolution of total pressure drop across the core as a function of mass flow rate is need. This plot is given in Figure 2-14. Natural circulation heat removal is discussed in Chapter 3.

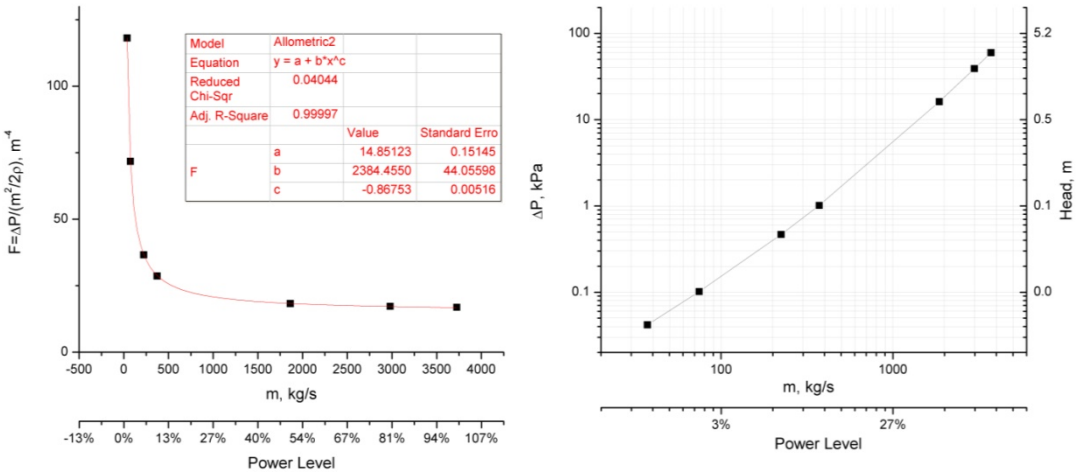

Figure 2-14. Core pressure drop correlation for the 2009 PB-AHTR with optimized flow distribution

2.4 Core resilience to hot and cold spots

The effects of buoyancy and temperature-dependent viscosity on the flow distribution in a pebble bed core with non-uniform heat generation, are investigated by studying a simplified geometry. Only the central core region is modeled here, with a total power input of 900 MW at full power operation, and the power density distribution given in Figure 2-15. Results are given here for axial flow through the core at 2% decay heat power.

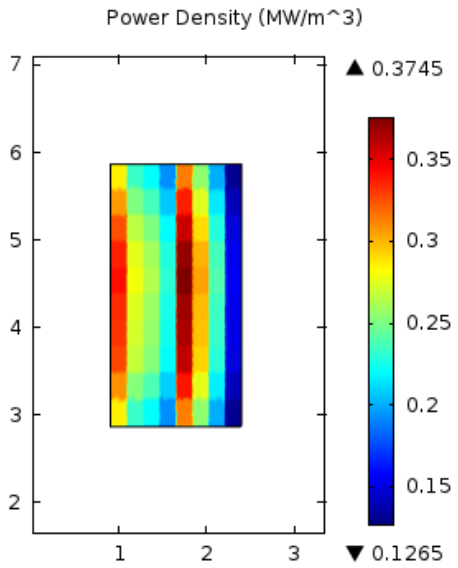

Figure 2-15. Power density distribution of the central core region, at 2% decay heat, with 18 MW total power generation in this region. (The r and z axes are shown in units of meters.)

Figure 2-16 shows the effect of buoyancy and temperature-dependent viscosity on the coolant outlet temperature. Without buoyancy forces, the core outlet temperatures span a range of 50°C. With buoyancy effects the outlet temperatures span a range of less than 10°C, with temperature-dependent viscosity they span a range of 45°C. Buoyancy forces lead to higher axial flow rates in the region of higher power generation, and hence a more uniform temperature distribution at the outlet of the core. Temperature-dependent viscosity leads to higher Reynolds and lower friction coefficient, therefore higher flow rates in the hotter regions of the core; hence temperature-dependent viscosity also leads to a more uniform temperature distribution at the outlet of the core, however the effect is much less significant than the effect of buoyancy. Figure 2-17 plots the Reynolds number in the core for each of these cases, calculated based on the pore velocity in the bed.

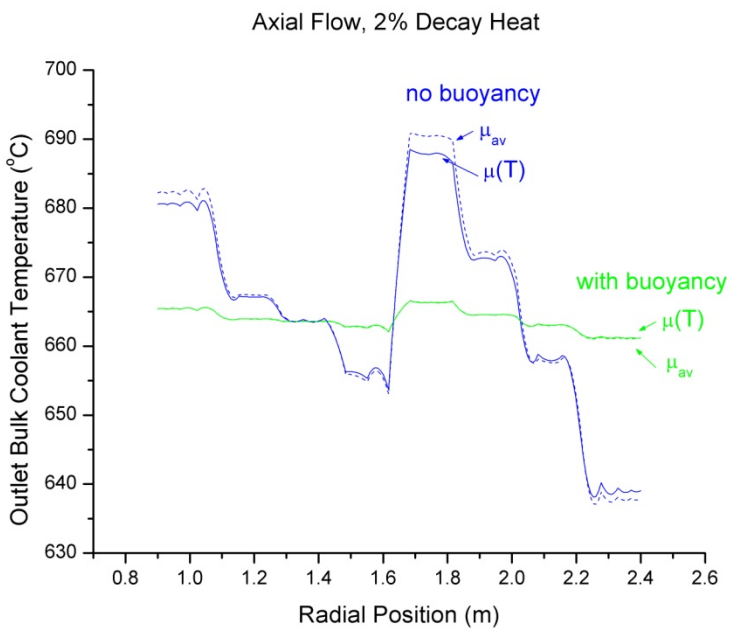

Figure 2-16. Effects of buoyancy and temperature-dependent viscosity on the coolant outlet temperature

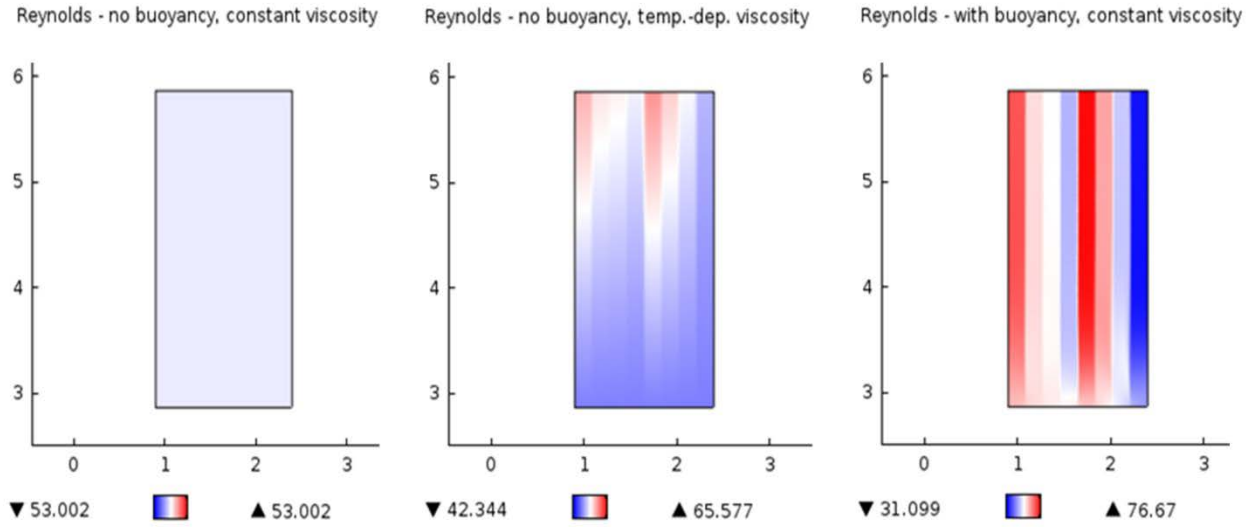

Figure 2-17. Reynolds number with and without buoyancy effects, and temperature dependence of viscosity. 2% decay heat power, axial flow, 100oC core temperature rise. (The r and z axes are shown in units of meters.)

These results have important implications for the design of PB-FHR. The results indicate that porous media cooled by fluoride salt mixtures exhibit resilience to development of hot spots, or cold spots. In PB-FHR, this has application to the pebble bed core, for scenarios in which local high power density regions arise. It also applies to heat exchangers with enhanced surfaces, which can be modeled as porous media, which can develop local regions of high heat

removal rate (cold spots), or of low heat removal rate (hot spots). A uniform coolant temperature distribution leads to higher margin to coolant freezing, and a higher margin to structural material damage due to exposures to high temperatures, or to high temperature gradients. It may also have important implications for instrumentation of the bulk coolant temperature, which is difficult to measure for a fluid that is not thermally homogeneous.

Components that are not thermally sensitive to variations in local heat fluxes may lend themselves to easier modeling, numerically and experimentally. For example, this is important for the core behavior under temperature reactivity feedback transients. If the coolant temperature is relatively uniform irrespective of the power peaking in the core, then it becomes easier to study thermal-hydraulic-neutronic transients: either full coupling is not needed, or a simplified thermal-hydraulic core model will suffice. For integral thermal-hydraulic experiments, modeling the behavior of the core as a simplified one-dimensional component may lead to less distortion, than if significant coolant non-homogeneities were expected at the outlet of the core.

The local buoyancy effects phenomenology in porous media cooled by liquid fluoride salt mixtures should be investigated further to understand the regimes in which these effects are important, and to characterize the integral behavior of such porous media systems. Separate effects experiments should be designed to validate these thermal-hydraulic models.

2.5 Conclusions

This chapter presents the modeling approach for heat-generating porous media, with multi-dimensional fluid flow. Fluid flow and pressure distribution in the core are solved using the momentum equation for flow through a homogenous porous media. The energy equation for the fluid phase is solved separately from the energy equation for the solid phase. For the solid phase, multi-scale conduction equations are solved for; heat generating fuel particles are embedded in pebble fuel elements that are randomly packed and form a homogeneous porous medium. The application of this modeling approach to the PB-FHR annular pebble bed core cooled by fluoride salt mixtures generated a model that is called *Pod*. Model verification shows good agreement of *Pod* results with analytical calculations for simple fluid flow configurations.

Pod is primarily a design tool for reactor design optimization, and for design of experiments. It can generate high resolution temperature and flow distributions, it is flexible in terms of changing the geometry and adding features or additional phenomenology, and the solving time is relatively short. Parametric studies can be automatically set-up, for optimization studies, or sensitivity studies. *Pod* also generates important data that can be used for code-to-code comparisons for thermal-hydraulic system codes used to model the transient response of PB-FHRs.

Loose coupling between *Pod* and neutronics calculations is necessary in order to predict the minimum temperature at which core subcriticality can be reached during an ATWS transient. This metric is important because the core outlet coolant temperature determines the peak temperature to which the metallic structural components of the core are exposed, which is a limiting constraint for the design of PB-FHRs. A steady state point reactor model is employed for the ATWS analysis.

Pod was used to generate a flow distribution in the core that optimizes core pressure drop and effective average fuel temperature in the core. This optimized core is used as a point design, and computation results are shown for full power operation, and decay heat removal operation

of this core. A correlation for the pressure drop through the core, as a function of core mass flow rate, was generated for this optimized core design; this is important for the design and transient analysis of natural circulation driven decay heat removal from the pebble bed core, which is discussed in Chapter 3.

Pod was used to show the effect of buoyancy on temperature distribution in the PB-FHR core. At decay heat power levels, with non-uniform heat generation in the pebble bed, buoyancy leads to significant flow redistribution in the core, and core outlet temperature variations are only a few degrees Celsius, compared to 50°C in the absence of buoyancy. This means that the core behavior during decay heat removal is relatively insensitive to the power peaking profile in the core. This has positive implications for the design of integral effects experiments, and for the modeling of transients that require coupling of thermal-hydraulics and neutronics core responses. The effects of the temperature-dependent viscosity were shown to be similar to those of buoyancy, but much less significant. Separate effects experiments that validate these effects in het-generating porous media cooled by fluoride salt mixtures should be designed. The temperature-dependence of viscosity is expected to have a second order effects, and investigating these effects should have lower priority than investigating buoyancy effects.

2.5.1 Future work

Experiments are needed to investigate the applicability of the Ergun equation for friction coefficients in a pebble bed to geometries more complex than straight channels. Multi-dimensional flow in cylindrical coordinates, and non-isothermal bed conditions may significantly modify the friction loss coefficients. *Pod* can be used as a tool for design of experiments.

To demonstrate the validity of the modeling approach describe here, experimental data should be obtained, and code-to-code benchmarking should be performed. In the future, if *Pod* will be used and developed by several users, some form of version control will have to be implemented.

2.5.2 Future Model Development

Future developments for *Pod*, which require relatively little effort include addition of thermal radiation heat transport, addition of dispersion effects for flow in porous media, migration for the *Mathematica* code for the fuel element conduction equation to the COMSOL model, and design of a temperature data output file that matches the mesh uses in the neutronics model.

More elaborate developments for *Pod* include demonstrating capability to run transient problems, and implementing semi-permeable walls as boundary conditions for the fluid outlet faces. As features are added to *Pod*, the built-in verification calculations should be updated, and additional checks should be added, as appropriate.

An automatic coupling between *Pod* and MCNP can be developed. This would enable faster iterations between thermal-hydraulic and neutronic modeling, making it a more convenient design tool.

CHAPTER 3

Natural Circulation Integral Effects Tests

Natural circulation can be used to design heat transport systems that have no moving mechanical parts, that require no energy input other than the temperature difference between a heat source and a heat sink, and that need no operator action for their activation. Such systems are called passive systems, they have high reliability and require less maintenance than active systems. Natural circulation systems that are driven by buoyancy require low friction flow losses, which generally leads to less compact systems than those driven by forced circulation, which use pumps or an otherwise imposed driving pressure differential.

This chapter discusses single-phase natural circulation, with application to heat removal from pebble beds, and with application to heat transfer fluids with high Prandtl number, high volumetric heat capacity, and high viscosity. The analysis presented here is for Boussinesq fluids, and non-uniform flow cross-sectional area loops with vertical heating and cooling sections. Design considerations for natural circulation heat removal systems are discussed, and a performance comparison of single phase heat transfer fluids is given. Experimental data for the steady state performance of a natural circulation loop is given. Scaling approaches and design of integral effects tests (IETs) for validation of numerical system models are discussed. Experimental data that can be used for as validation data for system models is given.

The design and analysis of the natural circulation decay heat removal system for the pebble bed fluoride salt high temperature nuclear reactor (PB-FHRs) is used as a case study. FHRs are cooled by liquid fluoride salts, which are high Pradtl number fluids with high volumetric heat capacity, and relatively high viscosity. While single phase natural circulation loops have been studied extensively for water[51,52] and liquid metals[53], there are a number of characteristics that are different for liquid fluoride salt coolants. The fluid thermophysical properties lead to design of systems with low flow velocities, and hence high fluid residence times. This, along with a high volumetric heat capacity, leads to relatively slow thermal transients of the reactor system, which is highly desirable feature for a nuclear reactor's response to an accident initiating event. Slow thermal response may also be a desirable feature if it leads to decoupling of thermal phenomena from other, more rapid phenomena, simplifying the modeling requirements of the system.

Section 3.1 provides an introduction to natural circulation phenomena. Section 3.3 provides a description of the PB-FHR natural circulation driven decay heat removal system. Section 3.4 gives the conservation equations for natural circulation, with special treatment for the section of the loop that consists of a heat-generating pebble bed. Section 3.5 discusses steady state behavior of natural circulation loops, with application to design of natural circulation heat removal systems. Section 3.6 gives the arguments for the scaling of transient natural circulation loops. The progression of the loss of forced circulation (LOFC) transient for FHR, which relies on natural circulation for decay heat removal, is presented here. It illustrates the integration of the scaling arguments with temporal decomposition of transient scenarios. Section 3.7 provides the experimental results for a natural circulation loop that uses simulant fluids for liquid fluoride salts.

3.1 Natural Circulation - Introduction

Natural circulation (NC) is buoyancy driven fluid flow, from a low elevation heat source to a high elevation heat sink, for fluids whose density decreases with temperature. Fluid of lower density located at a lower elevation than fluid of higher density rises, thus initiating natural circulation flow. Figure 3-1 shows a schematic of a rectangular loop consisting of a heater, a cooler, and connecting piping; this represents a simple example of a natural circulation loop. Such loops are at the basis of natural circulation driven heat removal systems for nuclear reactors. This chapter is concerned primarily with single phase incompressible Boussinesq liquids for natural circulation, but compressible gasses and boiling/condensing liquids can also establish natural circulation loops, often times more efficiently than Boussinesq liquids.

It is important to note that the local flow regime at each point around such a loop is forced convection, not natural convection. The driving force for flow around the loop is the global buoyancy force, integrated over the entire loop. On the other hand, natural convection flows are driven by local buoyancy forces; a representative example would be a heat source immersed in a pool of cold fluid. In natural circulation loops, flow along the heat exchange surfaces is driven primarily by the loop buoyancy forces, and the orientation of the heat exchange surface can be either vertical or horizontal. For sufficiently low natural circulation flow rates, and sufficiently high heat fluxes, local buoyancy may have an effect on the local velocity profile, and hence on the convective heat transfer coefficients and the friction loss coefficients for each individual section of the loop; this flow regime is termed mixed convection.

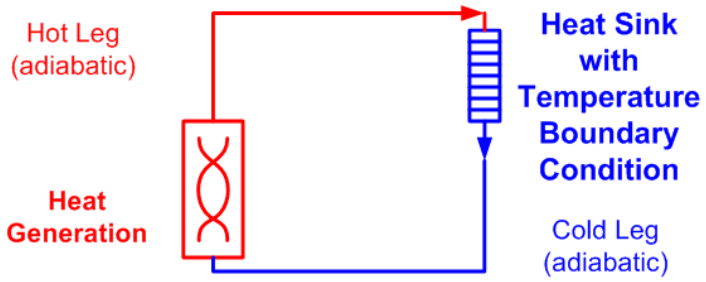

Figure 3-1. Simple natural circulation loop

Examples of natural circulation systems in nature are abundant. Earth magma flows in a circuit from the hot inner core of the earth, to the outer cold crust; the interaction of the magma flows with the tectonic plates can have an effect on seismic and volcanic activity[54]. Similar phenomena occur on other planets as well; the effectiveness of natural circulation in magma oceans on Mars after high-intensity asteroid impact determines the time to magma crystallization, and subsequently may have determined the geological structure of Mars[55]. Water circulation patterns in oceans and lakes are also driven by natural circulation; the water circulation response to the change in thermal gradients affects the transport of nutrients, and dispersion of pollutants in the body of water. The circulation patterns of global winds, from the hot equator to the colder poles, the circulation patterns of winds along a mountain, and the air circulation inside of a room all function on the same principles[56]. Minarets are an example of a historical architectural feature that takes advantage of natural circulation to keep buildings cool. Minarets are tall towers with windows at the top; cold air enters at the base of the building, and is heated by people and solar radiation; the hot air then rises to the top of the tall

towers, and exits through the minaret windows: a fully passive building ventilation system. Thermal chimneys and other modern architectural structures follow similar principles[57,58].

Figure 3-2. Windows at the top of a minaret, for natural circulation ventilation, viewed from the inside. Alhambra Palace, Spain, built in the Xth century AD. (photograph by C. Scarlat)

In the energy field, natural circulation systems have applications such as heat removal from nuclear reactors[53,59], water circulation in solar water heaters[60], and passive extraction of heat from a geothermal reservoir. Greif provides a review of the use of applications of natural circulation to the cooling of engineered systems, such as engines and computers[61].

In addition to buoyancy, chemical potential, magnetic fields, electric fields and any other potential field can also establish natural circulation loops. Often times gradients in several potential fields couple to enhance or to reduce natural circulation. For example, in solar ponds the salinity gradient in a water pond inhibits thermally-driven natural circulation. Solar ponds have been observed in nature, and have also been used as engineered systems for capturing and storing solar thermal energy[62].

3.2 Scaled Experiments - Introduction

Scaled models are experiments that replicate, with various levels of distortion, the behavior and phenomenology of the prototypical system. In nuclear engineering, being able to demonstrate system performance at reduced scale, temperature, pressure, or power input leads to significant cost and time savings in the development and licensing of a reactor design. Therefore, reduced scale models are of most interest. In chemical engineering, the problem is similar, but posed differently. Chemical processes are designed and demonstrated at small scale. For production at larger scale, the processes must be scaled up with sufficiently little distortion

to the key transport and reaction kinetics phenomena to ensure that the final product is reproduced. With the advent the micro-reactors, which enable rapid scanning across a large number of processes or reactions, scale-down of chemical processes is also of interest. Thus, in the field of chemical engineering, design of scaled systems minimal distortion has applicability to process implementation across scales of micro-reactors, bench-top reactions, small industrial installations, and large industrial installations[63].

To design a scaled system, the model and the prototypical system must be characterized by conservation equations and boundary conditions that are mathematically identical. The model can be at different temporal and spatial scales, at different operating conditions, it can be built with different materials, and be governed by different phenomenology than the prototypical system. For thermal-hydraulic scaled experiments that do not use the prototypical fluid, the model fluid is referred to as the simulant fluid. For PB-FHRs, water and heat transfer oils are used as liquid salt simulant fluids, for thermal-hydraulic, hydro-dynamic, and pebble dynamics experiments. The simulant fluids provide the tremendous advantage of low distortion experiments at significantly lower temperatures, reduced geometric scale, and reduced thermal power input. It is sometimes possible to use different phenomenology, which is easier to investigate experimentally, than the prototypical phenomenology. One such example is the extension of convective mass transfer data to the development of convective heat transfer correlations[64].

To minimize distortion in the replication of prototypical system behavior, the nondimensional coefficients in front of each term of the conservation equations, boundary conditions, and initial conditions must have comparable values between the model and the prototype, and non-dimensionalization must be done using the appropriate characteristic length, time, temperature, and mass scales. Because these nondimensional coefficients represent ratios of competing effects (for example the Grashoff number represents the relative contributions of buoyancy versus viscous forces in the momentum conservation equation), it is particularly important to match closely those coefficients that have the highest values for a particular conservation equation, because they indicate the most dominant phenomena.

Integral effects tests (IETs) are scaled models that integrate multiple important phenomena and multiple components for the purpose of replicating the overall behavior of a system. Experimental data from IETs is used to validate codes that predict system behavior. At the sub-component scale, the components of scaled IETs may or may not replicate the geometry and phenomenology of the prototypical system; what is required for the design of IETs is that the overall behavior of each component, with respect to the way that it affects system performance, and the way that the system performance affects its behavior are replicated. So each system component must generate appropriate initial and boundary conditions, even if internally it does not mimic in detail the prototypical system's phenomenology.

Separate effects tests (SETs) are scaled models that investigate specific phenomenology, generally at the sub-component scale where it is easier to externally impose a large range of initial and boundary conditions, and to provide more instrumentation and diagnostics. A good understanding of the phenomenology is necessary in order to adopt an accurate simplified treatment of the integral behavior of each component, and to quantify the uncertainty in the system behavior arising from these simplifications. For example, in an IET that investigates natural circulation in the primary coolant system of a reactor, to enable studies at reduced power the core is likely modeled as a simplified 1-D or 0-D component; SETs that study the 2-D or 3-D core are needed to validate the understanding of phenomenology in the core, which is

then used to generate analytical or semi-empirical relationships that characterize the integral behavior of the core in 1-D or 0-D space, and to quantify the distortion arising from the simplified treatment of the core.

This chapter provides the non-dimensional equations and the scaling arguments for a single phase natural circulation loop. These scaling arguments stand at the basis of design of IETs. They also identify the SETs that are needed in support of accurate scaling of the IETs.

3.3 Description of the PB-FHR Natural Circulation Driven DRACS System

Nuclear reactors continue to generate heat, after the core is shutdown, due to radioactive fission reaction products, which decay exponentially (see Figure 3-11). The ability to remove this decay heat is a key safety feature that nuclear reactors must demonstrate. The damage that was done to three of the units at the Fukushima Dai-Ichi Nuclear Power Plant in March of 2011, was due to the inability of the systems to remove the decay heat generated by the cores after shutdown[24,65]. The accident was initiated by a massive earthquake followed by Tsunami waves of unprecedented height, which disabled all off-site and on-site power sources (extended station black-out). Without power, the emergency core cooling systems could not operate, and overheating of the core caused fuel melting, hydrogen generation and over-pressurization of the reactor and containment vessels. The accident lead to severe land contamination, and required evacuation and relocation of the population in the affected areas. Furthermore, the unavailability of the reactors for energy production lead to significant power shortages. This highlights the value of passive safety systems for nuclear reactors, which do not require power or operator action, to perform their safety functions.

The Direct Reactor Auxiliary Cooling System (DRACS) is a natural circulation driven passive emergency decay heat removal system for fluoride salt cooled high temperature nuclear reactors (FHRs) and liquid metal nuclear reactors (LMRs). The main function of the DRACS is to provide a diverse and redundant means to remove decay heat, in the event that the normal shutdown cooling system does not function. The DRACS transfers heat to ambient air, which serves as the ultimate heat sink for decay heat.

The DRACS Heat Exchangers (DHXs) are located in the top part of the reactor vessel, with the primary coolant on the shell side, and DRACS coolant on the tube side. The DRACS coolant loop uses natural circulation to transfer heat from the DHX to an air-cooled heat exchanger, the Natural Draft Heat Exchanger (NDHX). The NDHX has the DRACS coolant on the tube-side, and ambient air on the shell side. The air flow in the NDHX is driven by natural circulation in a chimney structure located above the NDHX. Figure 1-3 shows a schematic diagram of the DRACS system in PB-FHR. The baseline primary coolant in FHR is flibe, and the DRACS coolant is potentially flibe, or another fluoride salt mixture. Fluoride salt mixtures are high-Prandtl number, Boussinesq fluids, with high volumetric heat capacity, and relatively high viscosity, very high boiling points, and relatively high freezing points (see

Table 3-7).

Normally, decay heat removal occurs using an active shutdown cooling system, that provides controlled heat removal to minimize thermal stresses in the reactor vessel. For emergency passive decay heat removal through the DRACS, natural circulation is established in the primary system, with flow upwards through the core and outlet plenum, then downwards through the DHX, fluidic diode, downcomer and inlet plenum. During normal operation of the reactor, the primary coolant flows in forced circulation upwards through the core, and a small amount of

coolant bypasses the core and flows upwards through the fluidic diode and DHX. The role of the fluidic diode is to provide high flow resistance for upwards flow during forced convection, and low flow resistance for downwards flow during natural circulation. Bypass flow during normal operation of the reactor leads to parasitic heat removal through the DRACS system, and to a lower core temperature at which heat is delivered to the power conversion system, through the IHX, thus lowering the efficiency of the system. Figure 3-3 shows a schematic diagram of the coolant flow paths and the bypass flows during forced circulation and natural circulation operational modes.

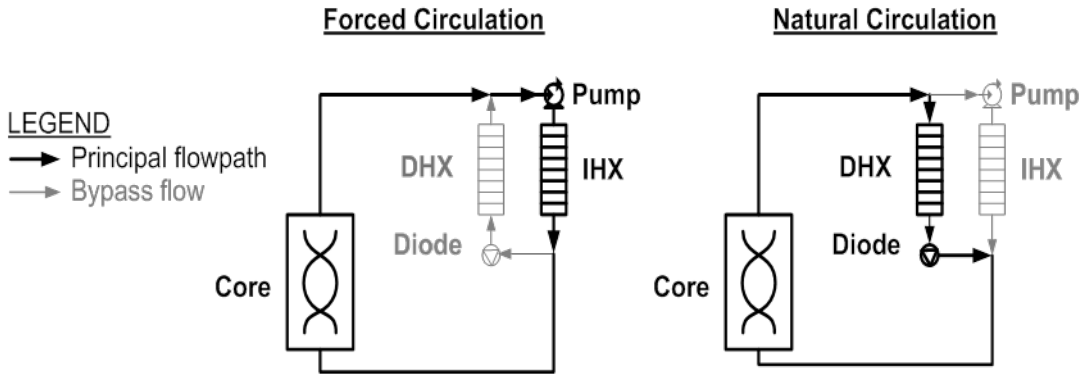

Figure 3-3. FHR primary coolant flow paths for forced convection and natural convection operational modes

The continuous parasitic heat removal from the core through the DRACS during normal operation demonstrates the availability of the DRACS system for heat removal. As Marques highlights in a reliability evaluation of passive safety systems for water-cooled reactors[66], passive safety systems need to be tested at prototypical conditions to demonstrate that they perform their function, unlike active systems which can be more easily isolated for inspection and testing.

To address the fact that parasitic heat loss through the DRACS system directly affects the efficiency of the reactor, a modification is made to this base design. The air intake stack can be outfitted with mechanical dampers at the inlet to the NDHX that can be closed in order to reduce the air flow through the NDHX, and hence reduce the parasitic heat loss during normal operation of the reactor and during normal shutdown cooling. In the event of an accident where normal shutdown cooling is not available, the reactor protection system automatically opens the louvers, and if the automatic system does not work, operators have on the order of an hour to remotely or manually open the dampers of the air stack, and allow the DRACS system to remove heat from the core at full capacity. During an extended station blackout, the dampers can be manually pulled open, with no need for electrical or compressed air power. The capability to control the NDHX air flow is a functional requirement of the DRACS system, and it is also subordinate to the FHR safety function to prevent overcooling and freezing. While an NDHX design that leads to reduced heat removal rate at low core outlet temperatures can be envisioned as a passive way to meet this functional requirement, the air dampers should also be considered as a diverse and redundant option. For severe accident management, during which the plant must respond to unforeseen scenarios, the option for operator action may be desirable, over a fully passive system[66]. Reactors are designed to facilitate operator actions if they might be

needed, particularly, to facilitate the ability to collect safety-related instrument readings to be able to diagnose and understand the condition of the plant.

FHRs are designed such that there is sufficient thermal mass in the primary system to accommodate the decay heat generation during the first hour after SCRAM, with the NDHX air dampers at the position of lowest opening. Galvez [67] calculated that the most significant thermal mass contributors in LOFC and LOHS transients are the primary coolant and the graphite reflectors. The power for which the decay heat removal system is sized is an optimization parameter, balancing peak coolant temperature during transients, and the size of the DRACS. As an example of this design optimization option, Figure 3-4 shows the elevation requirements for the primary coolant natural circulation loop, as a function of power for which the DRACS is designed, for two potential primary coolants for PB-FHR, flibe and frbzr (section 3.5.3 provides further details about this calculation). The current baseline design is a DRACS sized for removal of 2% of the core power[67].

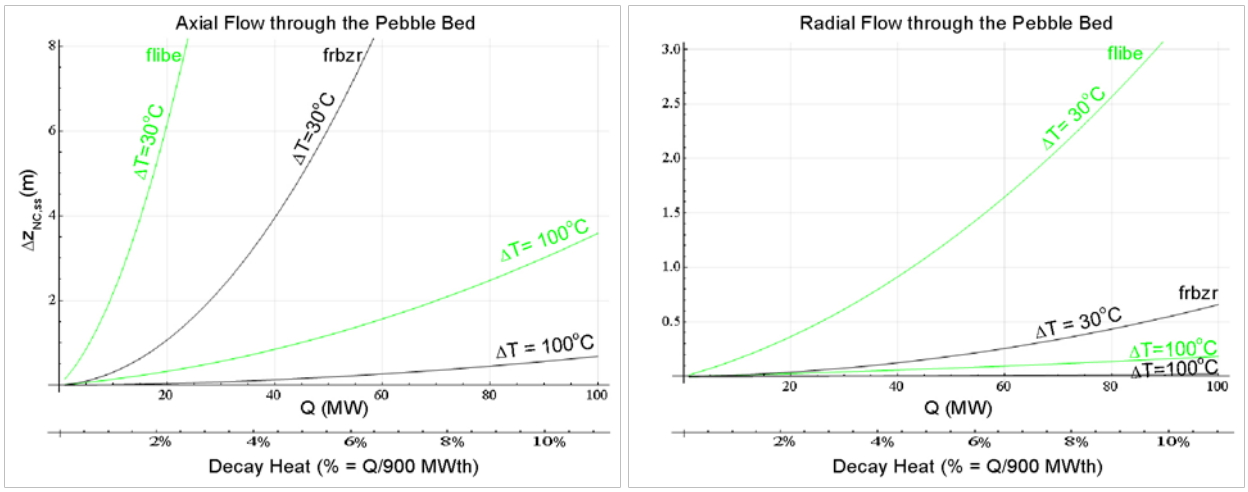

Figure 3-4. Natural circulation loop elevation requirements for the PB-FHR primary coolant circuit, as a function of power inpu and for two values of temperature rise across the core.

In summary, the DRACS system uses multiple coupled natural circulation loops to transfer heat from the FHR core to air (three loops in the baseline design). It can be designed to be a fully passive system that does not require valves, pumps, or any other kind of active components, moving mechanical parts, or operator action. In order to optimize its performance mechanical air dampers are needed on the NDHX air inlet stack; the dampers would be external to the containment and reactor building, and hence relatively easily accessible for manual operation, and they would be maneuverable with very little energy input, both of which are important features in the event of a station black-out, or other challenging states of the plant. Such a passive system would be fully operational during an extended station blackout, as was experienced at the Fukushima Dai-Ichi plant in Japan, in March 2011, as a consequence of a devastating earthquake and the consequent tsunami waves. The functional requirements of the DRACS, which were an outcome of the modified PIRT exercise describe in Chapter 1, are summarized in Table 3-1.

Table 3-1. Functional requirements for subsystems of the DRACS System

DRACS SYSTEM FUNCTIONAL REQUIREMENTS	
1	Provide a high reliability emergency heat sink
2	Capability to control heat removal rate
3	Minimize parasitic heat loss during normal operation
4	Meet operational requirements for start-up and shutdown
DRACS SALT TO SALT HEAT EXCHANGER (DHX) & DIODE	
1-1	Transfer decay heat from primary coolant to DRACS coolant, in natural circulation downwards primary coolant flow through the DHX
1-2	Transfer decay heat from primary coolant to DRACS coolant, in forced circulation upwards flow through the DHX (this scenario occurs when the primary pumps fail on, and the normal decay heat removal system is not available; in forced circulation mode sufficient flow through the DHX must be ensured)
1-3	Maintain low LMTD compared to NDHX LMTD, to prevent freezing of the DRACS system
DRACS PIPING & INSULATION/ELECTRICAL HEATING	
2-1	Protect against flow blockages under all conditions, including overcooling and design-basis external events
2-2	Transfer heat from primary loop to ultimate heat sink during an accident
2-3	Prevent overcooling and freezing, recover from localized freezing
NATURAL CONVECTION SALT TO AIR HEAT EXCHANGER (NDHX)	
3-1	Use ambient air as the ultimate heat sink for decay heat removal
3-2	Control air flow with rapid response time (tens of seconds) to prevent overcooling, using air dampers that fail open
3-3	Minimize heat loss under power operation and normal shutdown cooling conditions
3-4	Ensure that no operator action or mechanical part movement is needed in the first hour after SCRAM (depends on the thermal mass of the primary system in relation to the core power, and affects the design of the air dampers, hence bounding the position of lowest air flow)
3-5	Maintain sufficient minimum airflow to provide cooling for concrete structures around NDHX chimney
3-6	Interface with the environment: prevent ingress of foreign objects and excessive deposition of dust
3-7	Interface with the environment: NDHX outlet air stream must entrain and mix with ambient air to temper the temperature of the air discharged from the stack
3-8	Security: prevent intentional ingress of objects
3-9	External event shield must protect the NDHX chimney from external missiles, and ensure that the geometry of the DRACS system is maintained

3.4 Governing equations for single phase natural circulation loops

Natural circulation loops rely on buoyancy to drive fluid flow in a closed loop, and the mass flow rate at steady state balances the buoyancy driving force with the total loop friction losses. When the loop integral of temperature versus elevation is negative, buoyancy forces will drive flow through the loop (assuming that the fluid density drops linearly with temperature). In other words, if there is a heat source located at lower elevation than the heat sink, lower density hot fluid will push fluid movement upwards, and high density cold fluid will push fluid

movement downwards. Natural convection operates on the same principles, but flow-paths establish freely in a large open cavity, and system models must be 2-D or 3-D. For natural circulation, a closed fluid circuit is needed, such as a pipe network, and a 1-D model is appropriate.

The coupled momentum and internal energy conservation equations for the flow loop must be solved, to characterize the behavior of natural circulation loops. This section presents the governing equations, in dimensional and nondimensional form, for natural circulation loops with single phase incompressible fluids, and vertical heat sink and heat source segments. Special treatment is given to natural circulation loops for which the heat generating segment is a pebble bed, with internal heat generation in the pebbles. Nondimensionalized equations are necessary for design of scaled experiments with non-prototypical fluids, for scale-up and scale-down of the prototypical system, and for simplified design scoping analyses.

3.4.1 Nomenclature and assumptions

The following analysis is for Boussinesq fluids, whose thermophysical properties are constant with temperature and pressure, with the exception of density in the buoyancy term of the momentum conservation equation. For the buoyancy term, density is assumed to vary linearly with temperature, which means that the thermal expansion coefficient is constant with temperature. The viscosity, μ, specific heat capacity, c_p, density, ρ_o, thermal conductivity, k, and the coefficient of thermal expansion, β, are evaluated at the average temperature T_o.

The natural circulation loop is modeled as a one-dimensional loop, where s is the position around the loop, t time, and $T(s,t)$ the bulk temperature of the fluid around the loop, as a function of time. It is generally convenient to segment the loop in discrete lengths, and consider only the integral behavior of each segment. The subscript n, indicates that the variable applies specifically for segment n. The PB subscript refers to the pebble bed.

The characteristic parameters of the loop, which are used for nondimensionalizing the conservation equations, are indicated with the subscript r. The nondimensionalized parameters have a * superscript.

The integral behavior of each segment is defined such that along the length of each segment the behavior in terms of the friction loss correlations, vertical or horizontal orientation, momentum inertia, advection, and energy boundary condition are treated as constants.

The flow cross-sectional area, A_n, is used for calculating the flow velocity in each segment, which determines the Reynolds number, the importance of the momentum inertia term in the momentum conservation equation, and the importance of the advection term in the energy conservation equation. Discretizing the loop such that each segment can be treated as a uniform cross-sectional area simplifies the treatment of the conservation equations on each segment; in this thesis, uniform cross-sectional area segments is adopted as a convention. For the pebble bed the flow cross-sectional area is taken for the filled bed.

The characteristic diameter, d_n, is used in the Reynolds number, the Nusselt number, and in expressing the friction coefficient. For most segments the characteristic diameter is the hydraulic diameter, d_h. The hydraulic diameter is defined in equation (3-1), where P is the wetted perimeter. For the pebble bed the characteristic diameter is the pebble diameter.

$$d_h = \frac{4A}{P} \tag{3-1}$$

The flow length, L_n, is used in expressing the friction coefficient, and in the advection term of the energy conservation equation. For segments with heat exchange between the fluid and the wetted solid, S_n is the heat exchange area between the fluid and the solid. The internal fluid volume, V_n, is used to calculate the residence time in each segment, and the total heat input for segments with internal heat generation.

For segments of non-uniform cross-sectional area, u_n is the average flow velocity of segment n, such that the following approximations are valid for the inertia and the friction terms of the momentum equation, where f is the friction coefficient, and L_n the length of the segment.

$$L_n \frac{\partial u_n}{\partial t} = \int_n \frac{\partial u}{\partial t} ds \tag{3-2}$$

$$u_n{}^2 f_n(u_n) L_n = \int_n \left[u^2(s) f\big(u(s)\big)\right] ds \tag{3-3}$$

Using equations (3-2) and (3-3) will lead to segment length, L_n, and cross sectional area, A_n, which cannot be used for calculating the fluid volume of the segment, V_n.

$$V_n \neq L_n A_n \tag{3-4}$$

For the special case where the friction coefficient is inversely proportional to Reynolds number, such as laminar flow or Darcy flow through a pebble bed, equation (3-3) simplifies to be identical to (3-2), and there is an additional degree of freedom in the definition of these parameters. In this case, either equation (3-5) can be applied, or an ad-hoc value for L_n can be selected.

$$V_n = L_n A_n \tag{3-5}$$

In the energy equation A_n appears in the advection term. It also indirectly appears in the convective heat transfer coefficient, because it is dependent on Reynolds number, which in turn depends on the flow cross-sectional area.

3.4.2 Selecting the characteristic parameters

These characteristic values typically depend on the initial conditions, and they will depend on the specific transient of interest.

$$m^* = \frac{m}{m_r}; T^* = \frac{T - T_o}{\Delta T_r};\ t^* = \frac{t}{t_r}; s^* = \frac{s}{L_r};\ \Delta P_n^* = \frac{\Delta P_n}{\Delta P_r} \tag{3-6}$$

The characteristic time interval, t_r, is defined here as the transit time of the fluid around the loop. Because fluoride salts have high volumetric heat capacity, the flow velocity is relatively low, and the fluid transit times are relatively long (see Table 3-15), compared to systems cooled by water, gas, or liquid metals.

$$t_r = \frac{\rho_o V_r}{m_r} \tag{3-7}$$

$$\Delta P_r = \frac{m_r^2}{2 A_r^2 \rho_o} \tag{3-8}$$

3.4.3 Mass conservation equation

For non-uniform flow cross-sectional area loops, it is most convenient to express the conservation equations in terms of mass flow rate, m, which is conserved around the loop, rather

than velocity. In the literature[68], the conservation equations are also often times written in terms of a reference velocity, u_r, which is the velocity in an arbitrarily chosen segment, of cross-sectional area A_r. The two approaches are algebraically equivalent. In this thesis, the first convention is chosen, and all the conservation equations are expressed in terms of the mass flow rate, m.

$$m = \rho_o u_n A_n \tag{3-9}$$

3.4.4 Momentum conservation equation

The momentum equation for one-dimensional flow is given as

$$\rho_o \frac{Du}{Dt} = \frac{\partial p}{\partial s} - \rho g \hat{e_z} \cdot \hat{e_s} - \frac{\rho_o u^2}{2} \frac{f}{d_h} \tag{3-10}$$

Because the fluid is incompressible, and the cross-sectional area of each segment is constant, the velocity gradient along the flow direction is assumed to be zero.

$$\frac{Du}{Dt} = \frac{\partial u}{\partial t} + u \frac{\partial u}{\partial s} \overset{\frac{\partial u}{\partial s}=0}{\Longrightarrow} \frac{Du}{Dt} = \frac{\partial u}{\partial t} \tag{3-11}$$

Re-writing the momentum equation in terms of mass flow rate, integrating the momentum equation over each segment n, and diving through by ρ_o, we obtain:

$$\overset{\frac{1}{\rho_o}\int_n [\ ]ds}{\overset{u_n=\frac{m}{A_n\rho_o}}{\Longrightarrow}} \frac{L_n}{A_n\rho_o}\frac{\partial m}{\partial t} = \frac{\Delta P_n}{\rho_o} - g\int_n \frac{\rho}{\rho_o}dz - \frac{m^2}{2A_n^2\rho_o^2}\left(\frac{1}{d_{h,n}}\int_n f ds\right) \tag{3-12}$$

The four terms of this equation represent fluid inertia (IT_n), driving head (HT_n), buoyancy (BT_n), and friction losses (FT_n).

$$IT_n = HT_n + BT_n - FT_n \tag{3-13}$$

3.4.4.1 Inertia term

The inertial term, IT_n, determines the time scale of accelerating and decelerating mass flow rate in response to changes in driving head. The inertial term expressed in terms of mass flow rate must use the correct cross-sectional area for each segment. Components with larger cross-sectional areas, or slower velocities, have less momentum inertia and lead to faster transients.

$$IT_n = \frac{L_n}{A_n\rho_o}\frac{\partial m}{\partial t} \tag{3-14}$$

For components with complex internal geometry, such as packed beds or the baffled shell-side of heat exchangers, it can be challenging to define a flow cross-sectional area that appropriately characterizes the integral behavior of the component across the operating conditions of the transient of interest. Sub-component-scale modeling and separate effects tests may be required to quantify the distortion associated with the 1-D integral treatment of the segment, and to demonstrate that the one-dimensional model is appropriate for the transient of interest.

For a pebble packed bed, the pore velocity should be used in the integral momentum conservation equation, so the filled bed flow cross-sectional area should be used, A_{PB}, rather than that of the empty bed. In Chapter 4, which discusses modeling of flow distribution within a

pebble bed and treats the bed as a homogenized medium, the superficial velocity is used instead. In the literature, the packed bed Reynolds number is often defined in terms of the superficial velocity (empty bed cross-sectional area)[44,69] because with this notation it is convenient to generalize among various porous media.

3.4.4.2 Friction term

Some simplifications can be made to the friction loss term for each segment, FT_n. The integration of the friction coefficient, and grouping together all the terms with subscript n, leads to a coefficient, F'_n, which fully characterizes the integral friction loss behavior of each segment. The coefficient C_n groups together the geometry parameters of segment n, with respect to which the friction term is proportionally dependent.

$$FT_n = \frac{m^2}{2\rho_o^2} F'_n = \frac{\Delta P_n}{\rho_o} \tag{3-15}$$

$$F'_n = \frac{1}{A_n^2}\frac{1}{d_{h,n}} \int_n f(s)ds = C_n f_n \tag{3-16}$$

$$C_n \equiv \left(\frac{1}{A_n^2}\frac{L_n}{d_n}\right) \tag{3-17}$$

where ΔP_n is the friction pressure drop, and f_n the average friction coefficient.

$$F' \equiv \sum_n F'_n \tag{3-18}$$

The friction coefficient is a semi-empirical correlation as a function of the Reynolds number, which is defined by equation (3-48). Equation (3-62) defines the correlation for friction losses through a pebble bed. Table 3-4 and Table 3-5 define the correlations for friction losses through a smooth-wall pipe for all flow regimes.

3.4.4.3 Buoyancy Term

Some simplifications can be made to the buoyancy term for each segment, BT_n, assuming that the fluid density varies linearly with temperature, and that the temperature profile is linear with respect to elevation for each of the segments

$$\beta = -\frac{1}{\rho}\frac{d\rho}{dT} \xrightarrow{(\rho\cdot\beta)=const} \frac{\rho}{\rho_o} = 1 - \beta(T - T_o) \tag{3-19}$$

$$BT_n = -g \int_n \frac{\rho}{\rho_o} dz \xrightarrow{\beta=const} BT_n = -g\Delta z_n + g\beta \int_n (T - T_o)\, dz \tag{3-20}$$

$$\sum_n BT_n = g\beta \oint T dz \tag{3-21}$$

$$\xrightarrow{T(z)=linear} BT_n = -g\Delta z_n + g\beta\Delta z_n \left(T_{av,n} - T_o\right) \tag{3-22}$$

For a simple loop, with a single heat input segment a single heat sink segment, both with linear temperature axial profiles, and with no heat loss in the piping segments, we can express the buoyancy term in terms of Δz_{ch}, which is the between the center of the heat sink segment, z_c, and the center of the heat input segment, z_h, and ΔT_h, the temperature rise across the heater.

$$\oint T dz = \Delta T_h \Delta z_{ch} \tag{3-23}$$

From equation (3-23), (3-21) we see that changing the elevation of the loop has the same effect on the buoyancy term as changing the power input to the loop.

For non-ideal simple loops it is convenient to define an effective elevation for the loop, thus maintaining the same equation form for (3-23). The effective elevation change of the loop, Δz_{NC}, is defined here as the ratio of the temperature integrated around the loop as a function of height, to the difference between the hottest and the coldest fluid temperatures on the loop.

$$\Delta z_{NC} = \frac{\oint T dz}{\Delta T_h} \tag{3-24}$$

where ΔT_h is the sum of fluid temperature rise across the heat input segments. For the case where there is only one segment with heat input, i.e. the core for a nuclear reactor system, ΔT_h is the temperature rise across the heat input segment. At steady state, ΔT_h can be expressed in terms of the power input to the loop, Q_h, and steady state mass flow rate, m_{ss}.

$$Q_h = m_{ss} c_p \Delta T_h \tag{3-25}$$

$$\sum_n BT_n = \frac{g\beta}{mc_{p,h}} Q_h \Delta z_{NC} \tag{3-26}$$

The ratio of Δz_{NC} to Δz_{ch}, provides a comparison of the loop of interest with an ideal simple natural circulation loop. A sensitivity analysis for this nondimensional parameter will quantify the effect of model parameters on the buoyancy driving term.

$$\Pi_{\boldsymbol{z}} = \frac{\boldsymbol{\Delta z_{NC}}}{\Delta z_{ch}} = \frac{\oint T dz}{\Delta z_{ch} \Delta T_h} = \frac{\sum_{\boldsymbol{n}}^{\boldsymbol{loop}} [\boldsymbol{T_{av,n} \cdot \Delta z_n}]}{\Delta z_{ch} \Delta T_h} \tag{3-27}$$

On a plot of temperature versus elevation (see Figure 3-5), the loop integration graphically represents the area enclosed by the loop. In the idealized case, the fluid describes a parallelogram, whose area is dependent only on the centerline distance between the heated and cooled sections, and independent of the effective lengths of the heater and cooler. For actual systems, such as reactor natural circulation loops, or scaled experimental natural circulation loops, the shape of the plot will deform from a parallelogram due to heat losses, as well as due to convective heat transfer boundary conditions that lead to temperature profiles that are non-linear with height (see Figure 3-5).

The net temperature change between the inlet and the outlet of each segment is proportional to the heat input for the segment and inversely proportional to the mass flow, so graphically the relative heat inputs for each segment are easy to identify on the same temperature versus height graph (see Figure 3-5).

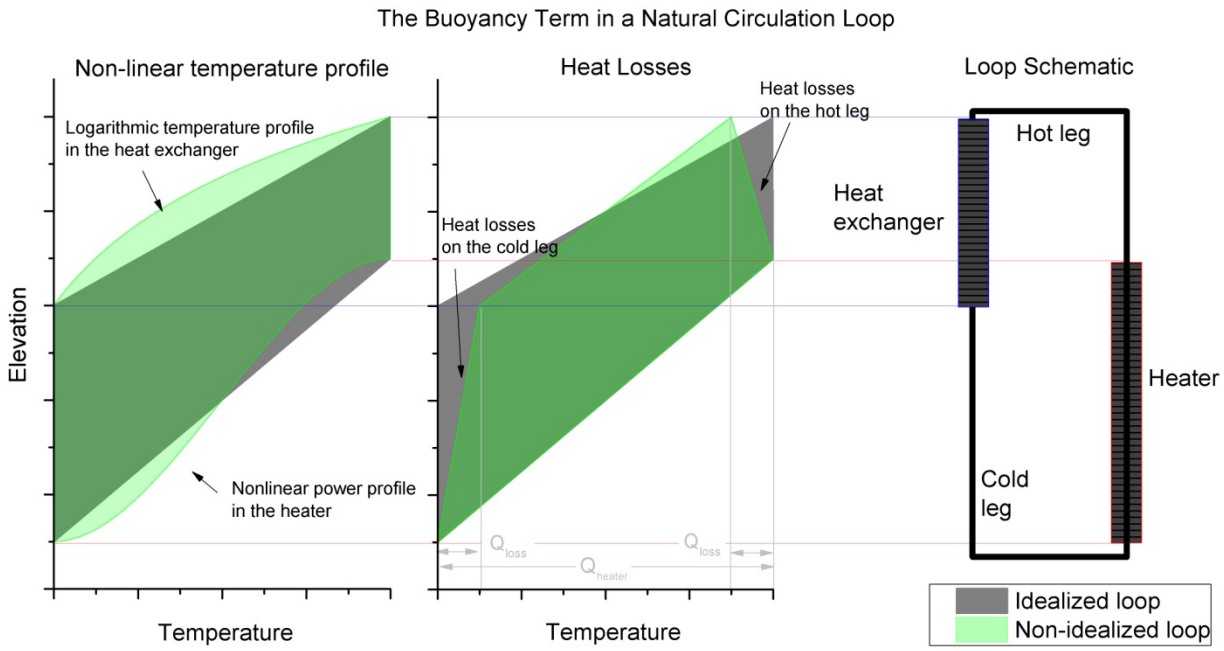

Figure 3-5. Schematic diagram of the buoyancy term in a natural circulation loop (OriginPro drawings generated in collaboration with Rohit Upadhya)

For the design of scaled IETs for natural circulation loops, it is sufficient to scale the value of the area enclosed by the flow loop on a temperature versus elevation plot, without matching its specific shape described by the coolant in the prototype loop. The evolution of this area over the course of the transient of interest must also be replicated by the IET. An evaluation of the sensitivity of its value to the parameters that vary during the transient will indicate whether it can be assumed to be a constant. For example, for the experimental data given in section 3.7, this area was up to 16% higher than the theoretical area for an ideal simple natural circulation loop, due to non-isothermal conditions in the hot leg and cold leg piping. Whenever possible, IETs should replicate the scaled geometry and the boundary conditions of the prototypical components. For example the geometry of a shell-and-tube heat exchanger can be replicated by building a model, of the appropriately reduced scale, and with a reduced number of tubes. Extreme peaking factors for the heat generation in the core can be replicated using an electrical heating element with variable axial electrical resistance. Isothermal hot leg and cold leg conditions can be reached by taking measures to limit heat losses in the experimental set-up; this can be achieved using electrical tracing of the piping, or heating the ambient temperature to the average temperature of the fluid in the IET. However, when temperature profiles cannot be identically matched, it is still possible to design a scaled IET that replicates the response of the prototypical system; it is sufficient to match the total area on the temperature versus elevation plot, and its evolution with the transient of interest.

3.4.4.4 Summary of the momentum equation for a loop

The momentum equation for each segment becomes:

$$\frac{L_n}{A_n \rho_o}\frac{\partial m}{\partial t} = \left(\frac{\Delta P_n}{\rho_o} - g\Delta z_n\right) + g\beta \int_n (T - T_o)dz - \frac{m^2}{2\rho_o^2}F_n' \tag{3-28}$$

Summing these equations around a closed loop:

$$\overset{\sum_n^{loop}}{\Longrightarrow} \frac{\partial m}{\rho_o \partial t}\sum_n \frac{L_n}{A_n} = g\beta \oint T dz - \frac{m^2}{2\rho_o^2}\sum_n F_n' \tag{3-29}$$

We then solve for the steady state natural circulation mass flow rate, m_{NC}.

$$m_{NC}^2 = 2\rho_o^2 g\beta \frac{\Delta z_{NC}\Delta T_h}{F'(Re(m,T(s)))} \tag{3-30}$$

If the system is at steady state, then the natural circulation mass flow rate can be expressed as a function of power input and temperature rise.

$$\overset{Q_h = m_{ss} c_p \Delta T_h}{\Longrightarrow} m_{NC,ss}^3 = \frac{2\rho_o^2 g\beta}{c_{p,h}} \frac{\Delta z_{NC}(T(z))Q_h}{F'(Re(m,T(s)))} \tag{3-31}$$

The residence time in the baseline core is 24 seconds at full forced circulation flow rate, and 410 seconds at 6% of forced circulation flow rate (see Table 3-15). This means that at the beginning of transients, there can be a significant time lag between the change in core power and the change in core temperature rise, and the power input should not be used in the momentum equation to replace the characteristic core temperature rise. In such cases equation (3-30) should be used. In cases where the transients of interest have much longer time scales than the residence time in the core, this substitution can be made, and equation (3-31) can be used.

3.4.5 Non-dimensional momentum equation

To nondimensionalize the momentum conservation equation for the loop, characteristic values must be selected for the mass flow rate, temperature difference, and time. Selection of the values for the characteristic parameters is discussed in section 3.4.2.

For completeness, the nondimensional equation for each segment is given here, but it is not needed for the scaling analysis discussed in this chapter.

$$\frac{L_n m_r^2}{A_n \rho_o^2 V_r}\frac{\partial m^*}{\partial t^*} = \frac{m_r^2}{2A_r^2\rho_o^2}\Delta P_n^* - \frac{g}{\rho_o}\int_n \rho\, dz - \frac{m_r^2}{2\rho_o^2}\left(\frac{1}{A_n^2}\frac{L_n}{d_{h,n}}f_n\right)m^{*2} \tag{3-32}$$

The nondimensional equation for a natural circulation loop is given.

$$\left(\frac{\sum_n \frac{L_n}{A_n}}{V_r/2}\right)\frac{\partial m^*}{\partial t^*} = \left(\frac{\rho_o^2 g\beta \Delta T_r \Delta z_{NC}}{m_r^2}\right) - \left(\sum_n F_n'\right)m^{*2} \tag{3-33}$$

$$\overset{1/FT}{\Longrightarrow} \frac{1}{\Pi_2}\frac{\partial m^*}{\partial t^*} = \Pi_6 - m^{*2} \tag{3-34}$$

$$\overset{\Pi_2 > 100}{\Longrightarrow} \Pi_6 = m^{*2} \tag{3-35}$$

$$\Pi_2 = \frac{V_r \sum_n F_n'}{2 \sum_n \frac{L_n}{A_n}};\ \Pi_6 = \frac{\rho_o^2 g \beta \Delta T_r \Delta z_{NC}(T^*(z^*))}{m_r^2 \sum_n F_n'(m^*, T^*(s^*))} \tag{3-36}$$

When Π_2 is large, which is normally the case for natural-circulation systems, the momentum inertia is negligible, and the friction losses match the buoyancy driving term for any system. For a pebble bed core with a flow distribution that is optimized for low pressure drop in the core, the values of Π_2 and representative time scales are given in Table 3-15 for each of the LOFC transient phases. To a first order approximation the inertia term is negligible. Higher core pressure drop flow configurations would lead to shorter inertia time scales, and an even less significant inertia term. A negligible inertial term means that the natural circulation flow rate responds instantaneously to the changes in temperature distribution around the natural circulation loop, and the transient time constant will be dominated by fluid residence time in the loop and the time constant of the thermal transients or disturbances driving the momentum transient. One must verify that the inertia term is also negligible with respect to all the other shorter time scale phenomena that participate in the transient.

When m_r is defined as the steady state natural circulation mass flow rate that corresponds to ΔT_r, Δz_{NC}, and F', Π_6 is by definition 1.0. Hence, to design a scaled model that replicates the transient response, it suffices to match the functional dependence of Π_6 with respect to m^*, $T(s)$, and $T(z)$. Another way to look at this requirement, since m^* equals $\Pi_6^{0.5}$, is that *the dependence between natural circulation mass flow rate and power input must be preserved.*

For example, based on equation (3-31), with the laminar friction coefficient through the piping, mass flow rate depends on power input and loop height to the power of 0.5; with transition regime flow the friction coefficient takes a power law dependence closer to 0.3 (see Table 3-4 and Table 3-5). Hence, the functional form dependence of the friction term F' on mass flow rate must be matched, in order for the relationship between mass flow rate and power input to be matched between the model and the prototype.

$$\frac{F_{n,m}'(m^*, T^*(s^*))}{F_m'} = \frac{F_{n,p}'(m^*, T^*(s^*))}{F_p'} \tag{3-37}$$

Because F' is a sum of friction factors, each with different functional forms for the Reynolds dependence, it is practical to match the friction factor in each respective (equation (3-37)). This will ensure that the functional form of the summation is matched between the prototype and the model loops. For segments that contribute minimally to the friction term over the entire range of operating conditions, the functional dependence does not need to be matched, only the order of magnitude relative contribution to the overall friction coefficient.

Careful attention must be paid to the point of transition from one flow regime to another, which leads to a change in the Reynolds dependence of the friction coefficient. *The model components should be designed such that the transition occurs at the same nondimensional mass flow rate and nondimensional temperature as for the prototypical system.* This condition is, of course, not necessary if for the transient of interest the flow remains in a single flow regime for each of the components.

In general, the low volumetric flow rates and Reynolds numbers that occur commonly with fluoride salts, particularly in natural circulation, due to their high heat capacity, creates strong incentives to design heat transfer surfaces to include enhancement. This may involve use of pebble fuels in FHR reactor cores, and twisted tubes in heat exchangers. Enhanced surfaces tend to increase the contribution of form-losses to pressure drop. Sections 3.6.2 and 0 discuss the implications of significant form-losses in the natural circulation loop, with regards to design

of scaled experimental models, and to performance evaluation of natural circulation decay heat removal systems.

For model components that replicate the geometry of the prototype components, it suffices to match the Reynolds number. Models that do not replicate the geometry of the prototype must be analyzed case by case; section 3.6.2 treats the scaling of a cylindrical heater used to simulate the behavior of a pebble bed core.

The other term of Π_6 that is dependent on power input is Δz_{NC}. Another way to think about it is in terms of Π_z, which quantifies the distortion from an ideal natural circulation loop: non-linear temperature distribution in the heat generation and heat sink segments, and non-adiabatic hot leg and cold leg. The evolution of Π_z in response to change in power input to the loop, or other system disturbances characteristic to the specific transient of interest must be matched between the prototype and the model.

3.4.6 Fluid internal energy conservation equation

The energy equation for one-dimensional flow, considering both internal heat generation and heat exchange is given here. For the core segment, the heat exchange term is often times insignificant; for the heat exchanger segment, the internal heat generation term is zero.

$$\frac{\partial T}{\partial t} + u(s)\frac{\partial T}{\partial s} - \frac{k}{\rho_o c_p}\frac{\partial^2 T}{\partial s^2} = \frac{1}{\rho_o c_p}\left[q''' - h\frac{S}{V}(T - T_{sink})\right] \tag{3-38}$$

where $\mathcal{Q}_n$ is the total heat generation in segment n, q''' the volumetric internal heat generation, h the convective heat transfer coefficient, and T_{sink} the temperature at the heat exchange surface.

Re-writing the equation for each segment in terms of mass flow rate, and assuming axially uniform internal heat generation on each segment:

$$\frac{\partial T}{\partial t} + \frac{m}{\rho_0 A_n}\frac{\partial T}{\partial s} - \frac{k}{\rho_o c_p}\frac{\partial^2 T}{\partial s^2} = \frac{1}{\rho_o c_p}\left[\frac{Q_n}{V_n} - \frac{hS_n}{V_n}(T - T_{sink})\right] \tag{3-39}$$

3.4.7 Non-dimensional fluid internal energy equation

To nondimensionalize the energy conservation equation, characteristic values must be selected for the mass flow rate, temperature difference, time, and length along the natural circulation loop. Selection of the values for the characteristic parameters is discussed in section 3.4.2. The nondimensional energy conservation equation is given.

$$\Rightarrow \frac{\partial T^*}{\partial t^*} + \frac{V_r/l_r}{A_n}\frac{m^*\partial T^*}{\partial s^*} - \frac{k/l_r^2}{m_r c_p/V_r}\frac{\partial^2 T^*}{\partial s^{*2}} = \frac{Q_n/V_n}{m_r c_p \Delta T_r/V_r} - \frac{hS_n(T^* - T^*_{sink})/V_n}{m_r c_p/V_r} \tag{3-40}$$

The characteristic temperature rise of the fluid in the loop is ΔT_r. The temperature difference between the heat exchange surface and the fluid in the loop, $\Delta T_{sink,r}$, is another characteristic parameter of the loop, and it is independent of ΔT_r. Thus, it is appropriate to define an additional nondimensionalized temperature variable, $\Delta\theta^*$, which is the temperature rise that drives convection normalized with respect to $\Delta T_{sink,r}$.

$$\Delta T^*_{sink,r} = \frac{T_{sink,r} - T_o}{T_r - T_o} = \frac{\Delta T_{sink,r}}{\Delta T_r} \Rightarrow \Delta\theta^* = \frac{T^* - T^*_{sink}}{\Delta T^*_{sink,r}} = \frac{T - T_{sink}}{\Delta T_{sink,r}} \tag{3-41}$$

The Peclet number, Pe, and Stanton number, St, are defined below, and they are introduced in the energy equation. Peclet is the ratio of energy transport by advection to transport by

diffusion. For the fluids of interest, the Peclet number is very large, and the conduction term is negligible. Stanton number is the ratio of convective heat transport to advective heat transport.

$$Pe = Re \cdot Pr = \frac{mc_p}{k} \cdot \frac{d_n}{A_n};\ St = \frac{Nu}{RePr} = \frac{hA_n}{mc_p} \tag{3-42}$$

$$Pr = \frac{\mu/\rho}{k/\rho c_p} \tag{3-43}$$

The fully simplified nondimensional energy equation for each segment n of the natural circulation loop is given. The equation is divided through by the coefficient of the thermal inertia term, and four nondimensional coefficients arise. The geometrical parameters in each of these coefficients are grouped together in parameters labeled Γ_i.`

$$\frac{\partial T^*}{\partial t^*} + \Gamma_1 \cdot \frac{m^* \partial T^*}{\partial s^*} - \frac{\Gamma_2}{Pe} \cdot \frac{\partial^2 T^*}{\partial s^{*2}} = \Pi_{E3} - St\Pi_{E4}\Delta\theta^* \tag{3-44}$$

$$\Gamma_1 = \frac{V_r}{l_r A_n};\ \Pi_{E3} = \Gamma_3 \Pi_Q;\ \Pi_{E4} = \Gamma_4 \frac{\Delta T_{sink,r}}{\Delta T_r} \tag{3-45}$$

$$\Gamma_2 = \frac{d_n V_r}{A_n l_r^2};\ \Gamma_3 = \frac{V_r}{V_n};\ \Gamma_4 = \frac{S_n V_r}{A_n V_n};\ \Pi_Q = \frac{Q_n}{c_p \Delta T_r m_r} \tag{3-46}$$

The conduction term is generally negligible. This statement must be verified for the pebble bed, where dispersion and conduction through the solid phase adds to the thermal diffusion term, increasing the effective thermal conductivity of the segment.

$$\frac{\Gamma_2}{Pe} < 0.01 \tag{3-47}$$

In order to design a scaled experiment, three parameters must be matched: Γ_1, Π_{E3}, and $St\Pi_{E4}$, where $\Gamma_{1,n}$ is the advection term. $\Gamma_{1,n}$ is matched for each segment if the relative flow cross-sectional areas are matched between the prototype and the model. $\Pi_{E3,n}$ is the heat generation term; when the volume of heat generation segment is used as the representative volume, and at the initial conditions the system is at steady state the value of $\Pi_{E3,n}$ is unity; $St\Pi_{E4}$ is the convective heat transfer term; in order to match the functional dependence of this term on mass flow rate and temperature, the Re_n, Pr_n, and Nu_n will be matched, hence Π_{E4} must also be matched; specific surface area, flow cross-sectional area, and temperature difference between the fluid and the heat sink are the model parameters that can be tuned in order to match Π_{E4}.

3.4.8 Reynolds number definition in a multi-dimensional pebble bed

The Reynolds number defined in terms of the mass flow rate:

$$Re = \frac{m}{\mu} \cdot \frac{d}{A} \tag{3-48}$$

The fluid velocity is written in terms of the variable flow cross-sectional area.

$$u(s) = \frac{1}{A(s)} \frac{m}{\rho_o} \tag{3-49}$$

Using equations (3-2) and (3-3), in conjunction with the Ergun friction coefficient correlation given by (3-62), a system of two equations is obtained, and L_n and A_n can be solved for analytically for the simple case of radial flow through the annular pebble bed. These values are independent of fluid density, bed height, and pebble diameter. The values are also insensitive to

the mass flow rate in the bed, to the coefficients f_1 and f_p for the Ergun pressure drop correlation, and to the fluid viscosity, within a variation of seven orders of magnitude on each of these parameters. The exact analytical solution is given in Appendix E. The numerical values for A_n and L_n for the PB-FHR core geometry are given in Table 3-2.

Using incorrectly averaged values for A_n and L_n leads to a segment pressure drop that is off by a factor of 0.8 at high flow rates, and 0.9 at lower flow rates (see Table 3-2 for a comparison with using the cross-sectional at the centerline of the annular bed). All calculation details are listed in Table 3-2, where F is defined by equations (3-15) and (3-16), and the geometry of the PB-FHR core was defined in Chapter 2.

Table 3-2. Effective flow cross sectional area and length for radial flow and axial flow through the annular central core region of PB-FHR.

			Radial flow				Axial flow
			Effective	Centerline	OD	ID	
	L_n	m	1.39	1.50	1.50	1.50	3.00
	A_n	m^2	10.6	31.1	45.2	6.79	6.22
	L_nA_n/V_n	m^3	0.79	1.00	1.45	0.45	1.00
	C_n	m^{-2}	0.41	0.32	0.15	1.09	2.58
LOFC Phase I	m	kg/s	3727	(100%)	t_{core}	s	9.8
	Re		1556	1331	915	2440	2661
	f		5.7	5.8	6.0	5.5	5.5
	F	m^{-4}	2.32	1.86	0.91	6.00	14
	$F_n/F_{n,effective}$		1.00	0.80	0.29	2.59	
LOFC Phase II	m	kg/s	224	(6%)	t_{core}	s	163.8
	Re		93	80	55	146	160
	f		12	14	18	10	9.5
	F	m^{-4}	5.09	4.43	2.68	10.7	24
	$F_n/F_{n,effective}$		1.00	0.87	0.53	2.10	
	d_n	m	0.030				
	V_n	m^3	18.7				
	μ (650°C)	Pa-s	0.006754		f_1	675	
	ρ_0 (650°C)	kg/m^3	1963		f_2	5.25	

When flow through the annular core has both a radial and an axial component, A_n and L_n must be computed numerically, and their sensitivity to boundary conditions and input parameters must be calculated. If significant flow redistribution occurs in the core, and A_n changes over the course of the transient of interest, then this must be accounted for in the integral model of the system. A_n can be treated as a parameter that varies with time, or that varies with another system parameter, such as core pressure drop, flow rate, or power input. PB-FHR core pressure drop for a broad range of coolant flow rates was numerically calculated in Chapter 2.

If the Reynolds number is uniform over the length of segment n, then f_n is a constant. Since segments have been defined above to have uniform cross-sectional area, f_n is a constant on isothermal segments. For non-isothermal segments, the temperature-dependent viscosity can lead to substantial variation of Reynolds along the segment, which must be accounted for. The viscosity dependence with temperature is a power function of temperature, but for temperature rises across a segment in the range of 100ºC, it can be approximated as linear; in this case using a constant friction coefficient, f_n, evaluated at the average temperature of the segment, $T_{av,n}$, introduces distortions in the friction losses of less than 2%. It is important that the average segment temperature as a function of time is used to evaluate the segment friction losses, not the loop reference temperature or the loop average temperature. This is a deviation from the Boussinesq approximation, which assumes constant fluid viscosity. The effects of temperature-dependent fluid viscosity on the pressure drop through a pebble bed are presented in Chapter 2.

$$f_n(u_n(t)) \equiv f_n(T_{av,n}(t), u_n(t)) \tag{3-50}$$

3.4.9 Higher complexity loops and networks

For single phase natural circulation loops with vertical heated and cooled sections, instabilities can arise when there are multiple parallel heated or cooled branches. Vijayan[70] provides a good review of instability analysis for single phase natural circulation systems. In order to study the stability of the FHR decay heat removal system, the assumption of a simple natural circulation loop is no longer appropriate. The system is rendered further nonlinear by the possibility for overcooling leading to freezing, and by the coolant viscosity being strongly dependent on temperature. This makes the study of the stability of the system with parallel branches even more pertinent. This thesis only treats simple natural circulation loops, but a brief discussion of how this analysis would be extended to flow networks is given here.

The mass generation term is zero everywhere in the system, and mass flow rate is constant around a simple loop without branching nodes. At branching nodes, in order for mass to be conserved, the sum of all inflows and outflows at each node must equal to zero. The convention adopted in this thesis, of writing the momentum and energy conservation equations in terms of the mass flow rate instead of flow velocity, facilitates the extension of this analysis to flow networks.

A single set of characteristic values is selected, just like for the simple loop case. Nothing changes for the treatment of the energy equation, (3-44), since each segment is treated individually. The appropriate mass flow rate must be used in the equation for each segment. The momentum equation needs to be integrated around each closed loop, and equation (3-29) must be applied for each of the loops.

3.5 Steady state natural circulation: design considerations for natural circulation heat removal systems

For the design of heat removal systems that rely on natural circulation, there is a trade-off among loop elevation, friction losses, and temperature difference between the hot leg and the cold leg. The values for these three parameters are decided by design optimization. The relationship among these terms depends on the thermophysical properties of the heat transfer fluid. As an illustrative simple example, section 3.5.1 considers a simplified loop for which all segments are straight channels with laminar flow. Section 3.5.2 repeats this analysis for a more generalized friction coefficient form, which is applicable to systems that are dominated by either

form losses or drag, but not a combination of both, and to systems for which flow through all components that contribute significantly to friction losses are in the same flow regime. These approaches are presented here because they have been previously used to generate figures of merit for the selection of natural circulation heat transfer fluids[71,72]. However, they have very narrow applicability to fluoride salt cooled systems. The low volumetric flow rates and Reynolds numbers that occur commonly with fluoride salts, creates strong incentives to design enhanced heat transfer surfaces, such as pebble fuel, and twisted tube heat exchangers. Enhanced surfaces tend to increase the contribution of form-losses to pressure drop, making the figures of merit of sections 3.5.1 and 3.5.2 inapplicable. Section 3.5.3 presents a fluid performance comparison for natural circulation heat removal from a pebble bed. The approach taken here is valid for any type of friction losses functional dependence on mass flowrate.

3.5.1 An example: Laminar Flow Through a Pipe

Assuming that all the components that contribute to friction loss in the natural circulation loop are straight channels with laminar flow, the natural circulation steady state temperature rise and residence times can be derived as explicit analytic expressions.

$$f_{lam} = \frac{64}{Re} \; (Re < 2000) \tag{3-51}$$

For convenience, all of the derived expressions are written as a product of three factors: (1) a factor that depends only on fluid properties, denoted by a Greek letter; (2) a factor that depends only on the geometric dimensions of the natural circulation loop, G, as defined by equation (3-52); and (3) the dependence on heat input to the loop.

$$G = \sqrt{\frac{64 \sum_n \left(\frac{l_n}{d_n^2} \cdot \frac{1}{A_n} \right)}{\Delta z_{NC}}} \tag{3-52}$$

The effectiveness of a heat transfer fluid to remove heat by natural circulation is characterized by the first term of the equation below, φ. Fluids with lower values of φ are more effective to remove heat by natural circulation, and a priori are preferred for the design of natural circulation loops (as discussed in the next section, this metric is not sufficient for the selection of a natural circulation fluid).

$$\Delta T_{h.lam} \approx \varphi_{lam} \cdot G \cdot \sqrt{Q_h} \tag{3-53}$$

$$\varphi_{lam} = \sqrt{\frac{\mu_o}{\rho_o^2 c_{p,h} g \beta}} \tag{3-54}$$

The mass-flow-rate at steady state will determine the residence time of the fluid around the natural circulation loop. For transients in which the fluid residence time determines the time constant of the system response, it is important to consider the effect of fluid thermophysical properties on the fluid transit time around the natural circulation loop. Fluids with lower values of ω will have a shorter residence time around the natural circulation loop at steady state.

$$m_{lam} \approx \frac{\rho_o}{\omega_{lam}} \cdot \frac{1}{G} \sqrt{Q_h} \tag{3-55}$$

$$\tau = \frac{V_{loop} \rho_o}{m} \tag{3-56}$$

$$\tau_{lam} = \omega_{lam} \frac{V_{loop} G}{\sqrt{Q_h}} \tag{3-57}$$

$$\omega_{lam} = \sqrt{\frac{\mu_o c_{p,h}}{g\beta}} \Rightarrow \omega_{lam} = \varphi_{lam} \cdot \rho_o c_{p,h} \tag{3-58}$$

To avoid instabilities, it is best if flow remains in the laminar flow regime. For flow in a smooth pipe, the transition to turbulence occurs around Re = 2000. Smaller values of ϑ lead to smaller Reynolds number and allow the system to stay in the laminar flow regime at higher power inputs to the loop. If flow is in the laminar regime, the alternative approach is to use enhanced surfaces, such as twisted tubes, or pebble beds, which don't have flow transitions that can lead to instabilities.

$$Re_{lam} = \vartheta \cdot \frac{d_n}{A_n G} \cdot \sqrt{Q_h} \tag{3-59}$$

$$\vartheta = \sqrt{\frac{\rho_o^2 g\beta}{\mu_o^3 c_{p,h}}} \Rightarrow \frac{1}{\vartheta} = \omega \cdot \frac{\mu}{\rho} = \varphi_{lam} \cdot \mu c_{p,h} \tag{3-60}$$

Table 3-3. Summary of key parameters for steady state heat removal by natural circulation, for laminar flow

Parameter	Parameter Definition	Equation that uses the parameter	Related Fundamental Equation
Geometric loop parameter, G	$G_{lam} = \sqrt{64 \sum_n \left(\frac{l_n}{d_n^2} \cdot \frac{1}{A_n} \right)}$		$f_{lam} = \frac{\Delta P}{C_n (m^2/2\rho_o)} = \frac{64}{Re}$ $m^3 = \frac{\rho_o^2 g\beta}{c_{p,h}} \frac{\Delta z_{HL} \cdot Q_h}{F'(Re(m))}$
Effectiveness, φ	$\varphi_{lam} = \sqrt{\frac{\mu_o}{\rho_o^2 c_{p,h} g\beta}}$	$\Delta T_{h.lam} = \varphi_{lam} \cdot G \cdot \sqrt{\Delta z_{NC} Q_h}$	$Q_n = m c_p \Delta T_n$
Rapidity, ω	$\omega_{lam} = \sqrt{\frac{\mu_o c_{p,h}}{g\beta}}$	$\tau_{lam} = \omega_{lam} \frac{V_{loop} G}{\sqrt{\Delta z_{NC} Q_h}}$	$\tau = \frac{V_{loop} \rho_o}{m}$
Maintain laminar flow, ϑ	$\vartheta_{lam} = \sqrt{\frac{\rho_o^2 g\beta}{\mu_o^3 c_{p,h}}}$	$Re_{lam} = \vartheta_{lam} \cdot \frac{d_n}{A_n G} \cdot \sqrt{\Delta z_{NC} Q_h}$	$Re_n = \frac{m}{\mu} \cdot \frac{d_n}{A_n}$

ϑ for flibe is 1000 times lower than for water, and 170 times lower than for liquid sodium (see Table 3-6). This means that for a system of a given geometry, and a given power input into the natural circulation loop, the Reynolds number through a particular segment will be 1000 times lower if flibe is the coolant, than if water is the coolant. Compared to water, flibe has a viscosity that is higher by a factor of 90, and a thermal expansion coefficient that is lower by a factor of 13, so for a given power input the resulting natural circulation flow rates are lower; this is balanced by the fact that the volumetric heat capacity of flibe is high and low flow rates are needed to

transport the same amount of heat; also, the viscosity of flibe being higher than for water, the Reynolds numbers are much smaller. Another way to pose the problem is to consider two different systems, one that is designed for water and another that is designed for flibe. They both have the same temperature rise across the core, at the same reference power. The Reynolds in the water system will be at least one order of magnitude higher than in the flibe system.

3.5.2 General treatment of the friction coefficient

The natural circulation steady state temperature rise and residence times can be treated analytically, with the assumption that all the components that contribute to friction loss in the natural circulation loop have a friction coefficient of the same functional form, which follows the functional form given in Table 3-4. This functional form for the friction coefficient is followed for flow through a pipe in all flow regimes, and for flow through a pebble bed in the extremes of very high or very low Reynolds number.

The parameters φ and ω group the thermophysical properties of the heat transfer fluid, and they can be used as metrics in the selection of heat transfer fluids. The parameter G groups the geometrical dimension variables for the loop.

Table 3-4. Steady state natural circulation parameters, for a generic friction coefficient.

Parameter	Parameter definition	Equation that uses the parameter
Geometric loop parameter, G	$G = \left\{ a \sum_n \left[\left(\frac{1}{A_n^2} \frac{l_n}{d_{h,n}} \right) \cdot \left(\frac{d_n}{A_n} \right)^b \right] \right\}^{1/(3+b)}$	$f = \frac{\Delta P}{C_n (m^2/2\rho_o)} = aRe^b$ $m^{3+b} = \frac{\rho_o^2 \beta g \mu^b}{c_{p,h}} \frac{\Delta z_{NC} Q_h}{G^{3+b}}$
Effectiveness, φ	$\varphi = \frac{\mu^{-b/(3+b)}}{(\rho_o^2 \beta g)^{1/(3+b)} c_p^{1-1/(3+b)}}$	$\Delta T_h = \varphi \, G \frac{Q_h^{1-1/(3+b)}}{\Delta z_{NC}^{1/(3+b)}}$
Rapidity, ω	$\omega = \frac{\rho_o^{(1+b)/(3+b)} c_{p,h}^{1/(3+b)} \mu^{-b/(3+b)}}{(\beta g)^{1/(3+b)}}$	$\tau_n = \omega \cdot GV_n \cdot (\Delta z_{NC} Q_h)^{-1/(3+b)}$
Maintain a single flow regime, ϑ	$\vartheta = \left(\frac{\rho_o^2 \beta g}{\mu^3 c_{p,h}} \right)^{1/(3+b)}$	$Re_n = \vartheta \cdot \frac{d_n}{A_n G} (\Delta z_{NC} Q)^{1/(3+b)}$

Table 3-5. Natural circulation steady state loop temperature difference and residence time, for various friction coefficients.

		f	ΔT_h	τ_n	φ	ω
Pebble bed	$Re_{PB} < 0.1$ f_1/f_2	$\frac{f_1}{Re}$	$\varphi \, G \frac{Q_h^{0.5}}{\Delta z_{NC}^{0.5}}$	$\omega \frac{GV_n}{(\Delta z_{HL} Q_h)^{0.5}}$	$\frac{\mu^{0.5}}{(\rho_o^2 \beta g)^{0.5} c_p^{0.5}}$	$\frac{c_{p,h}^{0.5} \mu^{0.5}}{(\beta g)^{0.5}}$
	$Re_{PB} > 10$ f_1/f_2	f_2	$\varphi \, G \frac{Q_h^{0.666}}{\Delta z_{NC}^{0.333}}$	$\omega \frac{GV_n}{(\Delta z_{HL} Q_h)^{0.333}}$	$\frac{1}{(\rho_o^2 \beta g)^{0.333} c_p^{0.667}}$	$\frac{(\rho_o c_{p,h})^{0.333}}{(\beta g)^{0.333}}$
Pipe flow	Laminar, $Re < 2000$	$\frac{64}{Re}$	$\varphi \, G \frac{Q_h^{0.5}}{\Delta z_{NC}^{0.5}}$	$\omega \frac{GV_n}{(\Delta z_{HL} Q_h)^{0.5}}$	$\frac{\mu^{0.5}}{(\rho_o^2 \beta g)^{0.5} c_p^{0.5}}$	$\frac{c_{p,h}^{0.5} \mu^{0.5}}{(\beta g)^{0.5}}$
	Transitional, $Re < 4000$	$\frac{Re^{0.33}}{381}$	$\varphi \, G \frac{Q_h^{0.7}}{\Delta z_{NC}^{0.3}}$	$\omega \frac{GV_n}{(\Delta z_{HL} Q_h)^{0.3}}$	$\frac{1}{\mu^{0.1} (\rho_o^2 \beta g)^{0.3} c_p^{0.7}}$	$\frac{\rho_o^{0.4} c_{p,h}^{0.3}}{\mu^{0.1} (\beta g)^{0.3}}$
	Turbulent, $Re < 30000$	$\frac{0.316}{Re^{0.25}}$	$\varphi \, G \frac{Q_h^{0.646}}{\Delta z_{NC}^{0.364}}$	$\omega \frac{GV_n}{(\Delta z_{HL} Q_h)^{0.364}}$	$\frac{\mu^{0.091}}{(\rho_o^2 \beta g)^{0.364} c_p^{0.636}}$	$\frac{\rho_o^{0.273} c_{p,h}^{0.364} \mu^{0.091}}{(\beta g)^{0.364}}$
	Turbulent, $Re > 30000$	$\frac{0.184}{Re^{0.20}}$	$\varphi \, G \frac{Q_h^{0.643}}{\Delta z_{NC}^{0.357}}$	$\omega \frac{GV_n}{(\Delta z_{HL} Q_h)^{0.357}}$	$\frac{\mu^{0.071}}{(\rho_o^2 \beta g)^{0.357} c_p^{0.643}}$	$\frac{\rho_o^{0.286} c_{p,h}^{0.357} \mu^{0.071}}{(\beta g)^{0.357}}$

Table 3-6. Natural circulation heat transport metrics, normalized to the respective values for flibe at 700oC. Comparison among fluoride salt coolants.

			flibe	**flibe**	**flinak**	**fnazr**	**frbzr**	**flizr**
melting point		°C	460	460	454	500	410	509
boiling point		°C	1400	1400	1570	1350	1450	??
vapor press. at 900°C		mmHg	1.2	1.2	0.7	5	1.3	77
ref. temp.		°C	700	650	700	700	700	700
ref. press.		atm	1	1	1	1	1	1
	μ	Pa-s	0.005494	0.006754	0.002900	0.005100	0.005100	0.005100
	ρ_o	kg/m^3	1938	1962	2019	3034	3223	3091
	cp	J/kg-K	2415	2415	1882.8	1171.52	836.8	983
	β	10-^{4}/K	2.53	2.50	3.62	2.90	3.10	2.99
	$\rho_o c_p$	MJ/m^3 K	4.680	4.739	3.801	3.554	2.697	3.039
	$\rho_o \beta$	kg/m^{3}K	0.491	0.491	0.730	0.880	1.000	0.925
	Pr	--	13	16	6	12	11	13
Pebble Bed	$Re_{PB} < 0.1$ f_1/f_2	φ/φ_{flibe}	1.00	1.10	0.66	0.83	0.89	0.87
Pebble Bed	$Re_{PB} > 10$ f_1/f_2	φ/φ_{flibe}	1.00	1.00	1.02	1.15	1.35	1.26
Pipe Flow	laminar, Re < 2000	φ/φ_{flibe}	1.00	1.10	0.66	0.83	0.89	0.87
Pipe Flow	transitional, Re < 4000	φ/φ_{flibe}	1.00	0.98	1.11	1.23	1.47	1.36
Pipe Flow	turbulent, Re < 30000	φ/φ_{flibe}	1.00	1.01	0.94	1.08	1.25	1.18
Pipe Flow	turbulent, Re > 30000	φ/φ_{flibe}	1.00	1.01	0.96	1.10	1.27	1.20
Pebble Bed	$Re_{PB} < 0.1$ f_1/f_2	ω/ω_{flibe}	1.00	1.12	0.54	0.63	0.51	0.57
Pebble Bed	$Re_{PB} > 10$ f_1/f_2	ω/ω_{flibe}	1.00	1.01	0.83	0.87	0.78	0.82
Pipe Flow	laminar, Re < 2000	ω/ω_{flibe}	1.00	1.12	0.54	0.63	0.51	0.57
Pipe Flow	transitional, Re < 4000	ω/ω_{flibe}	1.00	0.99	0.90	0.93	0.85	0.88
Pipe Flow	turbulent, Re < 30000	ω/ω_{flibe}	1.00	1.03	0.77	0.82	0.72	0.77
Pipe Flow	turbulent, Re > 30000	ω/ω_{flibe}	1.00	1.02	0.78	0.83	0.73	0.78
PB	$Re_{PB} < 0.1$ f_1/f_2	$\vartheta/\vartheta_{flibe}$	1.0	0.7	3.7	2.7	3.5	3.0
Pipe	laminar, Re < 2000	$\vartheta/\vartheta_{flibe}$	1.0	0.7	3.7	2.7	3.5	3.0

Table 3-7. Natural circulation heat transport metrics, normalized to the respective values for flibe at 700oC. Comparison of flibe performance with other single phase coolants.

			water	Na	Pb	Pb-Bi	Dowtherm A	Drakesol 260
melting point		°C	-1	98	327	123.5	12	n/a
boiling point		°C	310	883	621	1670	257	265
vapor press. at 900°C		mmHg	>760	>760	>760	8		
Ref. temp.		°C	302	627	627	627	90	140
Ref. press.		atm	10	0.101	0.101	0.101	0.101	0.101
	μ	Pa-s	0.000086	0.000201	0.001461	0.001140	0.001122	0.0007124
	ρ_o	kg/m^3	711.9	805	10255	9875	1006	735
	c_p	J/kg-K	5723	951	143.1	146.5	1767	2000
	β	10^{-4}/K	32.33	2.95	1.32	1.40	8.19	6.80
	$\rho_o c_p$	MJ/m^{3}K	4.074	0.765	1.467	1.446	1.779	1.470
	$\rho_o \beta$	kg/m^{3}K	2.30	0.237	1.350	1.380	0.826	0.500
	Pr	--	0.967	0.004	0.010	0.012	15	15
Pebble Bed	$Re_{PB} < 0.1$ f_1/f_2	φ/φ_{flibe}	0.06	0.68	0.56	0.49	0.57	0.64
	$Re_{PB} > 10$ f_1/f_2	φ/φ_{flibe}	0.47	3.18	2.70	2.67	1.29	1.56
Pipe Flow	laminar, Re < 2000	φ/φ_{flibe}	0.06	0.68	0.56	0.49	0.57	0.64
	transitional, Re < 4000	φ/φ_{flibe}	0.70	4.33	3.70	3.74	1.52	1.86
	turbulent, Re < 30000	φ/φ_{flibe}	0.32	2.40	2.02	1.95	1.11	1.32
	turbulent, Re > 30000	φ/φ_{flibe}	0.35	2.55	2.15	2.10	1.15	1.37
Pebble Bed	$Re_{PB} < 0.1$ f_1/f_2	ω/ω_{flibe}	0.05	0.11	0.17	0.15	0.21	0.20
	$Re_{PB} > 10$ f_1/f_2	ω/ω_{flibe}	0.41	0.52	0.85	0.82	0.49	0.49
Pipe Flow	laminar, Re < 2000	ω/ω_{flibe}	0.05	0.11	0.17	0.15	0.21	0.20
	transitional, Re < 4000	ω/ω_{flibe}	0.61	0.71	1.16	1.16	0.58	0.58
	turbulent, Re < 30000	ω/ω_{flibe}	0.28	0.39	0.63	0.61	0.42	0.42
	turbulent, Re > 30000	ω/ω_{flibe}	0.31	0.42	0.68	0.65	0.44	0.43
PB	$Re_{PB} < 0.1$ f_1/f_2	$\vartheta/\vartheta_{flibe,}$	436	102	114	163	12	15
Pipe	laminar, Re < 2000	$\vartheta/\vartheta_{flibe}$	436	102	114	163	12	15

3.5.3 Fluid comparisons for a pebble bed system

For designing a system that relies on natural circulation for heat removal, the selection of working fluid may depend on the natural circulation performance of the fluid. Various single phase reactor coolants are compared here. In addition to fluoride salt coolants, calculations are also shown for liquid metals and pressurized water, as a point of comparison of FHRs with PWRs and LMRs. The operation conditions for water were selected based on the NuScale[73] reactor design, which is a small modular pressurized water reactor that relies on natural circulation for decay heat removal.

Jens recommends two figures of merit for natural circulation heat transport, one for laminar flow, and another for turbulent flow through pipes[71,72]. This approach is valid for loops in which flow through all the segments is in the same regime, and hence the friction coefficient has the same functional form dependence on Reynolds number. In these cases, the mass flow rate can be factored out of the summation in equation (3-18), and the steady state natural circulation mass flow rate can be solved analytically from equation (3-31).

The approach proposed by Jens can only be applied to selecting among fluids that will lead to the same flow regime in the loop. For the same flow regime, the ratio of φ for two fluids is a constant that depends on the thermophysical properties of the two fluids and the power coefficient of the Reynolds number in the friction coefficient correlation, b (see Table 3-4). For this case Jens recommends using the coefficient φ for comparing the effectiveness of natural circulation of various fluids. Since φ depends on b, the comparison of natural circulation effectiveness must always be done for a specific geometry, and a specific flow regime. For different flow regimes, the elevation of the loop for the water-cooled system has a different functional dependence on the power, the core temperature rise (ΔT), and the geometry parameters of the bed. Hence, for different flow regimes, the ratio of φ's is no longer a constant.

Williams et al. uses the approach proposed by Jens to rank the natural circulation effectiveness of various fluoride salts, and to compare them to water and liquid metals[71,72]. This approach is only valid when the salt system is designed to operate in turbulent regime. Due to the high volumetric heat capacity of the salt, and the relatively high viscosity, the natural circulation Reynolds number is very low, and is likely to fall in the laminar regime, whereas the same system cooled with water or with liquid metal will be in the turbulent regime. Furthermore, this approach does not apply to flow through a pebble bed, or flow through a geometry for which form losses are significant and the friction coefficient does not follow the functional form of flow through a pipe (see Table 3-4).

The pebble bed friction coefficient is a summation of two terms: a Reynolds dependent (drag), and a Reynolds-independent term (form losses). At very high or very low Reynolds number, only one of the two terms is significant, and equation (3-31) can be solved analytically, as for the pipe flow. When the pebble bed Reynolds number is between 13 and 1300, both terms contribute to the friction coefficient, and the natural circulation effectiveness of the fluid, ie φ, would depend on the Reynolds number. Hence William's method is not applicable to flow through a pebble bed with Reynolds number in this range. As a broad guidance, the method can be applied for the two extremes of Reynolds below 13, and Reynolds above 1300.

The Reynolds number in the bed varies significantly among the fluids, for a given power input and loop geometry and dimensions. For example, water will have a Reynolds number that is 436 times that of flibe, and liquid sodium 102 times that of flibe. Among the fluoride salts, the Reynolds number varies by a factor of about 4. These numbers are summarized in Table 3-6 and

Table 3-7. It is likely that for water and liquid metals the Reynolds number in the bed will be sufficiently high that the friction coefficient is Reynolds independent, whereas for flibe the friction coefficient will be heavily Reynolds-dependent. The equivalent for pipe flow is that water and liquid metals will have turbulent flow, whereas fluoride salts are likely to have laminar or transitional flow, with flibe having the lowest Reynolds number of all the fluids compared here.

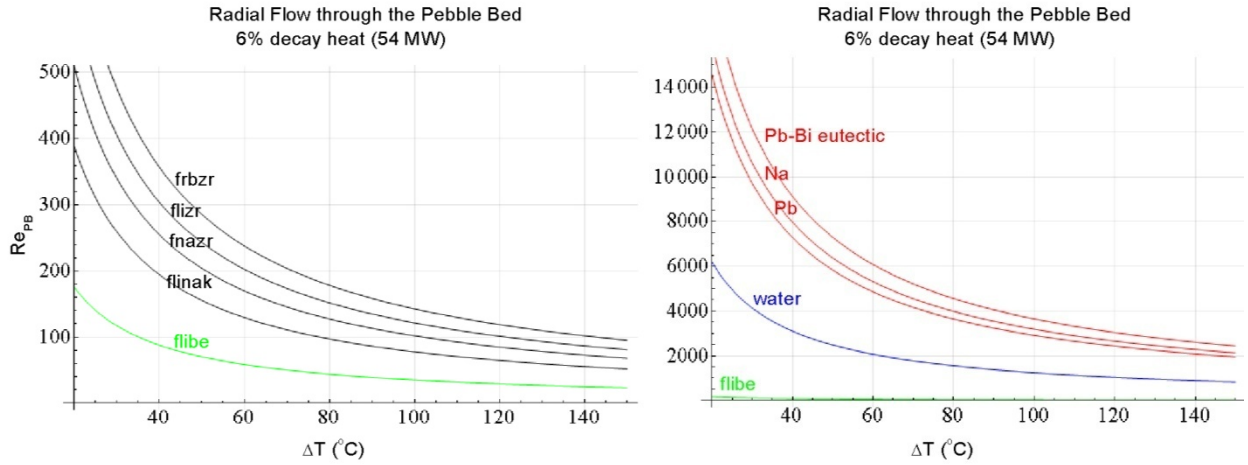

Figure 3-6. Reynolds number in the PB-FHR core, for various coolants, for steady state natural circulation decay heat removal.

For a pebble bed, if the Reynolds number is below 1300 and above 13, there is no appropriate figure of merit that depends only on fluid properties. Working fluid selection must be made based on calculations for specific design conditions. For PB-FHR with flibe coolant the Reynolds number is in the range of 10 to 1000 (see Figure 3-6). For water, liquid sodium, and liquid lead, the Reynolds number for the same conditions remains above 1,300 and the friction coefficient is a constant. Similarly, when two natural circulation fluids lead to different flow regimes in the loop, it is not possible to compare the natural circulation heat removal effectiveness of the two fluids independently of the power, the ΔT, and the geometry of the bed. *A universal comparison of natural circulation effectiveness for fluids is not possible.*

The coefficient φ quantifies the tradeoff between loop elevation and temperature rise, and we've used it so far as a metric for natural circulation effectiveness. However, one also needs to consider that the acceptable temperature rise varies among fluids. FHRs can tolerate a temperature rise of 100°C, or slightly higher. Fluoride salts operate with over 700°C margin to boiling, and the limiting parameter for the core outlet temperature is the temperature to which metallic structural materials can be exposed, which should be kept below 700°C for extended periods of time. The limiting parameter for the core inlet temperature is a desired margin to freezing of 100°C, which sets the minimum core inlet temperature at 600°C or slightly below. Pressurized water reactors (PWRs) must maintain a margin to departure from nucleate boiling (DNB) because above this limit convective heat transfer degrades significantly. PWRs operate close to the boiling point of water, and the temperature rise is limited to a few tens of degrees. NuScale is a small modular advanced PWR that employs natural circulation decay heat removal and it operates with a core temperature rise of 40°C[73]. AP-1000 is a large PWR and it operates

with a temperature rise of 40°C[74]. For this comparison, the acceptable temperature rise for natural circulation cooling of LMRs is taken to be 150°C. The temperature rise in liquid metal reactors is limited by similar constraints to FHRs: the upper end is limited by material performance for the fuel, cladding, or structural materials, and the lower end is limited by the freezing point of the coolant. Liquid metals require much taller natural circulation loops than liquid salts or water, but, in theory they could accommodate high temperature rises in the core because of the lower freezing point of the coolant. However, LMRs generally operate with a temperature rise in the vicinity of 150°C[53,75], in order to maintain a high average coolant temperature, which is important for the power conversion efficiency of the plant. Designing the decay heat removal system to lead to a significant drop in average coolant temperature compared to normal operation presents thermal-hydraulic and materials challenges, in terms of thermal shock, and differential expansion.

As a representative example for natural circulation cooling of a pebble bed core, Figure 3-7 shows calculations for two flow configurations through the central core: fully axial, and fully radial. These two cases bound the behavior of the PB-FHR core. Two decay heat power levels are considered: 18 MW, which represents 2% of 900 MW; and 54 MW, which represents 6% of 900 MW. For illustration, only friction losses through the core are considered in this analysis. If the friction loss correlations for the heat exchanger are similar to those for porous media, with significant contributions from both drag and form losses, then the results are expected to follow similar trends as depicted in this analysis. Complete design of the natural circulation loop will entail an optimization study for the DHX. The analysis presented here discusses only optimization of the natural circulation loop with regards to operational parameters for the core.

Figure 3-7 shows that the loop elevation requirement for a water cooled system with 40°C temperature rise is the same as for a flibe cooled system with 107°C temperature rise, for axial flow through the PB-FHR core, with 6% decay heat generation. Even though, water is more effective at transferring heat by natural circulation than flibe, because flibe can tolerate a higher temperature rise, the loop elevation requirements for the two fluids are the same. If we re-evaluate the elevation requirements with radial flow through the pebble bed core, the water elevation requirements with 40°C temperature rise, are matched by salt with 150°C temperature rise. In this case water is a more effective natural circulation fluid. The liquid metal coolants require higher loop elevations than both water and salts.

Figure 3-7 also shows a comparison of various fluoride salts. Frbzr has the most effective natural circulation heat removal for both pebble bed flow configurations considered. The performance of flizr as compared to flibe depends on the flow configuration and the temperature rise; for axial flow flizr has worse performance, for radial flow with temperature rise above 65°C, flizr has better performance. This example illustrates the importance of considering fluid comparison on case by case scenarios, for systems with flow through a pebble bed.

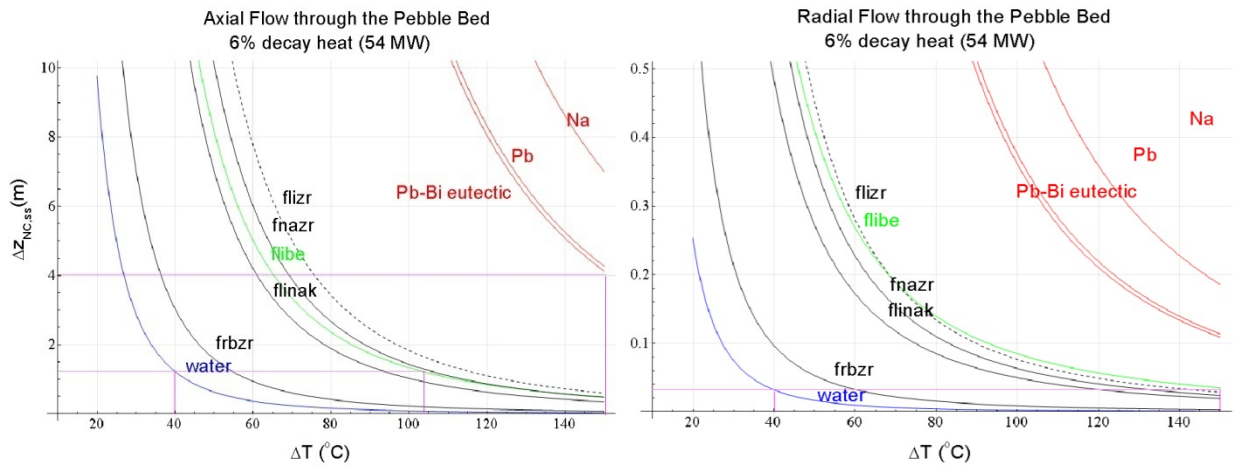

Figure 3-7. Natural circulation loop elevation requirements, PB-FHR primary circuit, for various coolants.

Figure 3-8 and Figure 3-9 compare the head loss and pumping power among the coolants, at full power operation. Head loss is an important parameter for the design of a pool-type pebble bed reactor with on-line refueling, because pebble injection is done through a stand-pipe, and the liquid level difference between the standpipe and the reactor pool is determined by the gauge pressure at the inlet of the core. Among the fluoride salts, flibe performs most favorably, with the heavier salts having higher core head loss by a factor of 2 to 3. The pumping power of flibe is lower than for water and much lower than for liquid metals. The other, heavier, fluoride salts have higher pumping power than flibe.

The calculations performed to generate the figures in this section are given in Appendix F.

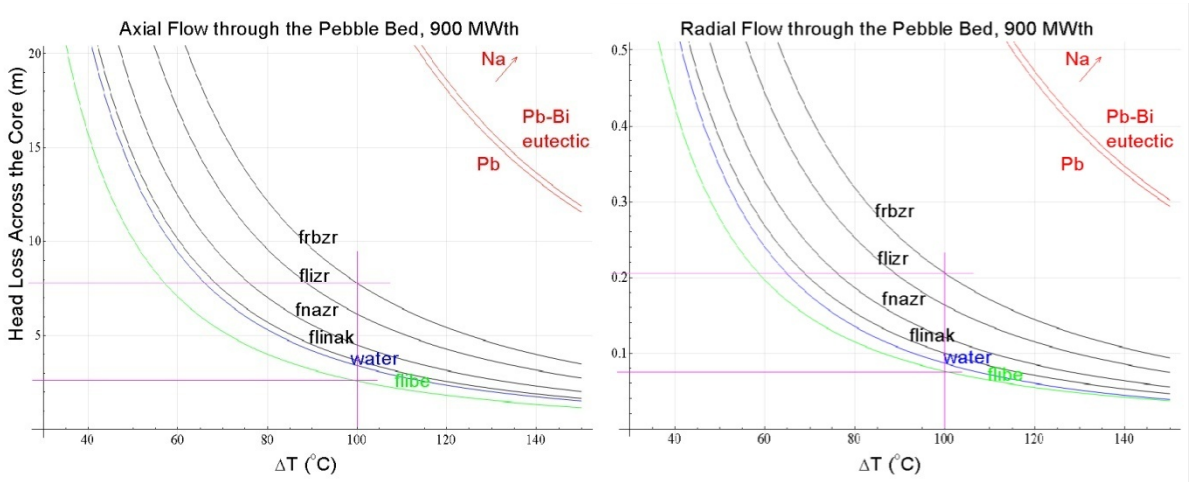

Figure 3-8. Head loss in the PB-FHR core, for various coolants, at full power operation.

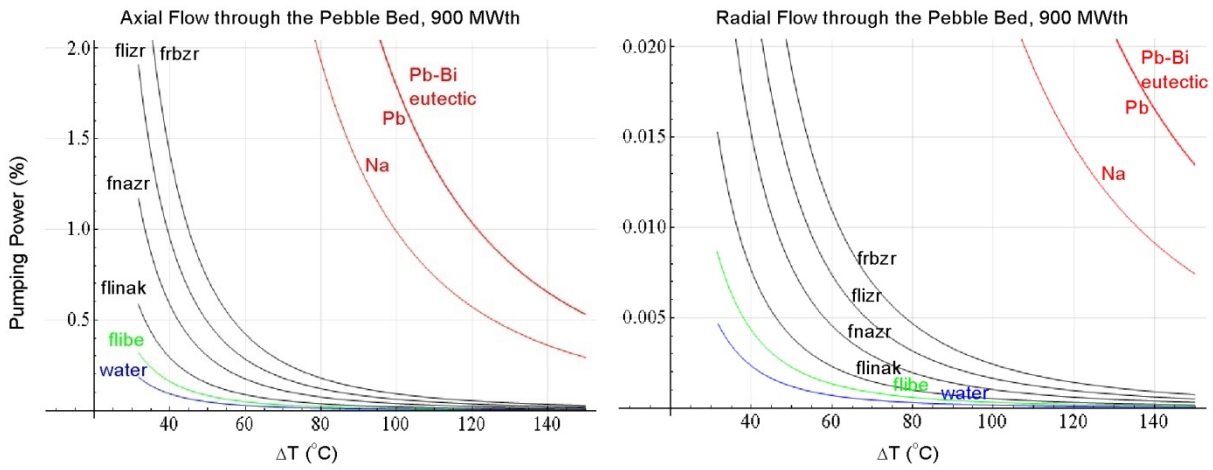

Figure 3-9. Pumping power for the PB-FHR core, for various coolants, at full power operation.

3.6 Transient natural circulation: design of scaled experiments

This section gives the scaling arguments for designing an experimental model that matches the transient behavior of a prototypical natural circulation loop. The scaling arguments are based on the nondimensionalized equations derived in Section 3.4. Subscript *m* refers to the scaled experimental model, the subscript *FHR* refers to the prototype. The subscripts *h*, *c*, *hp*, *cp* refer to the heated section, cooled section, hot leg piping, and cold leg piping of the experiment. The subscripts *PB*, *HX*, *HL*, *CL* refer to the core, DHX, hot leg and cold leg of the prototypical system.

There are four characteristic parameters of the loop that are specific to the transient of interest: the mass flow rate, the heat input, loop temperature rise, and the difference between heat sink temperature and loop average temperature. The transient of interest must be decomposed in time phases, with each time phase having its set of characteristic parameters. The scaling arguments must then be applied for each set of parameters.

3.6.1 Entire loop

The transient non-dimensionalized 1D momentum conservation equation for the core and the heater section is given below.

$$\frac{1}{\Pi_2}\frac{\partial m^*}{\partial t^*} = \Pi_6 - m^{*2} \tag{3-61}$$

Assuming that the value of $1/\Pi_2$ is sufficiently small for the inertia term to be neglected, only the functional form of the dependence of the friction term on mass flow rate must be matched. The friction term on each segment is scaled individually. The relative contribution of each segment to the total friction losses is matched. The functional form of the friction correlation with respect to nondimensional mass flowrate is matched for the segments with dominant contribution to the friction losses.

For and idealized natural circulation loop $\Pi_z = 1.0$. If the temperature profiles in the heat sink and the heat source are significantly non-linear with elevation, or if the hot leg and the cold leg

are not adiabatic, Π_z deviates from unity. The evolution of Π_z over the course of the transient is a scaling parameter that must be replicated between the model and the prototype.

The energy equation is studied separately for each segment of the loop. Table 3-8 gives the scaling arguments pertaining to the entire loop.

Table 3-8. Scaling requirements pertaining to the entire natural circulation loop

Physical meaning of the scaling requirement	Scaling Requirement	Equations	Experiment Design Variables
Steady state natural circulation flow rate		$m_r^2 = \frac{\rho_o^2 g \beta \Delta T_r \Delta z_{NC}}{\sum_n F_n'(m^*, T(s))}$	
Friction term evolution over the course of the transient	$\frac{F_{n,m}'(m^*, T^*(s^*))}{F_m'} = \frac{F_{n,p}'(m^*, T^*(s^*))}{F_p'}$		
Buoyancy term evolution over the course of the transient	$\Pi_{z,m}(T^*(\boldsymbol{s}^*)) = \Pi_{z,p}(T^*(s^*))$	$\Pi_z = \frac{\Delta z_{NC}}{\Delta z_{ch}}$	$m_{r,m}, \Delta z_{HL,m}, \Delta T_{r,m}$
The inertia term is negligible	$\Pi_2 \gtrsim 100$	$\Pi_2 = \frac{\frac{V_r}{2}\sum_n F_n'}{\sum_n \frac{L_n}{A_n}}$	

3.6.2 Scaled model of the pebble bed momentum equation

For IETs, it is more convenient to use a straight pipe geometry to model the integral behavior of the pebble bed, instead of constructing a reduced scale pebble bed. Using heated pebbles involves several problems: heating pebbles electrically is difficult, the pressure drop may be too high for a reduced scale pebble bed, wall effects become significant and can cause significant distortion, and the thermal inertia may be difficult to scale. Because pebble beds have higher friction pressure losses than straight channels, it is possible to use a straight channel in conjunction with a needle valve to replicate the friction coefficient of a pebble bed, for which wall effects are not significant. The straight channel can be designed with very low thermal inertia, and the thermal inertia of the pebble bed is replicated in the experimental model using a computer-controlled power input into the heater. Actual pebble bed heat transfer and fluid mechanics can then be studied in separate effect test experiments.

The experimental model for flow through a pebble bed core will use a simulant fluid flowing through a straight channel heater element and a valve with Reynolds-independent pressure drop. This section discusses the sizing of the heater element and valve, such that the Reynolds-functional dependence of the pebble bed friction coefficient is replicated.

The natural circulation decay heat removal flow rates in the PB-FHR correspond to the pebble bed flow regime in which both the Reynolds-dependent and the Reynolds-independent terms of the friction coefficient are significant. In order to model the dynamic behavior of the

natural circulation loop, it is important that the friction coefficient of the pebble bed is replicated over the entire range of probable flow rates. The pebble bed friction coefficient, f_{PB}, is given by

$$f_{PB} = \frac{f_1}{Re_{PB}} + f_2 \tag{3-62}$$

Table 3-9. Empirical coefficients for the friction losses through a porous media, with 40% porosity

	Formula	Blake-Carman-Kozeny[40,44]
E_1	Empirical	150
E_2	Empirical	1.75
f_1	$2E_1\left(\frac{1-\varepsilon}{\varepsilon}\right)^2$	675
f_2	$2E_2\frac{1-\varepsilon}{\varepsilon}$	5.25
f_1/f_2	$\frac{E_1}{E_2}\frac{1-\varepsilon}{\varepsilon}$	129

E_1 and E_2 are Ergun correlation coefficients, f_1 and f_2 friction coefficients based on pore velocity, and ε the bed porosity.

To match the Reynolds-dependent part of the pebble bed friction coefficient, the straight channel friction coefficient must have an inverse reciprocal dependence on Reynolds. Laminar flow through a pipe has the 1/Re functional form, so the channel will have to be sized to ensure that flow remains in the laminar regime.

$$f_{pipe} = \frac{64}{Re_{pipe}} \tag{3-63}$$

$$Re_{pipe} < 2000 \tag{3-64}$$

To match the Reynolds-independent part of the pebble bed pressure drop, needle valves are convenient to use because once installed, their pressure drop can be tuned to ensure that scaling is appropriately achieved in the as-built experiment. Deltron needle valves[76] have Reynolds-independent friction coefficient. Pressure drop through the valve, ΔP_{valve}, is calculated using the expression below, where Q_v is the volumetric flow rate in English units (1 gpm=6.31E-05 m^3/s) and C_v the flow coefficient. Valve curves provided by the manufacturer give the value of C_v as a function of the percent opening of the valve.

$$\Delta P_{valve}[psi] = \frac{Q_v^2[gpm]\cdot SG}{^{Engl}C_v^2};\ SG = \frac{\rho}{1000\,[\frac{kg}{m^3}]} \Rightarrow \Delta P_{valve}[Pa] = \frac{m^2}{\rho \cdot C_v^2} \tag{3-65}$$

$$\Rightarrow C_v = {}^{Engl}C_v \cdot 0.08655;\ F'_{valve} = \frac{\Delta P_{valve}}{m^2/(2\rho)} = \frac{2}{C_v^2} \tag{3-66}$$

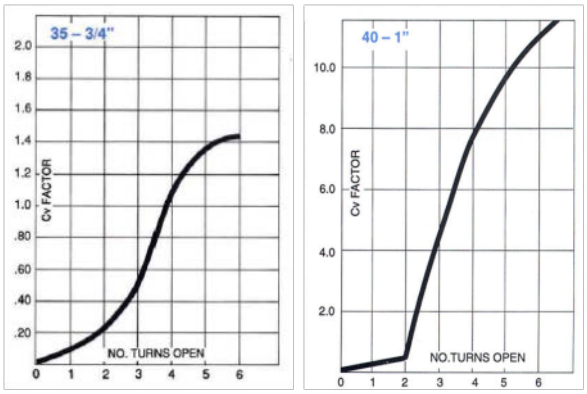

Figure 3-10. Valve curves for Deltrol needle valve76, English Units. 3/4" (1.905 cm) diameter piping (left), and 1" (2.54 cm) diameter piping (right).

Writing the total friction terms for the prototype and the model:

$$F'_{PB} = C_{PB} f_{2,p} \left(\frac{f_{1,p}/f_{2,p}}{Re_{PB}} + 1 \right) = \Pi_{61,PB} \left(\frac{\Pi_{62,PB}}{m^*} + 1 \right); \Pi_{61,PB} = C_{PB} f_{2,p};\ \Pi_{62,PB} = \mu_{PB} \frac{f_{1,p}/f_{2,p} \cdot A_{PB}}{m_{p,r} d_p} \quad (3\text{-}67)$$

$$F'_h = \frac{2}{C_v^2} \left(\frac{32 C_h C_v^2}{Re_h} + 1 \right) = \Pi_{61,h} \left(\frac{\Pi_{62,h}}{m^*} + 1 \right);\ \Pi_{61,h} = \frac{2}{C_v^2}; \Pi_{62,h} = \mu_h \frac{32 C_h C_v^2 A_h}{m_{h,r} d_h} \quad (3\text{-}68)$$

Thus, the scaling requirement is to match the Π_{62} parameter, and the heater flow must remain in the laminar regime.

$$\Pi_{62,PB} = \Pi_{62,h} \quad (3\text{-}69)$$

3.6.3 Heater section

The transient non-dimensionalized 1D energy conservation equation for the core and the heater section is given below. The scaling requirements are summarized in Table 3-10.

$$\frac{\partial T^*}{\partial t^*} + \Gamma_1 \cdot \frac{m^* \partial T^*}{\partial s^*} = \Pi_{E3} \quad (3\text{-}70)$$

The special case of a pebble bed core modeled by a straight pipe heated section was analyzed in the previous section, as an example of integral scaling of components without replicating component geometry. This analysis generated two additional scaling parameters, Π_{61} and Π_{62}. These parameters are included in Table 3-10, and can be omitted if the geometry of the core is replicated.

Table 3-10. Scaling requirements pertaining to the reactor core

Physical meaning of the scaling requirement	Scaling Requirement	Equations	Experiment Design Variables
Function form of the pebble bed friction coefficient	$\Pi_{62,h} = \Pi_{62,PB}$	$\Pi_{62,h} = \frac{32 C_h C_v^2}{Re_h}; \Pi_{62,PB} = \frac{f_{1,p}/f_{2,p}}{Re_{PB}}$ $Re = \frac{m_r d_n}{\mu A_n}; C_h = \frac{l_h}{A_h^2 d_h}$ $\frac{f_{1,p}}{f_{2,p}} = \frac{E_1}{E_2}\frac{1-\varepsilon}{\varepsilon}; E_1 = 150; E_2 = 1.75$	$m_{r,h}, d_h, A_h, l_h, C_v$
Advective heat transport (the relative velocities in each segment should match; relates to fluid transit time)	$\Gamma_{1,h} = \Gamma_{1,PB}$	$\Gamma_1 = \frac{V_r}{l_r A_n}$	$V_r, l_{r,m}, A_h$
Heat generation	$\Pi_{3E,h} = \Pi_{3E.PB}$	$\Pi_{3E} = \frac{Q_n}{c_p \Delta T_r m_r}\frac{V_r}{V_n}$	$Q_h, V_h, m_{r,h}, V_{r,m}, \Delta T_{r,m}$
Maintain laminar flow in the model heater	$Re_h < 2000$	$Re_h = \frac{m_{h,r}}{\mu_h}\cdot\frac{d_h}{A_h}$	$m_{r,h}, d_h, A_h$
Relative contribution to loop friction losses (F'_n/F')	$\frac{\Pi_{61,h}}{F'_m} = \frac{\Pi_{61,PB}}{F'_p}$	$\Pi_{61,PB} = C_{PB} f_{2,p}; \Pi_{61,h} = \frac{2}{C_v^2}$ $C_n \equiv \left(\frac{1}{A_n^2}\frac{L_n}{d_n}\right); F'_n = C_n f_n$	size all the other components with respect to F'_{PB} and F'_h. instead of F'_p and F'_m.
Axial conduction is negligible	$\frac{\Gamma_2}{Pe} < 0.01$	$\Gamma_2 = \frac{d_n V_r}{A_n l_r^2}; Pe = RePr = \frac{c_p m}{k}\cdot\frac{d_n}{A_n}$	

3.6.4 Heat Exchanger

The transient non-dimensionalized 1-D energy conservation equation for the heat exchangers is given here. The scaling requirements are summarized in Table 3-11.

$$\frac{\partial T^*}{\partial t^*} + \Gamma_1 \cdot \frac{m^* \partial T^*}{\partial s^*} = -St\Pi_{E4}\Delta\theta^* \tag{3-71}$$

If the geometry is replicated, the heat transfer correlation will match as long as Reynolds and Prandtl numbers are matched. At low mass flow rate and high power, the flow will be in the mixed convection regime, and buoyancy effects will significantly affect the heat transfer coefficient as well as the friction coefficient. In the mixed convection regime, the Reynolds, Grashoff and Prandtl numbers must be matched. Sub-component modeling and separate effects experiments should identify whether or not the Grashoff number needs to be matched, for the transients of interest. It is important to note that the characteristic temperature used to compute the Grashoff number depends on the temperature of the heat sink and it is different from the characteristic temperature of the natural circulation loop.

Table 3-11. Scaling requirements pertaining to the DRACS Heat Exchanger

Physical meaning of the scaling requirement	Scaling Requirement	Equations	Experiment Design Variables
Match the friction coefficient and the convective heat transfer coefficient functional forms	Replicate the geometry, and match Re, Pr, Gr		
Advective heat transport (the relative velocities in each segment should match; relates to fluid transit time)	$\Gamma_{1,c} = \Gamma_{1,HX}$	$\Gamma_1 = \frac{V_r}{l_r A_n}$	V_r, l_r, A_c
Heat exchanger	$St_c \Pi_{E4,c} = St_{HX} \Pi_{E4,HX}$	$St = \frac{Nu}{RePr} = \frac{hA_n}{mc_p}$	
Functional form of the heat transfer correlation must match (depends on temperature, velocity, and power input)	$Nu_c = Nu_{HX}$	$Nu = f(Re, Gr, Pr)$ *for mixed convection*	
Match the Nu correlation	$Pr_c = Pr_{HX}$	$Pr = \frac{c_p \mu}{k}$	$T_{av,c}$
Match the friction loss correlation, and Nu correlation for forced and mixed convection	$Re_c = Re_{HX}$	$Re = \frac{m_r}{\mu} \cdot \frac{d_n}{A_n}$	$m_{r,m}, d_c, A_c$
Match the Nu correlation (for mixed convection regimes)	$Gr_c = Gr_{HX}$	$Gr = \frac{\rho_o^2 g \beta \Delta T_{sink,r}}{\mu_0^2 \mu_o} \cdot {d_n}^3$	$\Delta T_{sink,r,m}, d_c$
Match the heat exchange term, after matching the functional form of the heat transfer correlation	$\Pi_{E4,c} = \Pi_{E4,HX}$	$\Pi_{E4} = \frac{S_n V_r}{A_n V_n} \cdot \frac{\Delta T_{sink,r}}{\Delta T_r}$	$\Delta T_{sink,r,m}, S_c, A_c, V_c$ $(\Delta T_{r,m}, V_{r,m})$
Remain in the same heat transfer regime (mixed convection or forced convection)	$\frac{Nu_n}{Nu_f}$ *or* $\frac{Gr}{Re^{0.5} Pr^{0.6}}$	Nu_f is for forced convection, Nu_n is for natural convection. Either condition is met if Pr, Re, Gr are matched.	
Axial conduction in the fluid is negligible	$\frac{\Gamma_2}{Pe} < 0.01$	$\Gamma_2 = \frac{d_n V_r}{A_n l_r^2}; Pe = RePr = \frac{c_p m}{k} \cdot \frac{d_n}{A_n}$	

3.6.5 Hot leg

The transient non-dimensionalized 1-D energy conservation equation for the hot leg is given here. The scaling requirements are summarized in Table 3-12. Friction and heat losses are considered to be negligible.

$$\frac{\partial T^*}{\partial t^*} + \Gamma_1 \cdot \frac{m^* \partial T^*}{\partial s^*} = 0 \tag{3-72}$$

Table 3-12. Scaling requirements pertaining to the hot leg

Physical meaning of the scaling requirement	Scaling Requirement	Equations	Experiment Design Variables
Advective heat transport (the relative velocities in each segment should match; relates to fluid transit time)	$\Gamma_{1,hp} = \Gamma_{1,HL}$	$\Gamma_1 = \frac{V_r}{l_r A_n}$	$A_{hp}, (V_r, l_r)$ *(solve for A; L can be any value)*
Friction losses in the hot leg are negligible	$\frac{F'_{hp}}{F'_h + F'_{HX}} < 0.01$	$F'_n = C_n f_n$	

3.6.6 Cold Leg

The transient non-dimensionalized 1-D energy conservation equation for the hot leg is given here. The scaling requirements are summarized in Table 3-13. If the cold leg contributes little to the overall friction term in the natural circulation loop, a larger margin of error is acceptable on matching the friction coefficient on this leg.

$$\frac{\partial T^*}{\partial t^*} + \Gamma_1 \cdot \frac{m^* \partial T^*}{\partial s^*} = 0 \tag{3-73}$$

Table 3-13. Scaling requirements pertaining to the cold leg

Physical meaning of the scaling requirement	Scaling Requirement	Equations	Experiment Design Variables
Advective heat transport (the relative velocities in each segment should match; relates to fluid transit time)	$\Gamma_{1,cp} = \Gamma_{1,CL}$	$\Gamma_1 = \frac{V_r}{l_r A_n}$	V_r, l_r, A_{cp}
In order to match the friction coefficient correlation	$Re_{cp} \approx Re_{CL}$	$Re = \frac{m_r}{\mu} \cdot \frac{d_{cp}}{A_{cp}}$	$m_{r,m}, d_{cp}, A_{cp}$

3.6.7 Degrees of freedom for experimental design

The heater is taken here as the representative segment of the loop. To simplify the scaling calculations, the volume of the heater is used for V_r, and the length of the heater will be used for l_r, rather than parameter values summed over the entire loop. A summary of the experimental design variables and the degrees of freedom for the design of a simple natural circulation loop are given in Table 3-14.

Table 3-14. Summary of degrees of freedom for the design of the scaled natural circulation loop

Number of Degrees of Freedom (DF)	Number of Equations	Geometry	Design Variables
	The heater is the reference segment	$l_{r,m} = l_h$ $V_{r,m} = V_h$	V_h, l_h
3 DF for the loop	1 equation (1 additional equation)	$(Q_h = \mathrm{c_{p,m}} m_{r,m} \Delta \mathrm{T_{r,m}})$	$\Delta z_{HL,m}, \Delta \mathrm{T_{r,m}}, m_{r,m}$
6 DF for the heater	4 scaling equations 2 geometry equations	Straight pipe $V_h = l_h A_h$ $A_h = \frac{\pi d_h^2}{4}$	$Q_h, C_v, d_h, l_h, A_h, V_h$
9 DF for the DHX	5 scaling equations 4 geometry equations	$\mathrm{d_c}$ = tube diameter p = pitch, n = number of tubes $\mathrm{V_c} = \mathrm{A_c l_c}$ $\frac{\mathrm{d_c}}{\mathrm{p_c}} = \frac{\mathrm{d_{HX}}}{\mathrm{p_{HX}}}$ $A_c = f(d_c, p_c, n_c)$ $S_c = f(d_c, p_c, n_c)$	$\Delta \mathrm{T_{sink,r,m}}, T_{av,c}, \mathrm{d_c}, \mathrm{A_c}, \mathrm{S_c}, \mathrm{V_c}, \mathrm{l_c}$ p_c, n_c
4 DF for the hot leg piping	1 scaling eqn. 2 geometry eqn.	Straight pipe $\mathrm{V_{hp}} = \mathrm{l_{hp}} \mathrm{A_{hp}}$ $A_{hp} = \frac{\pi d_{hp}^2}{4}$	A_{hp} V_{hp}, l_{hp}, d_{hp}
4 DF for the cold leg piping	2 scaling eqn. 2 geometry eqn.	Straight pipe $\mathrm{V_{cp}} = \mathrm{l_{cp}} \mathrm{A_{cp}}$ $A_{cp} = \frac{\pi d_{cp}^2}{4}$	$d_{cp}, A_{cp},$ l_{cp}, V_{cp}
26 DF total	24 Equations	Rectangular natural circulation loop with vertical heater and vertical heat exchanger	Q_h can be selected as desired, and it will determine the size of the loop $\mathrm{l_h}$ can be selected as practical for the experimental loop, and it will not impact the scaling.

3.6.8 Case study: Description of the LOFC Transient for FHRs

In order to identify the characteristic parameters of the prototypical system, a conceptual understanding of the time progression of the transient is needed. An important step initial step in the design of IETs is definition of the scenario, and decomposition in temporal phases. As an illustration, an analysis of an FHR transient is given here.

Loss of forced circulation (LOFC) and loss of heat sink (LOHS), are two classes of design basis accidents (DBAs) for FHRs[17], which employ the DRACS system for natural circulation decay heat removal. The accident progression of LOFC with SCRAM is representative of transients in these two classes, in terms of the phenomenology and the components that play a role in the transient progression.

The LOFC transient is initiated by a failure of one or several of the primary pumps to provide forced circulation. The reactor shuts down, and decay heat is removed through the DRACS. Based on the dominant phenomenology, the LOFC transient is decomposed in three temporal phases. Table 3-15 gives representative timescales for the phenomenology during each phase.

Table 3-15. Time scales for phenomena during FHR LOFC

		LOFC Phase I	LOFC Phase II	LOFC Phase III
Initial Conditions	$Q/Q_{full\ power}$[c]	100%	6%	2%
	$m/m_{full\ power}$	100%	6%	2%
	Core ΔP	50,000 Pa	240 Pa	41 Pa
System response	Π_2	17	22	34
	Inertia time scale[a]	0.74 s	9.3 s	18 s
	Fluid thermal response[b]	1.0 s	16 s	48 s
	Residence time	24 s	6.8 min	41 min
Transient drivers	Power generation transient	SCRAM: 10 s Reactivity feedback: 3 s Buoyant rod insertion[77]: 40 s Decay heat curve: 5 s	Decay heat curve: 2 h	Decay heat curve: days
	Fluid momentum transients	Pump trip: 20 s Air damper opening: 20 s	Flow reversal in DHX	Air damper closing: 20 s

[a] The inertia time scale is calculated as the kinetic energy of the fluid divided by pumping power times volumetric flow rate before pump trip. Numerical results for PB-FHR core pressure drop calculations are given in Chapter 2.

[b] The fluid thermal response is calculated as $Q/Mc_p\Delta T_{tr}$, where Q is the power generation at initial conditions, M the mass inventory of primary coolant in the core, and ΔT_{tr} the change in average primary coolant temperature. $M = 36{,}631\ kg$. $\Delta T_{tr} = 10^oC$ (10% of the core temperature rise during normal operation.)

[c] $Q_{full\ power} = 900$ MWth. $m_{full\ power} = 3727$ kg/s, which is calculated based on a 100°C core temperature rise with flibe primary coolant.

During Phase I, the signal to SCRAM is sent after the primary coolant pump fails, and the pump coast-down begins. In the event that the active SCRAM system fails to shut down the reactor, the passive shutdown mechanisms (buoyant rod, or temperature reactivity feedback) shutdown the reactor in response to temperature rise of the core. If the fluid residence time in each branch is much longer than all the other phenomena time-scales, then, in the extreme case, the fluid can be considered to be stationary, and the average temperature of the core during Phase I rises proportionally with the cumulative energy produced. Once critical power generation stops, the temperature difference between the coolant and the fuel drops, and the excess fuel thermal energy transfers to the coolant.

The beginning of Phase II is the point at which mass flow rate in the DHX is zero. If fluid inertia has a rapid time-scale compared to the pump coast-down curve, this occurs when the head generated by the pump equals the buoyancy driving head on the DHX leg. If the pump coast-down curve has a more rapid time-scale than the fluid inertia on the DHX leg, then it will determine when the mass flow rate in the DHX reaches zero. Based on Table 3-15, the pump coast-down is the driver for the initiation of Phase II. The coolant temperature distribution at the beginning of Phase II is a hot core, likely above its normal operating temperature, a cold DHX, and a cold IHX, likely colder than normal operating temperatures, if heat removal continues on the secondary side of the IHX after the initiation of the transient.

Once Phase II has initiated, the flow through the IHX continues in parallel with flow through the DHX, until the pump head is zero. The pump head balances the friction losses in the IHX, and determines the mass flow rate through the IHX branch. The power at the initiation of Phase II depends on the time of SCRAM, and the decay heat curve. If the pump coast-down time is comparable with the time to insert the shutdown rods in the reactor, then the power at the beginning of Phase II will be at 100% of full core power, and it will rapidly drop to 6% within 5 to 15 seconds of the core shutdown. If the time to insert the shutdown rods is shorter than the pump coast-down curve, then the power will have dropped to 6% by the initiation of Phase II. Based on Table 3-15, rod-insertion is more rapid than the pump coast-down, and the core is likely generating power at 6% of the full core power.

The characteristic parameters for Phase II of LOFC are defined as follows: The characteristic mass flow rate is the steady state natural circulation mass flow rate at 2% power, which is reached at the end of the end of Phase II. The characteristic primary loop temperature rise is the core temperature rise during normal operation, which is reached also at the end of Phase II. The characteristic power is the power at the initial conditions of the transient, which is likely 6% of the core full power. Table 3-16 provides additional considerations for experimental design of IETs that validate FHR LOFC transients.

Table 3-16. FHR LOFC transient description and IET design considerations

Phase I: Pump trip and SCRAM, power drops from 100% to approximately 6% (5-15s after SCRAM[78]; see Figure 3-11), core flow rate drops, normal shutdown cooling system fails to function, reactor protection system opens air supply dampers to NDHX.

- *Initial condition:* normal power operation.
- *Phenomena of interest:* heat generation in the core, heat removal from the IHX, thermal inertia of the fuel, coolant, and graphite reflectors, momentum inertia of the coolant and pump.
- *Experimental objective:* maintain core temperature rise, identify the maximum pump head at which establishment of natural circulation through the DHX branch can occur. The second objective is important because (1) having one or more of the primary pumps remain on with LOHS on the IHX changes the functionality of the DRACS systems (the primary pumps cause upwards flow through the vortex diodes and DHXs), and (2) it will provide an understanding of when Phase I ends and Phase II of the transient begins.
- *Manipulated experimental parameters:* pump head, IHX heat removal rate, decay heat generation in the fuel, relative friction losses in IHX branch/core/DHX branch.
- *Main flow loop:* primary pump, inlet-plenum, core, outlet-plenum, IHX.
- *By-pass flow loop:* primary pump, inlet-plenum, diode-up, DHX, outlet-plenum, IHX.

Phase II: Flow reversal in the DHX and establishment of natural circulation, power drops from approximately 6% to 2%.

- *Initial conditions:* end of Phase I (one of the objectives of Phase I is to determine these conditions).
- *Phenomena of interest:* establishment of NC flow, decay heat generation in the core, heat removal from the DHX, thermal inertia of the fuel, coolant, and graphite reflectors.
- *Objective:* identify peak coolant temperature during transient, identify timing for when quasi-steady state is achieved.
- *Manipulated experimental parameters:* NDHX heat removal rate, initial conditions of coolant temperature distribution, decay heat generation in the fuel, simulated effect of graphite and fuel thermal inertia on the coolant in the core region, heat transfer rate in the DHX.
- *To consider:* importance of core coolant distribution and variation of coolant residence time along different flow streamlines. This may be important to study for identifying peak local temperature differences at the outlet-plenum headers. However, for this study, it is important to understand if this effect plays an important role on the establishment of natural circulation, or on the peak locally-averaged coolant temperatures during the Phase II of the transient.
- *Main flow loops:* (1) inlet-plenum, core, outlet-plenum, DHX, diode-down. (2) DHX secondary side, hot leg, NDHX primary side, cold leg.
- *By-pass flow loops:* (1) outlet-plenum, IHX, primary pump, inlet plenum, core (2) other core by-pass routes.

Phase III: Quasi-steady state natural circulation decay heat removal, power at 2% (2-14h after SCRAM[78]) and slowly dropping.

- *Initial conditions:* end of Phase II, quasi-steady state natural circulation flow at 2% power, with two out of three DRACS loops removing heat with fully open air dampers.
- *Phenomena of interest:* decay heat generation in the core, NC heat removal from the DHX.
- *Objective:* control core temperature rise and core outlet temperature, prevent overcooling.
- *Manipulated experimental parameters:* decay heat generation in the core and heat removal rate from the DHX, relative elevation difference of DHX and core, length of heater section.
- *Main flow loops:* (1) inlet-plenum, core, outlet-plenum, DHX, diode down. (2) DHX secondary side, hot leg, NDHX primary side, cold leg flow.
- *Bypass flow loop:* (1) outlet-plenum, IHX, primary pump, inlet plenum, core (2) other core by-pass routes.

The time-scale of the LOFC transient is determined by the decay heat curve, and the thermal response of the system. Figure 3-11 shows the decay heat curve for low enriched uranium (LEU) cores. Unlike light water reactors (LWRs), the ultimate heat sink for decay heat removal in FHRs is at a temperature below the freezing point of the coolant, and overcooling transients can lead to freezing. The ANS71 standard is a decay heat curve that most likely over-predicts the actual value, and it is recommended by the NRC as a conservative approach for analysis of LWR transients. However, for FHR overcooling transients, a conservative assumption should select an under-predicting estimate of the decay heat curve. Figure 3-11 highlights the difference between the ANS71 and ANS94 standards. 2% power is reached after 14 hours according to the NRC decay heat curve, and only after 2 hours according to the updated standard. Therefore operator action to control the heat removal rate from DRACS and prevent overcooling is needed much more rapidly than predicted by the ANS71 standard.

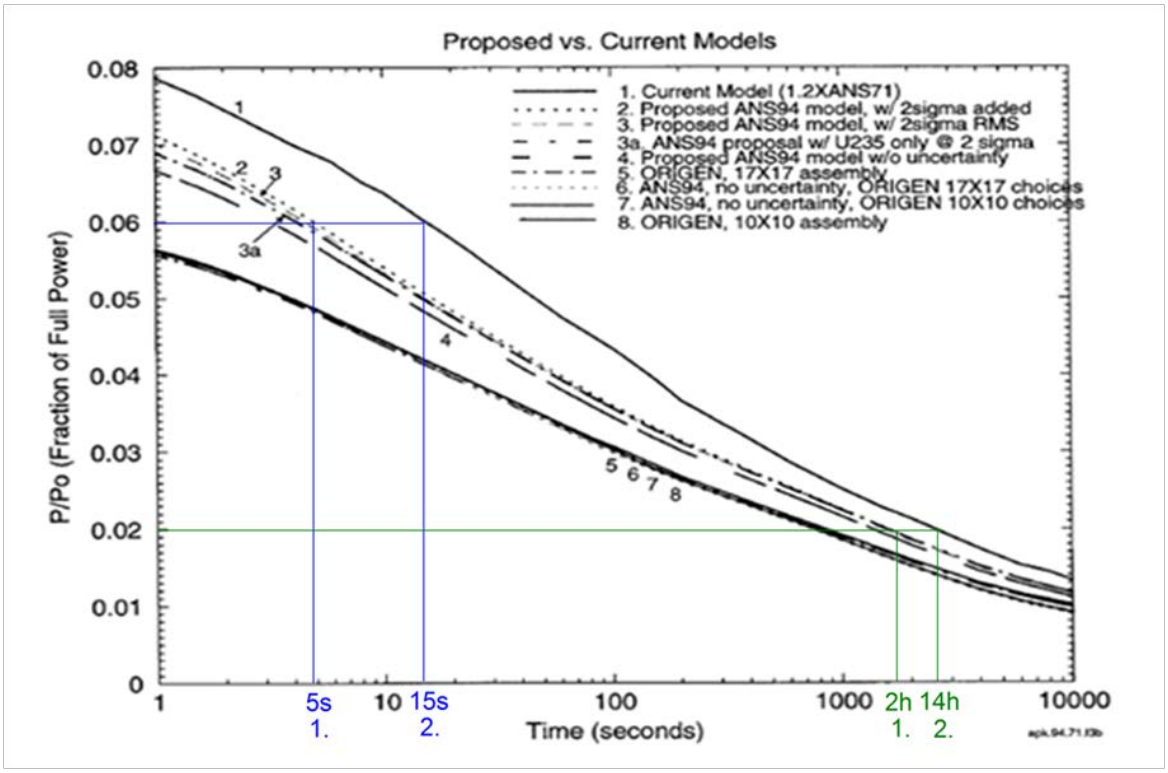

Figure 3-11. Decay heat curve for light water reactors, with moderate fuel enrichment78. "1" is based on the ANS94 standard and hasn't been accepted by the NRC. "2" is based on the ANS71 standard and is currently accepted by the NRC for licensing of LWRs.

3.7 The CIET Test Bay Natural Circulation Experiment

Steady state and transient data are presented here. For the steady state data, a comparison with analytical prediction of the results is given. While the main objective of this experiment was to provide steady state natural circulation data in support of design of DRACS, transient data preceding the steady state points was also recorded and archived. The transient data is presented without theoretical experimental predictions, and qualitative conclusions are drawn about the transient behavior of the natural circulation loop. This data will be used in the future

as an initial simple validation case for RELAP5-3D code's application to liquid fluoride salts and their simulant fluids. The transient data collected from the CIET Test Bay is plotted in Figure 3-19.

A natural circulation experimental loop with simulant fluid for the liquid salts was built, the CIET Test Bay. The fluid used was a heat transfer oil, commercially available under the name of Dowtherm A or Therminol VP. Figure 3-12 shows the equipment diagram of the CIET Test Bay. The natural circulation loop consists of a vertical annular heated section, a vertical straight pipe heat exchanger with four parallel branches, and the connected piping. The hot leg is the piping connecting the top of the heater to the top of the heat exchanger. The cold leg is the piping connecting the bottom of the heat exchanger to the bottom of the heater. Appendix G provides a description of the CIET Test Bay experimental set-up.

3.7.1 Pre-prediction plots

Before the CIET Test Bay was run, the plots in Figure 3-13 were generated to predict the expected results. In this figure Qh is the heat input to the heater, m is the natural circulation mass flow rate, calculated based on equation (3-31), Re heater is the Reynolds number in the heater, DTh is the fluid temperature rise across the heater, Th is the bulk fluid temperature in the heater and the average, inlet, and outlet temperature points are shown, DP are friction pressure losses, and Head is the friction pressure losses in mm column of oil. These calculations are based on literature correlations for the friction loss coefficients in each leg of the loop.

Mass flow rates are expected to be in the range of 0.01 and 0.04 kg/s, and the Reynolds number in the heater is expected to be in the laminar flow regime for most of the experiment's operational space, and in the transition region at high average temperature and power inputs above 5kW. The pressure drop on the heater is expected to be the dominant contribution to pressure losses in the loop, and in the range of 14-70 kPa (2-10 psi), which corresponds to head losses of 1 to 7 mm.

At higher temperatures the natural circulation heat removal is more effective, with the heater temperature rise is smaller, and the mass flow rate higher, for a given power input. Since loop operation is limited to 200°C maximum fluid temperature, we expect to be able to operate the loop up to a power of 9kW, when the average bulk fluid temperature in the heater is 150°C. Since the cooling water temperature is 10°C or slightly below, the loop can be run only up to 2kW, if the desired average bulk fluid temperature in the heater is 40°C. The average heater temperature is set by the power level and the heater inlet temperature. The heater inlet temperature can be controlled by varying the heat exchange surface area.

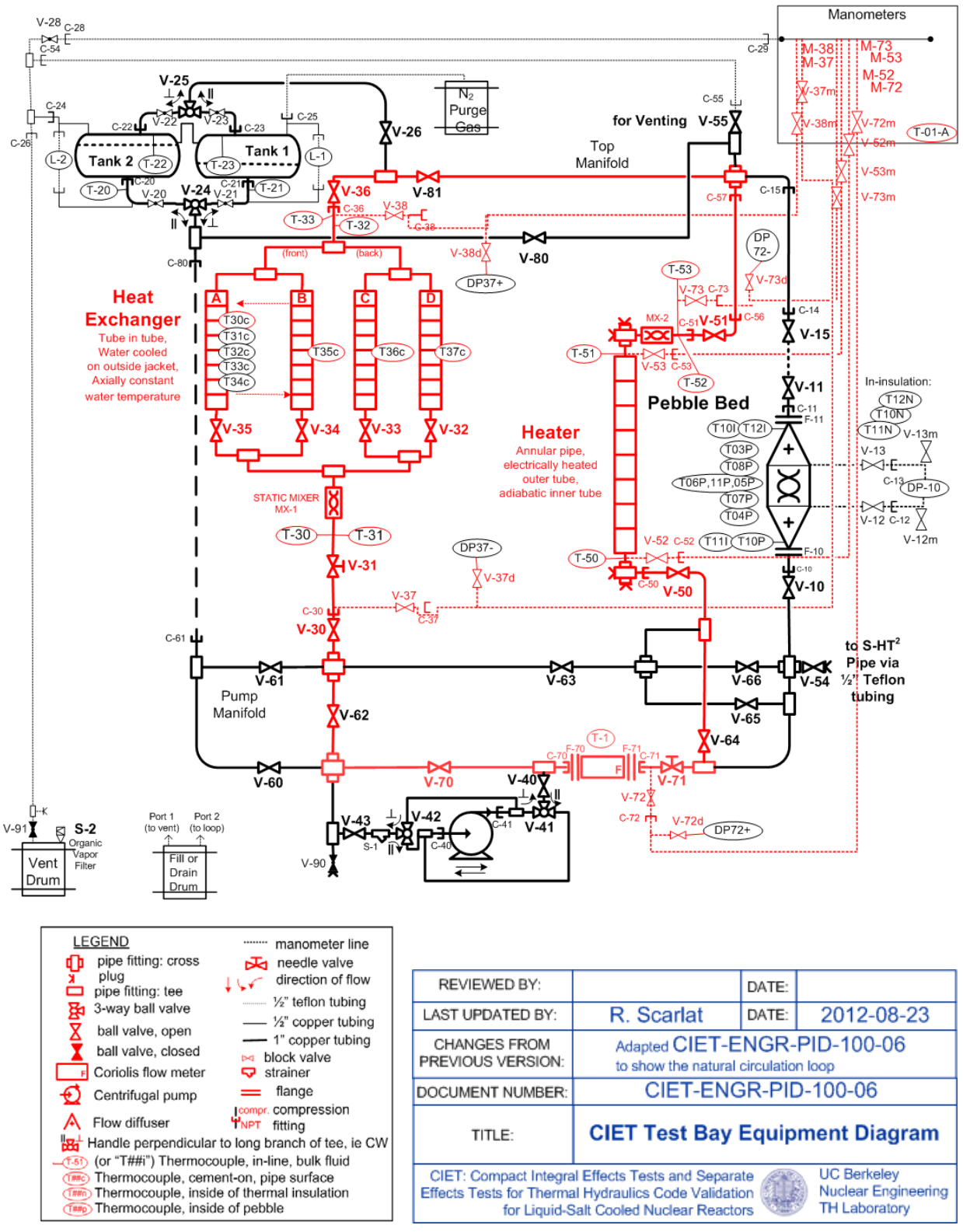

Figure 3-12. CIET Test Bay equipment diagram for the as-built. The flow path and instrumentation for the natural circulation experiment are indicated in red.

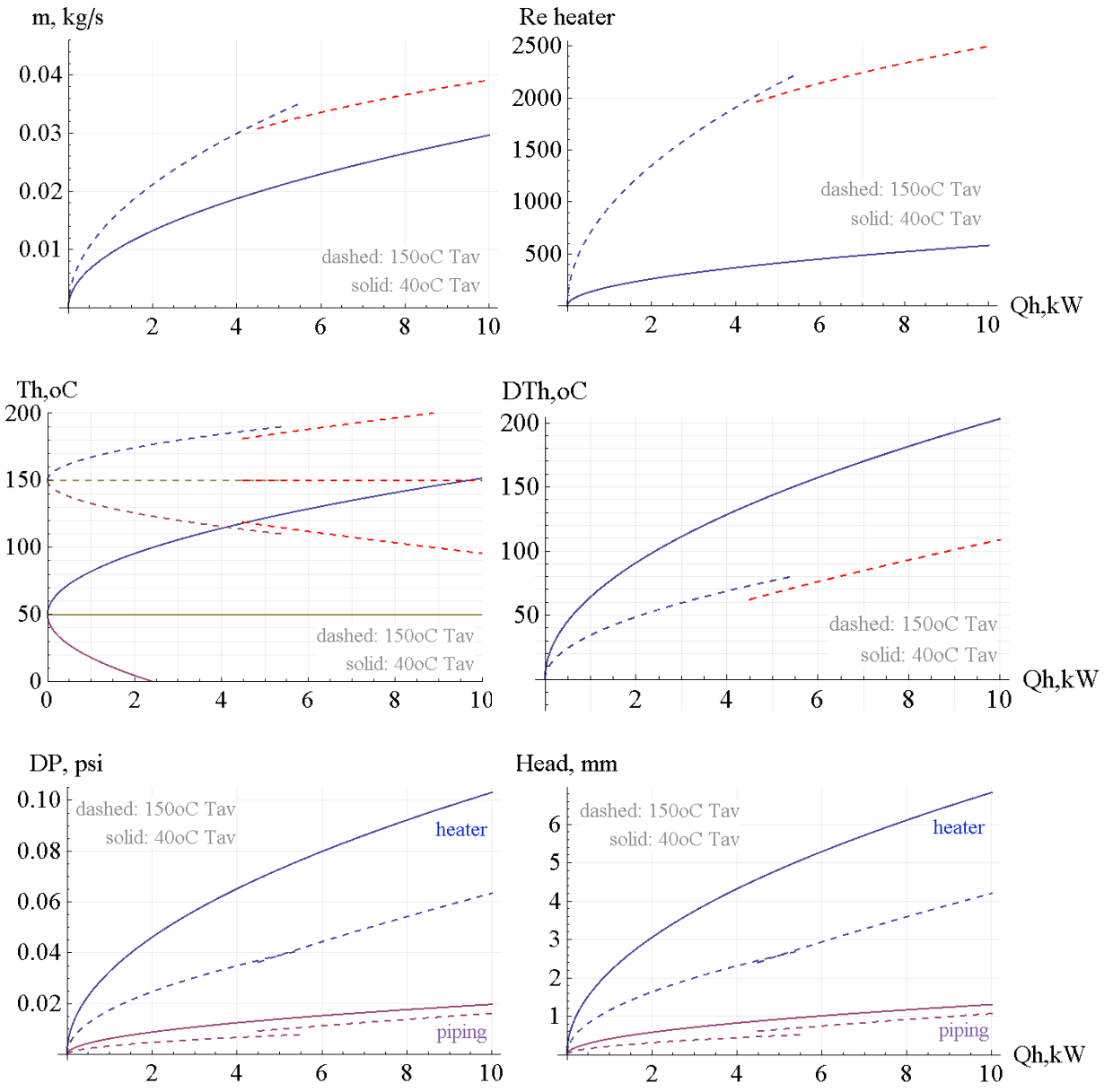

Figure 3-13. Pre-prediction for the CIET Test Bay natural circulation flow loop. Red plots use the transitional flow friction coefficient, blue plots use the laminar flow friction coefficient.

Heat losses are an important experimental parameter that can affect experimental results. The effect of heat losses for the CIET Test Bay is estimated in Figure 3-14, where dzHL is the effective loop elevation as defined by equation (3-24), dz the physical elevation of the loop as defined in equation (3-23), Qn the heat loss in each segment, and Qh the heat input to the heater. Heat losses on the hot and cold legs change the effective elevation of the loop, which is equivalent to changing the heat input to the loop, with regards to steady state natural circulation behavior. For example, reading from the plot in Figure 3-14, 20% heat losses on the

cold leg lead to a 21% reduction in the effective elevation of the loop or the effective power input (see equation (3-31)). Thus, for 10 kW power input with 2 kW heat loss on the cold leg, the steady state natural circulation parameters can be obtained from Figure 3-13 by reading the values for Qh = 7.9 kW. Similarly, 20% heat losses on the hot leg will lead to an 1% increase in the effective elevation of the loop or the effective power input. Thus, for 10 kW power input with 2 kW heat loss on the hot leg, the steady state natural circulation parameters can be obtained from Figure 3-13 by reading the values for Qh = 11 kW.

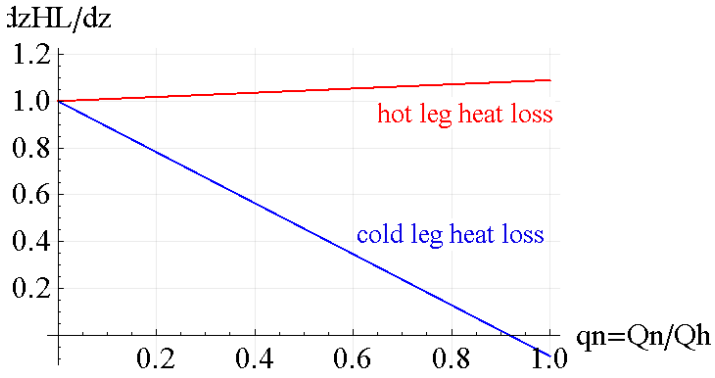

Figure 3-14. Pre-predicted effect of heat losses on the buoyancy term.

3.7.2 Pressure drop measurement for the heater element

Friction losses across the heater, the heat exchanger, and the piping in between were measured using three pairs of manometers. The heater element is the principal contributor to friction losses in the natural circulation loop. The section shows the data and the calculation for the heater element only. The rest of the manometer readings are documented in Appendix G, and they demonstrate that the heater generates the primary friction losses.

Calculations on the data are performed using equations (3-74), (3-75), (3-76). The values for the parameters that characterize the heater geometry, C_h, d_h, and A_h, are given in Appendix G. The thermophysical properties of the Dowtherm A fluid, which are given in Appendix C, are evaluated at the average temperature of the heater, which is the average of the inlet and outlet temperature measurements. The density of the fluid in the manometer lines is evaluated at the measured ambient temperature.

$$F'_h = \frac{2\rho(T_{h,av})}{m^2}\Delta P_h; f = \frac{F'_h}{C_h} \tag{3-74}$$

$$Re_h = \frac{m}{\mu(T_{h,av})}\cdot\frac{d_h}{A_h} \tag{3-75}$$

$$\Delta P_h = \rho(T_{amb})g\Delta h \tag{3-76}$$

Pressure drop measurements were taken with forced convection using the pump, with flow downwards through the heater and upwards through the heat exchanger. The loop was isothermal, with less than 1°C temperature rise across the heater, and less than 4°C between the maximum and the minimum temperatures on the loop. Data for pressure drop was collected on three days. The collected data is given in Table 3-17. The calculation for the predicted friction coefficient, $f_{h,predicted}$, assumes laminar flow.

Table 3-17. Data for friction losses in the heater element of the CIET Test Bay

#	m	ΔP_h (M73-M72)	$T_{h,av}$	$T_{ambient}$	μ_h	ρ_h	Re_h	ΔP_h	F'_h	f_h	f_h predicted
	[kg/s]	[m]	[°C]	[°C]	[Pa-s]	[kg/m3]	[--]	[Pa]	[1/m4]	[--]	[--]
1	0.0514	2.100	31.8	18.6	0.00319	1051.0	622	21,882	1.74E+10	1.14	0.10
2	0.0481	2.053	32.8	18.6	0.00308	1050.1	601	21,392	1.95E+10	1.28	0.11
3	0.0444	1.894	33.1	18.6	0.00306	1049.9	560	19,736	2.10E+10	1.38	0.11
4	0.0428	1.797	33.6	18.6	0.00301	1049.5	548	18,725	2.15E+10	1.41	0.12
5	0.0408	1.721	34.0	18.5	0.00297	1049.1	531	17,934	2.26E+10	1.48	0.12
6	0.0397	1.658	34.4	18.5	0.00293	1048.8	523	17,278	2.30E+10	1.51	0.12
7	0.0372	1.587	34.8	18.6	0.00290	1048.5	495	16,537	2.50E+10	1.64	0.13
8	0.0947	1.535	27.3	20.4	0.00375	1054.8	973	15,972	3.76E+09	0.25	0.07
9	0.1131	1.465	29.4	19.8	0.00347	1053.0	1,258	15,251	2.51E+09	0.16	0.05
10	0.1378	1.455	30.8	19.8	0.00330	1051.9	1,608	15,147	1.68E+09	0.11	0.04
11	0.1586	1.470	31.4	19.8	0.00324	1051.4	1,890	15,303	1.28E+09	0.08	0.03
12	0.1706	1.760	32.6	19.7	0.00311	1050.3	2,116	18,323	1.32E+09	0.09	0.03
13	0.1417	2.505	33.4	19.6	0.00303	1049.7	1,804	26,081	2.73E+09	0.18	0.04
14	0.1314	1.465	25.0	20	0.00412	1056.8	1,228	15,248	1.87E+09	0.12	0.05
15	0.1889	2.180	25.0	20	0.00412	1056.8	1,766	22,690	1.34E+09	0.09	0.04

C_h	[1/m^4]	1.52E+10
d_h/A_h	[1/m]	38.56

In order to minimize uncertainty, instead of calculating a correlation for the nondimensional friction coefficient, f_h, we calculate F'_h. The parameter $F'_h(Re_h)$ is an input to calculating the natural circulation steady state mass flow rate is. To obtain the nondimensionless friction coefficient, f_h, from F'_h, one must divide by the constant C_h that depends on the dimensions of the heater. Because the dimensions of the heater annulus are very small, the uncertainty for C_h is 17%. To avoid the introduction of this large uncertainty, we will work with F'_h instead of f_h.

Assuming a laminar friction coefficient, it is possible to back-calculate the dimensions of the annulus from measured pressure drop data; the results are given in Table 3-18. There is a 5% (+/- 1mm) discrepancy between the back-calculated values, and the measured dimensions of the annular heater; this is outside of the measurement uncertainty bands, which are 1% for the back-calculated value, and 2% for the measured value. Thus, there must be a systematic system error that leads to a smaller effective hydraulic diameter. These reasons could be:

- the steel tubes are not perfectly concentric
- the teflon spacers that separate the two tubes may disrupt the laminar boundary layer, and thus boundary layer development may be occurring several times along the length of

the tube; boundary layer development is associated with higher friction losses, which then necessarily appear as a smaller effective hydraulic diameter

- the annulus is physically smaller due to deposition of decomposed organic material in contact with the hot heater surface, or deposition of other debris; inspection of the heater element upon disassembly can verify this, however, given that the loop operated a total of less than ten days at high temperature, it's hard to believe that a 1mm coating could have formed in such a short time.

Note, however that d_h/A_h, which is needed for calculating Reynolds, changes only by 1% or less between the back-calculate geometry dimensions and the assumed geometry dimensions. So generating a correlation for F' versus Reynolds number, from the pressure drop measurements, is a good approach to circumventing the large uncertainty in C_h, d_h, and A_h.

Table 3-18. Dimensions of annular heater element on the CIET Test Bay

(SI units)	As measured before assembly, at room temperature	Back-calculated from pressure drop data
OD of annulus	0.01930	0.01827
ID of annulus	0.01372	0.01441
Hydraulic diameter, d_h	0.005580	0.003867
Annulus length, L_h	1.7810	1.78100
Cross-sectional area, A_h	1.447E-04	9.925E-05
d_h/A_h	38.56	38.96
C_h	1.52E+10	4.68E+10

Figure 3-15 shows the correlation for F' versus Re from data runs 8-15, and the correlation from all data. The data that was collected at lower mass flow rates (run #1-7) yields a suspiciously high friction coefficient, and a Reynolds correlation with an expectedly high exponent for the Reynolds number. At Reynolds number below 700, we expect laminar flow with a 1/Re dependence, and instead we observe a $1/Re^{2.3}$ dependence. This type of erroneous data can be caused by bubbles entrained in the flow, or gas pockets trapped in the manometer lines. The data for Reynolds below 700 was collected in one day and repeatability cannot be verified, the data in the higher Reynolds range was collected on two different days and we see an indication of good repeatability. Because at this point additional data is not available, the best option is to use the correlation based on runs 8-15, and extrapolate it in the lower Reynolds region.

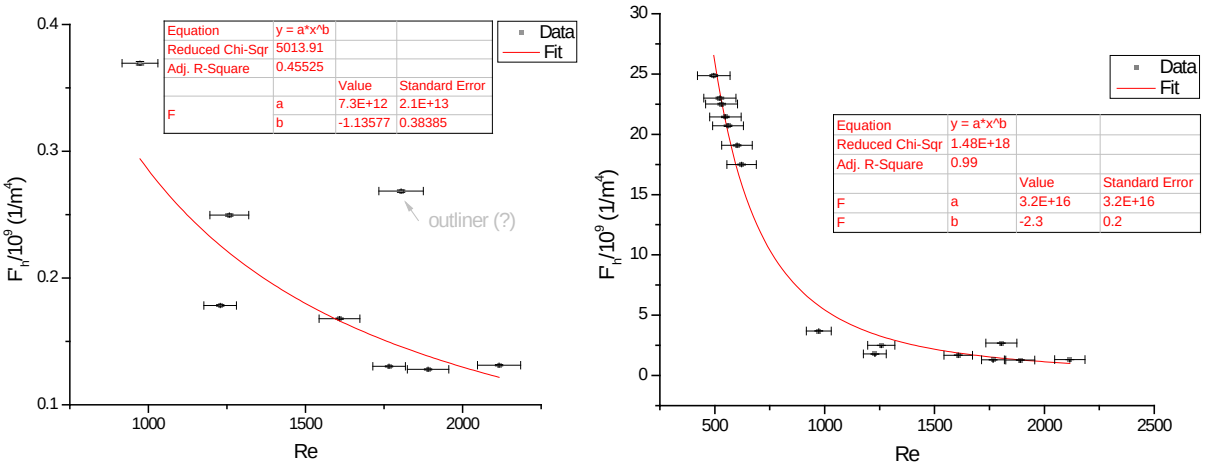

Figure 3-15. Empirical friction coefficient for the heater element of the CIET Test Bay. Correlation used, showing data runs 8-15 (left), and all collected data (right).

3.7.3 Natural circulation transients

Even though the CIET experimental natural circulation was not scaled to simulate specific transients of FHR, a few conclusions can be drawn from the transient data collected on CIET. Figure 3-16 shows the data for a natural circulation transient, as a representative example. The two key metrics that characterize natural circulation performance are mass flow rate and temperature rise across the heater.

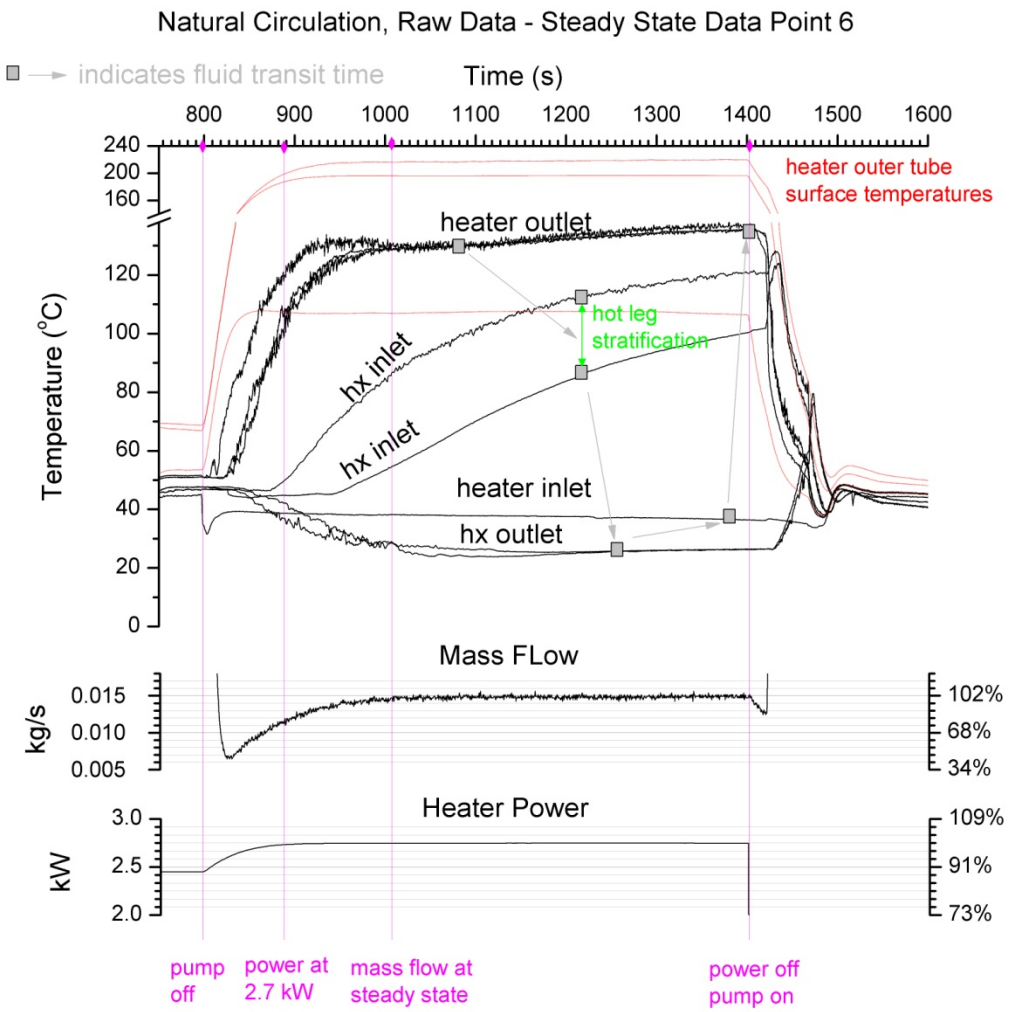

Figure 3-16. Experimental data for natural circulation transient

Mass flow rate is a directly measured parameter for natural circulation flow. From a mass flow rate point of view, the loop reaches steady state instantaneously, since the Π_2 non-dimensionless parameter for the CIET natural circulation transients is much greater than 100; for data point 6 is it 418, with the reference mass flow rate defined as the steady state natural circulation mass flow rate (see Table 3-20). This means that the response of the natural circulation loop to power fluctuations is driven by the change in temperature distribution around the loop.

The temperature rise across the heater is an important metric for the performance of heat removal systems driven by natural circulation. For the CIET Test Bay, the thermal response of the heater depends on the fluid residence time, which is 6% of the residence time in the entire loop (18 seconds for Data Point 6). If the heat input to the fluid is increased by a step change, then the temperature rise across the heater will reflect the full power only after a duration equal to the residence time of the fluid in the heater.

The thermal response of the heater also depends on the thermal inertia of the stainless steel heater element, for transients that lead to a significant change in the average temperature of the heater. The temperature of the heated outer tube is measured and it depends on the power input, the bulk fluid temperature, and the convective heat transfer coefficient. The temperature of the adiabatic inner tube reaches equilibrium with the fluid temperature at steady state.

For example, if there is a power ramp up that leads to 100°C increase in the average temperature of the heater, the power input required to raise in 100s the temperature of the outer steel tube is 1.8kW, and the inner steel tube 0.6 kW. These are not insignificant values, compared to the 2.7 kW power input to the heater. The thermal inertia of the outer stainless steel tubes will lead to a power input to the fluid that has a slower step change than the power input to the steel tube. The thermal inertia of the inner tube will act as a temporary heat sink, further slowing down the step change in the power input to the fluid. This effect will depend on the convective heat transfer coefficient between the fluid and the inner and outer tubes, and its timescale is likely dominant compared to the fluid residence time in the heater.

The heater outlet is instrumented with three in-fluid thermocouples: one immediately downstream of the heater, and one a few inches downstream. As long as there is a time-variation in the power input to the fluid (due to thermal inertia of the steel tubes, or due to change in power input to the heater), the temperatures at the two locations will read slightly different values. This is indeed what is observed in Figure 3-16.

The data shows significant temperature drop on the hot leg, and significant temperature stratification at the end of the hot leg. It also shows a temperature rise on the cold leg. This can be due to one or several of the following phenomena: thermal inertia of the piping, and mixing between flowing fluid and fluid in the static legs that branch off from the hot leg, and heat losses.

The thermal mass of the copper piping alone cannot account for the temperature drop across the hot leg. The power loss and the energy loss between the inlet and the outlet of the hot leg, as a function of time, are plotted in Figure 3-18. Heat losses alone cannot account for the temperature drop on the hot leg as long as this temperature drop, as well as the stratification at the heat exchanger inlet, continue to diminish over time, while the heater outlet temperature and the mass flowrate remain relatively constant.

The effect of static legs was investigated by installing temperature measurements on the surface of a hot leg piping. There is a point on the hot leg where two static legs connect to the hot leg, through a cross fitting. Thermocouples were installed on the exterior surface of the copper piping immediately upstream and immediately downstream of the cross (see Figure 3-17). A very large temperature drop was observed across this cross. Thermocouples were also installed on the exterior surface of the copper piping immediately downstream of the heater assembly, at the same point in the flow line, but at three different locations around the copper pipe. These measurements indicated that some vertical stratification can be detected at the outlet of the heater, despite conduction around the copper pipe, and despite some mixing in the fittings at the outlet of the heater. However, the magnitude of this stratification is much smaller compared to the temperature drop at the cross. This indicates that the static legs lead to fluid exchange between the cold fluid in the static legs and the hot fluid flowing in the hot leg. In this arrangement, the fluid exchange is aided by buoyancy; it is possible that fluid exchange with static legs also occurs in a horizontal arrangement, without the aid of buoyancy.

The energy stored in the total mass of fluid in the static legs cannot account for the observed temperature drop in the hot leg. The temperature drop across the cross persists over a long

period of time during natural circulation, and is zero during forced circulation. Neither of the static legs is insulated, so they provide a continuous source of cold fluid. A local natural convection cell likely establishes between the hot leg, and the higher elevation uninsulated static leg. If the cold fluid is 80°C below the hot fluid, then in order to maintain a 10°C temperature drop on the hot leg, the fluid exchange rate with the static leg must be 14% of the natural circulation flowrate in the loop.

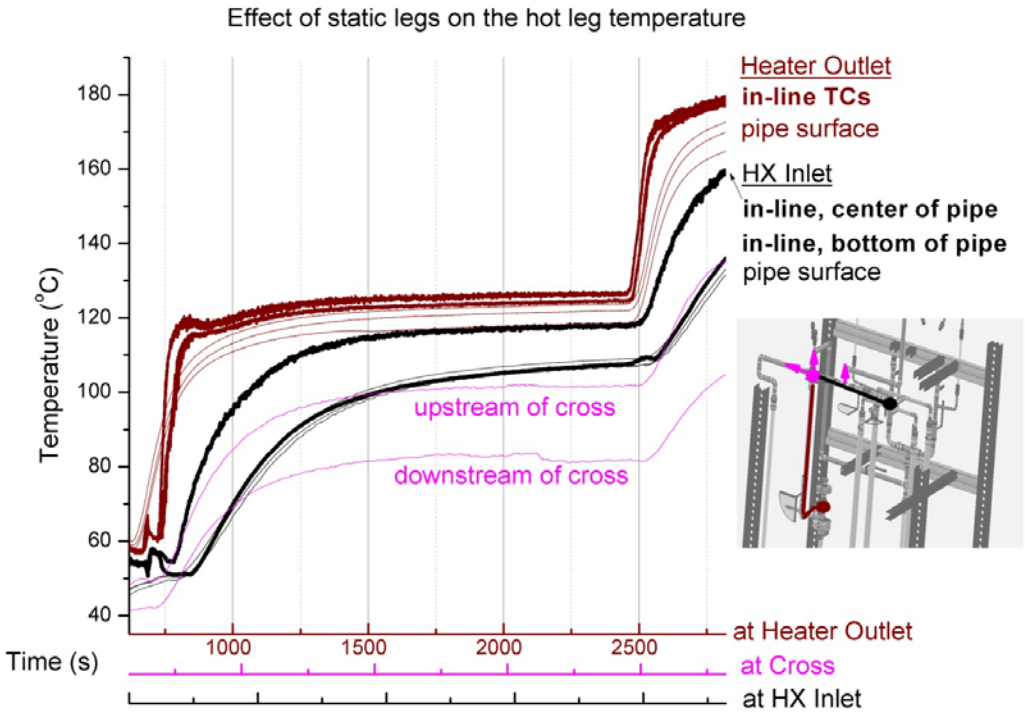

Figure 3-17. CIET Test Bay Natural Circulation Data - Effect of static legs

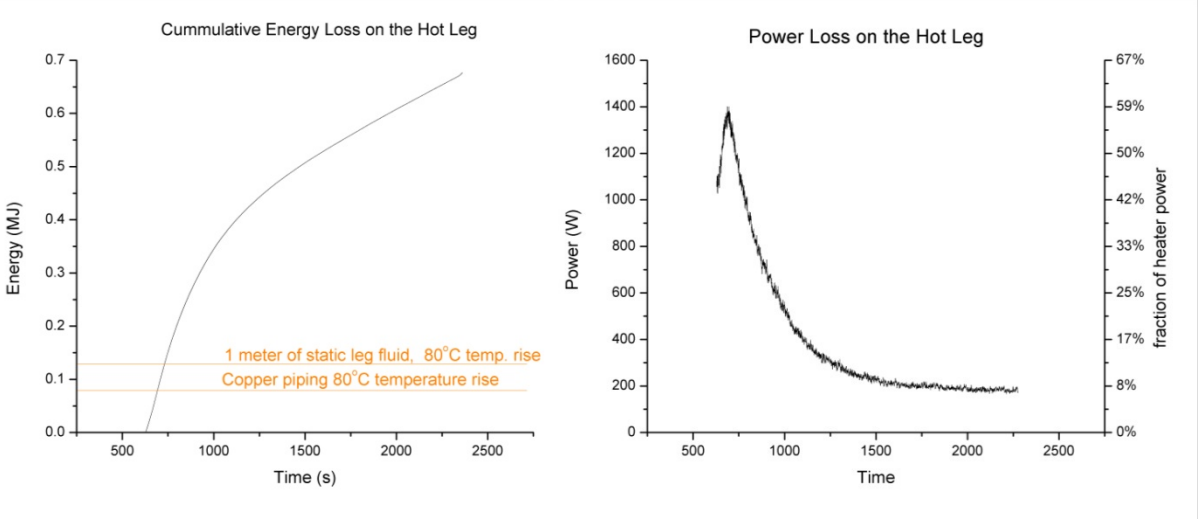

Figure 3-18. CIET Test Bay Natural Circulation Data - Effect of static legs

This transient natural circulation data provides an important data set for validation of the application of thermal-hydraulic systems codes to the modeling of heat removal by natural circulation with liquid fluoride salts and its simulant fluids. Liquid fluoride salt coolants are high Prandtl number fluids (10-20), they have a high volumetric heat capacity, which leads to very low flow rates and high fluid transit times. They also have a relatively high viscosity, which leads to very low Reynolds numbers, which, among other effects, leads to ample opportunities for local buoyancy effects to play a role in the temperature and flow distribution of the fluid. Buoyancy effects were studied in Chapter 2,, and were demonstrated to have an important effect on the temperature distribution in the core, during decay heat removal. The experimental data in this section provides another example of local buoyancy forces driving fluid exchange of the natural circulation flow loop with fluid in otherwise static legs.

Figure 3-19 plots the transient natural circulation data that can be used for validation studies. Three type of transients were run: initiation of natural circulation from isothermal conditions, upon pump shutdown, power ramp-up, and power ramp-down, while the loop operates in natural circulation. The system code should be capable of modeling fluid flow with natural circulation, with appropriate fluid residence times around the loop; it should also model thermal inertia of the piping; it should be able to simulate mass exchange with the static legs in a simplified manner, as a mass source immediately followed by a mass sink; and it should be able to simulate heat losses through the piping. Momentum inertia effects are negligible.

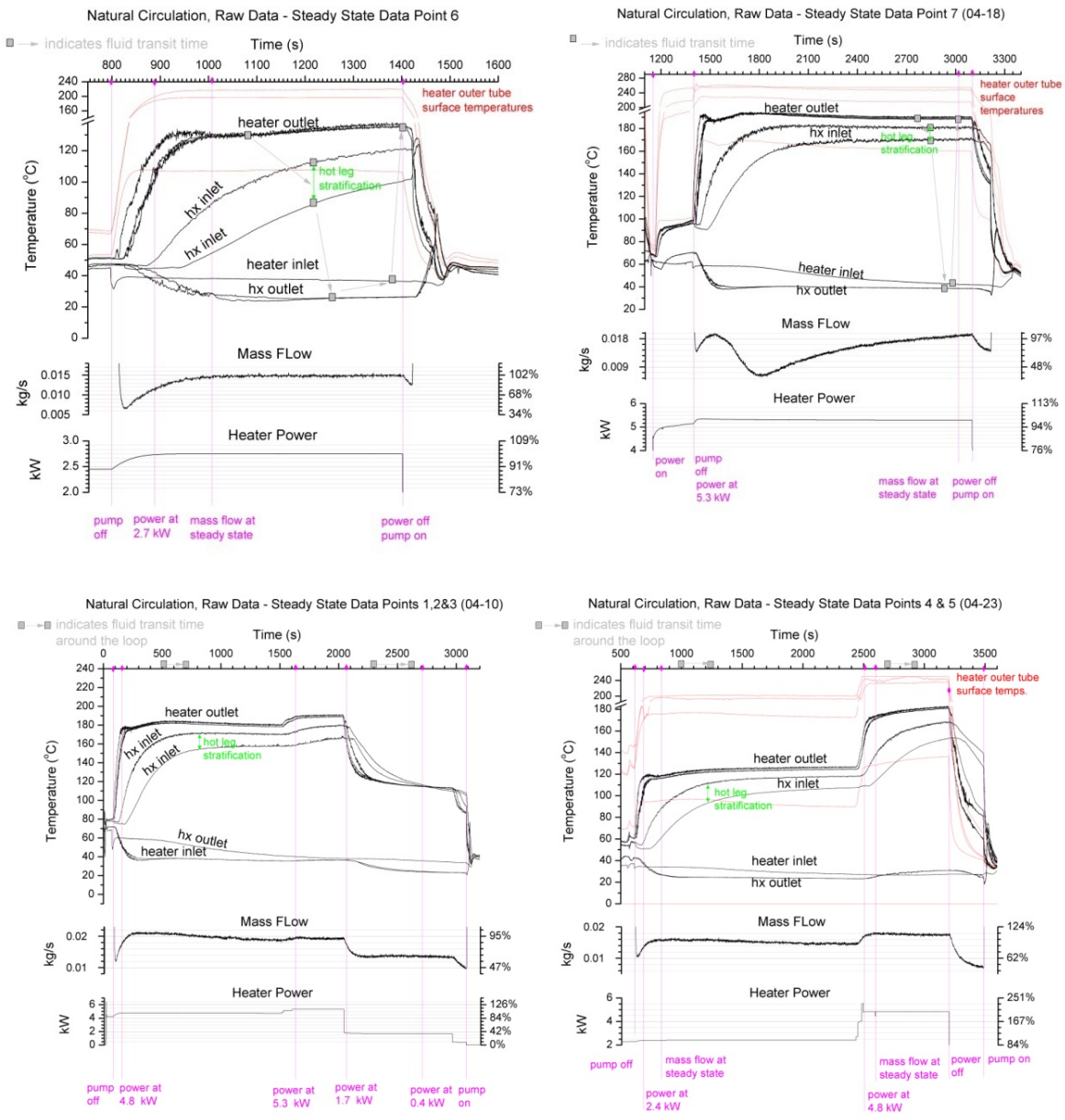

Figure 3-19. CIET Test Day Natural Circulation Transient Data

3.7.4 Steady state natural circulation results

Steady state natural circulation data is compared against natural circulation calculations based on the measured friction losses in the heater element. The effective loop elevation, Δz_{NC}, is calculated based on the measured temperatures around the natural circulation loop. Bulk fluid temperature around the natural circulation loop is measured at discrete points, and the temperature profile was assumed to be linear on each pipe segment between two adjacent temperature measurement points. The results are given in Figure 3-20. With the exception of

one data-point, the data agrees with the expected values for temperature rise across the heater, and mass flow rate.

Table 3-19. Natural Circulation Steady State Data, Raw Data

Run	Power	m	m err	$T_{h,av}$	ΔT heater	ΔT hot leg	ΔT HX	ΔT cold leg	ΔT hx inlet stratification
#	W	kg/s	%	°C	°C	°C	°C	°C	°C
1	4,725	0.0188	13%	111	138.7	-16.45	-128.15	5.9	12.5
2	5,317	0.0193	13%	114	152.5	-18.1	-136.1	1.7	13.4
3	1,707	0.0133	19%	74	79.2	-2.75	-87.55	11.1	2.3
4	2,396	0.0145	17%	77	99	-13.95	-89.05	4	10.5
5	4,821	0.0175	14%	104	154.6	-22.2	-128.9	-3.5	15.6
6	2,748	0.0147	94%	86	100.4	-25.85	-84.35	9.8	20.5
7	5,295	0.019	73%	116	148	-15	-137	4	10

Table 3-20. Natural Circulation Steady State Data, Calculated Parameters

Run #	z_{NC} (m)	Re_h	Π_2
1	1.12	867	246
2	1.09	922	229
3	1.23	398	595
4	1.12	452	515
5	1.05	757	287
6	1.20	520	440
7	1.11	921	230

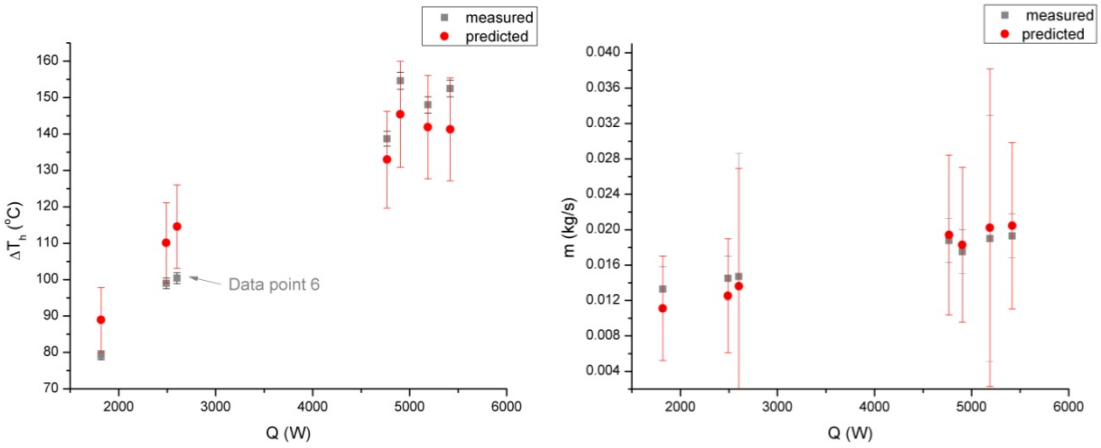

Figure 3-20. Experimental results for steady state natural circulation.

There is one data-point for which the temperature rise across the heater is lower than predicted. The reason for this discrepancy could be that the loop hadn't yet fully reached steady state. The transient that lead to this steady state data point, data point 6, was a loss of forced circulation (the pump was turned off), and the transient data is plotted in Figure 3-16. The initial condition was an almost isothermal loop with temperatures between 45 and 50°C. The transient ran for 10 minutes after initiation, and with the residence time around the loop at the measured steady state flow rate being 4.6 minutes. It is difficult to estimate the temperature at the top of the heat exchanger, because the two adjacent thermocouples at that location read temperatures that were 20°C apart, due to significant stratification in the hot leg. It is also possible that the assumption of linear temperature profile with elevation, for the hot leg, is inaccurate for this data point, which has a very high temperature drop across the hot leg. If the static legs provide cold fluid to the hot leg, the effective elevation, z_{NC}, of the natural circulation loop will increase, because the static legs connect to the hot leg at an elevation that is higher than the heat exchangers.

It is also informative to compare the results against the pre-predictions (Figure 3-21). The pre-predictions were calculated for two average heater temperatures, 40°C and 150°C. The average heater temperature for collected data was in-between these two values, and its value is shown at the top of the plot. The temperature rise was much higher than the pre-predictions, because the friction losses on the heater were much higher than expected. This discrepancy is partly a consequence of small geometric dimensions with large tolerances, which leads to high uncertainty in the flow velocity through the heater element.

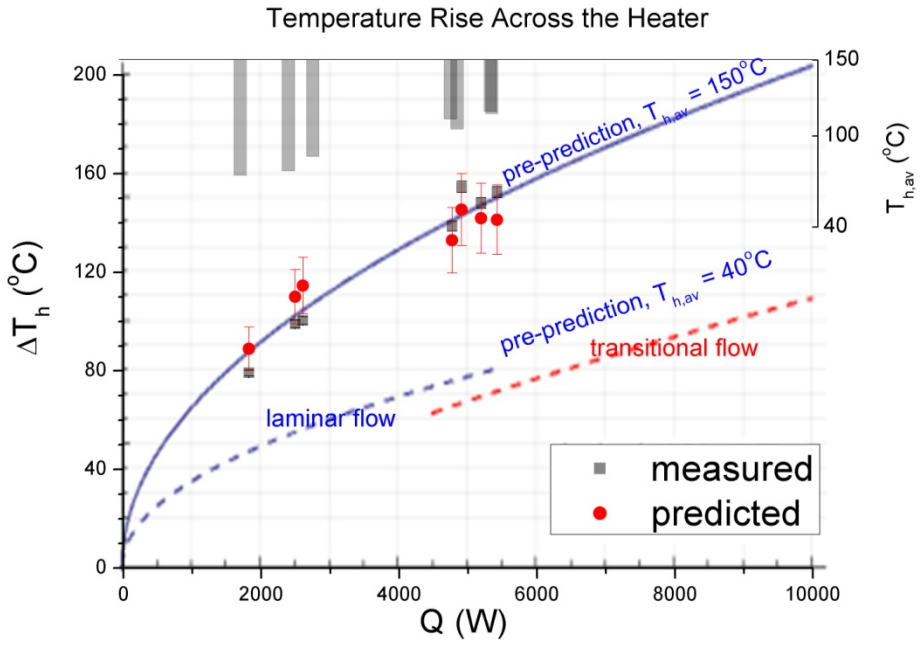

Figure 3-21. Data comparison with prediction (experimentally derived correlation for friction losses), and with pre-prediction (literature correlations for friction losses)

3.8 Conclusions

The non-dimensionalized governing equations for a one-dimensional model of a natural circulation loop, cooled by a single phase fluid, were presented here. The scaling arguments were established for a transient natural circulation loop, for loops that have long fluid residence time, and negligible contribution of fluid inertia to the momentum equation. An degree of freedom analysis shows that models with simulant fluids can be designed at any power level. The temporal decomposition of a nuclear reactor transient that relies on natural circulation decay heat removal is given as an illustrative example.

The special case of natural circulation decay heat removal from a pebble bed reactor was analyzed. A way to define the Reynolds number in a multi-dimensional pebble bed was identified. This method allows for a one-dimensional treatment of the packed bed, while preserving the integral behavior of the core from the point of view of friction losses and heat transfer coefficient. A way to replicate pebble bed friction losses by using an annular pipe and a needle valve was proposed. The scaling methodology was presented. It is a significant convenience for the design of IETs to construct a straight channel heater section, which models the behavior of a pebble bed with very little distortion.

A comparison among liquid coolants, of the performance of steady state natural circulation heat removal from a pebble bed was performed. Unlike for flow through a pipe, a constant performance metric cannot be derived for pebble bed systems; fluid comparisons must be done for the specific power level, and flow configuration of interest. For the PB-FHR core, flibe has the best performance of all the alternative fluoride salt coolants, and it has far better performance than liquid metal coolant. Compared to pressurized water, flibe has equivalent performance for axial flow through the pebble bed, and poorer performance for radial flow through the bed.

Natural circulation experimental data indicates that static legs can play a significant role in the performance of natural circulation loops. The effect of non-linear temperature profiles on the hot or cold legs or other segment of the flow loop, which may develop during transient scenarios, should be considered when modeling the performance of natural circulation loops.

The fluid thermophysical properties of liquid fluoride salts lead to design of systems with low flow velocities, and hence high fluid residence times. This, along with a high volumetric heat capacity, leads to relatively slow thermal transients of the reactor system, which is highly desirable feature for a nuclear reactor's response to an accident initiating event. Slow thermal response may also be a desirable feature if it leads to decoupling of thermal phenomena from other, more rapid phenomena, simplifying the modeling requirements of the system. The low flow velocity and the relatively high viscosity of the fluoride salts lead to low Reynolds number flows, and a low Reynolds number in conjunction with a sufficiently high coefficient of thermal expansion makes the system susceptible to local buoyancy effects. Buoyancy effects on sub-component temperature distribution and pressure drop should be investigated by phenomena characterization models. This topic was addressed in Chapter 2, for a heat generating pebble bed cooled by liquid fluoride salts.

The transient natural circulation data provided here is an important data set for validation of the application of thermal-hydraulic systems codes to the modeling of heat removal by natural circulation with liquid fluoride salts and its simulant fluids.

3.8.1 Future work

For future experimental studies, better approaches should be explored for the measurement of bulk fluid temperature, when significant stratification of the flow is expected. Heavy instrumentation of the exterior surface of piping is also recommended, in order to identify thermal stratification, when it occurs, and in order to verify the assumptions about the temperature vs. elevation profile of the loop.

System design and future experimental studies should avoid design of components with geometries that require small dimensional tolerances and lead to high uncertainties in the flow velocity, and hence to high uncertainties in the operational parameters of the system of experimental set-up. With regards to this consideration, changes in geometry due to thermal expansion, vibration, erosion, corrosion and material deposition, and other operational conditions should also be taken into account. As a negative example, a long annular heater, with high aspect ratio between the outer heater diameter and the annulus width, and high aspect ratio between length and diameter leads to high uncertainty in the flow cross-sectional area due solely to manufacturing tolerances for the heater tubes. Differential thermal expansion, and the potential tube-curving and non-concentricity lead to further distortion.

Numerical system models for transient natural circulation cooling with liquid salts should have the capability to appropriately average flow velocity through the pebble bed, and to appropriately model the fluid transit time, and the thermal inertia of the piping. Modeling of the momentum inertia can tolerate relatively larger distortions. Capability to model the effects of static legs is desirable. Capability to integrate local buoyancy effects is also desirable, and the implementation approach should be guided by separate studies for characterization of buoyancy effects at the sub-component scale. The transient natural circulation data presented here should be used as an initial validation case. For use in future validation studies, the isothermal pressure drop measurements for the heater element on the CIET Test Bay facility should be repeated at lower Reynolds number.

CHAPTER 4

Conclusions

This dissertation treated system design, modeling of transient system response, and characterization of individual phenomena, and demonstrated a framework for integration of these three activities, early in the design process of a complex engineered system. The case studies used in this dissertation were derived from the design and safety analysis of a pebble bed fluoride salt cooled high temperature nuclear reactor (PB-FHR), currently under development at the university and national laboratories level.

A system analysis framework for prioritization of experiments, modeling, and development of detailed design is proposed. Two fundamental topics in thermal-hydraulics were discussed, which illustrate the integration of modeling and experimentation with reactor design and safety analysis: thermal-hydraulic modeling of heat generating pebble bed cores, and scaled experiments for natural circulation heat removal with Boussinesq liquids.

The phenomena identification and ranking table (PIRT) is a structured methodology that relies on expert elicitation to identify and prioritize modeling capabilities and experimental facilities that are needed for design and analysis of complex systems. PIRT was developed as one of the tools in the probabilistic safety analysis of nuclear reactors, and it has applicability to any well-defined complex system. Previously, the PIRT process has been applied to reactor designs much further down on the technology development pathway (reactors in operation, or reactors for which detailed engineering design exists), and for designs where a wider base of expert knowledge exists. This chapter studied the application of the PIRT process much earlier in the design of the reactor. In the context of the PIRT methodology, new tools and approaches were proposed and demonstrated here, which are specifically relevant to technology in the early stages of development, and to analysis of passive safety features. The case study discussed here was thermal-hydraulic analysis of PB-FHR.

The well-known PASSC and H2TS system decomposition schemes were applied in a complementary manner. Definition of system functional requirements complemented identification and compilation of the current knowledge base for the behavior of the system. Two new graphical tools were developed for ranking of phenomena: phenomena ranking map, and phenomena identification matrix (PIRM). Phenomena ranking is performed for each of the fields defined by the H2TS scheme, and an important element that these new tools add is the ranking of system and subsystem coupling.

The functional requirements established through this methodology were used for the design and optimization of the core, and for the transient analysis and design of the passive natural circulation driven decay heat removal system for PB-FHR. The PIRM results guided the modeling approach for the annular pebble bed reactor core, in terms of the phenomenology included in the model, and the system-to-system coupling taken into account in the model. The phenomena ranking map guides the design of integral effects experiments for the natural circulation decay heat removal system. The thermal-hydraulic PB-FHR PIRM identified a decomposition scheme, the major components of the natural circulation loop in the primary system, and the dominant phenomena. The knowledge level raking applied to the PB-FHR

PIRM, identified convective heat transfer in pebble beds as an important phenomenon with significant knowledge gaps.

A numerical modeling approach for heat-generating porous media, with multi-dimensional fluid flow was presented. Fluid flow and pressure distribution in the core were solved for using the momentum equation for flow through a homogenous porous media. The energy equation for the fluid phase was solved separately from the energy equation for the solid phase. For the solid phase, multi-scale conduction equations were solved for; heat generating fuel particles are embedded in pebble fuel elements that are randomly packed and form a homogeneous porous medium. The application of this modeling approach to the PB-FHR annular pebble bed core cooled by fluoride salt mixtures generated a model that is called *Pod*. Model verification shows good agreement of *Pod* results with analytical calculations for simple fluid flow configurations.

Pod is primarily a design tool for reactor design optimization, and for design of experiments. It can generate high resolution temperature and flow distributions, it is flexible in terms of changing the geometry and adding features or additional phenomenology, and the solving time is relatively short. Parametric studies can be automatically set-up, for optimization studies, or sensitivity studies. *Pod* also generates important data that can be used for code-to-code comparisons for thermal-hydraulic system codes used to model the transient response of PB-FHRs.

Pod was used to generate a flow distribution in the core that optimizes core pressure drop and effective average fuel temperature in the core. This optimized core is used as a point design, and computation results are shown for full power operation, and decay heat removal operation of this core. A correlation for the pressure drop through the core, as a function of core mass flow rate, was generated for this optimized core design; this is important for the design and transient analysis of natural circulation driven decay heat removal from the pebble bed core, which is discussed in Chapter 3.

Pod was used to show the effect of buoyancy on temperature distribution in the PB-FHR core. At decay heat power levels, with non-uniform heat generation in the pebble bed, buoyancy leads to significant flow redistribution in the core, and core outlet temperature variations are only a few degrees Celsius, compared to 50°C in the absence of buoyancy. This means that the core behavior during decay heat removal is relatively insensitive to the power peaking profile in the core. This has positive implications for the design of integral effects experiments, and for the modeling of transients that require coupling of thermal-hydraulics and neutronics core responses. The effects of the temperature-dependent viscosity were shown to be similar to those of buoyancy, but much less significant. Separate effects experiments that validate these effects in het-generating porous media cooled by fluoride salt mixtures should be designed. The temperature-dependence of viscosity is expected to have a second order effects, and investigating these effects should have lower priority than investigating buoyancy effects.

The non-dimensionalized governing equations for a one-dimensional model of a natural circulation loop, cooled by a single phase fluid, were presented here. The scaling arguments were established for a transient natural circulation loop, for loops that have long fluid residence time, and negligible contribution of fluid inertia to the momentum equation. A degree of freedom analysis shows that models with simulant fluids can be designed at any power level. The temporal decomposition of a nuclear reactor transient that relies on natural circulation decay heat removal was given as an illustrative example, of the progression of an accident scenario that relies on natural circulation for decay heat removal from the nuclear reactor core.

The special case of natural circulation decay heat removal from a pebble bed reactor was analyzed. A way to define the Reynolds number in a multi-dimensional pebble bed was identified. This method allows for a one-dimensional treatment of the packed bed, while preserving the integral behavior of the core from the point of view of friction losses and heat transfer coefficient. A way to replicate pebble bed friction losses by using an annular pipe and a needle valve was proposed. The scaling methodology was presented. It is a significant convenience for the design of IETs to construct a straight channel heater section, which models the behavior of a pebble bed with very little distortion.

A comparison among liquid coolants, of the performance of steady state natural circulation heat removal from a pebble bed was performed. Unlike for flow through a pipe, a constant performance metric cannot be derived for pebble bed systems; fluid comparisons must be done for the specific power level, and flow configuration of interest. For the PB-FHR core, flibe has the best performance of all the alternative fluoride salt coolants, and it has far better performance than liquid metal coolant. Compared to pressurized water, flibe has equivalent performance for axial flow through the pebble bed, and poorer performance for radial flow through the bed.

Natural circulation experimental data indicates that static legs can play a significant role in the performance of natural circulation loops. The effect of non-linear temperature profiles on the hot or cold legs or other segment of the flow loop, which may develop during transient scenarios, should be considered when modeling the performance of natural circulation loops.

The fluid thermophysical properties of liquid fluoride salts lead to design of systems with low flow velocities, and hence high fluid residence times. This, along with a high volumetric heat capacity, leads to relatively slow thermal transients of the reactor system, which is highly desirable feature for a nuclear reactor's response to an accident initiating event. Slow thermal response may also be a desirable feature if it leads to decoupling of thermal phenomena from other, more rapid phenomena, simplifying the modeling requirements of the system. The low flow velocity and the relatively high viscosity of the fluoride salts lead to low Reynolds number flows, and a low Reynolds number in conjunction with a sufficiently high coefficient of thermal expansion makes the system susceptible to local buoyancy effects. Buoyancy effects on sub-component temperature distribution and pressure drop should be investigated by phenomena characterization models. This topic was addressed in Chapter 2, for a heat generating pebble bed cooled by liquid fluoride salts.

The transient natural circulation data provided here is an important data set for validation of the application of thermal-hydraulic systems codes to the modeling of heat removal by natural circulation with liquid fluoride salts and its simulant fluids.

4.1 Future Work

Future PIRM studies should map system coupling across multiple fields: neutronics, fluid momentum equation. As further understanding is gained about the PB-FHR system, the matrices should be updated.

Experiments are needed to investigate the applicability of the Ergun equation for friction coefficients in a pebble bed to geometries more complex than straight channels. Multi-dimensional flow in cylindrical coordinates, and non-isothermal bed conditions may significantly modify the friction loss coefficients. *Pod* can be used as a tool for design of experiments.

To demonstrate the validity of the *Pod* model describes here, experimental data should be obtained for heated multi-dimensional flow in porous media, and code-to-code benchmarking should be performed. In the future, if *Pod* will be used and developed by several users, some form of version control will have to be implemented.

Future developments for *Pod* that require relatively little effort include addition of thermal radiation heat transport, addition of dispersion effects for flow in porous media, migration for the *Mathematica* code for the fuel element conduction equation to the COMSOL model, and design of a temperature data output file that matches the mesh uses in the neutronics model. More elaborate developments for *Pod* include demonstrating capability to run transient problems, and implementing semi-permeable walls as boundary conditions for the fluid outlet faces. As features are added to *Pod*, the built-in verification calculations should be updated, and additional checks should be added, as appropriate.

For future experimental studies better approaches should be explored for the measurement of bulk fluid temperature when significant stratification of the flow is expected. Heavy instrumentation of the exterior surface of piping is also recommended, in order to identify thermal stratification, when it occurs, and in order to verify the assumptions about the temperature vs. elevation profile of the loop.

System design and future experimental studies should avoid design of components with geometries that require small dimensional tolerances and lead to high uncertainties in the flow velocity, and hence to high uncertainties in the operational parameters of the system of experimental set-up. With regards to this consideration, changes in geometry due to thermal expansion, vibration, erosion, corrosion and material deposition, and other operational conditions should also be taken into account. As a negative example, a long annular heater, with high aspect ratio between the outer heater diameter and the annulus width, and high aspect ratio between length and diameter leads to high uncertainty in the flow cross-sectional area due solely to manufacturing tolerances for the heater tubes. Differential thermal expansion, and the potential tube-curving and non-concentricity lead to further distortion.

Numerical system models for transient natural circulation cooling with liquid salts should have the capability to appropriately average flow velocity through the pebble bed, and to appropriately model the fluid transit time, and the thermal inertia of the piping. Modeling of the momentum inertia can tolerate relatively larger distortions. Capability to model the effects of static legs is desirable. Capability to integrate local buoyancy effects is also desirable, and the implementation approach should be guided by separate studies for characterization of buoyancy effects at the sub-component scale. The transient natural circulation data presented here should be used as an initial validation case.

References

1. Safety Goals for the Operations of Nuclear Power Plants; Policy Statement. (Nuclear Regulatory Commission, 1986, 10 CFR Part 50.).

2. *Defence in Depth in Nuclear Safety. A Report by the International Nuclear Safety Advisory Group.* (International Atomic Energy Agency, 1996, INSAG-10.).

3. Powers, D. The Role of Defense in Depth in a Risk-Informed Regulatory System. (Nuclear Regulatory Commission, 1999). at ‹http://www.nrc.gov/reading-rm/doc-collections/acrs/letters/1999/4621827.html›

4. *US Design Certification. Defense in Depth Approach for the Pebble Bed Modular Reactor.* (Pebble Bed Modular Reactor, 2006, 043593.).

5. Hayns, M. R. The Evolution of Probabilistic Risk Assessment in the Nuclear Industry. *Trans. IChemE* **77,** 117–142 (1999).

6. Kaplan, S. & Garrick, B. J. On The Quantitative Definition of Risk. *Risk Analysis* **1,** 11–27 (1981).

7. *NGNP Licensing Basis Event Selection White Paper.* (Idaho National Laboratory, 2010, INL/EXT-10-19521.).

8. *US Design Certification. Licensing Basis Event Selection for the Pebble Bed Modular Reactor.* (Pebble Bed Modular Reactor, 2006, 040251 Rev. 1.).

9. *Final Safety Evaluation Report Related to Certification of the AP1000 Standard Design.* (U.S. Nuclear Regulatory Commission, NUREG-1793, Initial Report.).

10. Post, R. L., Hendershot, D. C. & Kers, P. Synergistic Design Approach to Safety and Reliability Yields Great Benefits. *Chemical Engineering Progress* 60–66 (2002).

11. Zuber, N. *An integrated structure and scaling methodology for severe accident technical issue resolution. Appendix D: A Hierarchical, two-tiered scaling analysis.* (U.S. Nuclear Regulatory Commission, 1991, NUREG/CR-5809.).

12. *Best Estimate Safety Analysis for Nuclear Power Plants: Uncertainty Evaluation.* (International Atomic Energy Agency, 2008, Safety Reports Series No. 52.).

13. *Next Generation Nuclear Plant Phenomena Identification and Ranking Tables (PIRTs) Volume 1: Main Report.* (Nuclear Regulatory Commission, 2007, NUREG/CR-6944 Vol. 1, ORNL/TM-2007/147 Vol. 1.).

14. *NGNP System Requirements Manual.* (Idaho National Laboratory, 2009, INL/EXT-07-12999 Revision ID: 3.).

15. Silady, F. *US Design Certification. Safety Classification Of Structures, Systems, and Components for the Pebble Bed Modular Reactor.* (Pebble Bed Modular Reactor, 2006, Doc. 04355 Rev. 1.).

16. Caron et. al., D. *A Modular Pebble-Bed Advanced High Temperature Reactor. 2008 NE170 Senior Design Project.* (Department of Nuclear Engineering, Univeristy of California Berkeley, 2008, UCBTH-08-001.).

17. Scarlat, R. O., Laufer, M., Cisneros, A. T., Zweibaum, N. & Seifried, J. *Preliminary Fluoride Salt-Cooled High Temperature Reactor (FHR) Subsystems Definition , Functional Requirement Definition and Licensing Basis (LBE) Identification. Department of Nuclear Engineering, University of California Berkeley* (Department of Nuclear Engineering, University of California Berkeley, FHR Workshop 1 White Paper Rev. 2.).

18. Cisneros, A. T., Zweibaum, N., Laufer, M., Scarlat, R. O. & Seifried, J. *Preliminary Fluoride Salt-Cooled High Temperature Reactor (FHR) Methods and Experiments Program. Department of Nuclear Engineering, University of California Berkeley* (Department of Nuclear Engineering, University of Califonia Berkeley, FHR Workshop 2 White Paper Rev. 1.).

19. Donoghue, J. E. *et al. Preapplication Safety Evaluation Report for the Power Reactor Innovative Small Module (PRISM) Liquid-Metal Reactor.* (Nuclear Regulatory Commission, 1994, NUREG-1368 Final Report.).

20. *Next Generation Nuclear Plant Phenomena Identification and Ranking Tables (PIRTs) Volume 2: Accident and Thermal Fluids Analysis PIRTs.* (Nuclear Regulatory Commission Office of Nuclear Regulatory Research, 2007, NUREG/CR-6944 Vol. 2, ORNL/TM-2007/174 Vol. 2.).

21. Khaled, A. R. A. & Vafai, K. The role of porous media in modeling flow and heat transfer in biological tissues. *Int. J. Heat Mass Transfer* **46,** 4989–5003 (2003).

22. Al-Hamamre, Z. & Al-Zoubi, A. The use of inert porous media based reactors for hydrogen production. *International Journal of Hydrogen Energy* **35,** 1971–1986 (2010).

23. *Technical Description of the PBMR Demonstration Power Plant.* (Pebble Bed Modular Reactor, 2006, 016956 Rev. 4.).

24. Miller, C. *et al. Recommendations for Enhancing Reactor Safety in the 21st Century.The Near-Term Task Force Review of Insights from the Fukushima Dai-Ichi Accident*. (U.S. Nuclear Regulatory Commission, 2011, ML111861807.).

25. Three Mile Island Accident. Backgrounder. *U.S. Nuclear Regulatory Commission* (2009). at ‹http://www.nrc.gov/reading-rm/doc-collections/fact-sheets/3mile-isle.pdf›

26. Hasnain, S. M. Review on sustainable thermal energy storage technologies, Part I: heat storage materials and techniques. *Energy Conversion and Management* **39,** 1127–1138 (1998).

27. Hong, R., Huber, S., Lee, K. & Purcell, P. *Reactor Safety and Mechanical Design for the Annular Pebble-Bed Advanced High Temperature Reactor. 2009 NE 170 Senior Design Project.* (Nuclear Engineering Department, Univeristy of California Berkeley, 2009, UCBTH09-001.).

28. The RELAP5-3D (c) Code Development Team. *RELAP5-3D © Code Manual Volume IV: Models and Correlations.* (Idaho National Laboratory, 2005, INEEL-EXT-98-00834 Rev. 2.3.).

29. Flownex Library Manual. (Flownex Simuation Environment, 2012).

30. To, K., Lai, P.-Y. & Pak, H. Jamming of Granular Flow in a Two-Dimensional Hopper. *Physical Review Letters* **86,** 71–74 (2001).

31. Rycroft, C., Grest, G., Landry, J. & Bazant, M. Analysis of granular flow in a pebble-bed nuclear reactor. *Physical Review E* **74,** 021306 (2006).

32. Laufer, M. *Granular Dynamics in Pebble-Bed Reactor Cores.* (University of California Berkeley, dissertation, in preparation.).

33. *Thorium fuel cycle - Potential benefits and challenges.* (International Atomic Energy Agency, 2005, IAEA-TECDOC-1450.).

34. Cisneros, A. T., Greenspan, E. & Peterson, P. Use of Thorium Blankets in a Pebble Bed Advanced High Temperature Reactor. in *Proceedings of ICAPP'10* (American Nuclear Society, 2010).

35. Cisneros, A. T., Scarlat, R. O., Laufer, M. R., Greenspan, E. & Peterson, P. F. Pebble Fuel Design for the PB-FHR. in *Proceedings of ICAPP'12* (American Nuclear Society, 2012).

36. Driscoll, M. J., Downar, T. J. & E., P. E. *The Linear Reactivity Model for Nuclear Fuel Management*. (American Nuclear Society, 1990).

37. *COMSOL Multiphysics User's Guide. Version 4.3.* (COMSOL AB, 2012, CM020002.).

38. *The CFD Module User's Guide. Version 4.3.* (COMSOL AB, 2012, CM021301.).

39. Prieur du Plessis, J. Analytical Quantification of Coefficients in the Ergun Equation for Fluid Friction in a Packed Bed. *Transport in Porous Media* **16,** 189–207 (1994).

40. Ergun, S., Orning, A. A., About, M. & Article, T. Fluid Flow through Randomly Packed Columns and Fluidized Beds. *Engineering* **41,** 1179–1184 (1949).

41. Seok, Y., Sung, C., Kim, J. & Kim, D. A Semi-empirical Correlation for Pressure Drop in Packed Beds of Spherical Particles. *Transport in Porous Media* **75,** 133–149 (2008).

42. Kaviani, M. *Principles of Heat Transfer in Porous Media*. (Springer-Verlag, 1995).

43. Bejan, A. Convection in Porous Media Convection in Porous Media Third Edition.

44. Chauk, S. S. & Fan, L. in *Handbook of Heat Transfer* Chapter 13 (McGraw-Hill, 1998).

45. Cho, N. Z., Yu, H. & Kim, J. W. Two-temperature homogenized model for steady-state and transient thermal analyses of a pebble with distributed fuel particles. *Annals of Nuclear Energy* (Elsevier Ltd, 2009). at ‹http://dx.doi.org/10.1016/j.anucene.2008.11.031›

46. Wang, J., Ballinger, R. G., Maclean, H. J. & Diecker, J. T. TIMCOAT: An Integrated Fuel Performace Model for Coated Particle Fuel. in *2nd International Topical Meeting on High Temperature* (2004).

47. *Gas Turbine-Modular Helium Reactor (GT-MHR) Conceptual Design Description Report*. (General Atomics, 1996, 910720 Rev. 1.).

48. Matzer, D. & Wallace, E. PBMR moves forward with higher power and horizontal turbine. *Modern Power Systems* **25,** 11–15 (2005).

49. San Onofre Nuclear Generating Station - NRC Augmented Inspection Team Report 05000361/2012007 and 05000362/2012007. (United States Nuclear Regulatory Commission, 2012).

50. World Nuclear News. Restart plan revealed for SONGS. (2012). at ‹http://www.world-nuclear-news.org/RS-Restart_plan_revealed_for_SONGS-0812127.html›

51. *Natural circulation data and methods for advanced water cooled nuclear power plant designs. Proceedings of a Technical Committee meeting held in Vienna. Proceedings of a Technical Committee meeting held in Vienna* (International Atomic Energy Agency, 2000, IAEA-TECDOC-1281.).

52. Aksan, N. *et al. Natural circulation in water cooled nuclear power plants. Phenomena, models, and methodology for system reliability assessments. International Atomic Energy Agency* (International Atomic Energy Agency, 2005, IAEA-TECTOC-1474.).

53. *Fast Reactor Database*. (International Atomic Energy Agency, 2006, IAEA-TECDOC-1531.).

54. Jellinek, A. M. & Kerr, R. C. Magma dynamics, crystallization, and chemical differentiation of the 1959 Kilauea Iki lava lake, Hawaii, revisited. *Journal of Volcanology and Geothermal Research* **110,** 235–263 (2001).

55. Reese, C. & Solomatov, V. Fluid dynamics of local martian magma oceans. *Icarus* **184,** 102–120 (2006).

56. Marshall, J. & Plumb, R. A. *Atmosphere, Ocean, and Climate Dynamics: An Introductory Text*. (Elsevier Academic Press, 2008).

57. Lee, K. H. & Strand, R. K. Enhancement of natural ventilation in buildings using a thermal chimney. *Energy and Buildings* **41,** 615–621 (2009).

58. Allard, F. & Santamouris, M. *Natural ventilation in buildings: a design handbook*. (James & James, 1998).

59. Aksan, N. *et al. Passive Safety Systems and Natural Circulation in Water Cooled Nuclear Power Plants. International Atomic Energy Agency* (International Atomic Energy Agency, 2009, IAEA-TECDOC-1624.).

60. Siddiqui, M. A. Heat transfer and fluid flow studies in the collector tubes of a closed-loop natural circulation solar water heater. *Energy Conversion and Management* **38,** 799–812 (1997).

61. Greif, R. Natural Circulation Loops. *Journal of Heat Transfer* **110,** 1243–1257 (1988).

62. Akbarzadeh, A. & Macdonald, R. W. G. Introduction of a Passive Method for Salt Replenishment in the Operation of Solar Ponds. *Solar Energy* **29,** 71–76 (1982).

63. Zlokarnik, M. *Dimensional analysis and scale-up in chemical engineering*. (Springer-Verlag, 1991).

64. Wakao, N., Kaguei, S. & Funazkri, T. Effect of Fluid Dispersion Coefficients Particle-to-Fluid Heat Transfer Coefficients in Packed Beds. *Chemical Engineering Science* **34,** 325–336 (1979).

65. *Report of the Japanese Government to the IAEA Ministerial Conference on Nuclear Safety. The Accident at TEPCO's Fukushima Nuclear Power Stations*. (Government of Japan, Nuclear Emergency Response Headquarters, 2011).

66. Marquès, M. *et al.* Methodology for the reliability evaluation of a passive system and its integration into a Probabilistic Safety Assessment. *Nuclear Engineering and Design* **235,** 2612–2631 (2005).

67. Galvez, C. Design and Transient Analysis of Passive Safety Cooling Systems for Advanced Nuclear Reactors. (University of California, Berkeley, 2011).

68. Levy, S. *Two-Phase Flow in Complex Systems*. 28–56 (John Wiley & Sons, 1999).

69. Kaviany, M. *Principles of Heat Transfer in Porous Media*. 45–53 (Springer, 1995).

70. Vijayan, P. K. & Nayak, A. K. *Introduction to Instabilities in Natural Circulation Systems.* (IAEA Traning Course on Natural Circulation Phenomena and Passive Safety Systems in Advanced Water-Cooled Reactors, 2010).

71. Jens, W. H. in *Nuclear Engineering Handbook* (Etherington, H.) 9–90 – 9–93 (McGraw-Hill Books Company, Inc., 1958).

72. Williams, D. F., Toth, L. M. & Clarno, K. T. *Assessment of Candidate Molten Salt Coolants for the Advanced High-Temperature Reactor (AHTR)*. (Oak Ridge National Laboratory, 2006, ORNL/TM-2006/12.).

73. Reyes, J. N. *NuScale Power Meeting Introduction and Overview of NuScale Design.* (US Nuclear Regulatory Commission, ML092810329.).

74. Westinghouse Electric Co. LLC. *The Westinghouse AP1000 Advanced Nuclear Plant. Plant Description.* (Westinghouse Electric Co., LLC, 2003).

75. Boardman, C. E., Hui, M., Carroll, D. G. & Dubberley, A. E. Economic Assessment of S-PRISM Including Development and Generating Costs. in *Proceedings of the 9th International Conference on Nuclear Engineering (ICONE-9)* (European Commission CORDIS, 2001).

76. Deltrol Corp. *In-line Hydraulic and Pneumatic Valves.* (Deltrol Fluid Products, Bulletin No. 1482-16.). at ‹http://www.deltrolfluid.com/catalog/pdf/›

77. Blandford, E. D. & Peterson, P. F. A Novel Buoyantly-Driven Shutdown Rod Design for Passive Reactivity Control of the PB-AHTR. in *Proceedings of the 4th International Topical Meeting on High Temperature Reactor Technology* (ASME, 2008).

78. Pietrangelo, A. R. Petition to rule making PRM-50-74: Amend Appendix K to 10CFR Part 50 to provide a voluntary alternative which would repalce the 1971 American Nuclear Society Decay Heat Standard with the 1994 American Nuclear Society Decay Heat Standard. *Nuclear Energy Institute* Attachment 1. (Nuclear Regulatory Commission, 2001).

APPENDIX A
FHR FUNCTIONAL REQUIREMENTS

A.1 Overview of FHR Technology

PB-FHRs are thermal nuclear reactors, cooled by liquid fluoride salt eutectic mixtures. The coolant boils at very high temperatures, and does not undergo radiolytic degradation. PB-FHRs deliver heat at temperatures above 600°C. The core is a randomly packed bed of fuel pebbles. The fuel form is highly robust coated particle fuel, compacted with graphite filler in the shape of pebble fuel elements. FHRs employ a passive reactor cooling system, which relies on natural circulation for decay heat removal, to ambient air as the ultimate heat sink.

UC Berkeley is developing a pebble fuel FHR (PB-FHR). Oak Ridge National Laboratory has worked on two fixed fuel reactor concepts, AHTR and SmAHTR. The Chinese Academy of Science (CAS) is developing a pebble fuel FHR, in parallel with beginning efforts for a molten salt reactor (MSR) program. MSRs are liquid fuel reactors the use the Thorium fuel cycle; the fuel and the fission products are dissolved in the fluoride salt coolant, and the reactor can be designed to operate with an on-line reprocessing facility.

A set of four expert workshops was organized in 2012, on the topic for FHR technology development. The topics of the workshops were (1) system functional requirements definition, and licensing strategy; (2) phenomena that are unique to FHRs, and modeling codes and experimental data needs for code validation; (3) materials, components, and instrumentation; and (4) functional requirements for the FHR test reactor and the technology path forward.

A.2 FHR Functional Requirements

This section identifies the major functional requirements for FHR systems and subsystems, with a focus primarily on end-user (economics and investment protection, IP) and on meeting the FHR safety design criteria (SDCs). When necessary other stakeholders requirements are considered with respect to such issues as safeguards (SG), nonproliferation (NP) and licensing. Table A-1 provides a preliminary list of plant-level functional requirements.

Table A-1. Preliminary list of plant-level functional requirements that the FHR design should satisfy

FHR PLANT
Provide synchronized electric power to a large power grid including responding to load changes from the grid dispatcher
Provide energy at a price that is competitive with other power sources
Protect the health and safety of the public and plant workers
Provide for convenient operation and expeditious maintenance of the plant
Provide for investment protection
Provide for radioactive waste and hazardous material handling and disposal
Protect the environment
Provide for spent fuel storage
Provide for plant security
Provide features to facilitate eventual plant decommissioning

A.3 Functional requirements for the Reactor System

The primary function of the reactor system is to provide heat for the power conversion system or the process heat application. The FHR reactor system uses a pool-type configuration with a low-pressure metallic reactor vessel with penetrations only the faulted salt free surface elevation. Graphite reflector blocks ensure the internal geometry of the core, and provide neutron shielding to the reactor vessel, neutron reflection, and some moderation. The fuel system is housed inside the graphite blocks, and the coolant flow paths are provided by channels in the graphite blocks and/or the fuel assemblies. A core barrel structure surrounds the graphite blocks and guides the primary coolant flow from the IHX down an annular down-comer to the bottom of the reactor vessel. Because graphite is buoyant in the primary coolant, upper core support structures transfer the vertical loads from the reflector structures and fuel to the reactor vessel and the building structures. The upper core support structures also house additional instrumentation and equipment. The baseline primary coolant pumps are located at the top of the reactor, using cantilevered pump shaft traversing the free liquid surface and connecting to the shaft bearing assemblies and pump motor located above the upper core support structures. The key subsystems comprising the reactor system are summarized in Table A-2.

Table A-2. Reactor subsystems

REACTOR
Fuel
Primary coolant
Primary pump
Graphite structures
Core barrel & downcomer
Upper core support structures

In addition to the sub-system specific functional requirements in the subsequent sections, Table A-3 lists a generic set of functional requirements that must be considered in the design of each of the sub-sub-systems.

Table A-3. Generic functional requirements for the Reactor System

GENERIC REQUIREMENTS AND CONSIDERATIONS
Emergency preparedness
Post-event instrumentation
Instrumentation for online monitoring
Online maintenance
Maintenance and personnel access requirements
Replaceability requirements
Interface requirements

A.3.1 Functional requirements for the Fuel Subsystem

The functional requirements for the fuel subsystem pertain to the ensemble of fuel elements and their associated supporting structures, the organization of the fuel elements in the core, the detailed design of the fuel elements, the detailed design of the coated particles that form the fuel, and the specific choice of nuclear fuel. These requirements equally apply across the range of design options for the fuel, such as fixed or pebble fuel, and whatever combination of TRU, LEU and thorium fuels are selected.

The baseline coated particle fuel is comprised of a fuel kernel enclosed in concentric layers of a buffer of porous graphite, pyrolitic carbon, silicon carbide, and a final layer of pyrolitic carbon. The porous buffer layer provides volume for the fission product gases, and the silicon carbide layer is designed to withstand the thermomechanical stresses from temperature gradients, build-up of fission product gases, and other mechanical stress. Overall the silicon carbide layer is designed to retain fission products, and the design of FHRs allows for uniquely large (several hundreds of degrees Celsius) thermal margins to the failure temperature of fuel particles.

These coated fuel particles are compacted in a graphite matrix to form the desired shape of the fuel element. The fuel element may contain an outer layer of inert graphite (pebble shell or fuel plate sleeve), to protect the fuel region from erosion and to prevent generation of dust that contains fission products or fuel particles. For mechanical strength, heat transfer, or other considerations, the fuel element may also contain other inert graphite regions.

The functional requirements for the fuel are summarized in Table A-4.

(1) The main function of the FHR to produce heat economically from the nuclear fuel in the fuel system.

The fuel must sustain a fission chain reaction to generate power (i.e. maintain criticality). Pebble-bed FHRs are designed to operate at steady-state with low excess-reactivity so that reactivity can be managed by continuous fuel recirculation and refueling using high-burnup fuel as a neutron poison rather than dedicated burnable poisons. Fixed fuel FHRs design for excess-

reactivity at the beginning of cycle of each fuel loading. The excess reactivity at the BOC (and beginning of equilibrium cycle for multi-batch systems) must be manageable by burnable poisons and the reactivity control system at normal operating conditions as well as cold zero-power conditions.

(2) The requirement for economic power generation limits FHR fuel to designs that are feasible to manufacture at a commercial scale. This requirement limits the coated particle packing fractions, fuel kernel diameters and coated layer thicknesses to values fuel venders will be confident in fabricating at a commercial scale. Furthermore, a fuel quality assurance program must be developed to ensure the fuel meets the design specifications.

The enrichment levels of the fuel also effects manufacturability of the fuel. Fuel fabrication facilities must increase their criticality safety limits if they upgrade existing light water reactor enrichment facilities to enrichments above 5w% ^{235}U. It is noteworthy that the new GE laser enrichment facility will be licensed to produce uranium enriched up to 8w%.

Finally, fuel venders must qualify their fuel for use in an FHR and this qualification process and associated lead-time must be considered in design of the FHR fuel system. Because FHR fuel has lower peak temperatures that HTGR fuel during normal operation, transients and accidents, appropriate reductions in qualification processes should be sought in the licensing of fuel fabrication facilities.

(3) Preliminary economics scoping studies have identified fuel costs as one of the main concerns for the FHR reactor.

The current fuel cost models for coated particle fuel compacts predict significantly higher costs per unit mass of nuclear fuel than for LWR fuel, do not account for specific fuel design parameters and are uncertain because no large scale production capacity exists.

Hand-fabrication batch-process manufacturing and tight quality control have resulted in high fuel costs for high temperature gas reactor (HTGR) fuel. However, it is envisioned that continuous manufacturing processes can be developed as the market for particle fuel expand and it has not been determined if the tight manufacturing tolerances for the HTGR are required for FHRs.

These fuel costs may be partially offset by going to higher burnups. High burnup can be achieved by using the highest permissible enrichment fuel and moderating the neutron spectrum to optimize the balance between fission and breeding while maintaining negative coolant void reactivity feedback.

(4) The fuel system must interface with the primary coolant system so it can remove the heat generated in the fuel.

The heat that is generated in each fuel particle kernel is transferred by conduction to the surface of the fuel particle, then again through conduction to the surface of the fuel element, and convected from the fuel element surface to the coolant. In the TRISO particle, the dominant resistance to heat transfer is the buffer layer, which has a low thermal conductivity that dependent on its porosity, burn-up, radiation damage and temperature.

At the fuel element scale, the resistance to heat transfer is the function of fuel element geometry and the thermal conductivity of the fuel and the non-fuel regions. Cracks or other undesired gaps in the fuel element, such as layer delamination, would increase the thermal resistance. The thermal conductivity of the graphite will be dependent on irradiation dose and temperature. Mechanical integrity of the fuel element is important, to ensure a predictable conduction path to the surface of the fuel element.

Convective heat transfer at the fuel element surface is a function of the geometry at the surface of the fuel element, and the geometry surrounding the fuel element which affects the thermal boundary layers formed on the fuel surface. The latter is dictated by the arrangement of the fuel in the core.

(5) The fuel must also interface with the fuel loading and unloading system.

In a pebble bed FHR, this requirement dictates that the fuel must be buoyant in the primary coolant, must be subcritical when being handled outside the core, must accommodate being moved either mechanically or hydrodynamically, must enable the fuel handling system to measure its burnup non-destructively and must minimize the probability of bridging or blocking the defueling channel of the core.

In a fixed fuel FHR, this requirement dictates that the fuel assemblies interface with a refueling and shuffling machine and must be subcritical when being handled outside the core. Because the position of each fuel element is known the burnup of each fuel element can be predicted with numerical simulation, so no burnup measurement system is required.

(6) The fuel system must provide a barrier to radionuclides generated in the fuel kernel.

The key barrier to radionuclide release is the silicon carbide layer in the coated fuel particle. To maintain this fission product retention function, the coated fuel particle must stay intact. Thus, the coated layers must endure internal fission gas pressure, thermomechanical stresses from temperature gradients with radiation-degraded properties and the coated fuel particle design must protect against kernel migration (i.e. the amoeba effect).

Furthermore, the fuel element must be resilient against crushing and other mechanical that could release fuel particle debris. The fraction of fuel elements that might fail mechanically must be kept small, and the means for recovering fuel element fragments from the coolant be provided in the reactor system design.

(7) The FHR fuel system must have a stable power level and power shape under all anticipated operating states, including start-up. Negative temperature reactivity feedback mechanisms are required to maintain stable reactor operating dynamics. The Doppler broadening effect in ^{238}U provides strong negative fuel kernel temperature reactivity coefficients. The graphite in the fuel element (coated particle layers, matrix and other fuel element graphite) does not significantly contribute to the reactivity feedback, because the graphite density is not sufficiently sensitive to temperature and its moderating effect remains relatively constant with temperature change. The fuel must also be under-moderated under all operating conditions, so that the coolant void and temperature reactivity coefficients are negative.

Establishing steady state is challenging for the pebble-bed variants of FHRs because the fuel is designed for equilibrium operation with a specific distribution of burnups (and thereby reactivities) in the pebbles. However, at the beginning of life only fresh pebbles with high reactivity and no burnup are available. The core loading and start-up strategy envisioned for the PBMR entails diluting the core with inert graphite pebbles and increasing the concentration of fueled pebbles until criticality is reached**Error! Reference source not found.**. FHRs cannot employ this strategy because the fuel-to-moderator in the pebbles should remain undermoderated during core loading to maintain negative coolant void reactivity coefficients (so voiding the coolant makes the system even more undermoderated removing reactivity). Therefore, employing the PBMR strategy would involve passing through a fuel to moderator ratio with positive coolant void reactivity coefficients. Therefore it is expected that the FHR core loading process should involve starting with pebbles that contain neutron poisons (e.g., thorium or other neutron absorbers) and gradually substitute fuel pebbles, ensuring that criticality is approached from an undermoderated condition.

(8) For Anticipated Transient Without Scram (ATWS) response, the difference between the average fuel temperature and the bulk coolant temperature under power operation should be well understood, because this temperature difference is a key parameter governing ATWS response. Under beyond design basis conditions where the reactor heat sink is lost and/or forced circulation of the primary coolant is stopped *and* the reactor does not scram, the reactor undergoes a transient where the coolant and fuel reach temperatures sufficiently to shut down the fission process. Because the coolant is at a lower initial temperature than the fuel, the coolant temperature will rise, inserting negative reactivity, while as the fuel temperature drops providing positive reactivity insertion. The final equilibrium temperature reached by the coolant is important to predict, as this will determine the maximum temperatures reached by key primary loop structures including the IHX and RPV for this beyond design basis event.

(9) In addition to the end-users and the NRC, the International Atomic Energy Agency (IAEA) is a stakeholder in the FHR program with respect to safeguards and non-proliferation. Therefore, the fuel cannot pose a significant safeguards or nonproliferation risk. The uranium enrichment must remain less than 20w% ^{235}U to remain classified as low-enriched uranium. Additionally, while previous studies have concluded that the TRISO fuel form provides greater challenges to reprocessing to recover fissionable material, FHR fuel handling systems must be designed to facilitate the application of IAEA safeguards.

Table A-4. Summary of functional requirements for FHR fuel. The highlighted requirements are directly derived from top-level safety requirements.

FUEL SUBSYSTEM FUNCTIONAL REQUIREMENTS	
1. supply heat for power conversion system	*economics*
2. be feasible to manufacture	*economics*
3. minimize energy output normalized fuel cycle costs	*economics*
4. interface with primary coolant system	*economics, SDC3*
5. interface with fuel handling system	*economics*
6. provide barrier to radionuclides generated in fuel kernel	*SDC 1*
7. have stable power level and power shape under anticipated	*SDC 2, SDC 1*
8. respond gently in transients events	*IP*
9. fuel enrichment	*SG, PS*

A.3.2 Functional requirements for the Primary Coolant Subsystem

Figure A-1 provides a schematic diagram of the coolant flow paths in the core. The functional requirements for the primary coolant are summarized in Table A-5 and they are discussed below.

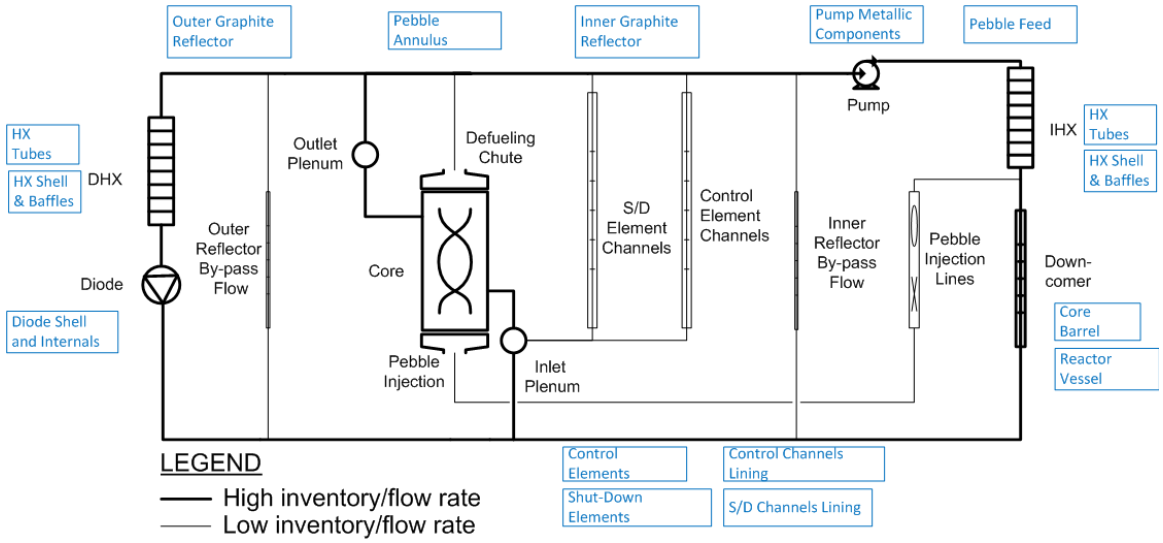

Figure A-1. Primary coolant flows and inventories, for a pebble bed FHR. The blue boxes indicate the solid constituents of the SSCs in contact with the primary coolant.

(1) The primary function of the primary coolant is to remove heat from the fuel and transfer it to the intermediate loop. This functionality corresponds to SDC 3.

To flow through the primary loop the coolant must remain the in the liquid phase in all states of the FHR including startup and DBEs. The thermal margin to its boiling point at atmospheric pressure is much higher than the thermal margin to its freezing point. Thus, overcooling transients must be protected against in FHRs.

The baseline primary coolant, flibe, intrinsically has beneficial thermal fluid properties such as high volumetric heat capacity and density temperature dependence that can establish natural circulation for effective passive heat removal.

(2) The primary coolant must interface with the primary pump and intermediate heat exchanger.

The candidate materials for the intermediate heat exchanger include Alloy N, SS 316, and Alloy 800H. The IHX must be designed in accordance ASME Section III, Division 5 code requirements, which specify allowable stresses that depend upon operating and transient temperatures, to prevent unacceptable creep deformation and damage. These limits are key topics for Workshops 2 and 3. This functionality corresponds to SDC 3.

(3) The primary coolant must interface with the fuel and fuel handling system.

The fuel and primary coolant systems are tightly coupled neutronically. Thus, to ensure stable power levels (a functional requirement for the fuel system) the coolant must have negative temperature reactivity coefficients and negative void reactivity coefficients. To ensure negative temperature feedback from the coolant, the coolant must provide neutron moderation, so when the coolant voids with increasing temperature, negative reactivity is inserted. This functionality corresponds to SDCs 2.

(4) The primary coolant must interface with the graphite reflector system.

(5) The primary coolant must interface with the core barrel and reactor vessel.

Like in the intermediate heat exchanger, the metallic components in the core barrel and reactor vessel must be designed in accordance with ASME Section III, Division 5. This functionality corresponds to SDCs 3, 4 and 5.

The primary coolant should have low corrosivity with all components it interfaces with. A primary function of the coolant chemistry, particulate and inventory control system is to maintain the chemistry of the salt can in a non-corrosive state.

Table A-5. Summary of functional requirements for FHR primary coolant. The highlighted requirements are directly derived from top-level safety requirements.

PRIMARY COOLANT FUNCTIONAL	
1. transfer heat from fuel systems to the intermediate loop	*economics, IP, SDC*
2. interface with primary pump and intermediate heat exchanger	*economics, IP, SDC*
3. interface with fuel and fuel handling systems	*economics, IP, SDC*
4. interface with graphite reflector system	*economics*
5. interface with core barrel and reactor vessel system	*economics,IP,SDC3,*

A.3.3 Functional requirements for the Primary Pump Subsystem

The primary coolant pumps are located at the top of the reactor, with the pump shaft traversing the free liquid surface and connecting to the pump motor located above the upper core structures.

(1) The primary pumps must circulate the primary coolant. The primary pumps must provide sufficient flow to maintain the design core temperature rise. The flow rate provided by the pump must be controllable, for start-up, shut-down, and reduced power operation. This requirement is associated with SDC 3.

The pump must interface with the primary coolant (2).

(4) The primary pump system must be designed with a siphon break to limit the amount of coolant removed from the primary coolant integral loop if there is a leak in the intermediate heat exchanger. This requirement is associated with SDC 4.

(5) The design of the primary pump system should protect against overload during accident transients. This involves developing control logic for the primary pump system during transients and possibly adjusting coast-down time in systems with passive shutdown rod insertion.

Table A-6. Summary of functional requirements for FHR primary coolant pumps. The highlighted requirements are directly derived from top-level safety requirements.

PRIMARY PUMP FUNCTIONAL REQUIREMENTS	
1. circulate primary coolant	*economics, SDC 3*
2. interface with coolant	*economics, SDC 3*
3. ensure anti-siphon behavior for intermediate heat exchanger leak	*IP, SDC 4*
4. maintain integrity of safety related components	*IP, SDC 3,4, and*

Mathematica code for calculating fuel temperatures for PB-FHR
Nov. 2011, R. Scarlat ;
optimization goal: minimize DT from coolant to fuel;
design goals for the pebble: C/HM = 300; density = 1700 kg/m3 (1.7 g/cc);
density depends on: r1, trisoPF, ρcore, (rk, r2);
C/HM depends on: r1, trisoPF, ρcore, (rk, r2);
optimization parameters:
for pebble DT - r1, r2
for TRISO DT - particle power (packing fraction), kernel size
uncertain parameters: k, kgr, kbuf, kk
->ranges
rk : 1.5*10^-4 to 3*10^-4 m; 4.5*10^-4 m stretch
trisoPF: 5% to 40% ; 50% stretch - note: when dk>0.5mm use max planar packing fraction
ρcore: 0.5 g/cc to 1.74 g/cc; 0.4 g/cc stretch

Picked a fuel point design, and generated Tav-Tsurf vs. qcore → implemented this in COMSOL (as part of *Pod*) for calculating average fuel temp, and for doing transients that account for graphite temp.
The parameter values shown below are for the fuel point design that was picked.

Calculations

```
(*geometry*)
r1 = 1.0 / 100; r2 = 1.3 / 100; r3 = 1.5 / 100;
V2 = π * 4 / 3 * (r2^3 - r1^3); A2 = 4 * π * r2^2;
A3 = 4 * π * r3^2; Vpebble = π * 4 / 3 * r3^3;
V1 = π * 4 / 3 * r1^3; V3 = π * 4 / 3 * (r3^3 - r2^3);
(*rT=4.3*10^-4;rk=2*10^-4;rbuf=3.2*10^-4;*)
rk = 1.5 * 10^-4; rbuf = rk + 1 * 10^-4; rT = rbuf + 3 * 0.35 * 10^-4;
ripic = rbuf + 0.35 * 10^-4; rsic = ripic + 0.35 * 10^-4; ropic = rsic + 0.35 * 10^-4;
VT = π * 4 / 3 * rT^3; Ak = 4 * π * rk^2; Vk = π * 4 / 3 * rk^3;
Vbuf = π * 4 / 3 * (rbuf^3 - rk^3); Vipic = π * 4 / 3 * (ripic^3 - rbuf^3);
Vsic = π * 4 / 3 * (rsic^3 - ripic^3); Vopic = π * 4 / 3 * (ropic^3 - rsic^3);
(*material properties*)
k = 15; kgr = k;
kfluid = 1;
kbuf = 0.5; kk = 3.7;

(* (* density calculation *)
ρcore=500;ρgr=1740;
ρk=10500;ρbuf=1000; ρpic=1870; ρsic=3200; ρmtrx=1600;
ρT=
 (ρk*Vk+ρbuf*Vbuf+ρpic*(Vipic+Vopic)+ρsic*Vsic)/(Vk+Vbuf+(Vipic+Vopic)+Vsic);
ρfuel=trisoPF*ρT+(1-trisoPF)*ρmtrx;
ρpebble=(ρcore*V1+ρfuel*V2+ρgr*V3)/(V1+V2+V3);
(* C/HM calculation *)
```

```
 trisoPF=0.11;
MWU=235*0.2+238*0.8;
mk=ρk*(Vk/VT)*trisoPF*V2;
mHM=mk*MWU/(MWU+0.5*12+2*16); (* (UC0.5O2) *)
mSi=ρk*(28/(28+12))*(Vsic/VT)*trisoPF*V2;
mT=ρT*V2*trisoPF;
mC=ρcore*V1+ρgr*V3+V2*(1-trisoPF)*ρmtrx+(mT-mk-mSi);
CHM=(mC/12)/(mHM/MWU); (* 20% enriched *) *)

(* density = 1700, ρcore=500; *)
Clear[trisoPF, ρcore]; ClearAll[trisoPF, ρcore];
ρgr = 1740;
ρk = 10 500; ρbuf = 1000; ρpic = 1870; ρsic = 3200; ρmtrx = 1600;
ρT = (ρk * Vk + ρbuf * Vbuf + ρpic * (Vipic + Vopic) + ρsic * Vsic) /
    (Vk + Vbuf + (Vipic + Vopic) + Vsic);
ρfuel = trisoPF * ρT + (1 - trisoPF) * ρmtrx;
ρpebble = (ρcore * V1 + ρfuel * V2 + ρgr * V3) / (V1 + V2 + V3);
(*thermal mass of the pebble = ρ*cp = sum(m.i*cp.i) / Vpebble*)
cp = 1725;
ρcppebble = ρcore * cp;
(* C/HM = 300,  trisoPF=0.11; *)
MWU = 235 * 0.2 + 238 * 0.8;
mk = ρk * (Vk / VT) * trisoPF * V2;
mHM = mk * MWU / (MWU + 0.5 * 12 + 2 * 16); (* (UC0.5O2) *)
mSi = ρk * (28 / (28 + 12)) * (Vsic / VT) * trisoPF * V2;
mT = ρT * V2 * trisoPF;
mC = ρcore * V1 + ρgr * V3 + V2 * (1 - trisoPF) * ρmtrx + (mT - mk - mSi);
CHM = (mC / 12) / (mHM / MWU); (* 20% enriched *)
(* goal seek trisoPF and ρcore *)
sol = Solve[{CHM == 300, ρpebble == 1700}, {trisoPF, ρcore}];
trisoPF = trisoPF /. sol[[1]];
ρcore = ρcore /. sol[[1]];

(*power*)
(*power - inputs*)
qcore = 10 * 10^6; (*W/m3, core power density*)
decay = 1; (* 1= full power, 0.06 = 6% power *)
(*power - derived values*)
q3 = decay * qcore / (0.6 * V2 / Vpebble); (* power density in fuel zone,W/m3*)
qpebble = q3 * V2; (* power per pebble *)
q3T = q3 / trisoPF; (* power density in TRISO *)
qT = q3T * VT; (* power per triso *)
q3k = qT / Vk; (* power density in kernel *)

(*convection at pebble surface*)
Ren = decay * 950; (* 30oC cone: Re = 950 *)
Pr = 17; Tfluid = 650;
Nu = 2 + 1.1 * Pr^(1 / 3) * Ren^0.6;
dp = 2 * r3;
h = Nu * kfluid / dp; DTconv = (q3 * V2 / A3) / h;
```

```
Tsurf = Tfluid + DTconv;
τ = h * (6 / dp) / ρcppebble;
Bi = h * dp / k;
(*graphite layer in pebble*)
C1gr = -q3 * V2 / A2 / kgr * r2^2;
C2gr = Tsurf + C1gr / r3 ;
Tgr[r_] = -C1gr / r + C2gr;
DT23 = Tgr[r2] - Tgr[r3];
Tavgr = NIntegrate[Tgr[r] * r, {r, r2, r3}] / NIntegrate[r, {r, r2, r3}] - Tsurf;
(*fuel layer in pebble*)
C1 = q3 / k * r1^3 / 3;
C2 = Tsurf + DT23 + q3 / k * r2^2 / 6 + C1 / r2;
T[r_] = -q3 / k * r^2 / 6 - C1 / r + C2;
DT12 = T[r1] - T[r2];
DTpebble = DT12 + DT23;
Tavfuel =
  NIntegrate[T[r] * r^2, {r, r1, r2}] / NIntegrate[r^2, {r, r1, r2}] - Tsurf;
(* TRISO buffer *)
C1buf = -q3T * VT / Ak / kbuf * rk^2;
C2buf = T[r1] + C1buf / rbuf;
Tbuf[r_] = -C1buf / r + C2buf;
DTbuf = Tbuf[rk] - Tbuf[rbuf];
DTfuel = DTbuf + DTpebble;
Tavbuf =
  NIntegrate[Tbuf[r] * r^2, {r, rk, rbuf}] / NIntegrate[r^2, {r, rk, rbuf}] - Tsurf;
(* TRISO kernel *)
C2k = Tbuf[rk] + q3k / kk * rk^2 / 6;
Tk[r_] = -q3k / kk * r^2 / 6 + C2k;
DTk = Tk[0] - Tk[rk];
DTfuel2 = DTfuel + DTk;
Tavk = NIntegrate[Tk[r] * r^2, {r, 0, rk}] / NIntegrate[r^2, {r, 0, rk}] - T[r1];
(*TRISO temperature rise, buffer+kernel *)
(* outputs *)
Grid[
 {{"Tpeakkernel-Tsurf" , "Tavkernel-Tsurf", "Tpeakkernel,oC" , "Tavkernel,oC"},
  {DTfuel2, Tavfuel + Tavk, Tk[0], Tavfuel + Tavk + Tsurf},
  {"Tcoolant", "Tsurf", "CHM", "ρpebble", ""}, { Tfluid, Tsurf, CHM, ρpebble, ""},
  {"r1,cm", "dk,um", "trisoPF", "ρcore"}, {r1 * 100,  rk * 10^6 * 2, trisoPF, ρcore},
  {"r2,cm", "qT,mW", "qpebble,W", "qcore,MW/m3"},
  { r2 * 100, qT * 1000, qpebble, qcore / 10^6}}, Frame → All]
Tavfuel + Tavk
```

RowReduce::luc : Result for RowReduce of badly conditioned matrix
$\{\{-2.42864\times10^{38}, 3.41808\times10^{42}, -9.62935\times10^{41}\}, \{2.56189\times10^{27}, 2.97079\times10^{30}, -4.54116\times10^{30}\}\}$
may contain significant numerical errors. ≫

Solve::ratnz : Solve was unable to solve the system with inexact coefficients. The answer
was obtained by solving a corresponding exact system and numericizing the result. ≫

Tpeakkernel-Tsurf	Tavkernel-Tsurf	Tpeakkernel,oC	Tavkernel,oC	
36.3494	30.6867	700.631	694.968	
Tcoolant	Tsurf	CHM	ρpebble	
650	664.281	300.	1700.	
r1,cm	dk,um	trisoPF	ρcore	
1.	300.	0.376633	1335.83	
r2,cm	qT,mW	qpebble,W	qcore,MW/m3	
1.3	23.3821	235.619	10	

30.6867

Plots

```
Pfuel = Plot[{T[r] - Tsurf}, {r, r1, r2},
   AxesOrigin → {0, 0}, Filling → Axis, FillingStyle → Orange];
Pavfuel = Plot[{Tavfuel}, {r, r1, r2}, AxesOrigin → {0, 0},
   PlotStyle → {Opacity[0.8], Thick, Purple}];
Pgr = Plot[Tgr[r] - Tsurf, {r, r2, r3}, AxesOrigin → {0, 0}, Filling → Axis];
Pcore = Plot[T[r1] - Tsurf, {r, 0, r1}, AxesOrigin → {0, 0}, Filling → Axis];
Pbuf = Plot[Tbuf[r - (r1 + r2) / 2] - Tsurf - (T[r1] - Tsurf - Tavfuel),
   {r, (r1 + r2) / 2 + rk, (r1 + r2) / 2 + rbuf}, AxesOrigin → {0, 0}, Filling → Axis,
   FillingStyle → Directive[Red, Opacity[0.6]], PlotStyle → {Opacity[1]}];
Pbufref = Plot[Tbuf[-(r - (r1 + r2) / 2)] - Tsurf - (T[r1] - Tsurf - Tavfuel),
   {r, (r1 + r2) / 2 - rbuf, (r1 + r2) / 2 - rk}, AxesOrigin → {0, 0}, Filling → Axis,
   FillingStyle → Directive[Red, Opacity[0.6]], PlotStyle → {Opacity[1]}];
Pk = Plot[Tk[r - (r1 + r2) / 2] - Tsurf - (T[r1] - Tsurf - Tavfuel),
   {r, (r1 + r2) / 2 - rk, (r1 + r2) / 2 + rk}, AxesOrigin → {0, 0}, Filling → Axis,
   FillingStyle → Directive[Red, Opacity[0.6]], PlotStyle → {Opacity[1]}];
Pavk = Plot[Tavk + Tavfuel, {r, (r1 + r2) / 2 - rbuf, (r1 + r2) / 2 + rbuf},
   AxesOrigin → {0, 0}, PlotStyle → {Opacity[0.8], Thick, Purple}];
Pcoolant = Plot[Tfluid - Tsurf, {r, 0, r3}, AxesOrigin → {0, 0},
   Filling → Axis, FillingStyle → Directive[Opacity[0.1]],
   FillingStyle → Green, PlotStyle → {Green}];
Show[ Pbuf, Pbufref, Pk, Pavk, Pcore, Pfuel, Pavfuel, Pgr, Pcoolant,
 PlotRange → {{0, r3}, {-30, DTfuel * 1.1}}, GridLines → Automatic,
 GridLinesStyle → Opacity[0.3], TicksStyle → Directive[10]]
```

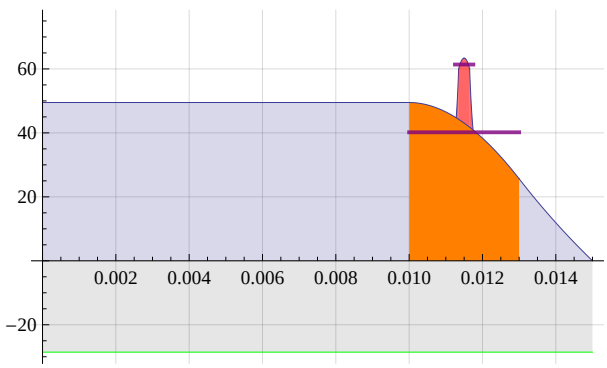

Derivations

```
(* derivation for fuel annulus
 -k*(1/r^2*d/dr*(r^2*T'[r])=q3
d(r^2*T'[r])=-q3/k*r^2*dr
r^2*d/dr*T[r]=-q3/k*r^3/3+C1
dT[r]=(-q3/k*r/3+C1/r^2)*dr
T[r]=-q3/k*r^2/6-C1/r+C2
T'[r]=-q3/k*r/3+C1/r^2
T'[r=r1]=0=-q3/k*r1/3+C1/r1^2
C1=q3/k*r1^3/3
T[r2]=Tsurf+DT23=-q3/k*r2^2/6-C1/r2+C2
                  C2=Tsurf+DT23+q3/k*r2^2/6+C1/r2 *)
```

```
(* derivation for graphite annulus
 -k*(1/r^2*d/dr*(r^2*Tgr'[r])=0
       d/dr*(r^2*Tgr'[r])=0
        r^2*Tgr'[r]=C1gr
         Tgr'[r]=C1gr/r^2
          Tgr[r]=-C1gr/r+C2gr
           -kgr*Tgr'[r2]=q3*V2/A2=-kgr*C1gr/r2^2
             C1gr=-q3*V2/A2/kgr*r2^2
              Tgr[r3]=Tsurf=-C1gr/r3+C2gr
                 C2gr=Tsurf+C1gr/r3 *)
```

```
(* derivation for TRISO buffer
 -k*(1/r^2*d/dr*(r^2*Tbuf'[r])=0
       d/dr*(r^2*Tbuf'[r])=0
        r^2*Tbuf'[r]=C1buf;
   Tbuf'[r]=C1buf/r^2;
   -kbuf*Tbuf'[rk]=q3T*VT/Ak=-kbuf*C1buf/rk^2;
   C1buf=-q3T*VT/Ak/kbuf*rk^2;
   Tbuf[r]=-C1buf/r+C2buf;
   Tbuf[rbuf]=T[r1]=-C1buf/rbuf+C2buf;
   C2buf=T[r1]+C1buf/rbuf;*)
```

```
(* derivation for TRISO kernel
 -kk*(1/r^2*d/dr*(r^2*Tk'[r])=q3k;
   d(r^2*Tk'[r])=-q3k/kk*r^2*dr;
   r^2*Tk'[r]=-q3k/kk*r^3/3+C1k;
   Tk'[r]=-q3k/kk*r/3+C1k/r^2;
   -kk*Tk'[0]=0=-kk(-q3k/kk*r/3+C1k/r^2);
   C1k=0;
   Tk'[r]=-q3k/kk*r/3;
   Tk[r]=-q3k/kk*r^2/6+C2k;
   Tk[rk]=Tbuf[rk]=-q3k/kk*rk^2/6+C2k;
   C2k=Tbuf[rk]+q3k/kk*rk^2/6;  *)
```

APPENDIX C.
Fluid Thermophysical Properties

C.1 Flibe Liquid Salt Properties

Flibe temperature dependent thermo-physical properties (temperature in K):

$$\mu = 0.116 \cdot 10^{-3} \cdot e^{3755/T}\ (kg/m \cdot s) \text{ (for T in the range of 873-1073 K) (2)}$$

$$c_p = 2415.78\ (J/kg \cdot K) \text{ (measured at 973 K) (2)}$$

$$k = \frac{k_1 + k_2}{2}\ (W/m \cdot K)$$

$$k_1 = 0.119\sqrt{T_M}\,\frac{\rho_m(T)^{0.667}}{\left(\frac{MW}{2.17}\right)^{1.167}};\ k_2 = 0.0005 \cdot T + \frac{32}{MW} - 0.34 \text{ (1)}$$

$$\rho = 2413.22 - 0.488 \cdot \mathrm{T}\ (kg/m^3) \text{ (for T in the range of 800-1080 K) (2)}$$

$$\rho_m = \frac{MW \cdot 1000}{\rho}\ (cm^3/mol\ ); \text{ MW= 33.04 g/mol for FLiBe}$$

Simplified correlations for the flibe temperature dependent thermo-physical properties in the range of 600 to 800°C (temperature in °C):

$$\mu = \frac{(4.638)10^5}{T^{2.79}}\ (kg/m \cdot s)$$

$$c_p = 2415.78\ (J/kg \cdot K)$$

$$k = 0.7662 + 0.0005 \cdot \mathrm{T}\ (W/m \cdot K)$$

$$\rho = 2279.92 - 0.488 \cdot \mathrm{T}\ (kg/m^3)$$

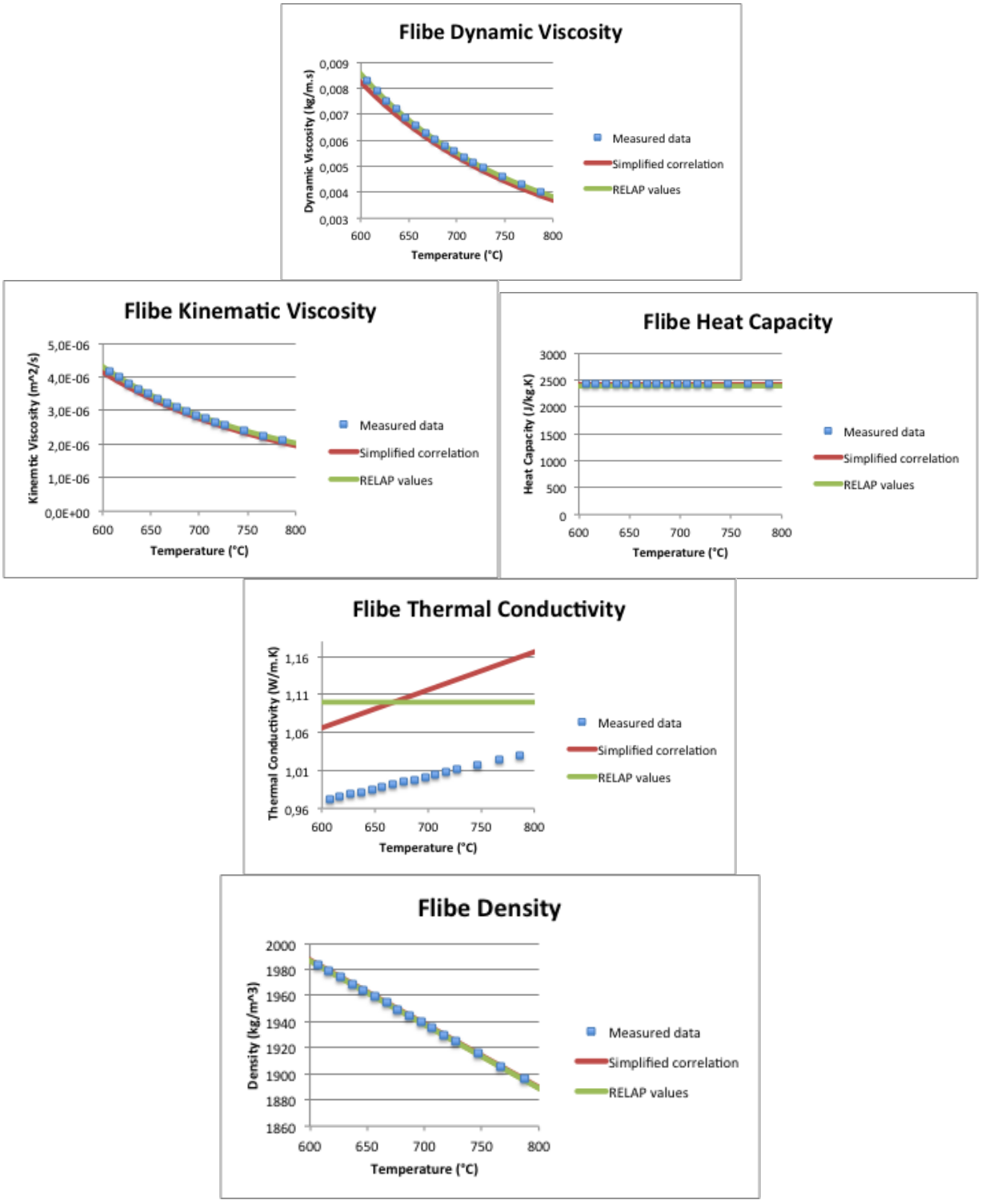

Figure C-1.Thermophysical properties of flibe

Table C-1.Variation of salt properties with temperature (based on simplified correlations)

	600°C	650°C reference	700 °C
μ, kg/ms	+25%	0.00658	-19%
k, W/mK	-2%	1.09	+2%
ρ, kg/m^3	+1%	1962.7	-1%
	600°C	**700°C reference**	**800 °C**
μ, kg/ms	+54%	0.00535	-31%
k, W/mK	-4%	1.12	+4%
ρ, kg/m^3	+3%	1938.3	-3%

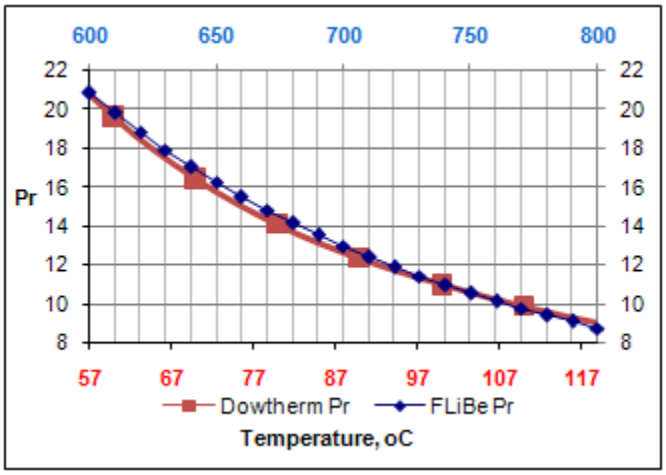

$$Pr = \frac{\nu}{\alpha} = \frac{\mu \cdot c_p}{k}$$

Figure C-2. Prandtl number matching between flibe and Dowtherm A simulant fluid, in the flibe temperature range of 600 to 800°C

C.2Dowtherm A Oil Properties

Dowtherm A temperature dependent thermo-physical properties (temperature in ^{o}C), based on data in the 20 to 180^{o}C range (3), (4):

$$\mu = \frac{0.130}{T^{1.072}} (kg/m \cdot s)$$

$$c_p = 1518 + 2.82 \cdot \mathrm{T}\ (J/kg \cdot K)$$

$$k = 0.142 - 0.00016 \cdot \mathrm{T}\ (W/m \cdot K)$$

$$\rho = 1078 - 0.85 \cdot \mathrm{T}\ (kg/m^3)$$

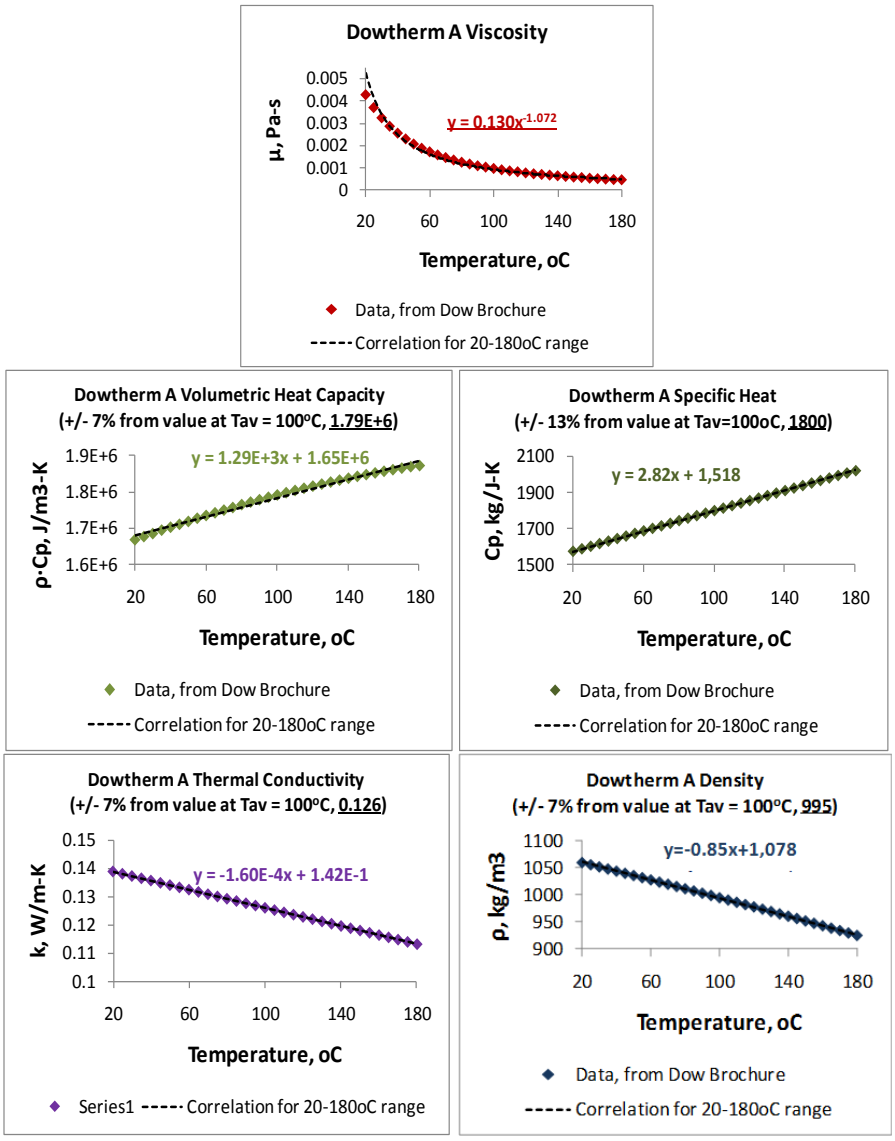

Figure C-3. Thermophysical properties of Dowtherm A oil

References

1. Williams, D. F., Toth, D. M. and Clarno, K. T. Assessment of Candidate Molten Salt Coolants for the Advanced High-Temperature Reactor (AHTR). s.l. : Oakridge National Laboratory Technical Report, March 2006. ORNL/TM-2006/12.
2. Sohal MS, Ebner MA, Sabharwall P, Shape P (INL). Engineering Database of Liquid Salt Thermophysical and Thermochemical Properties. INL/EXT-10 18297. March 2010.
3. The Dow Chemical Company. Dowtherm A Heat Transfer Fluid Product Technical Data. 1997.
4. Solutia. Therminol VP-1 Vapor Phase Liquid Phase Heat Transfer Fluid, 12ºC to 400ºC. 1998.

APPENDIX D
Fuel Conduction Equations

1. Temperature rise across the outer graphite layer of the fuel pebble.

$$\nabla^2 T = 0 \Rightarrow T(r) = \frac{C_1}{r} + C_2 \Rightarrow \Delta T_3 = T(r_3) - T(r_2) = C_1\left(\frac{1}{r_3} - \frac{1}{r_2}\right) \tag{D-1}$$

$$-k_{fuel}\nabla T(r_2) = \frac{q_{pebble}}{A_2} \Rightarrow C_1 = -\frac{q_{pebble}}{8\pi \cdot k_{gr}} \tag{D-2}$$

2. Temperature rise from the outer surface of the fuel layer to the average temperature of the fuel layer.

$$-k_{fuel}\nabla^2 T = q_3 \Rightarrow T(r) = -\frac{q_{pebble}/V_2}{6\,k_{fuel}} r^2 - \frac{C_1}{r} + C_2 \tag{D-3}$$

$$-k_{fuel}\nabla T(r_1) = 0 \Rightarrow C_1 = \frac{q_{pebble}/V_2}{k_{fuel}} \frac{r_1^3}{3} \tag{D-4}$$

$$T_{av,2} = \frac{\int_{r_1}^{r_2} T(r) r^2 dr}{\int_{r_1}^{r_2} r^2 dr}; \Delta T_{av,2} = T_{av,2} - T(r_2)$$

3. Temperature rise across the buffer layer of the TRISO particle.

$$\nabla^2 T = 0 \Rightarrow T(r) = \frac{C_1}{r} + C_2 \Rightarrow \Delta T_{buf} = T\left(r_{buf}\right) - T(r_k) = C_1\left(\frac{1}{r_{buf}} - \frac{1}{r_k}\right) \tag{D-5}$$

$$-k_{buf}\nabla T(r_k) = \frac{q_{kernel}}{A_k} \Rightarrow C_1 = -\frac{q_{kernel}}{8\pi \cdot k_{buf}} \tag{D-6}$$

Mathematica input for calculating the effective cross-sectional area, *An*, and bed length, *Ln*, for radial flow through an annular pebble bed. This leads to proper evaluation of the friction losses through the bed. Variables: r1 and r2 are ithe inner and outer radius of the pebble bed annulus, respectively; H the bed height; d the pebble diameter; μ and ρ the fluid properties.
Author: R. Scarlat; Last edit: 25 Oct. 2012.

Equations

```
ClearAll[An, un, m, μ, ρ, f2, f1, Ln, r1, r2, H, d, A, u];

r1 = 0.9; r2 = 0.9 + 1.5;
A[s_] = 2 π * (s + r1) * H;
u[s_] = m / (ρ * A[s]);
Rey[s_] = m * d / (μ * A[s]);
Ren[un_] = ρ * un * d / μ;
f[R_] = f1 / R + f2; (*Ergun correlation*)
un = m / (ρ * An);
IT = (Ln * un == Integrate[u[s], {s, 0, r2 - r1}]);
FT = (Ln * un^2 * f[Ren[un]] == Integrate[u[s]^2 * f[Rey[s]], {s, 0, r2 - r1}]);
```

Analytical Results

```
Lnav = Ln /. Solve[{IT, FT}, {Ln, An}]
```

$$\left\{\frac{4.73833\times10^{23}\,\mathrm{d}\,\mathrm{f2}\,\mathrm{m}}{3.42039\times10^{23}\,\mathrm{d}\,\mathrm{f2}\,\mathrm{m}-5.73708\times10^{8}\,\mathrm{f1}\,\mathrm{H}\,\mu}\right\}$$

```
Anav = An /. Solve[{IT, FT}, {Ln, An}]
```

$$\left\{\frac{3.03537\times10^{24}\,\mathrm{d}\,\mathrm{f2}\,\mathrm{H}\,\mathrm{m}}{3.42039\times10^{23}\,\mathrm{d}\,\mathrm{f2}\,\mathrm{m}-5.73708\times10^{8}\,\mathrm{f1}\,\mathrm{H}\,\mu}\right\}$$

Numerical Results

```
f2 = 5.25; f1 = 675;
μ = 0.00678; ρ = 1962.67;
m = 3000; H = 3;
d = 0.03;

{Lnav, Anav * 0.4}
```

```
{{1.38532}, {10.6492}}
```

Mathematica code for generating natural circulation steady state plots of loop elevation requirements, and Reynolds numbers, as functions of temperature rise.
Flow through the central core region of the 900 MWth PB-FHR pebble bed. Flow distribution will determine L and A for the core. Q is the decay heat generation in the core. 6% = 54 MW. 2% = 18 MW. Several coolants are considered. Plots labels and annotations are subsequently added in OriginPro (Mathematic exports graph as *.png file).

Author: R. Scarlat. Last updated: 22 October 2012.

```
Needs["PlotLegends`"]; ClearAll[ΔT, m]
```

Flibe Properties

```
μp[T_] = 4.638 * 10^5 / T^2.79; cpp[T_] = 2415.78; kp[T_] = 0.7662 + 0.0005 * T;
ρp[T_] = 2282 - 0.49 * T; βp[x_] = -D[ρp[x], x] / ρp[x]; To = 630;
ρ = ρp[To]; μ = μp[To]; cp = cpp[To]; k = kp[To]; β = βp[To];
```

Other Fluids Properties

water properties are at 10 MPa, and 300 oC; source: mathematica database; other fluid properties are at 630 or 700oC;
w = water, na = sodium, pb = lead, k = flinak, rb = frbzr, nz = fnazr, lz = flizr, bi=lead-bismuth eutectic

```
ρw = 715; μw = 8.65 * 10^-5; cpw = 5681; βw = 0.00317;
ρna = 805; μna = 0.000201; cpna = 951; βna = 0.000295;
ρpb = 10 255; μpb = 0.001461; cppb = 143.1; βpb = 0.000132;
ρk = 2072.3; μk = 0.004114; cpk = 1905.6; βk = 0.000352; ρrb = 3223;
μrb = 0.0051; cprb = 836.8; βrb = 0.00310; ρnz = 3034; μnz = 0.0051;
cpnz = 1171.52; βnz = 0.00029; ρlz = 3091.5; μlz = 0.0051; cplz = 983;
βlz = 0.000299; ρbi = 9875; μbi = 0.001140; cpbi = 146.51; βbi = 0.000140;
```

PB-FHR Geometry

```
d = 0.03; f1 = 675; f2 = 5.25;
A = 6.22; l = 3.0; (*axial flow*)
(*A=26.6; l=1.39; radial flow, effective values*)
Q = 54 / 6 * 10^6 {100}; g = 9.81;

m[ΔT_] = Q / (cp * ΔT);
R[ΔT_] = m[ΔT] * d / (μ * A);
Δz[ΔT_] = 1 / Q * m[ΔT]^3 * (((ρ^2 * β * g) / cp)^-1) * (1 / A^2 l / d) * (f1 / R[ΔT] + f2);
ΔP[ΔT_] = m[ΔT]^2 / (2 * ρ) * (1 / A^2 l / d) * (f1 / R[ΔT] + f2);
H[ΔT_] = ΔP[ΔT] / (ρ * g); Qpump[ΔT_] = ΔP[ΔT] * m[ΔT] / ρ;
```

$$mw[\Delta T\_] = Q / (cpw * \Delta T);\ Rw[\Delta T\_] = mw[\Delta T] * d / (\mu w * A);$$

$$\Delta zw[\Delta T\_] = 1 / Q * mw[\Delta T]^3 * \left(\left(\frac{\rho w^2 * \beta w * g}{cpw}\right)^{-1}\right) * \left(\frac{1}{A^2}\ \frac{l}{d}\right) * (f1 / Rw[\Delta T] + f2);$$

$$\Delta Pw[\Delta T\_] = mw[\Delta T]^2 / (2 * \rho w) * \left(\frac{1}{A^2}\ \frac{l}{d}\right) * (f1 / Rw[\Delta T] + f2);$$

$$Hw[\Delta T\_] = \Delta Pw[\Delta T] / (\rho w * g);\ Qpumpw[\Delta T\_] = \Delta Pw[\Delta T] * mw[\Delta T] / \rho w;$$

$$mna[\Delta T\_] = Q / (cpna * \Delta T);\ Rna[\Delta T\_] = mna[\Delta T] * d / (\mu na * A);$$

$$\Delta zna[\Delta T\_] = 1 / Q * mna[\Delta T]^3 * \left(\left(\frac{\rho na^2 * \beta na * g}{cpna}\right)^{-1}\right) * \left(\frac{1}{A^2}\ \frac{l}{d}\right) * (f1 / Rna[\Delta T] + f2);$$

$$\Delta Pna[\Delta T\_] = mna[\Delta T]^2 / (2 * \rho na) * \left(\frac{1}{A^2}\ \frac{l}{d}\right) * (f1 / Rna[\Delta T] + f2);$$

$$Hna[\Delta T\_] = \Delta Pna[\Delta T] / (\rho na * g);\ Qpumpna[\Delta T\_] = \Delta Pna[\Delta T] * mna[\Delta T] / \rho na;$$

$$mpb[\Delta T\_] = Q / (cppb * \Delta T);\ Rpb[\Delta T\_] = mpb[\Delta T] * d / (\mu pb * A);$$

$$\Delta zpb[\Delta T\_] = 1 / Q * mpb[\Delta T]^3 * \left(\left(\frac{\rho pb^2 * \beta pb * g}{cppb}\right)^{-1}\right) * \left(\frac{1}{A^2}\ \frac{l}{d}\right) * (f1 / Rpb[\Delta T] + f2);$$

$$\Delta Ppb[\Delta T\_] = mpb[\Delta T]^2 / (2 * \rho pb) * \left(\frac{1}{A^2}\ \frac{l}{d}\right) * (f1 / Rpb[\Delta T] + f2);$$

$$Hpb[\Delta T\_] = \Delta Ppb[\Delta T] / (\rho pb * g);\ Qpumppb[\Delta T\_] = \Delta Ppb[\Delta T] * mpb[\Delta T] / \rho pb;$$

$$mk[\Delta T\_] = Q / (cpk * \Delta T);\ Rk[\Delta T\_] = mk[\Delta T] * d / (\mu k * A);$$

$$\Delta zk[\Delta T\_] = 1 / Q * mk[\Delta T]^3 * \left(\left(\frac{\rho k^2 * \beta k * g}{cpk}\right)^{-1}\right) * \left(\frac{1}{A^2}\ \frac{l}{d}\right) * (f1 / Rk[\Delta T] + f2);$$

$$\Delta Pk[\Delta T\_] = mk[\Delta T]^2 / (2 * \rho k) * \left(\frac{1}{A^2}\ \frac{l}{d}\right) * (f1 / Rk[\Delta T] + f2);$$

$$Hk[\Delta T\_] = \Delta Pk[\Delta T] / (\rho k * g);\ Qpumpk[\Delta T\_] = \Delta Pk[\Delta T] * mk[\Delta T] / \rho k;$$

$$mrb[\Delta T\_] = Q / (cprb * \Delta T);\ Rrb[\Delta T\_] = mrb[\Delta T] * d / (\mu rb * A);$$

$$\Delta zrb[\Delta T\_] = 1 / Q * mrb[\Delta T]^3 * \left(\left(\frac{\rho rb^2 * \beta rb * g}{cprb}\right)^{-1}\right) * \left(\frac{1}{A^2}\ \frac{l}{d}\right) * (f1 / Rrb[\Delta T] + f2);$$

$$\Delta Prb[\Delta T\_] = mrb[\Delta T]^2 / (2 * \rho rb) * \left(\frac{1}{A^2}\ \frac{l}{d}\right) * (f1 / Rrb[\Delta T] + f2);$$

$$Hrb[\Delta T\_] = \Delta Prb[\Delta T] / (\rho rb * g);\ Qpumprb[\Delta T\_] = \Delta Prb[\Delta T] * mrb[\Delta T] / \rho rb;$$

$$mnz[\Delta T\_] = Q / (cpnz * \Delta T);\ Rnz[\Delta T\_] = mnz[\Delta T] * d / (\mu nz * A);$$

$$\Delta znz[\Delta T\_] = 1 / Q * mnz[\Delta T]^3 * \left(\left(\frac{\rho nz^2 * \beta nz * g}{cpnz}\right)^{-1}\right) * \left(\frac{1}{A^2}\ \frac{l}{d}\right) * (f1 / Rnz[\Delta T] + f2);$$

$$\Delta Pnz[\Delta T\_] = mnz[\Delta T]^2 / (2 * \rho nz) * \left(\frac{1}{A^2}\ \frac{l}{d}\right) * (f1 / Rnz[\Delta T] + f2);$$

$$Hnz[\Delta T\_] = \Delta Pnz[\Delta T] / (\rho nz * g);\ Qpumpnz[\Delta T\_] = \Delta Pnz[\Delta T] * mnz[\Delta T] / \rho nz;$$

```
mlz[ΔT_] = Q / (cplz * ΔT);
Rlz[ΔT_] = mlz[ΔT] * d / (μlz * A);
Δzlz[ΔT_] = 1 / Q * mlz[ΔT]^3 * ((ρlz^2 * βlz * g / cplz)^-1) * (1 / A^2 l / d) * (f1 / Rlz[ΔT] + f2);
ΔPlz[ΔT_] = mlz[ΔT]^2 / (2 * ρlz) * (1 / A^2 l / d) * (f1 / Rlz[ΔT] + f2);
Hlz[ΔT_] = ΔPlz[ΔT] / (ρlz * g); Qpumplz[ΔT_] = ΔPlz[ΔT] * mlz[ΔT] / ρlz;

mbi[ΔT_] = Q / (cpbi * ΔT); Rbi[ΔT_] = mbi[ΔT] * d / (μbi * A);
Δzbi[ΔT_] =
  1 / Q * mbi[ΔT]^3 * ((ρbi^2 * βbi * g / cpbi)^-1) * (1 / A^2 l / d) * (f1 / Rbi[ΔT] + f2);
ΔPbi[ΔT_] = mbi[ΔT]^2 / (2 * ρbi) * (1 / A^2 l / d) * (f1 / Rbi[ΔT] + f2);
Hbi[ΔT_] = ΔPbi[ΔT] / (ρbi * g); Qpumpbi[ΔT_] = ΔPbi[ΔT] * mbi[ΔT] / ρbi;
```

Plots

```
P1h = Plot[H[T], {T, 20, 150}, PlotStyle → Green];
P2h = Plot[Hw[T], {T, 20, 150}, PlotStyle → Blue];
P3h = Plot[Hna[T], {T, 20, 150}, PlotStyle → Red];
P4h = Plot[Hpb[T], {T, 20, 150}, PlotStyle → Red];
P5h = Plot[Hk[T], {T, 20, 150}, PlotStyle → Black];
P6h = Plot[Hrb[T], {T, 10, 150}, PlotStyle → Black];
P7h = Plot[Hnz[T], {T, 20, 150}, PlotStyle → Black];
P8h = Plot[Hlz[T], {T, 20, 150}, PlotStyle → Black];
P9h = Plot[Hbi[T], {T, 20, 150}, PlotStyle → Red];

P1p = Plot[ΔP[T], {T, 20, 150}, PlotStyle → Green];
P2p = Plot[ΔPw[T], {T, 20, 150}, PlotStyle → Blue];
P3p = Plot[ΔPna[T], {T, 20, 150}, PlotStyle → Red];
P4p = Plot[ΔPpb[T], {T, 20, 150}, PlotStyle → Red];
P5p = Plot[ΔPk[T], {T, 20, 150}, PlotStyle → Black];
P6p = Plot[ΔPrb[T], {T, 10, 150}, PlotStyle → Black];
P7p = Plot[ΔPnz[T], {T, 20, 150}, PlotStyle → Black];
P8p = Plot[ΔPlz[T], {T, 20, 150}, PlotStyle → Black];
P9p = Plot[ΔPbi[T], {T, 20, 150}, PlotStyle → Red];

P1q = Plot[Qpump[T] / (900 * 10^6 / 100), {T, 20, 150}, PlotStyle → Green];
(*pumping power in percentage of full power*)
P2q = Plot[Qpumpw[T] / (900 * 10^6 / 100), {T, 20, 150}, PlotStyle → Blue];
P3q = Plot[Qpumpna[T] / (900 * 10^6 / 100), {T, 20, 150}, PlotStyle → Red];
P4q = Plot[Qpumppb[T] / (900 * 10^6 / 100), {T, 20, 150}, PlotStyle → Red];
P5q = Plot[Qpumpk[T] / (900 * 10^6 / 100), {T, 20, 150}, PlotStyle → Black];
P6q = Plot[Qpumprb[T] / (900 * 10^6 / 100), {T, 10, 150}, PlotStyle → Orange];
P7q = Plot[Qpumpnz[T] / (900 * 10^6 / 100), {T, 20, 150}, PlotStyle → Black];
P8q = Plot[Qpumplz[T] / (900 * 10^6 / 100), {T, 20, 150}, PlotStyle → Black];
P9q = Plot[Qpumpbi[T] / (900 * 10^6 / 100), {T, 20, 150}, PlotStyle → Red];
Sh = Show[{P1h, P2h, P3h, P4h, P5h, P6h, P7h, P8h, P9h}, GridLines → Automatic,
    GridLinesStyle → Directive[Opacity[0.2]], AxesStyle → Directive[20],
    PlotRange → {{30, 150}, {0, 0.5}} , AxesOrigin → {30, 0}];
Sp = Show[{P1p, P2p, P3p, P4p, P5p, P6p, P7p, P8p, P9p}, GridLines → Automatic,
    GridLinesStyle → Directive[Opacity[0.2]], AxesStyle → Directive[20] ];
Sq = Show[{P1q, P2q, P3q, P4q, P5q, P6q, P7q, P8q, P9q},
  GridLines → Automatic, GridLinesStyle → Directive[Opacity[0.2]],
  AxesStyle → Directive[20] , PlotRange → {{10, 150}, {0, 2}}]
```

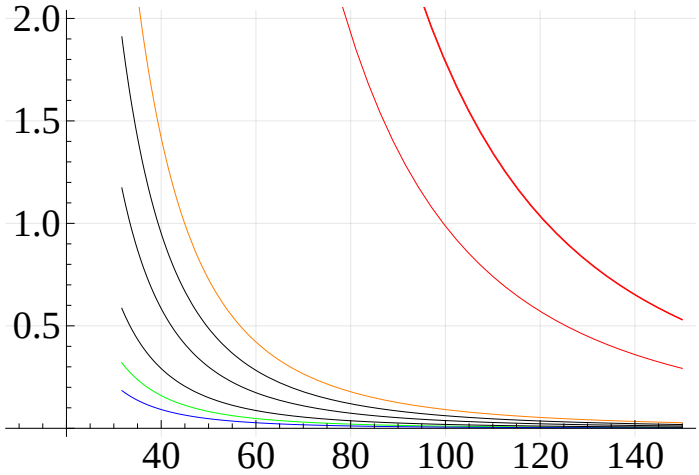
2.0
1.5
1.0
0.5
40
60
80
100
120
140

```
Tmax = 150;
P1 = Plot[{Δz[ΔT]}, {ΔT, 1, Tmax}, PlotStyle → {Green}];
P2 = Plot[{Δzw[ΔT]}, {ΔT, 1, Tmax}, PlotStyle → {Blue}];
P3 = Plot[{Δzna[ΔT]}, {ΔT, 1, Tmax}, PlotStyle → { Red}];
P4 = Plot[{Δzpb[ΔT]}, {ΔT, 1, Tmax}, PlotStyle → {Red}];
P5 = Plot[{Δzk[ΔT]}, {ΔT, 1, Tmax}, PlotStyle → {Black}];
P6 = Plot[{Δzrb[ΔT]}, {ΔT, 1, Tmax}, PlotStyle → {Black}];
P7 = Plot[{Δznz[ΔT]}, {ΔT, 1, Tmax}, PlotStyle → {Black}];
P8 = Plot[{Δzlz[ΔT]}, {ΔT, 1, Tmax}, PlotStyle → {Black}];
P9 = Plot[{Δzbi[ΔT]}, {ΔT, 1, Tmax}, PlotStyle → { Red}];
Show[{P1, P2, P3, P4, P5, P6, P7, P8, P9}, GridLines → Automatic,
  GridLinesStyle → Directive[Opacity[0.2]], PlotRange → {{10, 150}, {0, 10}},
  AxesStyle → Directive[20], AxesOrigin → {10, 0}];
Show[{P1, P6}, GridLines → Automatic, GridLinesStyle → Directive[Opacity[0.2]],
 PlotRange → {{10, 150}, {0, 7}}, AxesStyle → Directive[20], AxesOrigin → {10, 0}]
```

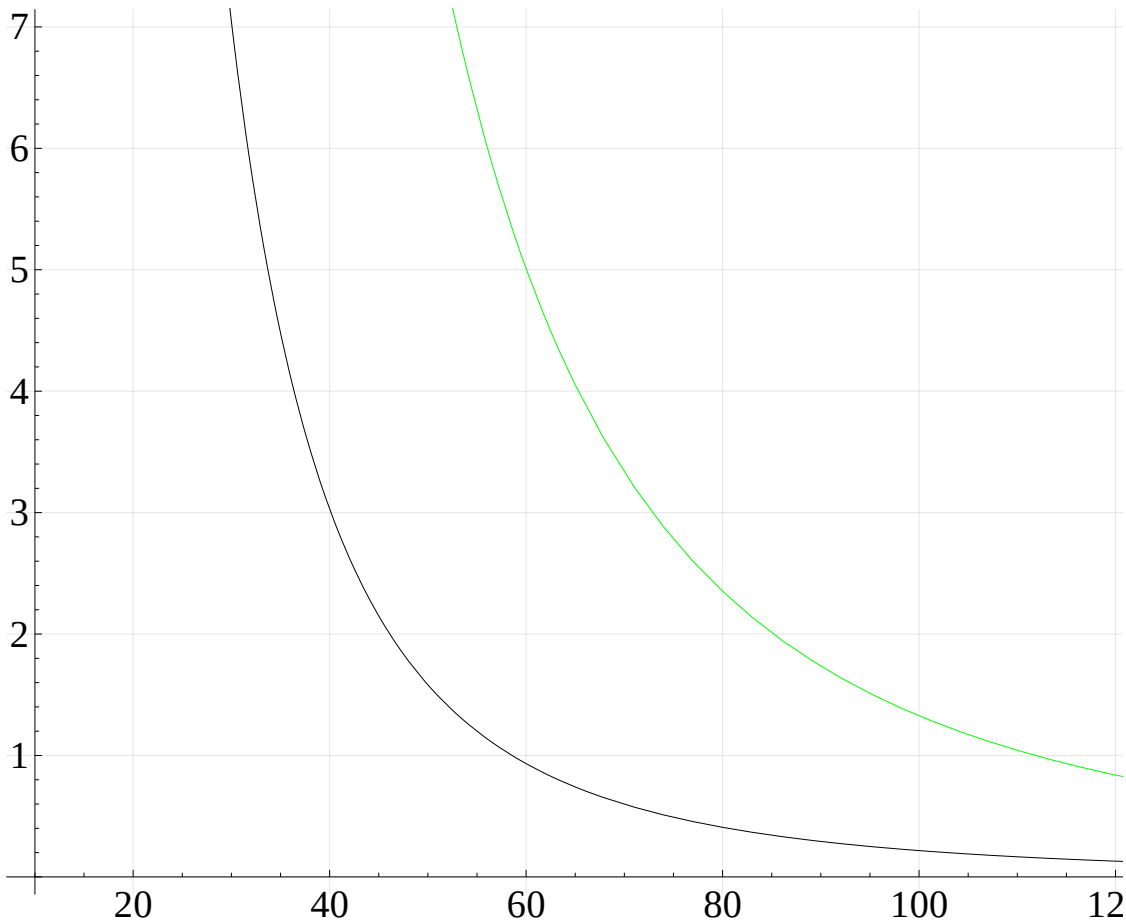

```
P1r = Plot[R[T], {T, 20, 150}, PlotStyle → Green];
P2r = Plot[Rw[T], {T, 20, 150}, PlotStyle → Blue];
P3r = Plot[Rna[T], {T, 20, 150}, PlotStyle → Red];
P4r = Plot[Rpb[T], {T, 20, 150}, PlotStyle → Red];
P5r = Plot[Rk[T], {T, 20, 150}, PlotStyle → Black];
P6r = Plot[Rrb[T], {T, 10, 150}, PlotStyle → Black];
P7r = Plot[Rnz[T], {T, 20, 150}, PlotStyle → Black];
P8r = Plot[Rlz[T], {T, 20, 150}, PlotStyle → Black];
P9r = Plot[Rbi[T], {T, 20, 150}, PlotStyle → Red];

Show[{P1r, P2r, P3r, P4r, P9r}, GridLines → Automatic,
 GridLinesStyle → Directive[Opacity[0.2]], AxesStyle → Directive[20],
 PlotRange → {{20, 150}, {0, 15 000}}, AxesOrigin → {20, 0} ]
```

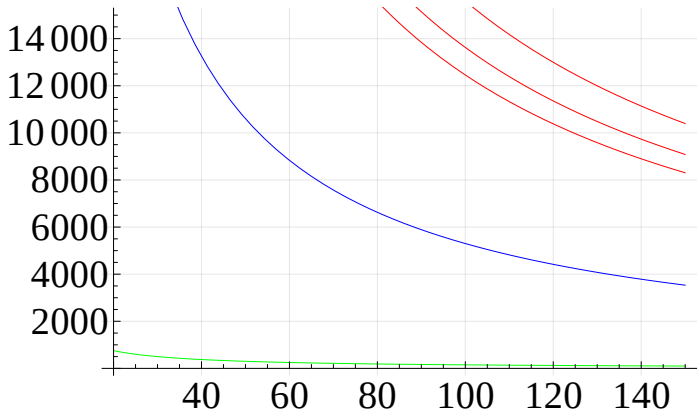

APPENDIX G
CIET Test Bay - Natural Circulation Experiment

Natural circulation data was collected on the CIET Test Bay. Figure G-1 shows a diagram of the experimental set-up. The natural circulation loop consists of a vertical annular heated section, a vertical straight pipe heat exchanger with four parallel branches, and the connected piping. The hot leg is the piping connecting the top of the heater to the top of the heat exchanger. The cold leg is the piping connecting the bottom of the heat exchanger to the bottom of the heater. The physical dimensions of each segment is given in Table G-1.

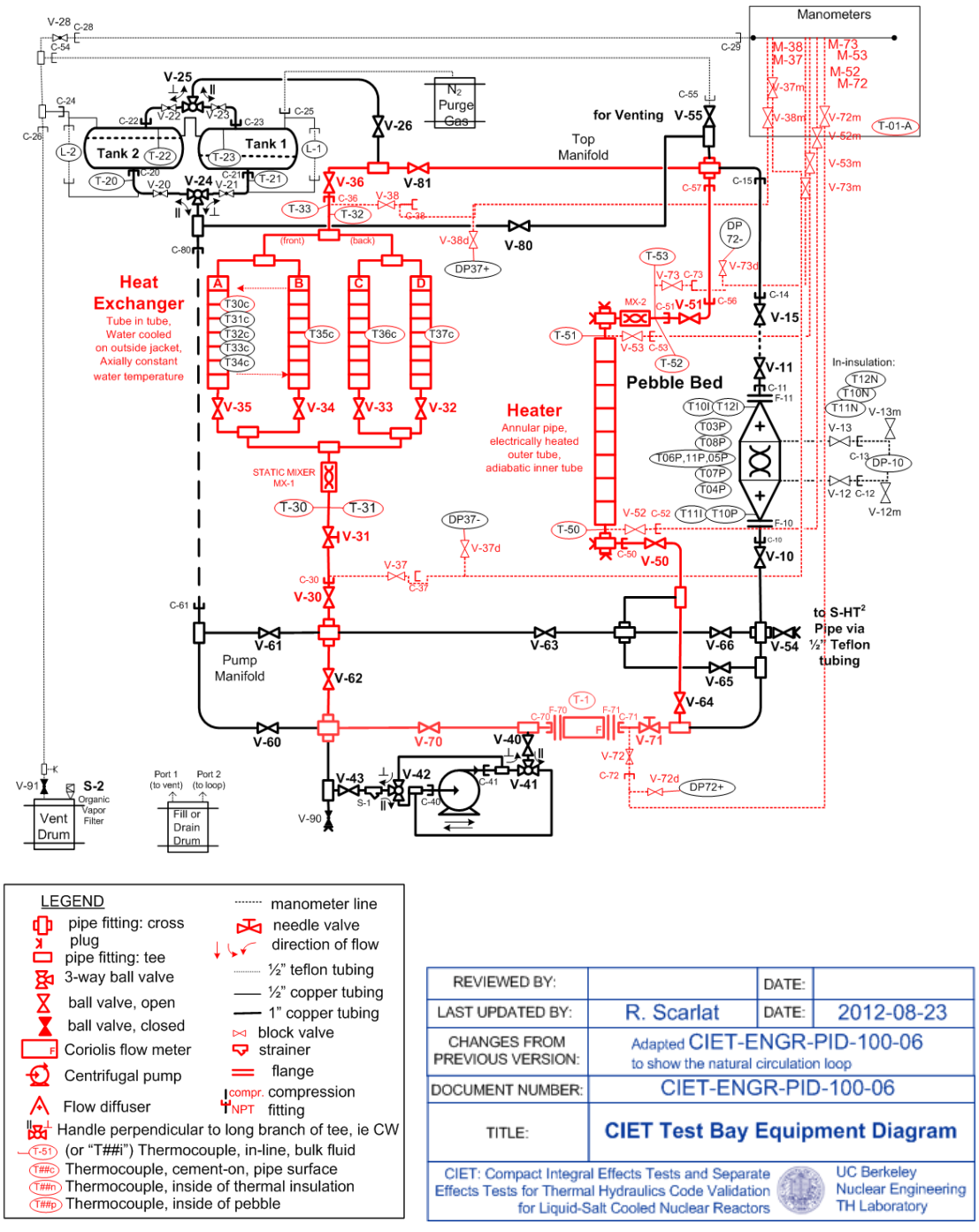

Figure G-1. CIET Test Bay, as-built diagram. Red color indicates the flow path and instrumentation for the natural circulation experiment.

Table G-1. Physical Parameters of the Natural Circulation Loop

Elevation Change (SI units)		
heated section	1.4605	dz.1
hot leg	0.8396	dz.2
cooled section	-1.0110	dz.3
cold leg	-1.2891	dz.4
buoyancy head	1.0643	dz.loop

Heated Section (SI units)		
OD of annulus	0.01930	
ID of annulus	0.01372	
hydraulic diameter	0.005580	dh
annulus length	1.7810	Lh
heated length	1.4605	
cross-sectional area	1.447E-04	Ah
	38.56	dh/Ah
	1.524E+10	Ch
	1	Dh

Piping (SI units)		
pipe diameter	0.02664	d1in
cross-sectional area	5.576E-04	A1in
length of hot leg	3.34700	
length of cold leg	2.36930	
total length of piping	5.71630	l1in
	47.79	d1in/A1in
	1.24	Re1in/Reh
	6.901E+08	C1in
	0.05	C1in/Ch
	0.04	D1in

Cooled Section (SI units)		
pipe diameter	0.02093	d34in
length	1.69560	l34in
cooled length	1.0111	
cross-sectional area	3.440E-04	A34in
	15.21	d34in/A34in/4
	0.39	Re34in/Reh
Cn = 1/A^2*l/d	6.844E+08	C34in
	0.04	C34in/Ch
	0.11	D34in

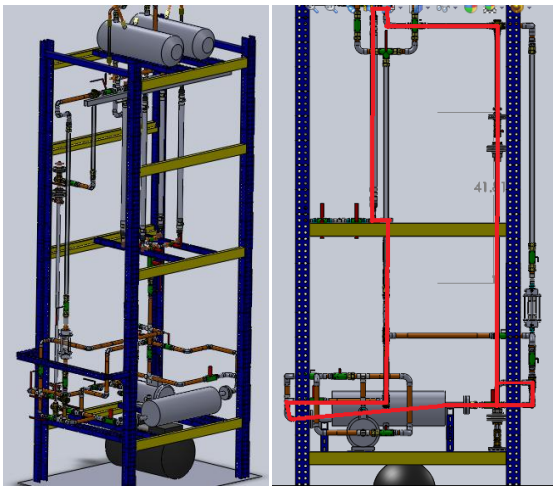

Figure G-2. CIET Test Bay front view (left), and side view showing natural circulation flow path (right). (SolidWorks model by A.J. Gubser).

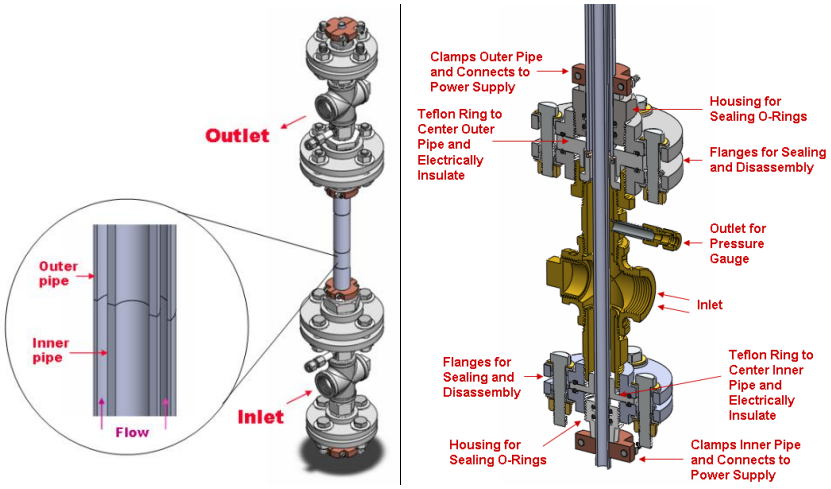

Figure G-3. Heater element for the CIET Test Bay (SolidWorks model by Niv Moran and Justin Tang).

Friction losses across the heater, the heat exchanger, and the piping in between were measured using three pairs of manometers. The locations of the manometers are indicated in . Figure G-1. The needle valves V-71 and V-31 were fully open for all experimental runs. The heater element is the principal contributor to friction losses in the natural circulation loop. The section shows the data and the calculation for the heater element only. The rest of the manometer readings are documented in the appendix.

Calculations on the data are performed using the following equations. The values for the parameters that characterize the heater geometry, C_h, d_h, and A_h, are given in Table G-1. The thermophysical properties of the Dowtherm A fluid are evaluated at the average temperature of

the heater, the average of T-50 and T-51 temperature measurements. The density of the fluid in the manometer lines is evaluated at ambient temperature, which is measured by T-01-A.

$$F'_h = \frac{2\rho(T_{h,av})}{m^2}\Delta P_h; f = \frac{F'_h}{C_h} \quad \text{(G-1)}$$

$$Re_h = \frac{m}{\mu(T_{h,av})} \cdot \frac{d_h}{A_h} \quad \text{(G-2)}$$

Manometer lines are paired such that at the connection point on the loop, the flow cross-sectional area is the same for the two manometer lines. This means that for pressure drop measurements, the velocity term of the Bernoulli equation can be disregarded. Manometer lines M-72, M-73, M-37, and M-38 connect to 1-inch tubing. Manometer lines M-52 and M-53 connect to the bottom and top heater head fittings, respectively; the heater head fittings have an annular internal geometry and they are identical to each other. Figure G-4 shows a photo of the heater head fittings; the tee-branch for connection of manometer line and in-line thermocouple is visible on the left fitting; the right fitting has an identical port, but it is not visible in the photo.

$$\Delta P = \rho(T_{amb})g\Delta h \quad \text{(G-3)}$$

Figure G-4. Photo of the heater head fittings for the CIET Test Bay.

Pressure drop measurements were taken with forced convection using the pump, with flow downwards through the heater and upwards through the heat exchanger. The loop was isothermal, with less than 1°C temperature rise across the heater, and less than 4°C between the maximum and the minimum temperatures on the loop. Data for pressure drop was collected on three days. The collected data is given in Table G-2. The calculation for the predicted friction coefficient, $f_{h,predicted}$, assumes laminar flow.

Table G-2. Isothermal pressure drop measurements, raw data

Date	Run #	pump direction	pump by-pass [%open] V-70	HX needle valve [x/6 open] V-31	heater needle valve [x/6 open] V-71	M-38 1	M-37 2	M-52 3	M-53 4	M-72 5	M-73 6	Flow Rate [kg/hr]	Av.HX bottom [oC] T-30, T-31	Av. HX top [oC] T-32, T-33	Av. Heater bottom [oC] T-50	Av. Heater top [oC] T-51, T-52, T-53	Flowmeter Temp [oC] T-71	Ambient temp [oC]
03-14	1	back	86	6	6	418	440	-1678	430	-1700	400	185	32.4	29.1	31.5	32.1	31.1	18.6
03-14	2	back	87	6	6	420	443	-1580	433	-1650	403	173	33.6	30	32.5	33.1	31.1	18.6
03-14	3	back	90	6	6	423	441	-1433	436	-1487	407	160	33.8	30.2	32.8	33.3	32.3	18.6
03-14	4	back	93	6	6	422	440	-1356	437	-1389	408	154	34.4	30.7	33.3	33.8	32.7	18.6
03-14	5	back	95	6	6	430	444	-1276	440	-1314	407	147	34.9	31	33.7	34.3	33.1	18.5
03-14	6	back	97	6	6	428	440	-1216	444	-1248	410	143	35.3	31.4	34	34.8	33.6	18.5
03-14	7	back	100	6	6	431	441	-1133	444	-1176	411	134	35.7	34.4	34.4	35.1	33.8	18.6
03-01	1	bkwd	100	6	6	610	V-37 closed	-930	580	-940	595	341	27		27.3			20.4
03-01	4	bkwd	100	6	6	605	V-37 closed	-900	555	-875	590	407	30.3	27.3	29	29.8	27.94	19.8
03-01	5	bkwd	99	6	6	610	V-37 closed	-900	555	-870	585	496	31.6	28.3	30.4	31.1	29.01	19.8
03-01	6	bkwd	95	6	6	605	V-37 closed	-915	555	-885	585	571	32.4	29	31.3	31.4	30.19	19.8
03-01	7	bkwd	85	6	6	590	V-37 closed	-1220	525	-1190	570	614	33.3	29.8	32.3	32.8	31.14	19.7
03-01	8	bkwd	75	6	6	570	V-37 closed	-1980	485	-1965	540	510	33.9	30.4	33	33.7	32.4	19.6
12-23	2	100	100	6	6	305	385	-1160	240	-1180	285	473	25					20
12-23	4	95	95	6	6	310	372	-1870	244	-1890	290	680	25					20

Figure G-5 shows a snapshot of the hot leg piping, with a view of two static legs that branch off from the cross fitting located at the top of the natural circulation loop.

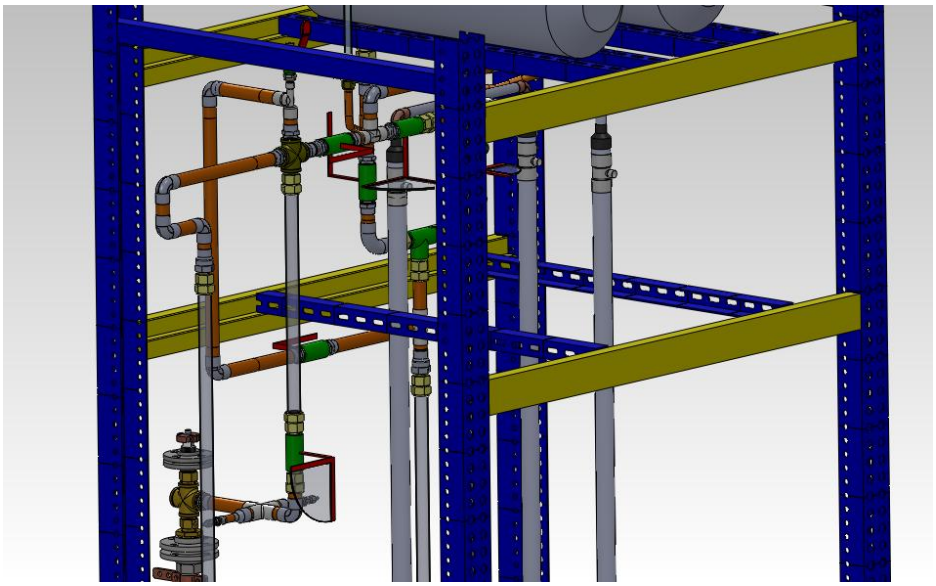

Figure G-5. SolidWorks snapshot of the hot leg, and the top heater head (SolidWorks drawings by A.J. Gubser)